

Simulation study of InGaN/GaN multiple quantum well solar cells

Yassine Sayad^a and AbdelKader Nouiri^b

^aDépartement de Science de la Matière, Faculté de Sciences et Technologies, Université Mohammed Chérif Messaâdia, Route de Annaba, Souk Ahras 41000, Algérie

^bDépartement de Science de la Matière, Faculté de Sciences, Université Larbi Ben M'hidi, Oum El-Bouaghi 4000, Algérie

Received: 30 April 2014, accepted 26 May 2014

Abstract

It's known that indium gallium nitride InGaN alloys has a direct band gap varying from 0.7 to 3.4 eV which covers nearly the whole solar spectrum making it material of choice to make tandem solar cells. In other hand, it's experimentally known that uses of InGaN/GaN multiple quantum well MQW structures in GaN based devices decreases surface recombination and, thus, enhances devices performance. Here, we present a simulation study of multiple quantum well MQW InGaN/GaN solar cells, where cell's active region is formed by a number of InGaN quantum wells (QWs) separated by GaN quantum barriers (QBs). We will present indium element content of In_xGa_{1-x}N wells and number of InGaN/GaN periods impacts on solar cell parameters.

Key words: solar cell, InGaN/GaN MQWs, photovoltaic parameters.

1. Introduction

III-nitrides compound semiconductors (GaN, InN, AlN) and their alloys have excellent physical properties, mainly, good thermal conductivity and high stability under extreme conditions of irradiation. They were find application in fabrication of blue and ultraviolet LEDs and lasers, and, since the 2000s were begun to be studied as photovoltaic materials. This came to the facts that this semiconductors have direct gaps covering the entire solar spectrum, for example, InN have optical gap of 0.7 eV (1771nm) and GaN a gap of 3.4 eV (366 nm), and theoretically a multijunction cell formed by the stacking of three In_xGa_{1-x}N cells can yield 70% of conversion efficiency [1]. In other hand, single junction *p-i-n* solar cells with multiple quantum wells InGaN / GaN have same potential of multijunction cells with a less complicated structure and, also, higher open circuit voltage [2] and less surface recombination velocities.

In this work we will look at photovoltaic properties of InGaN/GaN MQW solar cells, especially, band structure, I-V characteristics and quantum efficiency.

2. Studied cells structure

Simulated cells structure (figure 1) consists of a 0.25 micron p type GaN top layer with doping level of $3 \cdot 10^{17} \text{cm}^{-3}$ and a 2 micron n type GaN bottom layer with doping level of 10^{18}cm^{-3} . Between top and bottom layers exist an undoped (experimentally, undoped GaN layers are lightly n type due to structure defects) multi-quantum wells MQW region where InGaN quantum wells QWs of 3nm thick are separated by GaN quantum barriers QBs of 7nm thick. We note that, thickness of QWs and QBs are fixed in all subsequent simulations.

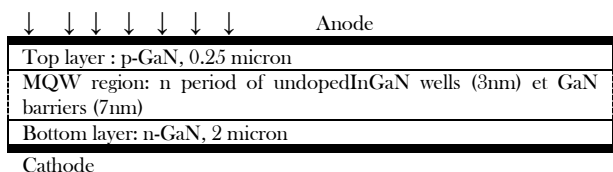


Fig.1 Schematic of simulated InGaN/GaN MQW solar cells.

In our simulation using SilvacoAtlas software package we have tacking into account spontaneous and piezoelectric

polarizations that naturally occurs in devices grown by Metal-Organic CVD technique on substrates with different lattice parameter [3]. Band structure of above simulated cell is presented below in figure 2 for 20% of indium element content.

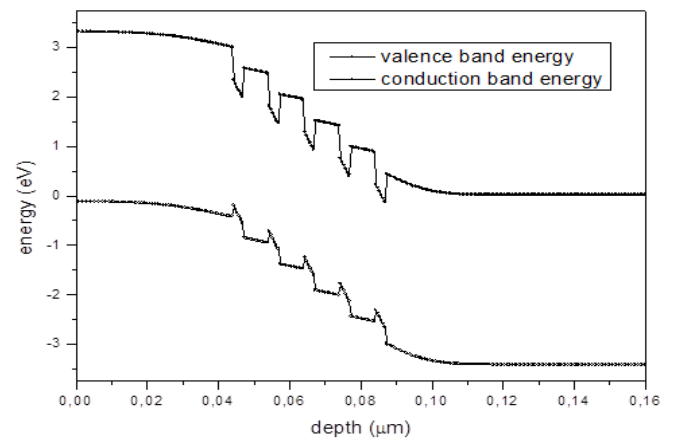


Figure. 2. Band structure of 5 period In_{0.2}Ga_{0.8}N/GaN MQW solar cell.

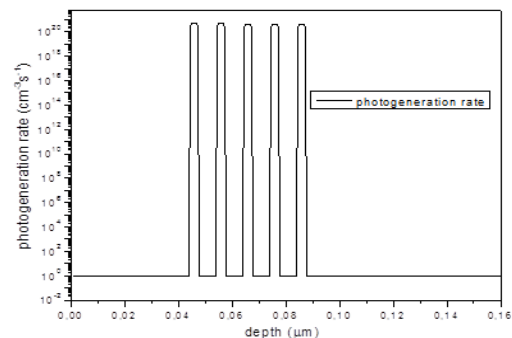


Figure 3. Photogeneration within a 5 period In_{0.2}Ga_{0.8}N/GaN MQW cell under AM1.5 spectrum.

3. Results and discussion

In figure 3 is shown photogeneration rate versus depth under AM1.5 spectrum where charge carriers are, namely, generated within InGaN quantum wells regions.

To our knowledge the best yield obtained experimentally on such cells is achieved by Dahl is around 2.95 percent under AM 1.5 irradiation [4]. Figure 4 shows dark and light (under AM1.5 illumination conditions) J-V characteristics as well as power versus bias curves of above cell, where shortcurrent is find to 0.112mA, open circuit voltage is 2.78V and conversion efficiency of 2.96 percent.

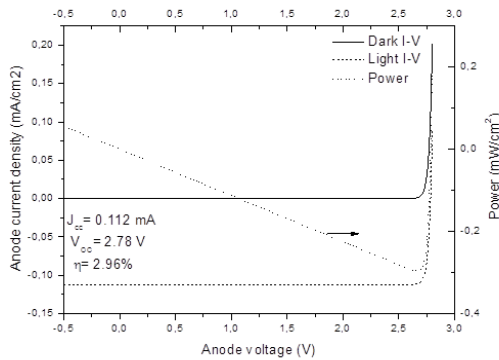


Figure 4. J-V characteristics of 5 period $\text{In}_{0.2}\text{Ga}_{0.8}\text{N}/\text{GaN}$ MQW solar cell

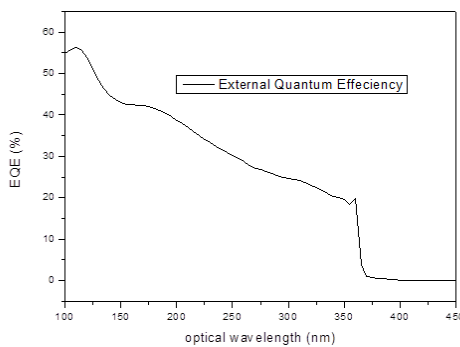


Figure 5. Calculated quantum efficiency of 5 period $\text{In}_{0.2}\text{Ga}_{0.8}\text{N}/\text{GaN}$ MQW solar cell

We after checked possible influence of indium content and number of InGaN/GaN pairs on cell parameters. In Table 1 are listed cell parameters for various contents of indium, where we find that there not any variation until 25% of

indium. But, on the contrary, increasing numbers of QW/WB periods enhances cells photovoltaic parameters, Table 2.

x.comp	0.15	0.2	0.25
Jcc (mA)	0.112	0.112	0.112
Voc (V)	2.78	2.78	2.78
Conversion efficiency (%)	2.96	2.96	2.96

Table 1. Photovoltaic parameters of InGaN/GaN MQW cell for different fractions of indium element.

Number of periods	single well	5	10	15
Jcc (mA)	0.108	0.112	0.212	0.284
Voc (V)	2.72	2.78	2.81	2.81
Conversion efficiency (%)	2.80	2.96	5.63	7.56

Table 2. Photovoltaic parameters of InGaN/GaN MQW cell for different numbers of QW/QB periods.

We are also performed external quantum efficiency calculation, figure 5, to see spectral response of cell. Where, comparing to crystalline cells, InGaN/GaN MQW cells present a higher efficiency in UV region and a sharp decrease beyond $0.37 \mu\text{m}$. This means that, for example, a tandem cell containing GaN top cell and Silicon bottom cell will have broader and higher quantum efficiency.

4. Conclusion

III-nitrides are very interesting materials in photovoltaic point of view, and multiple quantum wells based solar cells structures have potential to achieve high efficiencies. We are find that more number of wells causes more efficiency and there are no impact of indium element content of well on cells parameters within 15-25% frame.

Acknowledgment

Present Silvaco® TCAD simulations were made at Institut des Nanotechnologies de Lyon INL at INSA de Lyon (France). Thus, first author would like to thanks Dr. Danièle Blanc-Pélissier for permission to use laboratory platform.

References

- [1] Bremner, S.P., Levy, M.Y. and Honsberg, C.B. Progress in photovoltaics: Research and Applications. 2008, Vol. 16, 225
- [2] Zhang Xiao-Bin et al, Chin. Phys. B Vol. 20, No. 2, 028402, 2011
- [3] Omkar K. Jani, Development of wide-band gap InGaN solar cells for high-efficiency photovoltaics, Ph. D thesis, Georgia Institute of Technology, 2008.
- [4] R. Dahal, J. Li, K. Aryal, J. Y. Lin, and H. X. Jiang, InGaN/GaN multiple quantum well concentrator solar cells, Appl. Phys. Lett. 97, 073115, 2010

Nanostructured metallic oxides coating

Mostefa Benhaliliba

Department of Material Technology, Physics Faculty, USTOMB University, BP1505 Oran, Algeria.

Received: 30 April 2014, accepted 26 May 2014

Abstract

This project has been focused on structural, morphological, optical and photoluminescence properties of pure ZnO thin film. Here, zinc oxide thin films are grown on glass via facile and low cost sol gel spin coating process @ fixed spinning speed of 1000 RPM. The X-ray patterns, the transmittance, the particle size by the atomic force microscope are investigated. The particle size is equal to 120 nm and the surface roughness is found to be 23.33 nm. The photoluminescence analysis reveals near band emission and strong visible emission 2.11 and 2.80 eV.

Keywords: Spin coated ZnO films; X-rays pattern; transmittance; photoluminescence; SEM; TEM; Electron diffraction; AFM.

1. Introduction

Nowadays, zinc oxide (ZnO) film is the most studied material due to its various properties such as high transmittance in visible range, direct band gap around 3.3 eV, high exciton binding energy of 60 meV [1]. Zinc oxide was prepared by many techniques such as sol gel spin coating [2], spray pyrolysis deposition (SPD) [3-4], sputtering [5] and chemical vapor deposition CVD [6]. We use the sol gel spin coating as film deposition technique because it is low cost, facile, rapid, unobtrusive and environmental process. All these prompted features of this multifunctional material, attract many researchers to use it in many applications like sensors, light emitting diodes, piezoelectric and catalytic devices. Here, ZnO nanostructures are achieved by facile sol gel route. ZnO nanostructures have been successfully prepared in several morphologies like nanorods and nanowires [7-8]. This paper consists on detailed study of the structural, surface morphology, optical, photoluminescence properties of zinc oxide grown onto glass by a facile spin coating route. Furthermore ZnO nanorods were successfully synthesized and investigated by high resolution field emission transmission electron microscope (FE-TEM), electron diffraction, field emission scanning electron microscope (FE-SEM) and

electron dispersive X-rays analysis (EDX) and atomic force microscope (AFM) analysis.

2. Experimental details

The ZnO films are produced by sol gel spin coating route. The substrate used is a microscope glass slides 76 x 26 mm supplied by object trager Isolab. 0.5 Molar of dehydrated zinc acetate ($Zn(CH_3COO)_2 \cdot 2(H_2O)$), (99.5%) supplied by Carlo Erba reagents, is dissolved in 10 ml of 2-Methoxyethanol stirred at 60°C for 10 mn and then 0.3 ml of the mono-ethanolamine (MEA) as stabilizer is added drop by drop, the clear solution is then obtained, the stirring continued for 1 hour. Consequently, the solution followed an ageing process for one day. Initially, the glass substrates were cleaned by a soft soap solution, washed systematically with the distilled water, then with ethanol in ultrasonic cleaner and finally were dried with argon. Using a micropipette the obtained gel was homogenously poured, on the substrate deposited on plates of spin coater (MTI, EQ-TC-100 desk-top type). The sample spins for one minute at 1000 RPM (rotate per minute); the sample is instantly heated at 150 °C for 10 mn. The process is repeated 5 times; finally the film is annealed at 400 °C for 1hour under air in furnace. In that way, the coated films are investigated by Shimadzu 3600 PC double beam UV-VIS-NIR spectrometer, the surface morphology is analyzed by the mean

of field emission scanning electron microscope JEOL JSM 7001F FE-SEM, the films are also examined by transmission electron microscope JEOL JEM 2100F FE-TEM and the chemical analysis of films is given by electron energy dispersive X-ray (EDX) spectrometers. Furthermore, morphology is explored by atomic force microscope Park system XE-100E Non contact cantilever Si used 256x256 pixels. Room temperature photoluminescence characterization is carried out using an experimental setup consisting of: a 325 nm 15 mW He-Cd laser (Kimmon), a 0.85 m double monochromator (SPEX, model 1404), and a GaAs photon counting photomultiplier (Hamamatsu). The range explored is from 350 to 600 nm, in 0.5 steps and a speed of 0.2 seconds/measured point.

3. Results and discussion

3.1. Structural properties investigation

The X-ray diffraction pattern for zinc oxide film recorded at room temperature is shown in Fig.1. The strong peak, well known (002) located at $2\theta=34.42^\circ$, given by JCPDS card N° 36-1451 is displayed by a red dash line as depicted in figure 1. The as-grown films were identified as polycrystalline ZnO with a wurtzite crystal structure and preferred orientation along the (002) plane. As can be seen in X-rays spectra, film exhibits a polycrystalline structure and most of peaks are broadened. Since base of peaks are enlarged, the full width at medium height (FWMH) increases and grain size G , expressed as follows, is reduced [4];

$$G = \frac{K\lambda}{\beta \cos\theta} \quad (1)$$

Where K is constant estimated at 0.94, λ is the wavelength of the X-ray used 1.54 Å, β is the full width at half maximum (FWHM) which has maximum intensity and 2θ is the Bragg angle.

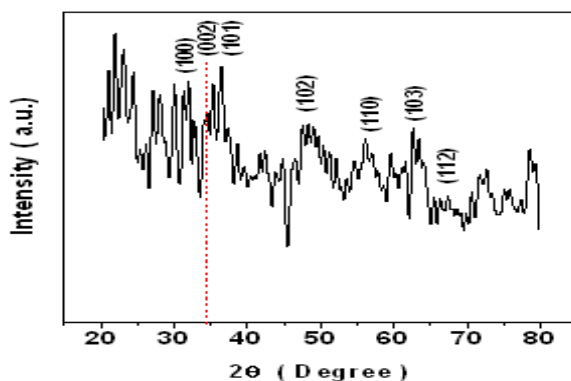


Figure 1: X-rays pattern of zinc oxide at room temperature; two-theta range is 20°-80°. Red dash line locates the peak (002) at 34.42°.

According the (002) orientation, the grain size G is about 120 nm, the reticular distance d is of 0.26 nm and the textural coefficient is 1.1.

3.2. Microscopy observation

The AFM micrographs reveal that zinc oxide exhibit the nanorods which have grown according to z-axis direction as shown in figure 2. This result is confirmed by SEM observation (see figures 2 and 3). All elements analyzed are normalized as described in EDX as listed in table 1, Zn occurrence is obviously indicated, silicon may come from substrate glass, insignificant amounts of calcium (Wollastonite, CaSiO₃) and magnesium (MgO) are present respectively as impurities in starting precursor. The Honeycomb architectures are apparent in picture having diameter found to be 10 nm (as indicated by red arrow). It is confirmed that FE-TEM picture exhibits regular inner of sample and very slight pores density. Electron diffraction pattern show spots which located according to X axis and Y axis, the scale is 50 nm (see the fig 3 top). The Honeycomb architecture is visible at the higher magnification image shown in figure 3 (bottom). 3D-AFM picture shows evidently nanorods which grown one beside each other perpendicular to substrate surface as depicted in figure 4.

3.3. Optical Characterization

Figure 5 shows the dependence of transmittance T (%) and reflectance R (%) on incident photon wavelength which ranges within 200-2500 nm. T increases rapidly in UV spectrum, and reaches up to 86 % in visible range, as depicted inset of figure 5, and then varies slightly between 82 and 93% both in VIS and IR spectra. Reflectance attains 9.5 % at 384 nm, but it still minor in the whole photon wavelength range. The band gap energy of the ZnO films can be determined by the following relation,

$$(\alpha h\nu)^2 = h\nu - E_g \quad (2)$$

Where E_g (eV) is the optical band gap, α (m⁻¹) is the absorption coefficient and ν (Hz) is the photon frequency. Figure 6 depicts how the direct energy gap of the coated film has been estimated by extrapolating the linear part of $(\alpha h\nu)^2$ plot versus photon energy to the wavelength axis. It found to be 3.26 eV, which agrees well with our previous result [1-4].

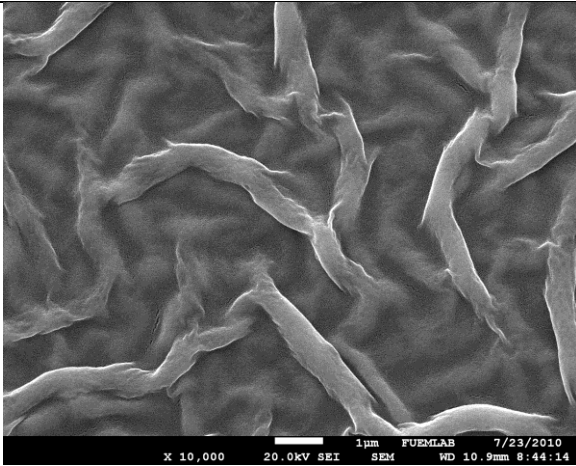


Figure 2: Field effect scanning electron microscope (FE-SEM) picture at low magnification (x10 000, 20KV) (top), EDX spectrum is displayed (bottom).

Element	App Conc.	Intensity Corr.	Weight%	Weight% Sigma	Atomic%
C K	1.15	0.2796	2.89	0.34	5.64
O K	53.67	0.9078	41.55	0.33	60.92
Mg K	1.06	0.5516	1.35	0.07	1.30
Si K	27.00	0.7730	24.54	0.20	20.50
Ca K	6.21	0.9854	4.43	0.08	2.59
Zn K	29.80	0.8297	25.24	0.30	9.06
Totals			100.00		

Table 1. EDX analysis results of ZnO film produced @ 1000 RPM.

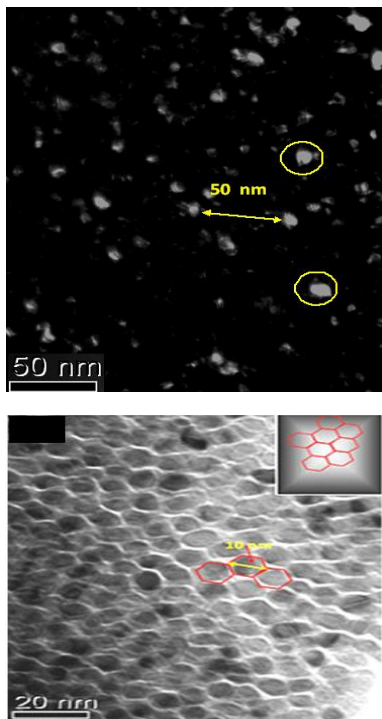


Figure 3. A high-resolution TEM image and an electron diffraction pattern obtained for coated sample ZnO produced at 1000 RPM (top), bright field TEM image (bottom).

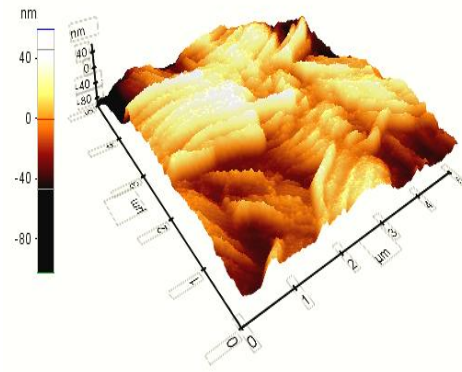


Figure 4. 3D-AFM view of spin coated ZnO film.

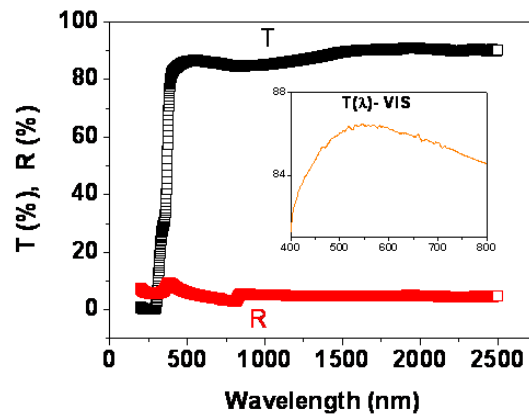


Figure 5. Transmittance (balck curve) and Reflectance (red curve) plots against photon wavelength of spin coated ZnO film, inset shows the transmittance in visible range.

3.4. Photoluminescence analysis

The optical properties of the coated zinc oxide films nanorods are examined using photoluminescence at room temperature as shown in figure 7. PL spectrum exhibits various emission bands, including strong near band edge emission peak located respectively at 442 nm (2.80eV) which corresponds to blue emission. This emission peak may prove that ZnO nanorods have high cristallinity. Others peaks of low intensity located at 447nm -538nm (2.77eV-2.30eV), which correspond respectively to green band emission. These bands might due to defects occurrence such as oxygen traps.

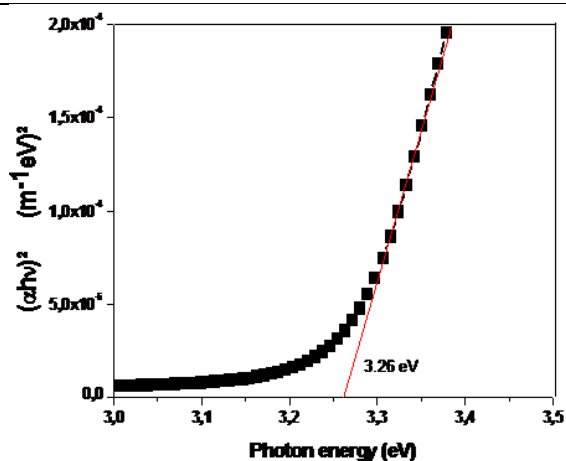


Figure 6. Absorbance variation versus photon wavelength of spin coated ZnO film, optical band gap, $E_g = 3.26$ eV, is deduced.

ZnO exhibits the emission peaks with different energies 2.11-2.82 eV as listed in table. The strong emission is apparent in visible spectrum. Photoluminescence spectrum shows near band edge NBE and defects emissions. The Gaussian deconvolution ascribed the strong PL peaks to the following positions: 587.73 ± 0.02 nm (2.11 eV), 534.38 ± 0.59 nm (2.32 eV), 545.88 ± 1.27 nm (2.27 eV) and 433.46 ± 2.57 nm (2.86 eV).

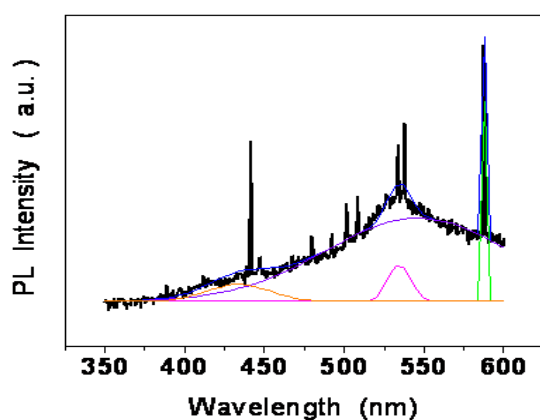


Figure 7: Room temperature photoluminescence spectra of undoped ZnO against wavelength (300-600 nm), curves of deconvolution fitting are displayed.

4. Conclusion

Zinc oxide nanorods were successfully synthesized by facile sol gel spin coating route. It reveals that zinc oxide was present in high amount in coated film by XRD pattern and EDX analysis. These ZnO nanorods were high transparent in VIS and IR ranges. SEM and TEM images reveal clusters presence at nanoscale, and the Honeycomb architecture is observed at high magnification. Strong visible emissions are detected by PL investigation.

Acknowledgements

The work, under contract number **D01920120039**, is included in project CNEPRU supported by the Algerian High Level Teaching and Scientific Research Ministry MESRS and Oran Sciences and Technology University USTOMB. The author would like to acknowledge the generous assistance of Mr. U. Akgül, FUMELAB laboratory, Firat University Turkey, for their fruitful help in performing SEM observations.

References

- [1] C. Aydın & M. Benhaliliba & Ahmed A. Al-Ghamdi & Zarah H. Gafer & Farid El-Tantawy & F. Yakuphanoglu, *J Electroceram.* DOI 10.1007/s10832-013-9829-5, (2013)
- [2] M. Benhaliliba, C.E. Benouis, A. Tiburcio-Silver, Y.S. Ocak, *EPJ Web of Conferences*, DOI: 10.1051/Owned by the authors, published by EDP Sciences, 2013,epjconf/20144 03003 (2013) 34403003.
- [3] M. Benhaliliba, C.E. Benouis, Z. Mouffak, Y.S. Ocak, A. Tiburcio-Silver, M.S. Aida, A.A. Garcia, A. Tavira, A. Sanchez Juarez, *Superlattices and Microstructures* 63 (2013) 228-239.
- [4] M. Benhaliliba, C. E. Benouis, M. S. Aida, F. Yakuphanoglu, A. Sanchez Juarez, *J Sol-Gel Sci Technol* (2010) 55:335-342 DOI 10.1007/s10971-010-2258-x
- [5] Y.S. Ocak, *J. Alloys Compd.*, 513 (2012) 130-134.
- [6] X. Li, Y. Yan, T.A. Gessert, C.L. Perkins, D. Young, C. DeHart, M. Young, T.J. Coutts, *J. Vac. Sci. Technol. A* 21 (3) (2003) 1342-1346.
- [7] Hoang-Si Honga, Gwi-Sang Chung, *Sensors and Actuators B*195 (2014) 446-451.
- [8] Y. Abdi, S.M. Jebreil Khadem, P. Afzali, *Current Applied Physics* 14 (2014) 227-231.

Electronic and structural properties of NaZnAs compound; an ab-initio study in the tetragonal and cubic α phases

S. Noui^a, Z. Charifi^b, H. Baaziz^b and M. Guezlane^a

^aDepartment of physics, Faculty of Science, University of Batna, 05000 Batna, Algeria

^bDepartment of physics, Faculty of Science, University of M'sila, 28000 M'sila, Algeria

E-mail adress: sameh.noui@gmail.com (S. Noui).

Corresponding author. Tel./ 0795697934

Received: 30 April 2014, accepted 26 May 2014

Abstract

A theoretical study of structural, and electronic properties of NaZnAs compound is presented by performing ab initio calculations based on density-functional theory using the full-potential linear augmented plane wave (FP-LAPW). The generalized-gradient approximation (GGA) and the local density approximation (LDA) are chosen for the exchange-correlation energy. The Engel-Vosko (EVGGA) formalism is applied for electronic properties. The calculated structural parameters, such as the lattice constant, bulk modulus and pressure derivative, the electronic band structures and the related total density of states and charge density are presented. The high-pressure α phase of the NaZnAs is investigated and phase transition pressure from tetragonal to high-pressure phase is determined. We have found that the Nowotny-Juza compounds NaZnAs is direct gap semiconductor at ambient pressure. The bonding character and the phase stability of NaZnAs compound are discussed. The nature and the size of the band gap of NaZnAs compound are associated with the bonding character of two kinds of bonds, namely, Na-As and Zn-As bonds.

Keywords: Electronic materials; Ab initio calculations; Electronic structure ;Phase transitions

1. Introduction

Generally the crystal structure of Nowotny-Juza compounds AIB₂ICV can be derived from the zinc-blende III-V compounds by transmuting the group III atom into an isovalent pair I+II, and are found to crystallize mostly in cubic zinc-blende-type related structures [1-6]. NaZnAs form a special case, which is found to crystallize in tetragonal Cu₂Sb-type of structure [1,7]. NaZnAs is also found to crystallize in the MgAgAs (order CaF₂-) type structure [1, 8, 9].

Although Lithium Nowotny-Juza compounds are studied elsewhere, to the best of our knowledge there has missed investigation of NaZnAs compound in terms of electronic, structural [1]. NaZnAs compound

which belong to the same group but with tetragonal Cu₂Sb type structure (space group P4/nmm) [1] in contrast to cubic lithium semiconductor such as LiZnAs

compound. In the present work, using the DFT approach we studied the tetrahedral Nowotny-Juza compound NaZnAs. We derived electronic properties for this compound and we also investigated the influence, of the pressure and As atomic on the electronic structure. In Section 2, we report some details about the crystal structure and the numerical calculations. We concentrate on the equilibrium lattice constant, bulk modulus in Section 3.1. We focus on the electronic properties in terms of band structures, density of states and charge density in Section 3.2. Finally; we draw conclusions in Section 4.

2. Calculation method

In this paper, we describe the results of the first principles electronic structure calculations of NaZnAs compound in the tetragonal Cu₂Sb-type and cubic α (MgAgAs-type) of zinc blende-type, related structures. The calculation are performed using ab initio

calculations based on density-functional theory using the full-potential linear augmented plane wave (FP-LAPW).

2.1. Crystal structure

NaZnAs compound crystallize at ambient pressure in the tetragonal structure with space group (129) P4/nmm. The unit cell contains two molecules per formula unit this is shown in Fig. 1. In the cubic (α) phase under pressure, there are 3 atoms by unit cell is shown in Fig. 2. The calculations presented in this work were performed using the full potential linearized augmented plane wave (FP-LAPW) method. We augmented plane wave (FP-LAPW) method. We use the WIEN2K [10] implementation of the method which allows the inclusion of local orbitals in the basis improving upon linearization and making, possible a consistent treatment of the semicore and valence states in an energy window. The electron-electron interaction was treated within local density approximation (LDA) [11] and generalized gradient approximation (GGA) by Perdew, Burke and Ernzerhof PBE) exchange-correlation potential [12] In addition, and for the electronic properties we also applied the Engel-Vosko (EV-GGA) scheme [13].

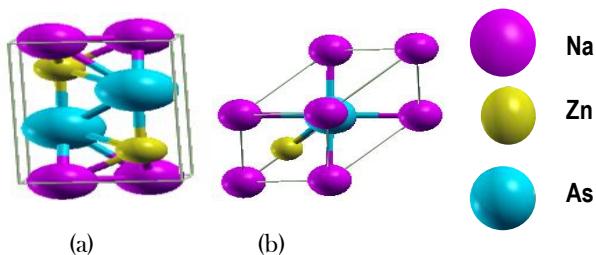


Fig.1. (a) Schematic diagram of the unit cell of NaZnAs in primitive tetragonal CuSb-type structure and (b) the unit cell of the α phase of cubic NaZnAs.

3. Results and discussion

3.1. Total energy calculations and phase transition

NaZnAs compound belong to Nowotny-Juza compounds AIBICV which based on three main group elements (A, B and C). They can be viewed as zinc-blende III-V compound in which the III column has been disproportionated into AI + BII atoms [1,8,14]. The most stable phase of NaZnAs in contrast to the most cubic Nowotny-Juza compounds which crystallize in α phase [1,8,14,15]. This fact is confirmed by Jaiganesh et al. [1] using the tight-binding linear muffin-tin orbital method within the local density approximation (LDA). The atomic position of NaZnAs in the tetragonal phase are

Na ($1/4, 1/4, z$); ($3/4, 3/4, 1-z$), Zn ($1/4, 3/4, 0$); ($3/4, 1/4, 0$), As ($1/4, 1/4, z$); ($3/4, 3/4, 1-z$), with z parameter for NaZnAs compound is; Na (0.3596), and As is (0.7807).

this structure transforms to cubic α phase with Fm-3m space group and the atomic position of NaZnAs in the cubic α are Na ($1/2, 1/2, 1/2$), Zn (0, 0, 0), As ($1/4, 1/4, 1/4$). The structure of this compound were optimized by calculating the total energy as a function of volume, which was followed by fitting the results with Murnaghan equation of state [16]. The calculated total energy versus volume using GGA approximation for NaZnAs compound in tetragonal and cubic α are shown in Table 1

Phase	NaZnAs compound		
	GGA This work	Exp [1,7,17]	Other work[1]
tetragonal			
a(A°)	4.192	4.176	4.121
c(A°)	7.115	7.088	/
c/a	1.697	1.697	1.697
B (GPa)	49.54	/	111.95
B'	3.87	/	/
E _{min} (Ry)	-16878.8226	/	/
α -phase			
a(A°)	6.350	/	5.916
B (GPa)	39.93	/	107.11
B'	4.33	/	/
E _{min} (Ry)	-8439.3747	/	/

Table 1 Calculated lattice constants (a and c) in Å, bulk modulus (B) in GPa and pressure derivative B' at equilibrium volume using GGA compared to and other works of NaZnAs.

Table 1 presents our calculated values obtained after optimization compared with the available experimental data and other theoretical results [1,7,18]. It is clearly seen that for the compound, the GGA overestimate the lattice parameter, Generally speaking our lattice parameters are in good agreement with those found experimentally and theoretically reported in Refs. [1,7]. Hardness measures a material's ability to resist deformation. Bulk modulus is the best indicator of hardness for materials. To estimate the bulk modulus, A big discrepancy was found in the values of the bulk moduli between the calculated values and those of Jaiganesh et al. [1], which is probably due to fact that they used the TB-LMTO method [1] within the LDA approximation.

NaZnAs compound transform from the initial tetragonal structure to the cubic structure under pressure (fig 2). The stability of a particular structure is decided by the minima of the Gibbs energy given by [19]:

$$G = E_{\text{tot}} + PV - TS$$

Since the theoretical calculations are performed at 0K the free energy becomes equal to the enthalpy (H):

$$H = E_{\text{tot}} + PV$$

The transition pressure from tetragonal phase to the α -phase for NaZnAs compound are listed and compared with the previous calculations and experimental data [1] Table 2. We note that a big disagreement is observed between our results and those of Ref. [1].

This is due to the fact that they have predicted the existence of tetragonal phase over a long range very short range. However from our calculation we predict it over very short range about 1 GPa. This suggest that NaZnAs compound prefer to be in the α phase like the majority of Nowotny- Juza compounds this is shown in fig 2

		Cu ₂ Sb \rightarrow α -phase	
		This work	other work[1]
NaZnAs	GGA	1.12	/
	LDA	1.26	15.75

Table.2. Calculated transition pressure values NaZnAs compound using LDA and GGA approximation

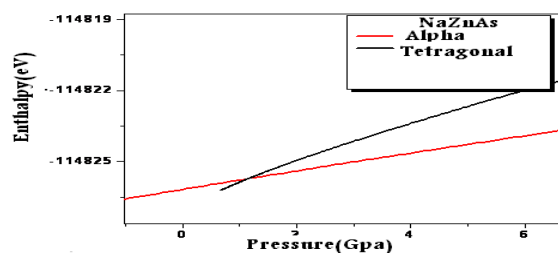


Fig.2. Variation of total enthalpy as a function of pressure of unit cell for tetragonal phase, α -phase using GGA for: NaZnAs compound

3.2. Electronic band structure and density of state

The self-consistent scalar relativistic band structures NaZnAs compound along representative symmetrical directions of the Brillouin zone were obtained in the tetragonal phase at equilibrium volume as well as at high pressure within the LDA, GGA and EV-GGA schemes. The Fermi level E_F is shown by a solide horizontal line. As a prototype we have shown the band structure and total density of states of NaZnAs using GGA approximation in the tetragonal and α - phase in Fig. 3. Accordingly, the conduction band minimum appears to be at the zone center C. Hence NaZnAs is direct gap semiconductor The calculated band gap E_{err} for NaZnAs is found to be 0.44 (0.39) eV using LDA (GGA), respectively in tetragonal phase The band structure calculated using the GGA and the EV-GGA for NaZnAs compound were similar except for the

value of their band gap which was higher within the EVGGA. The band gap values are given in Table, 3 compared with available theoretical works.

compound	tetragonal	α -phase
NaZnAs		
LDA	0.44	0
GGA	0.39	0
EVGGA	0.79	0
Exp[1,7,17]	/	/
Other work[1,20]	0.163	0

Table.3 Band gaps of NaZnAs compound within LDA, GGA and EVGGA calculated in all phases tetragonal, and α phases (all values are in eV).

It is shown that the calculated energy gap values decrease with increasing (the size).

. However NaZnAs transforms to a metal under the effect of pressure

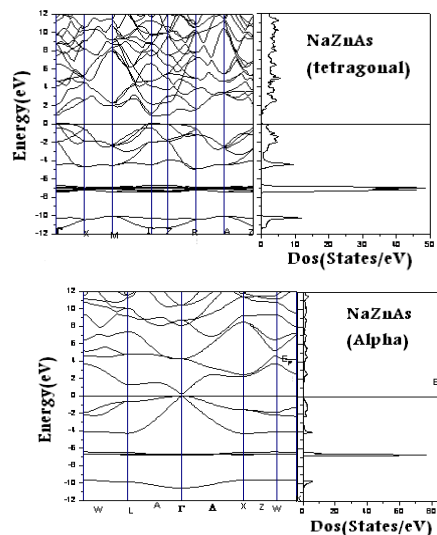


Fig 3. Band structure along the symmetry lines of the Brillouin zone and total densities of states for NaZnAs using EVGGA approximation for tetragonal phase. The position of the Fermi level is shown by the horizontal line for tetragonal phase and cubic α .

The total and partielle density of states (DOS) for NaZnAs compound at the equilibrium lattice constant is displayed at Fig.3. and Fig.4. respectively It is shown that there are two regions of the valence band, the upper valence bands are dominated by As-p and Zn-s, p orbitals while the bottom valence band is dominated by the As-s and Zn-d orbitals as shown in Fig. 4, the peaks are various according to the kind of structure. The nature of the bond for NaZnAs compound. We have calculated the total charge density of NaZnAs compound, in different planes and for different Phases.

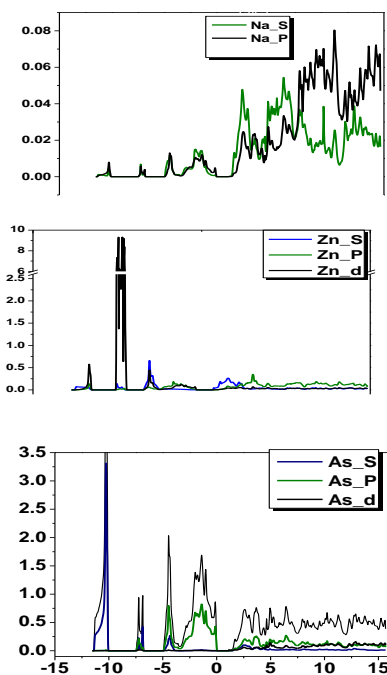


Fig 4. Partiell Density of states (Dos) for NaZnAs using EVGGA approximation for tetragonal phase.

Fig. 5 illustrates all the bonds in the (010) plane for tetragonal phase and (011) plane for α phase containing Na, Zn and As atoms. when the atom is As the Na-As bond becomes less ionic, and Zn-As becomes covalent in tetragonal phase.

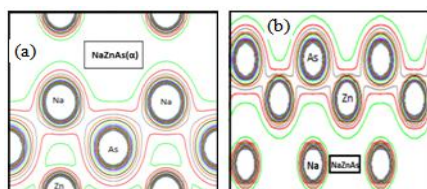


Fig .5. Calculated electron charge density in the (010) plane for tetragonal phase (a) and (011) plane for α -phase (b) of the NaZnAs compound.

4. Conclusions

The electronic and structural properties of NaZnAs, Nowotny-Juza compounds have been studied using both methods, the self consistent full-potential linear augmented plane wave (FP-LAPW). The bonding and the phase stability of NaZnAs compound is studied and it is concluded that the more stable phase, is the tetragonal phase under pressure this later transforms to α phase. The bulk modulus has been calculated using LAPW and gave excellent agreement with others. Basing on electronic band structure calculations

NaZnAs is a direct band gap semiconductor in the tetragonal phase with band gap of 0.79 eV using EVGGA approximation. The bonding in NaZnAs is characterized by the fact that Na-As and Zn-As bonds being nearly pure ionic and covalent, respectively in tetragonal phase. In α phase the small band gap. It is predicted that under high pressure, NaZnAs is a metal.

Reference

- [1] G. Jaiganesh, T. Merita, J. Phys.: Condens. Matter 20 (2008) 085220J.
- [2] S.Noui, Magister Thesis, 2012, Universiyof Batna (Algeria).
- [3] H. Nowotny And K Bachmayer Manatsh.Chem.81, 488,(1950)
- [4] H. Nowotny and Glatzl B Manatsh. Chem. 82, 720, (1951).
- [5] R juza and F. hund 1948 Z Anorg. Chem. 257 1 (1984)
- [6] R juza W Dethlefsen H Seidel and K banda Anorg Allg. Chem., 356, 253(1986).
- [7] P,Villars and L D Calverts earson's Handbook of Crystallographic Data for Intermetallic Phases 2nd edn, Vol 1 and 4 (Materials park, OH; ASM international, the materials international society) p1188,4508 ,4520.
- [8] A. E. Carisson, A. Zunger and D. M. Wood Phys. Rev. B 32 1386 (1985).
- [9] R. Bacewicz and T. F Cizek , Appl. Phys. lett. 52 1150 (1988).
- [10] P. Blaha, K. Schwarz, G. K. H. Madsen, D. Kvasnicka, J. Luitz, WIEN2K, An Augmented Plane Wave + Local Orbitals Program for Calculating Crystal Properties, Karlheinz Schwarz, Techn. Universitat, Wien, Austria, ISBN3-9501031-1-1-2, 2001.
- [11] D. M. Ceperley , B. J. Alder, Phys. Rev. Lett. 45, 566 (1980j).
- [12] J. P. Perdew, S. Burke et M. Ernzerhof, Phys. Lett. 77, 3865 (1996).
- [13] E. Engel, S. H.Vosko, Phys. Rev. B47, 20 (1993).
- [14] K. Kuriyama, T. Kato, K. Kawada, Phys. Rev. B 49 (1994) 11452.
- [15] K. Kuriyama, T. Kato, T. Tanaka, Phys. Rev. B 49 (1994) 4511.
- [16] F.D. Murnaghan, Proc. Natl. Acad. Sci. USA 30 (1944) 244
- [17] F. S. Gallasso Structure and Properties of Inorganic Solids 1st edn (oxford ;Pergamon) p 95 (1970)..
- [18] H. Kabbour, L. Cario, F. Boucher, J. Mater. Chem. 15 (2005) 3525.
- [19] M. Born, K. Huang, Dynamical Theory of Crystal Lattices, Clarendon, Oxford, 1954.
- [20] G. K. H. Madsen Am J. Chem.Soc.128 12140-6 (2006).

Photocatalytic degradation of Methylene blue by modified porous silicon nanowires

N. Brahiti^a, T. Hadjersi^b, H. Menari^b

^a *Université Mouloud MAMMERRI de TiziOuzou*

Département de physique, Nouvelle Ville, BASTOS, Algeria

^b *Centre de recherche en technologie des semiconducteurs pour l'énergie (CRTSE)*

2 Bd. Frantz Fanon, B.P. 140 Alger-7 Merveilles, Alger, Algeria

Received: 30 April 2014, accepted 26 May 2014

Abstract

In this paper, the effect of the time deposition of metal nanoparticles on the photodegradation of methylene blue is studied. The modified silicon nanowires were used as heterogeneous photocatalysts for the decomposition of methylene blue under UV light irradiation. The above reactions were monitored by UV-Vis spectrophotometer which shows the positive effect of the time deposition of metal nanoparticles on the photodegradation of methylene blue. 91% of the degradation was observed with the hydrogen terminated porous silicon nanowires and the degradation is about 95% for the modified porous silicon nanowires with Au (80min) and the same degree was obtained with Pt (120min) at 200 minutes of irradiation. The rate of the degradation reaches 100% at 90min of illumination with the decorated porous silicon nanowires with Pd nanoparticles.

Keywords: *silicon nanowires, chemical etching, photocatalysis, organic pollutants.*

1. Introduction

Photocatalysis has attracted much interest because of its potential application in clean energy sources to degrade organic pollutants from water [1, 2]. Semiconductors are commonly used as photocatalysts because of their wide ranging bandgaps. Among them TiO₂ has been studied the most because of its exceptional stability towards chemical and photochemical corrosion. Silicon is a low cost semiconductor and environmental friendly, which dominates integrated microelectronics. Although silicon displays a small energy band gap (1.1 eV), it is not used in pollution control because its valence band is not positive enough to oxidize

pollutant species. However, earlier reports by Yoneyama et al. showed that platinized n-type crystalline silicon and silicon powder are good photocatalysts for formic acid

decomposition [3]. More recently, Chen et al. used one dimensional hydrogen-terminated silicon nanowires (SiNWs), prepared by oxide-assisted-growth, under ultrasonic agitation for the degradation of methyl red. Independently, Shao et al. investigated the performance of hydrogen-terminated SiNWs and noble metal-modified (Pt, Pd, Au, Rh, Ag) SiNWs substrates for the degradation of rhodamine B and oxidation of benzyl alcohol to benzoic acid under visible light irradiation. It was found that hydrogen-terminated SiNWs exhibited better photocatalytic activity than Pd-, Au-, Rh- or Ag-modified SiNWs in the degradation of rhodamine B [4]. Also, Megouda et al. reported high performance of H-SiNWs and SiNWs coated with metal (Ag, Cu) nanostructures for the photodegradation of Rhodamine B under UV and visible light irradiation. In this study, we show that the modified SiNWs by metal nanoparticles (Au, Pt and Pd) with different time's deposition have an important effect on the photodegradation of methylene blue under UV light irradiation.

2. Experimental

2.1 Synthesis of porous silicon nanowires

n-Type (100) substrates with a resistivity of 0.0019–0.024 Ω .cm were used in this study. The silicon substrates were first cleaned by ultrasonication in ethanol, acetone and deionized water (30 min each), The cleaned silicon pieces were immersed into a beaker contained piranha solution for 20 min at room temperature, followed by disoxidation in HF10% for 1 min to remove the native oxide just before the Ag electroless chemical deposition in a solution containing 0.005M AgNO₃ and 4.8M HF for 1 min at room temperature. The silver-deposited Si pieces were rinsed with de-ionized water to remove extra silver ions and then immediately immersed into an etching bath containing 4.8MHF and 0.4M H₂O₂ for 60 min. The silver metal was removed from the nanowires by immersing the Si pieces in the concentrated nitric acid for 10 minutes. The SiNWs were decorated with metal nanoparticles by electroless deposition method.

2.2 Photocatalytic Experiment

The methylene blue solution with first concentration of 10⁻⁴M was prepared by dissolving methylene blue powder (Aldrich, 99.99%) in DI water. The dilute solution of the dye (10⁻⁶M) was prepared by diluting the mother solution with DI water with a magnetic stirrer at room temperature for 10 minutes. The experience of the photodegradation was carried out in a vat exposed to UV light irradiation in dark for 200 minutes; the measurement of the absorbance is effectuated each 20 minutes of illumination. The photocatalytic performance was measured by the decay of the absorption of the dye as a function of irradiation time.

3. Results and discussions

3.1 Morphological characterization

The SEM plan and cross section images of silicon nanowires were showed in figure.1.

The SEM images show that the silicon nanowires are porous, vertically aligned to the surface and reveal a length of 15 μ m approximatively and a diameter range of 50–200nm. The nanowire bundles were observed due to agglomeration at their tops-ends because of the von der waals force [5].

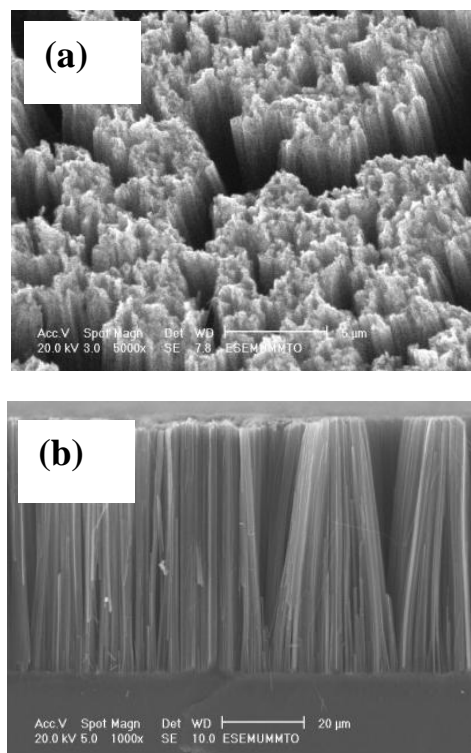


Figure1. Plan (a) and cross section (b) image of silicon nanowires.

3.2. Photocatalytic degradation of methylene blue

In this communication, we report on the high efficiency of hydrogen terminated porous silicon nanowires and decorated porous SiNWs with gold, platinum and palladium nanoparticles for the photodegradation of methylene blue under UV light irradiation. The photocatalytic degradation reaction was carried out at room temperature by immersion of the substrate into 4 mL aqueous solution of methylene blue. The photocatalytic performance was measured by the decay of the absorption of the dye as a function of irradiation time. Fig. 2 exhibits UV/vis spectra of methylene blue before and after UV light irradiation in the presence of a hydrogen-terminated silicon nanowires (H-SiNWs) substrate. The characteristic absorption band of methylene blue at 663 nm decreased significantly with increasing irradiation time. We have further examined the photocatalytic activity of oxidized SiNWs (SiNWs-Ox) and SiNWs loaded with Au, Pt and Pd nanoparticles substrates at different concentrations under UV light irradiation.

Figure 3. shows the comparison between the photolysis of methylene blue and the photocatalysis of the dye using oxidized silicon substrate (Ox-Si), oxidized porous silicon nanowires (Ox-SiNWs) and hydrogen terminated porous silicon nanowires (H-SiNWs), the results indicate that the photolysis presents a degradation of 29% of the dye at 200min, 40% of degradation is obtained with Ox-Si. The photocatalytic degradation with Ox-SiNWs substrate is much lower than that of the hydrogenated sample; the rates of the degradation are respectively 58% and 91%. Loading the porous silicon nanowires with Au, Pd and Pt nanoparticles at different concentrations show a positive effect on the performance of the photocatalyst. However, when the concentration of the metal nanoparticles NPs was significantly increased, a significant increase in the photoactivity was obtained. The degree of the degradation for SiNWs-Au (10min) is about 60% in comparison to 61% for Au (15min), 70% for Au (20min), 78% for Au (30min) and 95% for Au (80min) after 200 min of irradiation (Figure.4).

As seen in figure 5, the photodegradation using the platinum decorated porous silicon nanowires displays a degradation of about 65% for Pt (60min) and 95% for Pt (120min). The degradation with Pd decorated porous silicon nanowires is about 95% with Pd (120min) at 200 min and reaches 100% with Pd (180min) at 90 min of illumination under UV light (Figure.6).

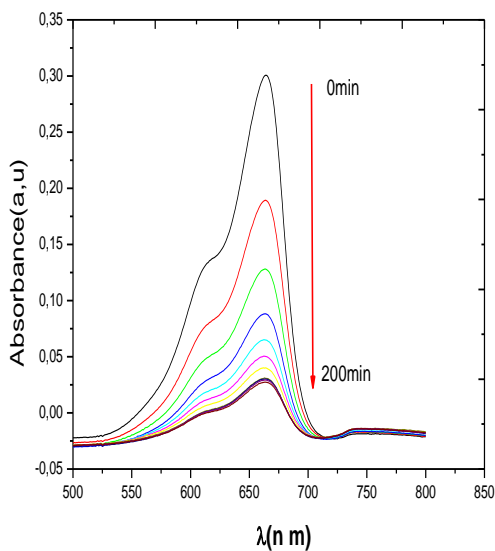


Figure 2. UV/vis absorption spectra of methylene blue before and after UV light irradiation in the presence of the hydrogen terminated SiNWs substrate as a function of irradiation time.

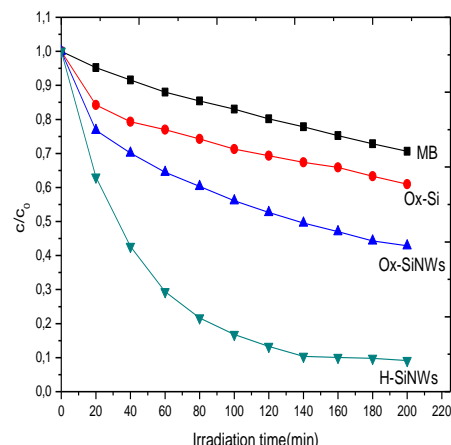


Figure 3. comparison between photolysis and photocatalysis of methylene blue using Ox-Si, Ox-SiNWs and H-SiNWs.

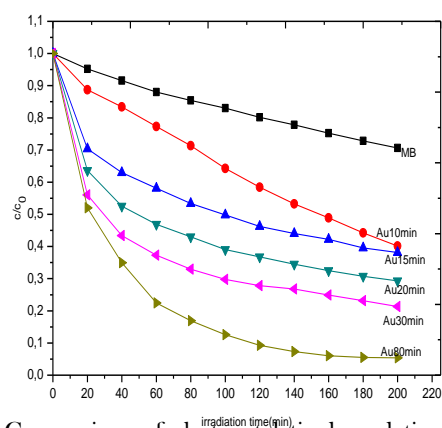


Figure 4. Comparison of photocatalytic degradation of methylene blue for different concentrations of Au nanoparticles as a function of time under UV light irradiation.

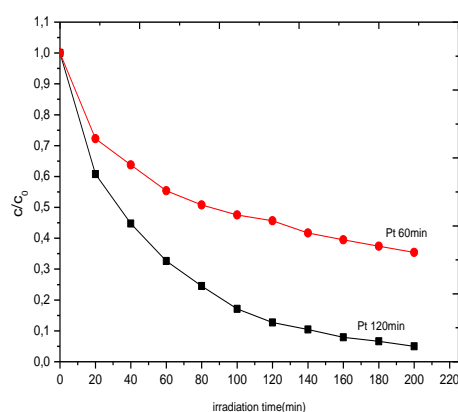


Figure 5. Comparison of photocatalytic degradation of methylene blue for different concentrations of Pt nanoparticles as a function of time under UV light irradiation.

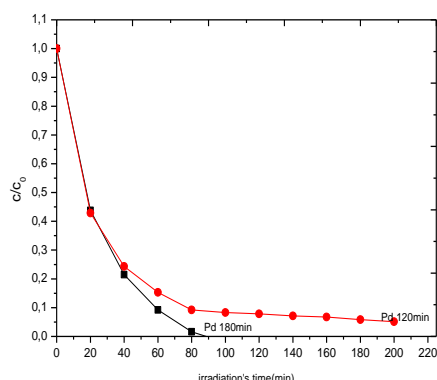


Figure 6. Comparison of photocatalytic degradation of methylene blue for different concentrations of Pd nanoparticles as a function of time under UV light irradiation.

Incorporating metal nanoparticles onto semiconductor photocatalysts can enhance the photocatalytic activity because the difference in their Fermi levels can introduce a Schottky barrier between the metal and the semiconductors. The increase of the concentrations of metal nanoparticles deposited onto porous silicon nanowires induces the increase on the electron trappers and in consequence reduces the rate of the recombination between the electrons and holes which is favorable for the photocatalytic activity.

The degree of the degradation with Au (80min) is about 95% and it is similar to the rates of the degradation with Pt (120min) and Pd (120min), this can be attributed to the fact that the Au nanoparticles can be deposit easily onto silicon nanowires at room temperature in comparison with Pd and Pt nanoparticles which require a higher time to deposit onto porous silicon substrates and which is effectuated at 50°C under magnetic stirrer.

For Pd (180min) the degradation is achieved at 90min of illumination because the concentration of the nanoparticles of palladium is very important so therefore the trappers of electrons are numerous.

4. Conclusion:

In this study, porous silicon nanowires were investigated with electroless chemical etching in HF/H₂O₂ solution and were decorated with noble metal nanoparticles by electroless chemical deposition. We have examined the net effect of the time deposition of gold, platinum and palladium nanoparticles onto porous silicon nanowires on the photodegradation of methylene blue under UV light irradiation. We have concluded that the photocatalytic activity of modified porous silicon nanowires increases with the concentration of metal nanoparticles, and the porous SiNWs -Au (80min), Pt(120min) and Pd(180min) exhibit better photocatalytic activity for the degradation of the methylene blue in comparison with porous H-SiNWs.

References:

- [1] SuoyuanLian, Chi Him A. Tsang, Zhenhui Kang, Yang Liu, Ningbew Wong, Shuit-Tong Lee, *Materials Research Bulletin* 46(2011) 2441-2444
- [2] SuoyuanLian, Chi Him A. Tsang, Zhenhui Kang Yang Liu, Ningbew Wong, Shuit-Tong Lee, *Materials Research Bulletin* 47(2012) 1119-1122
- [3] YongquanQu, Xing Zhong, Yujing Li, Lei Liao, Yu Huangbc and XiangfengDuan, *Journal of Materialschemistry* 20(2010) 3590-3594
- [4] Nacera Megouda, YannickCofinimier, Sabine Szunerits, Toufik Hadjersi, Omar ElKechaiand Rabah Boukherroub, *Chem. Commun.* 47(2011) 991-993.
- [5] Zhongyi Guo, Jin-Young Jung, Keya Zhou, Yanjun Xiao, Sang-won Jee, S. A. Moiz, Jung- Ho Lee, *Proceeding of SPIE* 7772(2010) 77721C

Design and simulation of a valveless piezoelectric micropump for fuel delivery in fuel cell devices

Yasser Rihan

Associate Prof., Atomic Energy Authority, Egypt.

Received: 30 April 2014, accepted 26 May 2014

Abstract

Micro- and nano-electromechanical systems (MEMS or NEMS)-based fuel delivery in direct methanol fuel cell (DMFC) devices offer opportunities to address unmet fuel cells related to fuel delivery. By applying an alternating electrical field across the actuator, the resultant reciprocating movement of the pump diaphragm can be converted into pumping effect. Nozzle/diffuser elements are used to direct the flow. To make the power system applicable for portable electronic devices, the micropump needs to meet some specific requirements: low power consumption but sufficient fuel flow rate. In this study, a theoretical method have been used to investigate the effects of materials properties, actuator dimensions, driving voltage, driving frequency, nozzle/diffuser dimension, and other factors on the performance of the whole system. As a result, a viable design of micropump system for fuel delivery in DMFC devices has been achieved and some further improvements are suggested. A mathematical model was used to simulate the behaviour of the micropump. The results of mechanical calculations and simulations show good agreement with the actual behaviour of the pumps.

Keywords: Simulation; micropump; piezoelectric; fuel cell.

1. Introduction

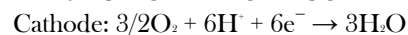
The piezoelectric effect is the ability of certain materials to produce an electric charge proportional to an applied mechanical stress. This is known as the direct piezoelectric effect. The electric charge can also be produced in the reverse direction, by reversing the direction of applied stress. The piezoelectric effect is reversible which implies that when an electric field is applied a mechanical strain is created in the material. The piezoelectric effect is defined as a linear relationship between a mechanical variable and an electric variable. Piezoelectric thick films are of major interest in the actuation of active structures in MEMS, they have been widely applied to micropumps, ultrasonic motors, resonators, microfluidic separators, high-frequency transducers, and energy harvesting, [1] because they exhibit properties such as larger displacement and quick response, high frequency, and can be precisely controlled.

The development of pumping devices in microscale is a part of the emerging research field of microfluidics [2]. Besides stand-alone micropumps, simple pump designs are required for integration in miniaturized chemical analyzers, which are often called micro total analysis systems (μ TAS) or lab on a chip (LOC). Low-voltage and low-power actuating schemes for the pump are needed for the use in hand-held devices which are usually powered by batteries.

Micropumps with surface mounted piezoelectric membrane actuation were first reported by van Lintel et al.

[3]. Piezopumps have been considerably developed over the past several years. They have many excellent abilities such as liquid handling in small and precise volume, providing a high actuation force with a relative fast mechanical response at high operation frequency, and miniaturization in a small size, etc. [4-6]. Therefore, they are able to serve in chemical, medical, and biomedical applications with great scientific and commercial potential [7-9].

A fuel cell is a kind of electrochemical device that converts the chemical energy of reactants directly into electricity, which offers advantages of high energy density, low volume and weight, no moving parts and no harmful emissions. Recently, miniature fuel cells have been drawing increasing attention as a possible solution to the search for improved power sources for portable power systems [10]. The direct methanol fuel cell (DMFC) is one of the fuel cells which have the potential to be miniaturized. The chemical reaction in DMFC is as follows:



From the equation above, it holds true that in a completely passive system, the entire surface area of the fuel cell cathode must be exposed to the exterior to allow air to reach the catalyst layer. For longer durations, however, in the absence of convection, the local oxygen concentration adjacent to the cathode will be depleted. So, one of the key technologies has been that of an active air

supply device which can feed sufficient air into the DMFC pack.

The cross-section of the DMFC power system with valveless piezoelectric micropump is shown schematically in Fig. 1. This system mainly consists of the following parts: fuel cell membrane electrode assembly (MEA), fuel chamber, nozzle/diffuser, micropump and pump chamber, and fuel supply manifold. All these parts are fabricated in a multi-layer structure to obtain a compact system. The fuel cell MEA is made of a Nafion117 membrane layer sandwiched by two electrode layers with catalysts deposited on them. And the micropump is fabricated by bonding a thin piezoelectric disk on a metal diaphragm. When applying an alternating voltage to the piezoelectric disk, the diaphragm is actuated to produce bending deformation that causes the volume change of pump chamber. By selecting appropriate shape and dimension of the nozzle/diffuser between pump chamber and fuel chamber, the fuel can circulate in the desired direction. And the fuel supply from the right chamber can compensate the fuel consumption.

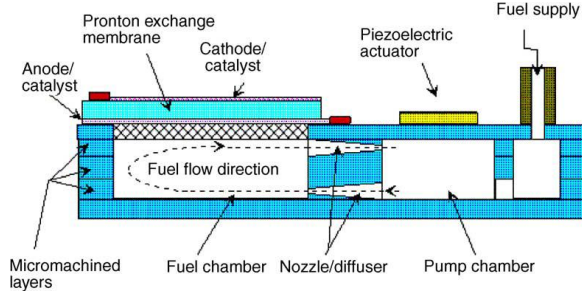


Fig. 1: Schematic of the miniaturized DMFC system driven by piezoelectric valveless micropump.

2. Model of micropump

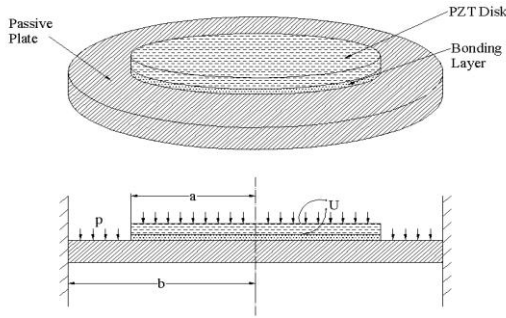


Fig. 2: Schematic of the piezoelectric micropump actuator.

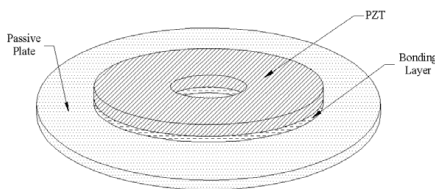


Fig. 2(a): Disk-type bending actuator.

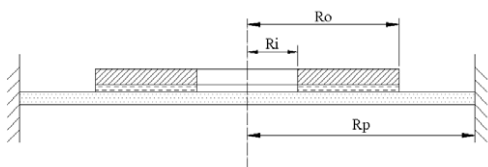


Fig. 2(b): Ring-type bending actuator.

The most important part of a micropump is the actuator, which in this case is actually a piezoelectric bending actuator made of three layers: PZT layer, bonding layer and passive plate. When applying an alternating electrical field across the PZT layer, it will generate a reciprocating deflection in the direction vertical to the surface of the actuator. This deflection is then transferred to the pumping effect that drives the fluid inside the pump chamber flowing through the inlet/outlet. Therefore the first thing need to do in the micropump modeling is to calculate this deflection. In most of the applications for micropumps, the PZT disk is smaller than the passive plate and therefore the edge of the PZT disk is often considered to be free. The schematic of the actuator part is illustrated in Fig. 2. As shown in the figure, the PZT disk is adhered to the passive plate by a thin layer of conductive epoxy.

The modeling process can be simplified assuming the whole structure is circumferentially symmetrical, the bonding between the PZT disk and the passive plate is perfect and the outer edge of the passive plate is fixed.

2.1. Desk-type deflection

The model developed by [11] for deflection caused by the applied voltage can be adopted here directly. The intermediate moment caused by the actuation of the PZT is:

$$M_0 = D_e \frac{-d_{31}U / h_{pzt}}{\frac{h}{2} + \frac{2}{h} \left(\frac{1}{E_{pzt}h_{pzt}} + \frac{1}{E_p h_p} \right) (D_{pzt} + D_p)} \quad (1)$$

The bonding moment M_1 , as delivered by Li et al [12] is:

$$M_1 = \frac{\eta d_{31}U (2h' + 2h_p + h_{pzt})(h'^3 + h^3)}{2[h^3 + (1-\alpha)h'^3 + (\alpha-\beta)(h' + h_p)^3 + \beta(h' + h_p + h_{pzt})^3]} \quad (2)$$

where,

$$\eta = \frac{E_{pzt}}{1 - \gamma_{pzt}^2}, \quad h' = h_p - h, \quad \alpha = \frac{1 - \gamma_p^2 E_b}{1 - \gamma_b^2 E_p}, \quad \beta = \frac{1 - \gamma_{pzt}^2 E_{pzt}}{1 - \gamma_{pzt}^2 E_p}$$

The deflection can be determined by the following equations:

$$W_1(r) = \frac{M_{11}a^2}{2D_p [(1-\gamma_p)b^2 + (1+\gamma_p)a^2]} \times (-r^2 + 2b^2 \log \frac{r}{b} + b^2) \quad (3)$$

The deflection W_2 for the three-layer structure can be expressed as follows [13]:

$$W_2(r) = \frac{M_{11}b^2}{2D_p [(1-\gamma_p)b^2 + (1+\gamma_p)a^2]} \times (-a^2 + 2b^2 \log \frac{a}{b} + b^2) \quad (4)$$

$$+ \frac{M_1}{2D_c(1+\gamma_c)} (a^2 - r^2)$$

The continuity condition is:

$$\frac{dW_1(r)}{dr} \Big|_{r=a} = \frac{dW_2(r)}{dr} \Big|_{r=a} \quad (5)$$

The moment M_{11} can be expressed as follows:

$$M_{11} = -\frac{M_1 D_p [(1-\gamma_p)b^2 + (1+\gamma_p)a^2]}{D_c(1+\gamma_c)(b^2 - a^2)} \quad (6)$$

The deflection equation can be rewritten as:

$$W_1(r) = \frac{M_1 a^2 (r^2 - 2b^2 \log r / b - b^2)}{2D_c(1+\gamma_c)(b^2 - a^2)}, \quad (a \leq r \leq b) \quad (7)$$

$$W_2(r) = \frac{M_1 [(b^2 - a^2)(a^2 - r^2) + a^2(a^2 - 2b^2 \log a / b - b^2)]}{2D_c(1+\gamma_c)(b^2 - a^2)}, \quad (0 \leq r \leq a) \quad (8)$$

Under constant pressure difference p , the deflection of the passive plate is:

$$W_3(r) = \frac{p}{64D_p} (b^2 - r^2)^2 + \frac{(M_{21} - M_2) a^2 (r^2 - 2b^2 \log r/b - b^2)}{2D_p [(1-\gamma_p) b^2 + (1+\gamma_p) a^2]} \quad (9)$$

Where M_2 and M_{21} are two intermediate bending moments, the continuity condition of the slope of the deflection at $r = a$ can be used to determine M_2 and the other moment can be expressed as:

$$M_{21} = \frac{p}{16} [(1+\gamma_p) b^2 - (3+\gamma_p) a^2] \quad (10)$$

The deflection of the three-layer structure can be expressed as follows:

$$W_4(r) = \frac{p}{64D_p} (b^2 - a^2)^2 + \frac{(M_{21} - M_2) a^2 (a^2 - 2b^2 \log a/b - b^2)}{2D_p [(1-\gamma_p) b^2 + (1+\gamma_p) a^2]} + \frac{p(a^2 - r^2)}{64D_p} \left(\frac{5+\gamma_c}{1+\gamma_c} a^2 - r^2 \right) + \frac{M_2(a^2 - r^2)}{2D_c(1+\gamma_c)} \quad (11)$$

For the bonding material, the stress follows:

$$\sigma_b = \frac{E_b}{1-\gamma_b} \varepsilon_b \quad (12)$$

where ε_b is the strain of the bonding material.

2.2. Ring-type deflection

Assuming the whole system is linear, the deflection equations for the ring-type actuator can be expressed as follow:

$$W_1(r) = \frac{M_0 [(R_p^2 - R_0^2)(R_0^2 - r^2) + R_0^2 (R_0^2 - 2R_p^2 \log(R_0/R_p) - R_p^2)]}{2[D_p [(1+\gamma_p) R_0^2 + (1-\gamma_p) R_p^2] + D_e (1+\gamma_e)(R_p^2 - R_0^2)]} - \frac{M_0 [(R_p^2 - R_i^2)(R_i^2 - r^2) + R_i^2 (R_i^2 - 2R_p^2 \log(R_i/R_p) - R_p^2)]}{2[D_p [(1+\gamma_p) R_i^2 + (1-\gamma_p) R_p^2] + D_e (1+\gamma_e)(R_p^2 - R_i^2)]}, \quad (0 \leq r \leq R_i) \quad (13)$$

$$W_2(r) = \frac{M_0 [(R_p^2 - R_0^2)(R_0^2 - r^2) + R_0^2 (R_0^2 - 2R_p^2 \log(R_0/R_p) - R_p^2)]}{2[D_p [(1+\gamma_p) R_0^2 + (1-\gamma_p) R_p^2] + D_e (1+\gamma_e)(R_p^2 - R_0^2)]} - \frac{M_0 R_i^2 (r^2 - 2R_p^2 \log(r/R_p) - R_p^2)}{2[D_p [(1+\gamma_p) R_i^2 + (1-\gamma_p) R_p^2] + D_e (1+\gamma_e)(R_p^2 - R_i^2)]}, \quad (R_i \leq r \leq R_0) \quad (14)$$

$$W_3(r) = \frac{M_0 R_0^2 (r^2 - 2R_p^2 \log(r/R_p) - R_p^2)}{2[D_p [(1+\gamma_p) R_0^2 + (1-\gamma_p) R_p^2] + D_e (1+\gamma_e)(R_p^2 - R_0^2)]} - \frac{M_0 R_i^2 (r^2 - 2R_p^2 \log(r/R_p) - R_p^2)}{2[D_p [(1+\gamma_p) R_i^2 + (1-\gamma_p) R_p^2] + D_e (1+\gamma_e)(R_p^2 - R_i^2)]}, \quad (R_0 \leq r \leq R_p) \quad (15)$$

The deflection caused by pressure difference can be expressed similar to the case of disk-type actuator; the deflection induced by mechanical pressure can be determined by using the superposition method as follows:

$$w_4(r) = w_5(R_i) + \frac{p(R_i^2 - r^2)}{64D_p} \left(\frac{5+\gamma_p}{1+\gamma_p} R_i^2 - r^2 \right) + \frac{M_1 (R_i^2 - r^2)}{2D_p (1+\gamma_p)}, \quad (0 \leq r \leq R_i) \quad (16)$$

$$w_5(r) = w_6(R_0) + \frac{p(R_0^2 - r^2)}{64D_e} \left(\frac{5+\gamma_e}{1+\gamma_e} R_0^2 - r^2 \right) + \frac{(R_0^2 M_2 - R_i^2 (M_1 - M')) (R_0^2 - r^2)}{2D_e (1+\gamma_e) (R_0^2 - R_i^2)} - \frac{R_0^2 R_i^2 (M_2 - M_1 + M') \log(r/R_0)}{D_e (1-\gamma_e) (R_0^2 - R_i^2)}, \quad (R_i \leq r \leq R_0) \quad (17)$$

$$w_6(r) = \frac{p(R_p^2 - r^2)^2}{64D_p} + \frac{(M'' - M_2) R_0^2 (r^2 - 2R_p^2 \log(r/R_p) - R_p^2)}{2D_p [(1-\gamma_p) R_p^2 + (1+\gamma_p) R_0^2]}, \quad (R_0 \leq r \leq R_p) \quad (18)$$

Where, M' and M'' are two intermediate bending moments, of which

$$M' = p(3+\gamma_e)(R_0^2 - R_i^2)/16 \quad (19)$$

$$M'' = p[R_p^2(1+\gamma_p) - R_0^2(3+\gamma_p)]/16 \quad (20)$$

The relation between the total generated current and the methanol solution flow rate can be written as:

$$I = Q \times D_M \times 6 \times F \quad (21)$$

(where D_M is the mole density of methanol solution and F is Faraday's constant).

3. Model validation and predicted results

Water is used as working fluid whose property is quite close to that of the methanol water solution. Comparison between the measured water flow-rate [14] under different pressure head were compared with the predicted results as shown in Figure 3. The larger flow rate corresponds to the lower pressure head. As shown in the figure there is a good agreement between the experimental and predicted results.

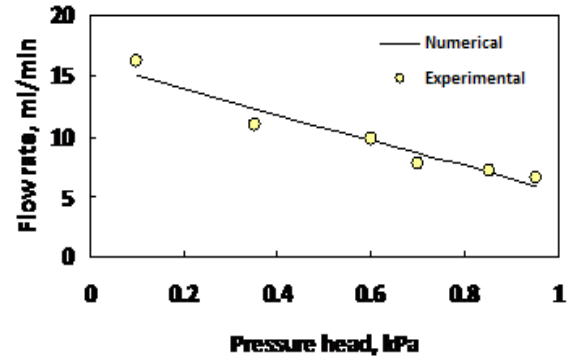


Fig. 3: Flow rate versus pressure head, $f = 200$ Hz.

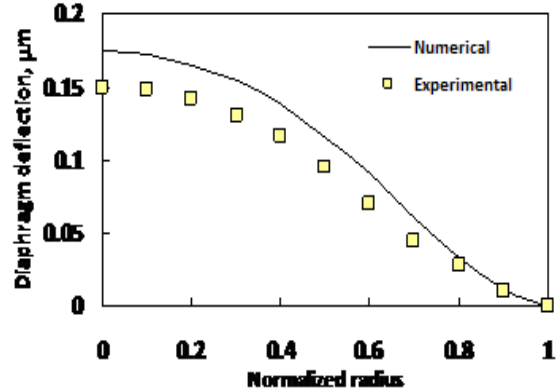


Fig. 4: Comparison between experimental and numerical results of the diaphragm deflections.

Figure 4 shows a comparison of the deflection of the diaphragm between the predicted results of the present model and the experimental results of Zhang et al. [15]. The predicted results have the same trend of the experimental data and the maximum deflection always appears at the center. The numerical deflection is smaller than the experimental this may tend to the fabrication process may result in some residual stress or strain and the boundary conditions are not ideal fixed. Also the actual deformation of the bending actuator in three-dimensional but the numerical result is two-dimensional. Furthermore, there may be deflections and non-uniformities in the materials used for experiments therefore the experimental data will not be accurate.

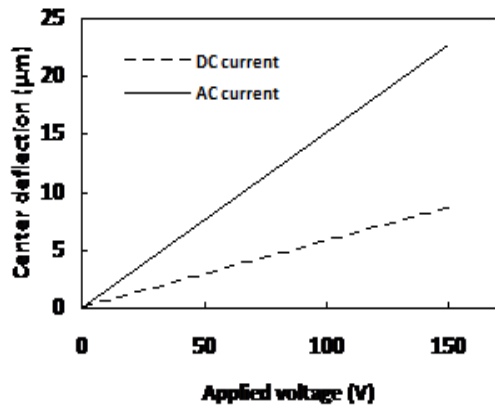


Fig. 5: Center deflection results of the diaphragm under different voltage.

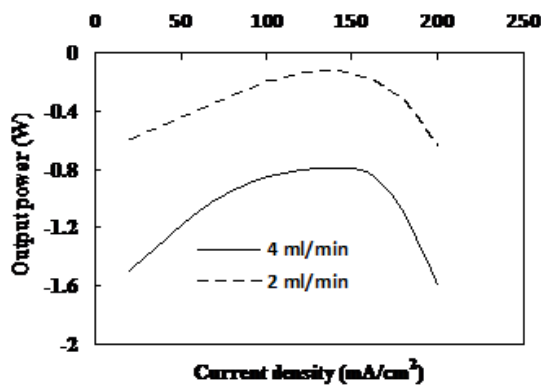


Fig. 6: Output power under different operation conditions, $f = 100$ Hz.

The predicted center deflection of the micropump and the applied voltage is linear as shown in Fig. 5. Increasing the applied voltage will increase the applied electric field; therefore the deflection and the volume displacement will increase. The applied electrical field cannot exceed a certain limit or the PZT material will be depolarized. The applied AC voltage is sinusoidal and the frequency is 100 Hz give much larger deflections as shown in Fig. 5. The output power under different conditions consumed by the piezoelectric micropump from the total power generated by fuel cell is shown in Fig.6. The power generated by the fuel

cell is not enough to drive the micropump for both 2 and 4 ml/min then the flow rate must be less than these values to get positive output power.

4. Conclusions

This research is focused on the development of a valveless piezoelectric micropump for miniaturized direct methanol fuel cell system as power source for portable electronics. A theoretical study is conducted to design, optimize, and characterize such a system. This work demonstrates that the working principle of the whole system design is sound and viable. A mathematical model was used to simulate the behavior of the micropump. The results of mechanical calculations and simulations show good agreement with the actual behavior of the pumps.

References

- [1] T. Yan, B.E. Jones, R.T. Rakowski, M.J. Tudor, S.P. Beeby, N.M. White, *Sens. Actuators A*, 115 (2004) 401.
- [2] N.T. Nguyen, S.T. Wereley, *Fundamentals and Applications of Microfluidics*, 1st ed., Artech House, Boston, MA, 2002.
- [3] H.T.G. van Lintel, F.C.M. vande Pal, S. Bouwstra, *Sensors and Actuators*, 15 (2) (1988) 153.
- [4] P. Woias, *Sens. Actuators B: Chem.*, 105 (1) (2005) 28.
- [5] D.J. Laser, J.G. Santiago, *J. Micromech. Microeng.*, 14 (6) (2004) 35.
- [6] N.T. Nguyen, X.Y. Huang, T.K. Chuan, *J. Fluids Eng. Trans., ASME*, 124 (2) (2002) 384.
- [7] D.A. Henderson, *NSTI Nanotechnol. Conf. Trade Show Technol. Proc.*, 3 (2007) 272.
- [8] S.B. Choi, J.K. Yoo, M.S. Cho, Y.S. Lee, *Mechatronics*, 15 (2) (2005) 239.
- [9] E.G. Chapman, S.L. Herdic, C.A. Keller, C.S. Lynch, *Proc. SPIE Int. Soc. Opt. Eng.*, 5762 (2005) 299.
- [10] K. Cowey, K.J. Green, G.O. Mepsted, R. Reeve, *Curr. Opin. Solid State Mater. Sci.*, 8 (2004) 367.
- [11] B. Minqiang, T. Melvin, G. Ensell, J. Wilkinson, A.G. Evans, *Journal of Micromechanics and Microengineering*, 13 (2003) S125.
- [12] S. Li, S. Chen, *Sens. Actuators A*, 104 (2003) 151.
- [13] S. Timoshenko, S. Woinowsky-Krieger, *Theory of plates and shells*, Second ed., McGraw-Hill, New York, 1959.
- [14] M. Richter, R. Linnemann, P. Woias, *Sensors and Actuators A*, 68 (1998) 480.
- [15] T. Zhang, Q. Wang, *J. of Power Sources*, 140 (2005) 72.

Thickness optimization of various layers of CZTS solar cell

H. Heriche^a, Z. Rouabah^a, S. Benabbes^a and L. Selmani^b

^{a)} *Materials and Electronic Systems Laboratory, University of Bordj Arréridj, El-Anasser, Bordj-Bou-Arreidj, Alegria.*

^{b)} *Department of Electronics, University of Bordj Bordj Arréridj, El-Anasser, Bordj-Bou-Arreidj, Alegria.*

Received: 30 April 2014, accepted 26 May 2014

Abstract

Thin film solar cells based on $\text{Cu}_x\text{Zn}_y\text{Sn}_z\text{S}_4$ (CZTS) absorbers are proposed with the structure glass/Mo/CZTS/buffer/ZnO. In this work we have simulated CZTS thin film solar cell using solar cell capacitance simulator (SCAPS). The influences of thickness of (CZTS) absorber, thickness of (CdS) buffer layer and Zinc oxide window Layer (ZnO) on the photovoltaic cell parameters are studied. It can be seen after reviewing the results, that for high conversion efficiency, the cell should have a thin buffer layer and a thick absorber layer. In addition, the effect of operating temperature on the cell performance shows that the efficiency will be strongly affected by the increased temperature.

Keywords: CZTS; solar cell; SCAPS.

1. Introduction

Recently, $\text{Cu}_x\text{Zn}_y\text{Sn}_z(\text{S}/\text{Se})_4$ (CZTS) has also been considered as a possible candidate for photovoltaic applications since it only consists of abundant elements [1]. However, potentially other p-type semiconductors with fewer elements and perhaps reduced complexity than CZTS are also available such as the ternary Cu-Sn-S system or SnS [2].

CZTS is an quaternary semiconducting compound which has received increasing interest as an absorber layer in a thin film solar cell because of a suitable band-gap energy of 1.4-1.5 eV and of a large absorption coefficient over 10^4cm^{-1} [3, 4]. Carrier concentrations and absorption coefficient of CZTS are similar to CIGS. Other properties such as carrier lifetime (and related diffusion length) are low (below 9 ns) for CZTS.

This low carrier lifetime may be due to high density of active defects or recombination at grain boundaries. However, chalcopyrite solar cells employing alternative buffers can reach the same efficiency as those with CdS buffers. Moreover, in some cases it is observed though that these alternative buffers, are mine prone to metastable effects like hight soaking and show less stability in damp heat testing [5].

In the present contribution, a numerical study has been realized in order to show the effect of thickness and doping of a window ,buffer and

absorbent layers in the photovoltaic cell parametres CZTS baser solar cells. The calculs have been performed using a numerical model with the solar cell capacitance simulation (SCAPS) program.

2. Device modelling

Numerical simulation is now almost indispensable for the understanding and design of solar cells based on crystalline, polycrystalline and amorphous materials [4]. SCAPS is a numerical device simulator for thin film solar cells, It is developed especially for CdTe and CIGS solar cells and Other such as CZTS [5].

In the model the CZTS the absorber is P-type, with a gap of 1.5 eV and the junction is made between the CZTS P-type and N-type CdS which has a gap of 2.45 eV. The window layer is formed of ZnO with a gap equal to 3.3 eV.

In the present work, numerical modeling of CZTS thin film solar cell has been performed SCAPS computer software program [6]. So as to investigate the effects of thickness and doping of layers such window layers , buffer layer and absorber layer on the photovoltaic cell paramtres grading on the overall CZTS solar cell device performance . Note that version SCAPS 2.8 car handle graded cell structures [7].

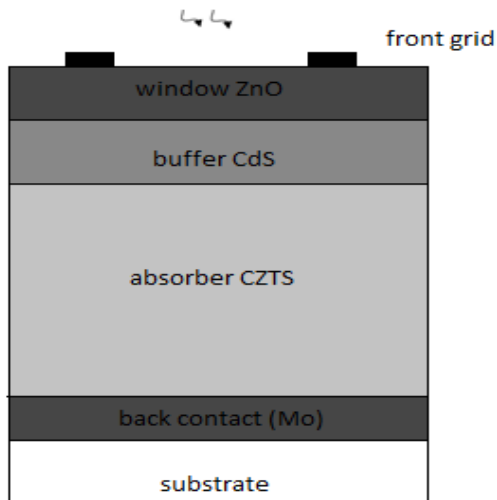


Fig1. Schematic view of CZTS solar cells.

3. Results and discussion

The structure has been studied under solar spectrum AM 1.5 with $p=1000W/m^2$ and at a temperature $T=300^{\circ}K$. The measurement of the photovoltaic parameters has been made in the case of a nul serie resistance and shunt resistance infinitely large. In What follows, we will present our result regarding the influence of the three layers, namely window layer ZnO, buffer layer CdS and absorber layer CZTS on the efficiency of the electric conversion .For that purpose, we have varied the thickness of one layer and kept unchanged the optimal value of the other two reaming layer.

3. 1. Influence of absorber layer thickness on conversion efficiency

The cell photovoltaic paramtres for various thicknesses of CZTS ranging from 1 to 4 μm are given in Fig 2. We observe that as the thickness of CZTS is increased both V_{oc} and J_{sc} of CZTS solar cells increased as will. In fact this allows the collection of lighten wave lengths which contribute to the generation of the electron- trou pairs [8], and result in the increases of the V_{oc} and J_{sc} .

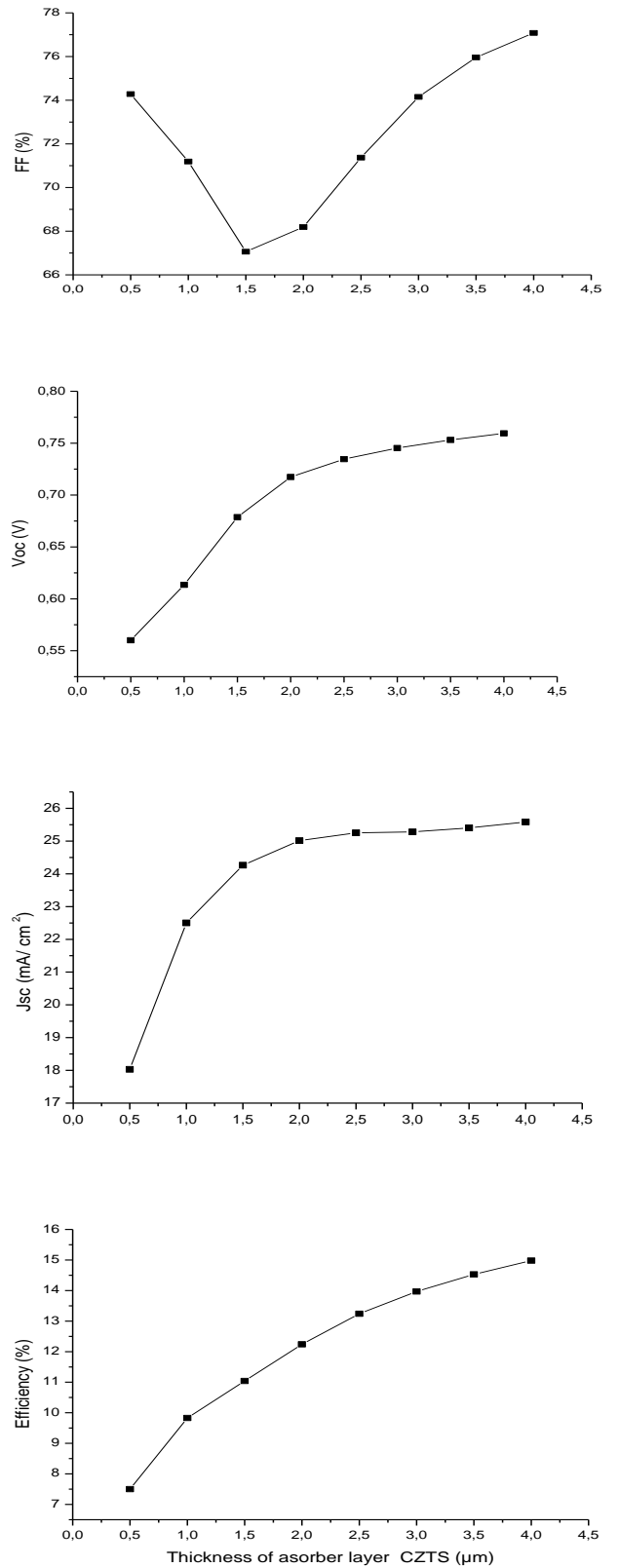


Fig.2. Variation of efficiency versus absorber layer thickness for CZTS.

It is generally agreed that values of V_{oc} and J_{sc} will be reduced if the thickness of the absorber layer is reduced. This may be caused by the recombination process at the back contact of the solar cell.

Note that as the thickness of CZTS increases the efficiency increases linearly. On the other hand, the fill factor of the solar cell as well as the increases of the thickness of the absorber layer (see Fig.2). This is in good. Moreover for Fig.2, we can notice that for a thickness of CZTS of $4\mu\text{m}$, an imported electric efficiency of 14.98% can be reached for the solar cell of interest.

3.2. Influence of window layer thickness on conversion efficiency

For the thickness of ZnO we have proceeded from $0.02\mu\text{m}$ to $0.1\mu\text{m}$. with regarding the cell photovoltaic parameters for various thickness of ZnO, we notice that as the thickness of the window layer of ZnO from 0.02 to $0.1\mu\text{m}$, the fill factor decreases significantly. The same trend can be observed from Fig.3 for the efficiency which decreases from 14.76% to 14.98%.

This means that the increases of the thickness of the window layer will affect efficiency. Besides, when the window layer thickness is very thin, the cell performance degrades. The reason could be to on the one hand the increases of series resistance (increases of losses) [9], and on the other hand to the thickness of the layer. As for as the thickness decreases, the absorption increases (for longer wave lengths). Consequently, on optimal thickness of ZnO layer necessary for best performance of solar battery.

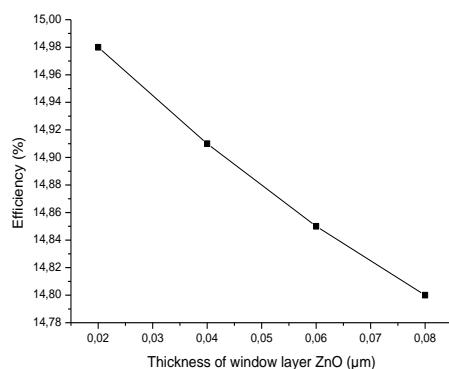


Fig.3. Variation of efficiency versus window layer thickness for ZnO.

3.3. Influence of buffer layer thickness on conversion efficiency

Let us now turn our attention to the influence of thickness of buffer layer on the solar cell efficiency. For that purpose, we now show the influence of the thickness of CdS buffer layer on the solar cell efficiency. In this respect, we present in Fig.3 the cell photovoltaic parameters for various thicknesses of CdS of ranging from 0.005 to $0.05\mu\text{m}$. we observe that except for the parameter V_{oc} which remain constant, cell remaining parameters of interest increases with varying the thickness of CdS layer. Fig.4 shows the variation of the efficiency as a function of the thickness of CdS buffer layer. Note that the efficiency increases momentarily with increase the thickness of CdS.

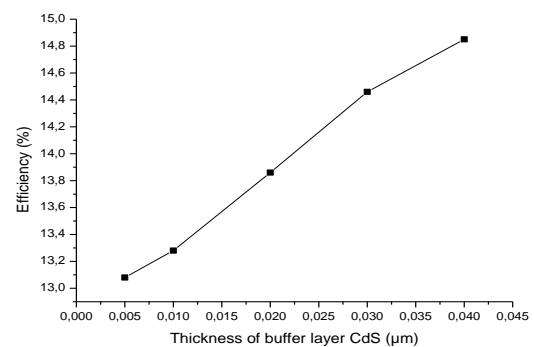


Fig.4. Variation of efficiency versus buffer layer thickness for CdS.

4. Conclusion

In the present study, the effect of thickness of the different layers of interest on the parameters of the photovoltaic cell has been investigated. We have determined the optimal parameters for each layer which constitute the solar structure (ZnO, CdS and CZTS) and which give the best efficiency. After that we have obtained the optimal structure of the solar cell of interest. By combining the optimal parameters of each layer, the study solved that the best structure must have a window layer (ZnO) of thickness of $0.02\mu\text{m}$, a buffer layer (CdS) of thickness of $0.05\mu\text{m}$ and an absorber layer (CZTS) of thickness of $4\mu\text{m}$. These characteristics show the best transport of carriers by reducing their recombinations at the back contact level. The solar cells with these parameters give an electric efficiency of 14.98% with a fill factor of 77.08%,

current density of 25.58 mA/ cm² and voltage of open circuit of 0.7595 Volt. The obtained efficiency in the present study is better than those reputed so far in the literature for CZTS based solar cells.

References

- [1] M. Dominik , Rabie Djemour, Levent Gütay, Guillaume Zoppi, Susanne Siebentritt, Phillip J. Dale, Thin Solid Films 520 (2012) 6291-6294.
- [2] M. Ristov, G. Sinadinovski, M. Mitreski, M. Ristova, Sol. Energy Mater. Sol. Cells 69 (2001) 17.
- [3] K. Ito, T. Nakazawa, Jpn. J. Appl. Phys. 27 (1988) 2094.
- [4] Th. M. Friedlmeier, N. Wieser, Th. Walter, H. Dittrich, H.-W. Schock, Proceedings of the 14th European PVSEC and Exhibition, 1997, P4B.10.
- [5] Siebentritt, S, Solar Energy. 77 , (2004) 767-775.
- [6] M. Burgelman, , SCAPS user manuel, Elis-University of Gent, 10 November, 2007.
- [7] M. Burgelman, J. Marlein , 23rd European Photovoltaic Solar Energy Conference, Valencia, (2008) 2151-2155.
- [8] P. Chelvanathan, M. I. Hossain, N. Amin, App. Phys. 10 (2010) 5387-5391.
- [9] S. Mostefa Kara, 2012, MSc., University of Tlemcen (Algeria).

The Effect of Ground albedo on the Performance GaInP and (a-Si: H) of Solar Cells

Abla Guechi^a and Mohamed Chegaar^b

^a*Institute of Optics and Precision Mechanics, Ferhat Abbas University, 19000, Setif, Algeria*

^b*Department of Physics, Faculty of Sciences, Ferhat Abbas University, 19000, Setif, Algeria*

Received: 30 April 2014, accepted 26 May 2014

Abstract

Solar radiation incident on vertical and inclined surfaces consists of beam, sky diffuse and ground reflected components. The ground reflected component may be significant, particularly in the northern latitudes due to low elevations of the sun and, at times, due to the presence of highly reflecting snow cover. Accurate estimation of ground reflected radiation would require knowledge of the foreground type and geometry, its reflectivity and the condition of the sky. The electrical current generated by the solar cells is very sensitive to the incident spectral distribution and intensity. This distribution varies greatly during the day due to changes in the sun's position or weather conditions. This work investigates the feasibility of using a solar spectral radiation model SMARTS2 to estimate the global solar irradiance on two different sites in Algeria (Setif and Bejaia) and assess the influence of varying ground albedo on the conversion efficiency of GaInP and amorphous (a-Si: H) solar cells. The results show an augmentation in the short circuit current of amorphous (a-Si: H) solar cell due to increasing albedo. It is 6.25% and 9.84% under global radiation and for Setif and Bejaia sites respectively. However for GaInP solar cell, the augmentation of the short circuit current is 6.97% and 10.93% for Setif and Bejaia sites respectively. Nevertheless, the efficiency increases with increasing albedo for GaInP and amorphous (a-Si: H) solar cells.

Keywords : Ground Reflectance ; Albedo ; Solar Cells, (a-Si:H) ; GaInP; Irradiance.

PACS: 72.20.Jv, 84.60.Jt, 85.30.De, 88.40.If, v 96.60.Ub, 96.40.Pq

1. Introduction

Accurate knowledge of solar radiation at the Earth's surface is an important issue in many disciplines related to solar energy, environment, climate, architecture, and agriculture, illumination engineering and biophysical impacts of atmospheric pollution in large cities, atmospheric physics and remote sensing[1].

Atmospheric parameters play a very important role in the earth's radiation budget and, therefore, are very important in climate change [2-3]. Due to natural spectral sensitivity of solar cell devices, the solar spectrum is one of those environmental factors which may strongly influence module's performance.

Surface albedo, defined as the ratio of reflected to incoming radiation fluxes, is acknowledged to be one of the dominating factors of the Earth's radiation budget [4]. Snow and ice have the highest albedo of all surface types on the Earth. Variations in the surface albedo of the Arctic region have a large effect on the

radiation budget of the earth atmosphere system and thereby on the global climate [5]. The ground albedo varies with a number of factors, such as the properties of ground surface material, solar position, sky clearness, ground vegetation, snow coverage, etc. An ideal white body has an albedo of 100% and an ideal black body, 0%. Visually we can estimate the albedo of an object's surface from its color. Albedo irradiation changes the spectral distribution of the incident irradiation on the surface of the PV device, which in turn affects system output [6].

In general, PV modules are optimized under Standard Testing Conditions (STC), which are defined as 1000 W/m² irradiance with an AM 1.5 spectrum at 25°C. In real operating conditions, the module output is strongly affected by various environmental conditions such as irradiance, temperature and spectral effects [7]. Furthermore the impact of each climatic factor on the energy production varies according to the module technology in use.

The main propose of this paper is to know how (a-Si: H) and GaInP solar cells, perform under possible

solar spectrum variations and which albedo parameters produce more influence. For this reason, the variations short circuit, and efficiency of (a-Si: H) and GaInP solar cells due to the possible variations of the global solar spectral irradiance are obtained. The solar irradiance striking solar cells is estimated using the spectral irradiance model for clear skies SMARTS2 (Simple Model of Atmospheric Radiative Transfer of Sunshine) on different site of Algeria (Setif and Bejaia).

2. Calculation procedures

2.1. Spectral solar irradiance calculation

A large range of atmospheric radiation models has been elaborated by different authors for calculating the spectral solar irradiation [8]. Several of these models have been developed by various climate research centers and are highly complex numerical models utilizing the satellite observations as inputs. A physical spectral model is proposed by Gueymard [9-10] and called SMARTS2 (Simple Model of Atmospheric Radiative Transfer of Sunshine) is introduced here to examine the seasonal variation on the thin film solar cells output. It can be used in a variety of applications to predict full terrestrial spectra under any cloudless atmospheric condition. It gained acceptance in both the atmospheric and engineering fields due to its low number of inputs, ease of use, to its versatility, execution speed, and various refinements. It can calculate punctual estimations of spectral irradiances using as input parameters the local geographic coordinates, atmospheric water vapor content, atmospheric pressure, ground reflectance and aerosol optical thickness. SMARTS2 is used to generate the global component of the solar spectra for two sites in Algeria (Setif, Bejaia).

2.2. Cell Parameters Calculation

One of the key device parameters of a solar cell is the short circuit current density (J_{sc}). This parameter can be calculated by convoluting the spectral response of the device and the incident solar spectrum using the following equation:

$$J_{sc} = \int E(\lambda)SR(\lambda)d\lambda \quad (1)$$

Where $SR(\lambda)$ is the spectral response of the device (A/W), $E(\lambda)$ the global irradiance ($W/m^2 \text{ nm}$) as a function of wavelength λ (nm)

The open-circuit voltage V_{oc} and short-circuit current are related as follows:

$$V_{oc} = n \frac{kT}{q} \ln \left(\frac{I_{sc}}{I_s} + 1 \right) \quad (2)$$

After the calculation of V_{oc} the fill factor (FF) can be calculated using the normalized open circuit voltage v_{oc} [11]:

$$FF = \frac{v_{oc} - \ln(v_{oc} + 0.72)}{v_{oc} + 1} \quad (3)$$

The ideality factor, n , and the saturation current, I_s , are computed from the I-V characteristics using an approach that involves the use of an auxiliary function [12].

The fill factor and the conversion efficiency of the solar cell are linked through:

$$\eta = FF \frac{V_{oc} I_{sc}}{P_i S} \quad (4)$$

Where: I_{sc} is the short circuit current, S is the solar cell area, and P_i is the total irradiance in W/m^2 and is given by:

$$P_i = \int_0^{\infty} E(\lambda) d\lambda \quad (5)$$

With $E(\lambda)$ is the spectral irradiance.

Figure 1 show the measured spectral response data of GaInP and amorphous (a-Si: H) solar cells [13-14].

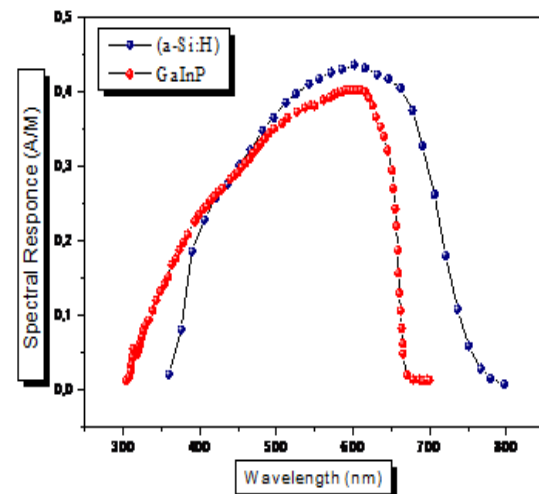


Figure.1 Spectral response of (a-Si: H) and GaInP solar cells [13-14].

3. Results and discussion

The global solar irradiance is calculated at Setif (36.11° N , 5.41° E and 1081m) and Bejaia (36.45° N , 5.04° E and 0.009 m) on a horizontal surface by

varying the albedo parameter and maintaining the others fixed (water vapor, air mass and turbidity) using SMART2. Then for each value of the ground albedo, we calculated the short circuit current, and the conversion efficiency of solar cells.

The variations of the short circuit current as a function of the ground albedo are illustrated in Table 1. The short circuit current increases with increasing albedo for the different types of solar cells. Whereas, the efficiency increases also with increasing albedo on the site of Setif and Bejaia for (a-Si: H) and GaInP solar cells. This increase is greater in the site of Bejaia then Setif. The augmentation in the short circuit current due to increasing Albedo (Table 1) is 6.25% and 9.84% under global radiation and for Setif and Bejaia sites respectively. However for GaInP solar cell, the augmentation of the short circuit current is 6.97% and 10.93% for Setif and Bejaia sites respectively. This is illustrated in Figure 2 and 3.

Albedo	Jsc (mA/cm ²) GaInP		Jsc (mA/cm ²) (a-Si: H)	
	SETIF	BEJAIA	SETIF	BEJAIA
0.1	135.120	133.420	175.819	165.845
0.2	136.965	136.207	177.975	169.013
0.3	138.861	139.128	180.185	172.287
0.4	140.811	142.197	182.453	175.708
0.5	142.817	145.424	184.779	179.284
0.6	144.882	148.825	187.166	183.029

Table 1: Influence of ground Albedo on Jsc under global for GaInP and (a-Si: H) solar cells.

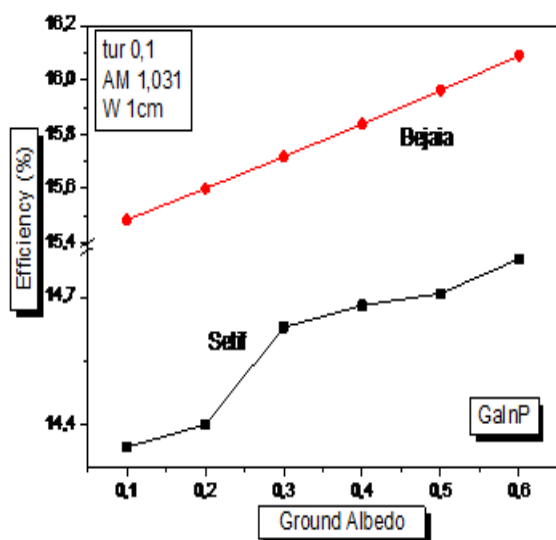


Figure.2 Efficiency as function of Albedo under global solar irradiance for GaInP solar cell

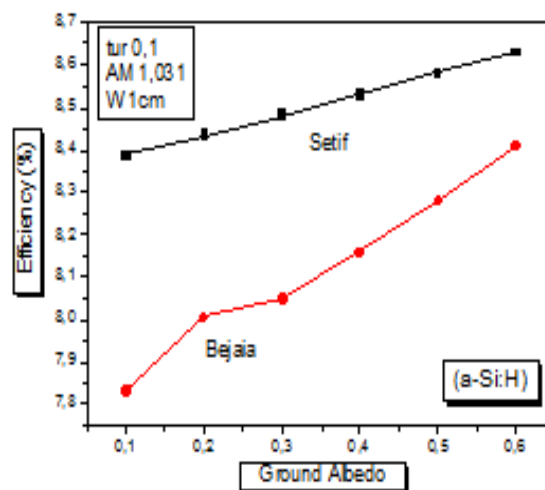


Figure.3 Efficiency as function of Albedo under global solar irradiance for amorphous (a-Si: H) solar cell.

4. Conclusion

The global solar irradiance incident irradiance on different types of solar cells on diverse site of Algeria is simulated using the spectral irradiance model SMARTS2 for varying atmospheric conditions. The analysis shows that the efficiency increases with increasing albedo for (a-Si: H) and GaInP solar cells. The effect is greater in the site of Bejaia then Setif and on the GaInP then (a-Si: H) solar cells.

References

- [1] B.E. Psiloglou, H.D.Kambezidis, Estimation of the ground albedo for the Athens area, Greece Journal of Atmospheric and Solar-Terrestrial Physics 71 (2009) 943-954
- [2] D.G. Kaskaoutis, H.D. Kambezidis, "The role of aerosol models of the SMARTS code in predicting the spectral direct-beam irradiance in an urban area", Renewable Energy 33, 2008; 1532-1543.
- [3] J. Polo, L. Martin, M. Cony, Revision of ground albedo estimation in Heliosat scheme for deriving solar radiation from SEVIRI HRV channel of Meteosat satellite, Solar Energy 86 (2012) 275-282.
- [4] D. Goto, T. Takemura, T. Nakajima, K.V.S. Badarinath, Global aerosol model-derived black carbon concentration and single scattering albedo

- over Indian region and its comparison with ground observations, *Atmospheric Environment* 45 (2011) 3277-3285.
- [5] P. Alton, A simple retrieval of ground albedo and vegetation absorptance from MODIS satellite data for parameterisation of global Land-Surface Models, *Agricultural and Forest Meteorology* 149 (2009) 1769-1775.
- [6] M.P.Brennan, A.L.Abramase, R.W.Andrews, J.M.Pearce Effects of spectral albedo on solar photovoltaic devices, *Solar EnergyMaterials&SolarCells* 124 (2014)111-116
- [7] C. Gueymard, H.D. Kambezidis, Solar spectral radiation. In: Muneer T, editor. *Solar radiation and daylight models*, 2nd Ed, Elsevier , 2004; 221-301.
- [8] C.Gueymard, "REST2: High-performance solar radiation model for cloudless-sky irradiance, illuminance, and photosynthetically active radiation -Validation with a benchmark dataset". *Solar Energy*, 2008; 82, 272-285.
- [9] C. Gueymard, R. George, "Gridded aerosol optical depth climatological datasets over continents for solar radiation modeling". *Proceedings of the Solar World Congress. International Solar Energy Society, Orlando, FL, 2005*
- [10] C. Gueymard, "SMARTS2, Simple Model of the atmospheric Radiative Transfer of Sunshine: Algorithms and performance assessment". Report. FSEC-PF-270-95, Florida-Solar Energy Center, Cocoa, FL, 1995.
- [11] M. A Green, *Solar Cells, Operating Principals, Technology, and System Applications*, Prentice-Hall Inc., Englewood Cliffs, 1982.
- [12] M. Chegaar, G. Azzouzi, and P. Mialhe. "Simple parameter extraction method for illuminated solar cells", *Solid-State Electronics*, 2006; 50, 1234 - 1237.
- [13] J. Meier, U. Kroll, E. Vallat-Sauvain, J. Spitznagel, U. Graf, A. Shah, "Amorphous solar cells, the micromorph concept and the role of VHF-GD deposition technique", *Solar Energy* , 2004; 77, 983-993.
- [14] Lu et al. "High-efficiency GaAs and GaInP solar cells grown by all solid-state Molecular- Beam-Epitaxy", *Nanoscale Research Letters*, 2011; 6, 576.

Electrical characteristics of Organic Light Emitting Diode “OLED” finite difference modeling

Benatia Khaoula ^{1*} and Telia Azzedine ¹

¹Instrumentation and Microsystems Laboratory (LMI), Constantine 1 University, route Ein El Bey, Constantine 25000, Algeria

*Corresponding author: benkdoc@gmail.com

Received: 30 April 2014, accepted 26 May 2014

Abstract

In this paper, a finite difference modeling of single layer organic light emitting diode “OLED” based on MEH-PPV [Poly (2-Methoxy, 5-(2'-Ethyl-Hexoxy)-1, 4-Phenylene-Vinylene)] and DP-PPV [Poly (2, 3-DiPhenyl-Phenylene-Vinylene)] is presented through the simulation of the basic equations i.e. the time independent continuity equations, with a drift diffusion form for current density, coupled to Poisson's equation. Thus, several parameters are extracted from this model; J (V) characteristics for the two devices which are compared to the experimental results and the spatial distributions of the potential, the electric field and the carrier concentrations.

Keywords: OLED; simulation ; finite difference; MEH-PPV; DP-PPV; J(V) characteristics

1. Introduction

Organic light emitting devices have been remarkably improved since the announcement of the first Organic light emitting diode “OLED” in 1987^[1]. These organic devices have a great potential indeed in various industries as are used in many applications such as lighting, handheld displays like smart phones, tablets and cameras and TV's of course. Even though this great development, OLED's are still lacking in some other areas related to the lifetime of these devices, the injection and transport mechanism which are not properly determined since the organic semiconductors have an amorphous structure unlike the inorganic ones that present a crystallized one.

To understand the operation principle of such devices, and before manufacturing them, we have to predict first their behavior by studying them through what we know now as “Numerical modeling”^[2], which is a powerful method of visualizing the dynamic behavior of physical systems of such devices. In this respect, we used an electrical model composed of Poisson's equation, coupled to the time independent continuity equations, with a drift diffusion form for the current density.

In this paper, we present the model that we worked on along with the boundary conditions^[3] where a set of equations were solved using finite difference method. Simulation results of J (V) characteristics for different organic semiconductor materials and for various thicknesses were compared to experimental data from^[4, 5], a spatial distribution of carrier density, potential and electric field are shown.

2. The device model

In this section, the electrical model is presented along with the boundary conditions; finite difference method was applied to solve the basic equations and Gummel iteration is used^[6].

2.1. Governing equations

To fully understand the mechanism of the transport and the injection of electrons /holes, we use the inorganic semiconductor devices equations i.e. the time independent continuity equations, with a drift diffusion form for current density, coupled to Poisson's equation, for modeling the organic semiconductor based devices as follows:

$$\frac{\partial J_n}{\partial x} = G - R; \quad \frac{\partial J_p}{\partial x} = G - R, \quad (1)$$

J_n (J_p) is the electron (hole) current density, G is the carrier generation rate which is very small for materials with an energy gap larger than 2 eV, and R is the carrier recombination rate, this latter is not that important for the single carrier structures^[1]. In the following expressions of J_n and J_p , the diffusivities are dependent of the mobilities using Einstein relation.

$$J_n = q \mu_n \left(n \cdot E + \frac{k_B T}{q} \frac{\partial n}{\partial x} \right);$$

$$J_p = q \mu_p \left(p \cdot E - \frac{k_B T}{q} \frac{\partial p}{\partial x} \right) \quad (2)$$

Where q is the electronic charge, $n(p)$ is the electron (hole) density, E is the electric field, k_B is Boltzmann's constant, T is the temperature and, $\mu_n(\mu_p)$ is the electron (hole) mobility which is expected to be Poole-Frenkel electric field dependent:

$$\mu_{PF} = \mu_0 \exp\left(-\frac{q\epsilon_a}{kT}\right) \exp\left(\frac{q\beta}{kT} \sqrt{E}\right) \quad (3)$$

Where μ_0 is the temperature independent pre-factor mobility, ϵ_a is the thermal activation energy and β is the Poole-Frenkel factor.

Poisson's equation is:

$$\frac{dE}{dx} = \frac{q}{\epsilon} (p - n + N_D - N_A) \quad (4)$$

The electrostatic potential V is related to E by:

$$E = -\frac{dV}{dx} \quad (5)$$

Where ϵ is the static dielectric constant, N_D is the donor density and N_A is the acceptor one.

2.2. Boundary conditions

Considering the boundary conditions for the potential:

$$V(0) = 0, \quad V(L) = V_d - V_a \quad (6)$$

Where $V_a(V_d)$ is the application (diffusion) potential.

The diffusion potential is expressed as:

$$V_d = \frac{k_B T}{q} \ln\left(\frac{n_L}{n_0}\right) = -\frac{k_B T}{q} \ln\left(\frac{p_L}{p_0}\right) \quad (7)$$

The equilibrium free carrier concentrations at the interfaces are^[8]:

$$n_0 = N_c \exp\left(-\frac{\Phi_{b1}}{k_B T}\right),$$

$$n_L = N_c \exp\left(-\frac{E_g - \Phi_{b1}}{k_B T}\right)$$

$$p_0 = N_v \exp\left(-\frac{\Phi_{b2}}{k_B T}\right), \quad (8)$$

$$p_L = N_v \exp\left(-\frac{E_g - \Phi_{b2}}{k_B T}\right)$$

Where N_c and N_v are assumed to be equal and correspond to the density of negatively and positively chargeable sites in the film, E_g the band gap energy, $\Phi_{b1}(\Phi_{b2})$ is the electron (hole) energy barrier.

The following expressions of the three main equations; (1), (2) and (5) are obtained using the finite difference method^[7]:

Poisson's equation:

$$V_{i+1} + V_{i-1} - 2V_i = \frac{h^2 q}{\epsilon} (n_i - p_i + N_a - N_D) \quad (9)$$

Coupled continuity and drift-diffusion equations:

$$[-(V_{i+1} - V_i) + V_T] n_{i+1} + [(V_i - V_{i-1}) - 2V_T] n_i + V_T n_{i-1} = 0$$

$$[-(V_{i+1} - V_i) - V_T] p_{i+1} + [(V_i - V_{i-1}) + 2V_T] p_i - V_T p_{i-1} = 0 \quad (10)$$

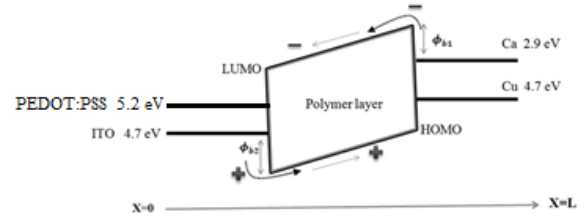


Fig.1 The model band diagram

3. Results and discussions

Fig.1 shows the band diagram of the device, where we consider a single layer organic diode based on: first: MEH-PPV [Poly (2-Methoxy, 5-(2'-Ethyl-Hexoxy)-1, 4-Phenylene-Vinylene)], taking into account the electron and hole energy levels $E_e = 2.8 \text{ eV}$ and $E_h = 5.3 \text{ eV}$, with the dielectric constant $\epsilon_s = 3$ and $n_0 = 10^{21} \text{ cm}^{-3}$. The organic layer is sandwiched between the anode ITO (Indium Tin Oxide) and the cathode Cu. The barrier for electron injection is 1.9 eV and for hole injection is 0.2 eV .

Second: DP-PPV with the electron and hole energy levels $E_e = 2.94 \text{ eV}$ and $E_h = 5.66 \text{ eV}$, with the

dielectric constant $\epsilon_s = 3$ and $n_0 = 10^{21} \text{ Cm}^{-3}$. The organic layer is sandwiched between the anode ITO and PEDOT:PSS [Poly (3,4-Ethylene Dioxy Thiophene): Poly(Styrene Sulphonate)], and the cathode Ca. The barrier for electron injection is 0.04 eV and for hole injection is 0.46 eV .

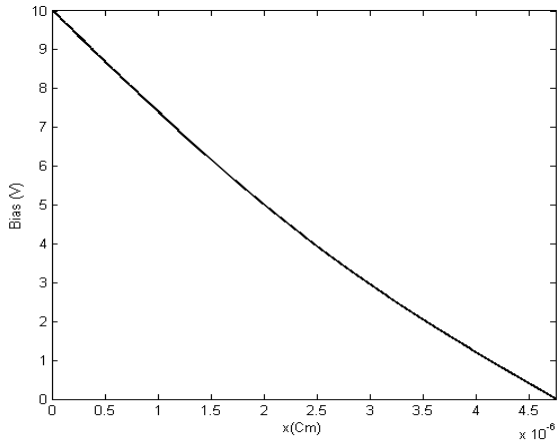


Fig.2 Spatial distribution of the potential

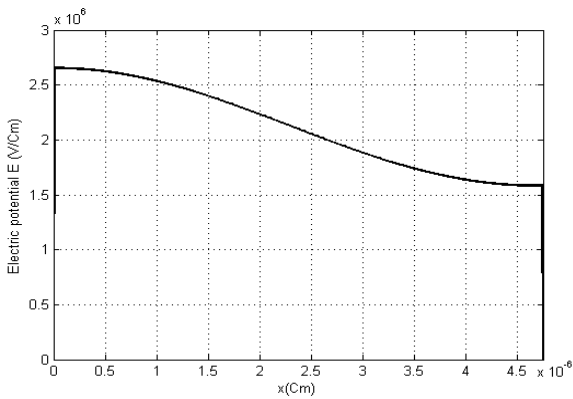


Fig.3 Electric field distribution

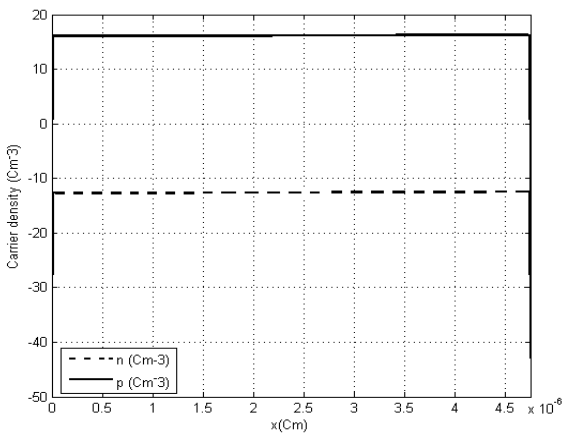


Fig.4 Carrier density distribution for holes and electrons (ITO/MAH-PPV/Cu)

Fig.2 and Fig.3 present the spatial distribution of the potential and the electric field respectively for ITO/MEH-PPV/Cu device with a thickness of 45.7 nm .

Fig.4 shows the spatial distribution of the carriers density for both holes and electrons where the density of holes is much greater compared to electrons. In fact, the holes barrier injection is too small that these carriers pass through this barrier, in the opposite of the electrons where only few of them can traverse through this barrier.

Using this model, we can also calculate the J-V characteristics for ITO/MEH-PPV/Cu device for different thicknesses where these results shown in Fig.5, Fig.6, and Fig.7 are compared with experimental ones from [4].

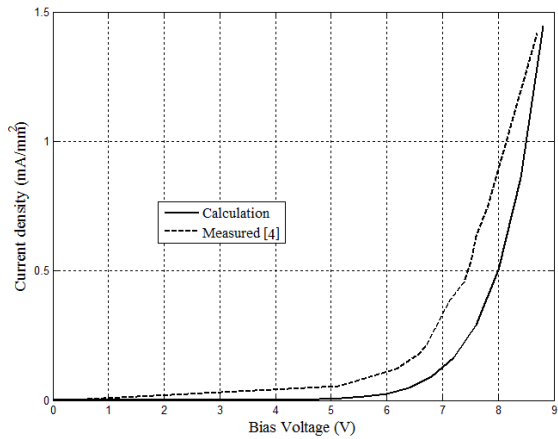


Fig.5 Current density versus bias voltage for 45.7 nm ITO/MEH-PPV/Cu device

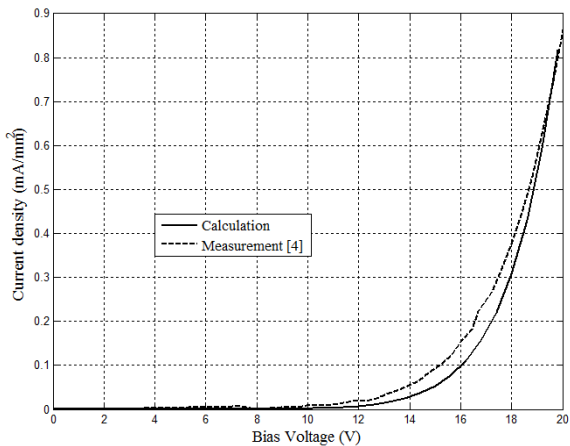


Fig.6 J(V) characteristics for 120 nm (ITO/MEH-PPV/Cu)

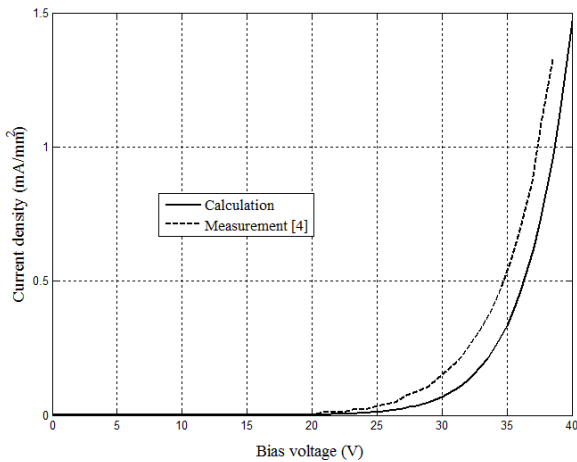


Fig.7 J(V) Characteristics for 210 nm (ITO/MEH-PPV/Cu)

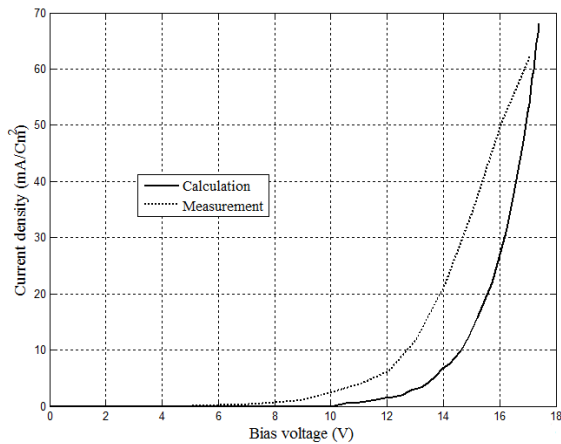


Fig.8 J(V) characteristics for 50 nm (PEDOT:PSS/ DP-PPV/ Ca)

We applied the model used previously on PEDOT: PSS/DP-PPV/Ca device. Fig.8 shows a comparison of calculated and measured J-V characteristics of a 50-nm- thick DP-PPV diode ^[5].

4. Conclusion

In this study, finite difference method was applied for modeling the basic equations that control the operation principle of an OLED. The hole density is much greater than that of the electrons. From the J-V characteristics, the turn-on voltage increase with the thickness of the polymer layer and in the two devices based on MEH-PPV and DP-PPV, the same behavior was noticed and a shift between the experimental data and the calculated results was observed.

References

- [1] C.W.Tang and S. A. VanSlyke, Appl. Phys. Lett.**51**, 913 (1987).
- [2] P. S. Davids, I. H. Campbell, and D. L. Smith, J. Appl. Phys.**82**, 6319, 1997.
- [3] J. HROMCOVA et al, phys. stat. sol. (a) **142**, 167 (1994)
- [4] I. D. Parker, J. Appl. Phys.**75**, 1656 (1994).
- [5] Sheng-Hsiung Yang, Jiun-Tai Chen, An-Kuo Li, Chun-Hao Huang, Kuei-Bai Chen, Bing-R. Hsieh, Chain-Shu Hsu, Thin Solid Films 477 (2005).
- [6] D. L. Scharfetter and H. K. Gummel, IEEE Trans. Electron Devices, vol. ED-16, pp. 64-77, 1969
- [7] Rostami, A.; Ahmadi, P.N.; Janabi-Sharifi, F., Optomechatronic Technologies (ISOT), 2010 International Symposium on , vol., no, pp.1,4, 25-27 Oct. 2010.

Synthesis, characterization and cytotoxic effect of ZnO nanoparticles obtained by mechanical alloying

S. Benchelia^a, S. Benosmane^b, D E. Mekki^a and N. Tabet^c

^aLESIMS laboratory, Department of Physics, Badji Mokhtar-Annaba University, Algeria

^bCellular toxicity laboratory Department of Biology, Badji Mokhtar-Annaba University, Algeria

^cQatar Environment and Energy Research Institute (QEERI) Qatar Foundation, Doha, Qatar

Received: 30 April 2014, accepted 26 May 2014

Abstract

ZnO nanoparticles with different grain sizes have been obtained by mechanical milling, after different treatment times: 3, 6, 12 and 24 hours.

The final products have been characterized by different analytical techniques, such as X Ray Diffraction, Photoluminescence, Fourier transform infrared (FTIR) and UV-Visible spectroscopies.

The cytotoxic effect of one selected concentration ZnO nanoparticles have been evaluated for paramecium growth kinetics and the mortality rate have been recorded as a function of time.

Findings demonstrated that the evolution of the paramecium cell number is clearly affected by ZnO Nps presence.

Keywords: mechanical milling, paramecium, nanoparticles, ZnO, alternative method;

1. Introduction

Nanotechnology is concerned with nanomaterials whose structures exhibit significantly, novel and improved physical, chemical, and biological properties, phenomena and functionality due to their nanoscaled size and to high surface area to volume ratios [1]. Oxide Nanoparticles (Nps) (size < 100nm) have also attracted considerable attention because of their potential use in a vast range of applications including nanoparticle-assisted drug delivery, cell imaging and cancer therapy in biomedicine [2] photocatalysis [3] and solar cells [4]. Among them, Zinc oxide (ZnO) has been reported to be effective in inactivating various microorganisms [5] and bacteria [6].

However, the mechanisms involved in these experiences remain the subject of intensive debate because of the complexity of the interaction between the Nps, the cells and the surrounding medium.

The objective of this preliminary work is to contribute to a better understanding, as well as the evaluation, of the ZnO Nps cytotoxic effects on paramecium, by using different parameters that reflects the state of cell metabolism.

2. Experimental

2.1 Preparation of ZnO nanoparticles

Commercial ZnO nanoparticles (99, 99% purity) has been milled during different times (3, 6, 12 and 24 h) in order to obtain ZnO Nps with several grain sizes.

2.2 Characterization of ZnO nanoparticles

The obtained powder has firstly been characterized by X-ray diffraction.

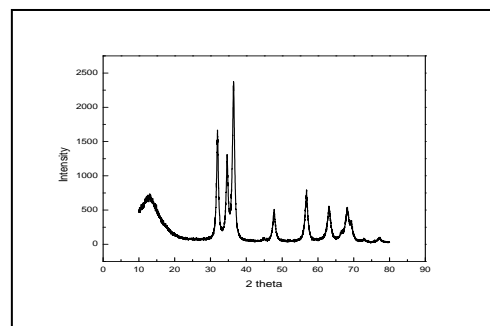


Figure 1 shows an example of X- ray diffraction pattern of ZnO nanoparticles.

2.3. Cytotoxicity effects of ZnO Nps on paramecium

Figure 2 shows the paramecium number variation versus time and that, for 4 different milling time obtained samples.

Moreover, the response percentage of treated paramecium versus time has been illustrated by Figure 3.

3. Results

Fig 1: X ray diffraction of ZnO nanoparticles

It clearly appears that the ZnO is crystalline in nature, and the diffraction peaks matched a hexagonal zincite phase of ZnO, in accordance with the standard ones. No characteristic peaks of any impurities were detected, suggesting that high-quality ZnO was obtained.

In addition, ZnO nanoparticle grain sizes has been deduced from the Debye -Scherrer formula: $D = K\lambda / (\beta \cos\theta)$, where K is the Scherrer constant (0.9 for ZnO), λ the X- ray wavelength (1.54016 Å for Cu K_{α} radiation), β the peak width of half maximum and θ the Bragg diffraction angle. The average crystallite size estimated was between 6 and 19 nm.

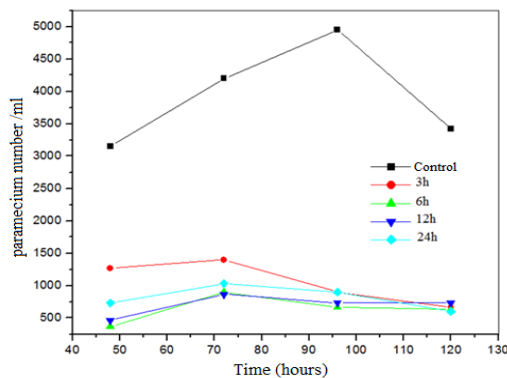


Fig 2 Growth kinetics of the paramecium treated by ZnO nanoparticles as function of time

It appears that the toxicity of Nano ZnO on paramecium cells is quite significant.

Generally, these effects occur primarily by a loss of mobility accompanied disorderly movements of ciliated protists, this brings us to confirm the influence of ZnO Nps within cells, despite the presence of the

cell membrane, is a barrier against the massive entrance of xenobiotic but is still permeable.

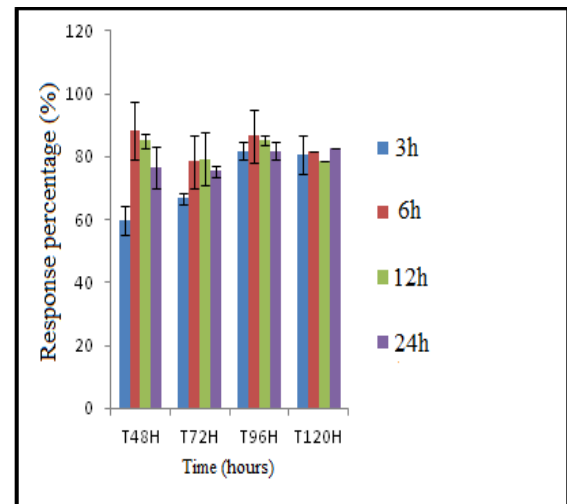


Fig 3 Response percentage of treated paramecium versus time.

The response percentage is a parameter confirms the evolution of growth curves paramecia treated with different grain size of ZnO Nps.

The chemical stress releases free radicals in the cell which leads to an alteration (peroxidation) of cellular components (lipids, proteins) so the membrane.

References

- [1] M. Premanathan, K. Karthikeyan, K. Jeyasubramanian, G.Manivannan, Nanomedicine7 (2011) 184-192.
- [2] A. Nel, T. Xia, L. Madler, N. Li, Science 311 (5761) (2006) 622-627.
- [3] Gupta Shipra Mital, Tripathi Manoj, Chin. Sci. Bull. 56 (2011) 1639-1657.
- [4] K.R. Catchpole, A. Polman, Opt. Express 16 (2008) 21793-21800.
- [5] A.A. Tayel, W.F. Tras-EL, S. Moussa, A.F. Baz, H.A. Mahrous, M.F. Salem, L. Brimer, J. Food Saf. 31 (2011) 211.
- [6] V.K. Mishra, A. Kumar, Digest J. Nanomater. Biostruct. 4 (2009) 587.

The effect of bath temperature on the electrodeposition of zinc oxide nanostructures via nitrates solution

Loubna Mentar¹, Hala Lahmar, Mohamed Redha Khelladi and Amor Azizi

Laboratoire de Chimie, Ingénierie Moléculaire et Nanostructures, Université Sétif-1, 19000, Algeria

Received: 30 April 2014, accepted 26 May 2014

Abstract

Zinc oxide (ZnO) nanostructures were electrodeposited onto ITO coated glass substrates from nitrate medium at different temperatures. The electrochemical deposition process was analyzed and the characteristics of the nanostructures were discussed. The electrochemical results showed that the deposition temperature had an important effect on the current density and the film morphology. From the Mott-Schottky measurements, the flat-band potential and the donor density for the ZnO nanostructure are determined. The morphological, structural and optical properties were studied by scanning electron microscopy (SEM), x-ray diffraction techniques (XRD) and spectrophotometer in the ultraviolet UV-visible region. SEM images demonstrated that the morphology of ZnO nanostructures depend greatly on the bath temperature. The XRD patterns revealed the formation of phase-pure ZnO nanostructure with hexagonal wurtzite phase. The optical transmittance spectrum gave a high transmittance of 82 % at low temperatures, and the optical band-gap (E_g) of the ZnO nanostructures was between 3.25~3.49 eV.

Keywords: Electrodeposition, ZnO nanostructures, Mott-Schottky, morphology, structure.

1. Introduction

The synthesis of semiconductor crystals with well-defined shapes, sizes, and structures has attracted extraordinary interest in order to realize their unique properties that not only depend on their chemical composition, but also on their shape, structure, phase, size, and size distribution [1, 2]. Zinc oxide (ZnO) is one of the most promising materials for nanotechnology due to its range of potential applications such as sensors, photovoltaic cells, light-emitting diodes and nanogenerators. Among various synthesis methods, electrochemical deposition represents a simple and inexpensive solution based method for synthesis of semiconductor nanostructures. In effect, electrodeposition of ZnO is a versatile growth method and many various nanostructures with a range of morphologies can be easily designed by the technique [3]. Consequently, in recent years, there has been extensive interest in synthesizing various ZnO nanostructures, including nanowires, nanoribbons and nanotubes; the nanostructures growth was controlled by deposition parameters such as electrolyte bath composition, pH, deposition potential or deposition current density and bath temperature [4]. Consequently, in this paper, we

report on the influence of deposition temperature on the properties of ZnO nanostructures.

2. Experimental Details

ZnO nanostructures were prepared by electrochemical deposition onto indium doped tin oxide (ITO) glass coated substrates with an exposed area of $1 \times 2 \text{ cm}^2$ (10–20 Ω/cm^2 sheet resistance). All the depositions were made in a three-electrode electrochemical cell with the substrate as the working electrode (ITO), a Platinum wire as a counter electrode, saturated calomel electrode (SCE) as reference. The ITO substrate was first degreased in acetone and ethanol by ultrasonication for 15 min, and lastly well rinsed with distilled water. The electrodeposition of ZnO nanostructures and cyclic voltammetry (CV) measurements were carried out using, a computer controlled potentiostat/galvanostat (Voltalab 40) as a potential source. The electrolyte consisted of a solution contained 0.1 M zinc nitrate with 1 M KNO_3 . The pH of solution is fixed at 6.5. Electrodeposition was performed at different temperatures ranging from 30 to 70 °C, without stirring. The ZnO nanostructure/electrolyte capacitance was measured at an AC frequency of 20

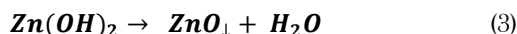
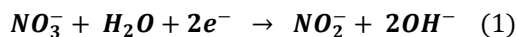
Hz using a Voltalab 40 Model PGZ301. Little frequency dispersion was observed for the measured capacitances in the frequency region 5–5000 Hz. The surface morphology and microstructure of the ZnO nanostructures were examined using Quanta 200 scanning electron microscope (SEM). Phases identification and crystallographic structure determination were carried out using XRD on a Philips X-pert pro diffractometer with $\text{CuK}\alpha$ radiation ($\lambda = 1.5418 \text{ \AA}$) in the θ - 2θ geometry. The optical transmittance spectra were obtained with a SHIMADZU 2401PC spectrophotometer in the ultraviolet UV-visible region. The spectra were corrected for glass substrates.

3. Results

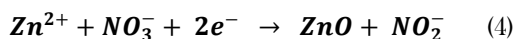
3.1. Electrochemical study

In this work, the applied potential was fixed at -1.3 V vs. SCE, and $[\text{Zn}^{2+}]$ at 0.1M and bath temperature were changed to systematically examine the electrochemical, morphological and structural properties of electrodeposited ZnO. In order to verify the influence of temperature on the electrochemical behavior of the electrodes in the electrodeposition bath, the cyclic voltammetry was performed. Fig. 1 shows the voltammograms obtained from 0.1 M zinc nitrate aqueous solution at different temperatures. It is clear that the intensity of the cathode current increases with the temperature of the electrolytic bath. Indeed, in the range from 30 and 70 °C, the intensity varies from -1.21 to -3.38 mA/cm², respectively. A change in the kinetics at the electrode can be mentioned as consequence of the shift of the peaks of Zn reduction to more negative values of the potential [5]. The crystallization accompanied by dehydration may depend on the deposition temperature [6].

It's well established that the electrodeposition of ZnO is a three-stage process [7]. At the first stage, hydroxide ions are contributed from both $\text{Zn}(\text{NO}_3)_2$ and KNO_3 . Chemical reactions taking place at the working electrode during the electrochemical deposition reaction of ZnO nanostructures are the following [8]:



This result in the following total reaction:



Referring to Fig. 1, two reduction picks in the potential range of 0 and -1.4 V vs. SCE are observed. One corresponds to reduce of nitrate ions (NO_3^-) to hydroxyl ions (OH^-) (eq. 1) which occurs around -0.65 V vs. SCE. The other reaction reduces Zn^{2+} ions to metallic Zn (eq. 2) which occurs below around -1.0 V. When the applied potential is around -0.7 V, OH^- ions are produced in the deposition solution, which in turn react with Zn^{2+} ions in the solution to form ZnO (eq.3)

The conduction type, the flat band (E_b), and the estimated donor densities of ZnO were determined using Mott-Schottky (M-S) measurements with $1/C^2$ vs. E at a fixed frequency of 20 kHz. The capacitance-potential measurements are presented as an M-S plot following the equation below [9]:

$$\frac{1}{C^2} = \frac{2}{N_D e \epsilon_0 \epsilon} \left[(E - E_{fb}) - \frac{kT}{e} \right] \quad (5)$$

where C is the space charge capacitance in the semiconductor; N_D is the hole carrier density; e is the elemental charge value; ϵ_0 is the permittivity of the vacuum; of free space; ($8.85 \cdot 10^{-12} \text{ F cm}^{-1}$); ϵ is the relative permittivity of the semiconductor (ϵ of ZnO is 8.5); E is the applied potential, E_b is the flat band potential, T is the temperature, and k is the Boltzmann constant.

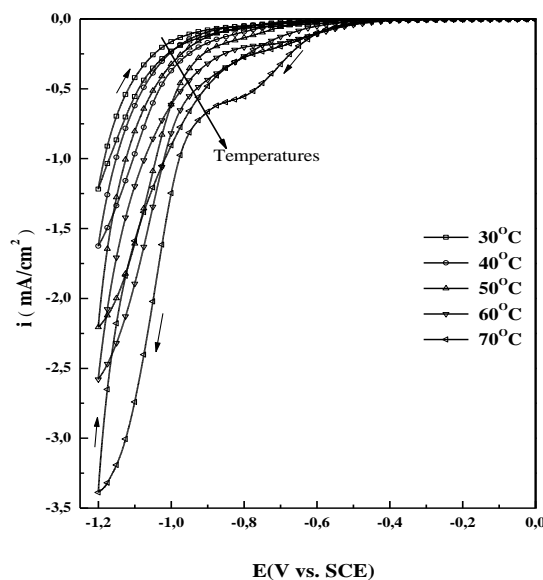


Fig. 1 Cathodic scan of 0.1 M $\text{Zn}(\text{NO}_3)_2$ with 1 M KNO_3 aqueous solution on a ITO electrode at pH 6.5 at different bath temperatures from 30 to 70 °C.

By plotting the $\frac{1}{C^2}$ versus E , the donor density and the flat-band potential of an n-type semiconductor can be obtained from the slope ($= \frac{2}{\epsilon\epsilon_0 e N_D}$) and intercept at $C = 0$. Thus from Fig. 2, the flat-band potential and the donor density of an n-type semiconductor of ZnO deposited at different temperatures are summarized in Table 1. As indicated, the estimated donor densities are found to decrease with increasing deposition temperature.

Table 1: Donor density and flat band potential (E_b) calculated from Mott-Schottky equation.

T (°C)	E_b (V)	$N_D (\times 10^{20} \text{ cm}^{-3})$
30	-0.870	4.96
40	-1.029	4.76
50	-0.800	2.58
60	-1.148	2.15
70	-1.026	4.31

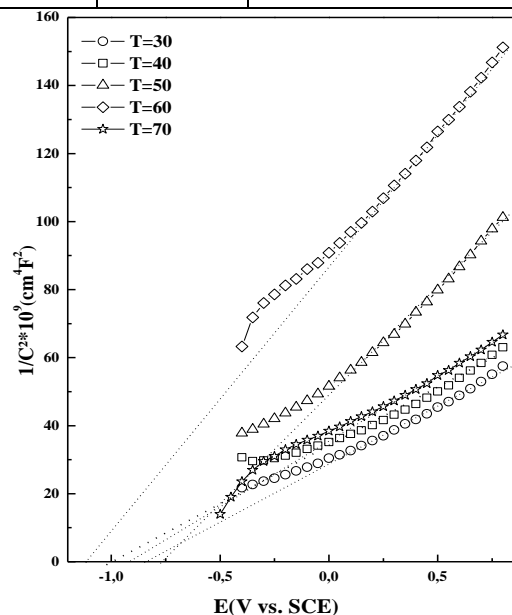


Fig. 2 Mott-Schottky plot for electrodeposited ZnO nanostructures of 0.1 M $\text{Zn}(\text{NO}_3)_2$ + 1M KNO_3 solution obtained at 20 Hz at different bath temperatures (30 → 70 °C). The corresponding flat band potential values are indicated. The lines were simply drawn through the data points.

3.2. Morphology

The morphology of deposited ZnO nanostructures was observed by SEM (Fig. 3), which exhibited different morphologies. The surface morphologies are found to change considerably as the deposition temperature is increased. For the growth at 30 °C, very thin nanosheet structures grown on the substrate are obtained as illustrated in Fig. 3a. When the deposition temperature is increased from 40 to 70 °C, some sheet structures become quite bigger as shown in Fig. 1b, d and e. In particular, for the deposition temperature around 50 °C, the surface morphology of deposit exhibited entangled nanostructures (Fig. 3c); these morphology is observed in the literature [10, 11].

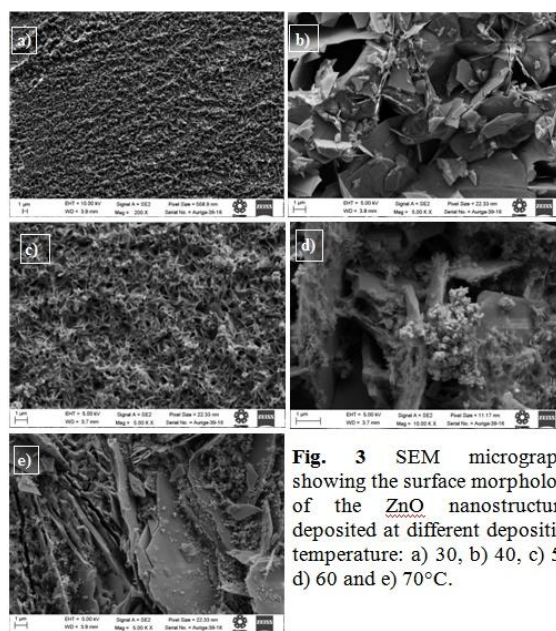


Fig. 3 SEM micrographs showing the surface morphology of the ZnO nanostructures deposited at different deposition temperature: a) 30, b) 40, c) 50, d) 60 and e) 70 °C.

3.3. Structural analysis

Fig. 4 shows the XRD patterns in the 2θ range of 25 to 75 of the ZnO nanostructures prepared at different temperatures. All samples are polycrystalline with hexagonal wurtzite structure (JCPDS 01-076-0704). Also, these patterns showed that the structure of the deposits was sensitive to the bath temperature used for the deposition of ZnO nanostructures. From the XRD patterns the crystallinity of ZnO was improved by increasing deposition temperature and as consequence intensities of other peaks also increase. In particular, the nanostructure deposited at 70 °C has a strong (101), (100) and (002) orientations; signed for height crystallinity. The average crystallite size was estimated from the full width at half- maximum

(FWHM) values of diffraction peaks using the Scherrer formula [12]:

$$D = \frac{0.9\lambda}{\beta \cos\theta} \quad (6)$$

where D is the crystallite size, β is the broadening of the diffraction line measured at FWHM, λ is the x-ray wavelength (1.5406 Å) used and θ is the diffraction angle.

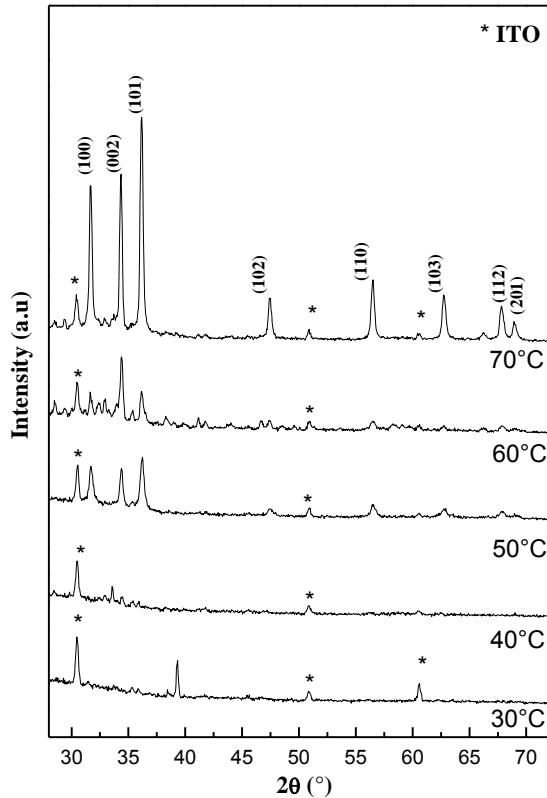


Fig.4 XRD patterns of ZnO nanostructures deposited at various temperature from 30 to 70°C. XRD peaks of ITO substrate are marked by *.

The crystallite size, calculated after correcting for instrumental broadening, along the (002) peak ranges from 55 to 64 nm. From these values, it is observed that the average crystallite size increases with the bath temperature.

3.4. Optical properties

The optical transmission spectra recorded in the range of 200 to 800 nm of the ZnO nanostructures deposited at different temperature are shown in Fig. 5.

The values of the transmission obtained vary from 82 to 74 % with increasing deposition temperature. It may be seen from this entire figure that all the prepared ZnO nanostructures films exhibited high optical transmittance (> 70 %) in the visible region. The decrease of the film transparency with the increase of temperature can be explained by the increasing of the thickness of nanostructures at high temperature [13].

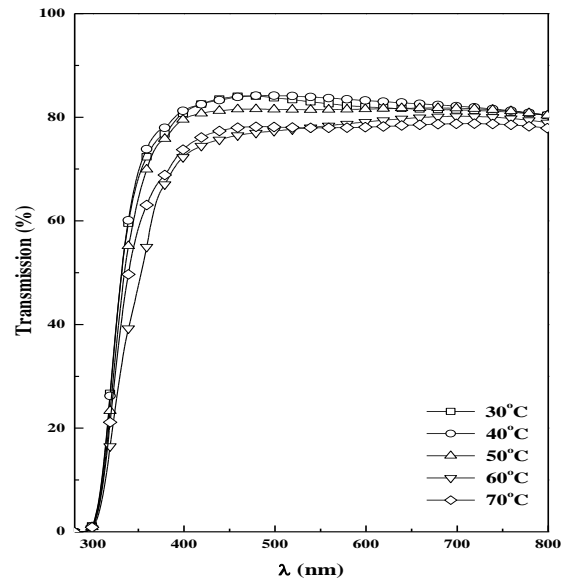


Fig. 5 Transmission spectra of the ZnO nanostructures deposited at different temperature.

The Tauc's plot were drawn to determine the energy band gap values of the deposited films, the nature of transition is determined using the following equation [14],

$$\alpha h\nu = A(h\nu - E_g)^n \quad (7)$$

where α is absorption coefficient in cm^{-1} , $h\nu$ is photon energy, E_g is an energy gap, A is energy dependent constant and n is an integer depending on the nature of electronic transitions. For the direct allowed transitions, n has a value of 1/2 while for the indirect allowed transitions, $n = 2$. The value of band gap at different deposition temperature was found to be in the range of 3.25-3.49 eV. These values decrease with increasing the temperature deposition.

It can be attributed to improvement in the crystallinity with temperature as supported by XRD studies.

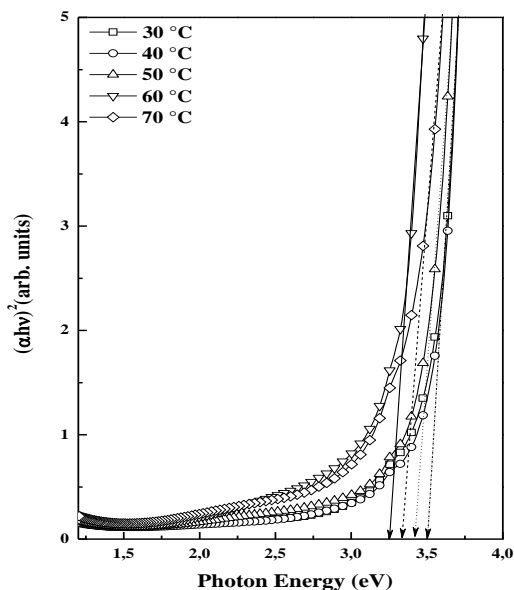


Fig. 6 Plot $(\alpha h\nu)^2$ versus $h\nu$ for ZnO nanostructures films deposited at different temperature. The band gap values obtained by extrapolating the linear part of the curves are also shown.

These results clearly show that the morphology and crystallite size of the ZnO deposits plays a very important role in the control of the light scattering. Indeed, nanostructures deposited at high temperatures, relatively large size (> 60 nm) are very interesting for inducing an effective dissemination throughout the wavelength range of visible light. This can be very important for their application in nanostructured solar cells.

4. Conclusion

We have studied the effects of bath temperature on the electrodeposition of nanostructures from nitrate medium. The carrier density of ZnO nanostructures decreased from 4.96×10^{20} to 2.15×10^{20} cm^{-3} with increasing deposition temperature. The

nanostructures with different morphology and high crystallinity could be obtained by increasing the temperature. The optical transmittance spectrum gave a relatively high transmittance ($\approx 80\%$) and the optical band-gap of the ZnO nanostructures was found to increase with temperature and to be in the range of 3.25-3.49 eV.

References

- [1] X. Lan, J. Y. Zhang, H. Gao, T. M. Wang. *CrystEngComm* 13 (2011) 636.
- [2] S. Chatterjee, S. Gohil, B. Chalke, P. Ayyub, 9 (2009) 4792.
- [3] M.R. Khelladi, L. Mentar, M. Boubatra, A. Azizi, *Mater. Lett.* 67 (2012) 331.
- [4] M. R. Khelladi, L. Mentar, A. Beniaïche, L. Makhloufi, A. Azizi, *J Mater Sci: Mater Electron*, 24 (2013) 153.
- [5] S. Otani, J. Katayama, H. Umemoto, M. Matsuoka, *J. Electrochem. Soc.* 153 (2006) C551.
- [6] Belavalli E. Prasad, P. Vishnu Kamath, S. Ranganath, *J Solid State Electrochem* 16 (2012) 3715.
- [7] T. Yoshida, D. Komatsu, N. Shimokawa, H. Minoura, *Thin Solid Films*, 451 (2004) 166.
- [8] S.J. Limmer, E.A. Kulp, J. A. Switzer, *Langmuir*, 22 (2006) 10535.
- [9] S.R. Morrison, *Electrochemistry at semiconductor and oxidized metal electrodes* (Plenum Press, New York, 1980).
- [10] K. Wuaz, J. biao Cuib, *ECS Solid State Letters*, 2 (2013) 8742.
- [11] T. Singh, D. K. Pandya, R. Singh, *International Conference on Physics of Emerging Functional Materials (PEFM-2010)*.
- [12] A.D. Krawitz, *Introduction to Diffraction in Materials Science and Engineering*, Wiley-VCH, April 2001.
- [13] R. Mariappan, V. Ponnuswamy, P. Suresh, *Superlattice Microst* 52 (2012) 500.
- [14] J. Tauc. *Optical Properties of Solids* 22, F. Abeles, Ed., North Holland Pub, Amsterdam, (1970).

Temperature effect on the vibration characteristics of carbon nanotubes

B. Kheroubi^a, H. Heireche^a, A. Benzair^a and A. Tounsi^b

^a *Département of Physic, University of Sidi Bel Abbès, Algéria*

^b *Materials and Hydrology Laboratory, University of Sidi Bel Abbès, Algéria*

Received: 30 April 2014, accepted 26 May 2014

Abstract

In this work, the thermal buckling properties of carbon nanotube with small scale effect are studied. Based on the nonlocal continuum theory and the Timoshenko beam model, the governing equation is derived and the critical buckling temperature is presented. The influences of the scale coefficients, the ratio of the length to the diameter, the transverse shear deformation and rotary inertia are discussed. It can be observed that the small scale effects are significant and should be considered for thermal analysis of carbon nanotube. The critical buckling temperature becomes higher with the ratio of length to the diameter increasing. Furthermore, for smaller ratios of the length to the diameter and higher mode numbers, the transverse shear deformation and rotary inertia have remarkable influences on the thermal buckling behaviors.

Keywords: carbon nanotube, scale effects, nondimensional critical buckling temperature, thermal buckling, Timoshenko beam.

PACS:

1. Introduction

Since their discovery, carbon nanotubes were quickly imposed in various areas, particularly in the area of nanotechnology. The unique structure of this compound derived graphene makes it one of the most interesting both electronic and mechanical perspective and promises many marketable outs.

Carbon nanotubes were discovered by chance among the soot obtained in the discharge of an electric arc between two carbon electrodes. It is in this type of experience as researchers from the Universities of Heidelberg and Houston had observed in 1986 carbon molecules of a new type: the fullerenes.

It is in these Sumio Iijima that soot [1] Japanese scholar observed in 1991 funny little hollow tubes made of carbon atoms and that no one had previously noticed. They were given the name of "carbon nanotubes".

Some researchers have shown that the mechanical behaviors of the carbon nanotube are sensitive to the thermal effects in the external environment [2-4]. Recently, considering the effects of the transverse shear deformation and rotary inertia,

Hsu et al. [5] and Lee and Chang [6] have been undertaken to study the thermal buckling properties of the carbon nanotubes using Timoshenko beam model. At the end to see the scale effect (e_0a) on the buckling properties of carbon nanotubes, equation involving the nonlocal Timoshenko beam theory has been established.

2. Motion equation

The nonlocal elasticity model was first presented by Eringen (1972). According to this model, the stress at a reference point in the body is dependent not only on the strain state at that point, but also on the strain state at all of the points throughout the body. The constitutive equation of the nonlocal elasticity can be written as follows

$$[1 - (e_0a)^2 \nabla^2] \sigma_{ij} = C_{ijkl} \varepsilon_{kl} \quad (2.1)$$

Where C_{ijkl} is the elastic modulus tensor of the classical isotropic elasticity; and σ_{ij} and ε_{kl} are the stress and strain tensors, respectively. In addition, e_0 is a nondimensional material constant, determined by experiments, and a is an internal characteristic length (e.g. a lattice parameter, granular distance). Therefore, e_0a is a constant parameter that showing the small-scale effect in nano-structures.

For the nonlocal Timoshenko beam theory, the Hook's law of carbon nanotube can be expressed as the following partial differential forms:

$$\sigma_x - (e_0a)^2 \frac{\partial^2 \sigma_x}{\partial x^2} = E \varepsilon_x, \quad (2.2a)$$

$$\tau_{x,z} - (e_0a)^2 \frac{\partial^2 \tau_{x,z}}{\partial x^2} = G \gamma_{x,z}, \quad (2.2b)$$

Where:

σ_x : The axial stress,

$\tau_{x,z}$: The shear stress,

ε_x : The axial strain,
 γ_{xz} : The shear strain,
 E : The Young's modulus,
 G : The shear modulus,
 e_0 : Scale effect coefficient.

The expressions of the axial strain and the shear strain are [7]:

$$\varepsilon_x = z \frac{\partial \psi}{\partial x}, \quad (2.3a)$$

$$\gamma_{xz} = \frac{\partial W}{\partial x} - \psi, \quad (2.3b)$$

Where W is the transverse displacement and ψ the rotation caused by bending.

For the Timoshenko beam model with the thermal stress, the following relation can be derived:

$$\frac{\partial S}{\partial x} = -N_T \frac{\partial^2 W}{\partial x^2}, \quad (2.4a)$$

$$\frac{\partial M}{\partial x} + S = 0, \quad (2.4b)$$

Where S is the shear force, M the resultant bending moment and N_T the thermal force which can be expressed as:

$$N_T = -\frac{E\alpha T A_c}{1-2\nu}, \quad (2.5)$$

Where α is the thermal expansion coefficient, T the temperature change, A_c the cross area and ν the Poisson's ratio.

The bending moment and the shear force can be defined by

$$M = \int_{A_c} z \sigma_x dA_c, \quad (2.6a)$$

$$S = K \int_{A_c} \tau_{xz} dA_c. \quad (2.6b)$$

Multiplying equation (2.1a) By $z dA_c$ and integrating the result on the surface of A_c , we obtain:

$$\int_{A_c} z \sigma_x dA_c - (e_0 a)^2 \int_{A_c} z \frac{\partial^2 \sigma_x}{\partial x^2} dA_c = E \int_{A_c} z \varepsilon_x dA_c$$

Substituting equations (2.2a), (2.5a), we obtain:

$$\int_{A_c} z \sigma_x dA_c - (e_0 a)^2 \int_{A_c} z \frac{\partial^2 \sigma_x}{\partial x^2} dA_c = E \int_{A_c} z^2 \frac{\partial \psi}{\partial x} dA_c$$

$$\text{Avec: } I = \int_{A_c} z^2 dA_c, \quad \frac{\partial^2 M}{\partial x^2} = \int_{A_c} z \frac{\partial^2 \sigma_x}{\partial x^2} dA_c$$

Or:

$$M - (e_0 a)^2 \frac{\partial^2 M}{\partial x^2} = EI \frac{\partial \psi}{\partial x}, \quad (2.7a)$$

By integrating equation (2.1b), one obtains:

$$\int_{A_c} \tau_{xz} dA_c - (e_0 a)^2 \int_{A_c} \frac{\partial^2 \tau_{xz}}{\partial x^2} dA_c = \int_{A_c} G \gamma_{xz} dA_c$$

Substituting equation (2.5b)

$$\text{and } \frac{\partial^2 S}{\partial x^2} = \int_{A_c} \frac{\partial^2 \tau_{xz}}{\partial x^2} dA_c$$

So we obtain:

$$S - (e_0 a)^2 \frac{\partial^2 S}{\partial x^2} = K A_c G \left(\frac{\partial W}{\partial x} - \psi \right) \quad (2.7b)$$

Where $I = \int_{A_c} z^2 dA_c$ is the moment of inertia and K the shear correction factor which is used to compensate for the error due to the constant shear stress assumption.

Based on Eqs. (2.3b) and (2.6a) the following relation can be obtained: (2.3b)

$$M = EI \frac{\partial \psi}{\partial x} + (e_0 a)^2 \left(-\frac{\partial S}{\partial x} \right). \quad (2.8)$$

Substituting Eq. (2.3a) into Eq. (2.7), we can obtain

$$M = EI \frac{\partial \psi}{\partial x} + (e_0 a)^2 \left(N_T \frac{\partial^2 W}{\partial x^2} \right). \quad (2.9)$$

Based on Eqs. (2.3a) and (2.6b), it can be derived that

$$S = K A_c G \left(\frac{\partial W}{\partial x} - \psi \right) + (e_0 a)^2 \left(-N_T \frac{\partial^3 W}{\partial x^3} \right). \quad (2.10)$$

Substituting Eq. (2.9) into Eq. (2.3a), we can obtain

$$K A_c G \left(\frac{\partial^2 W}{\partial x^2} - \frac{\partial \psi}{\partial x} \right) + (e_0 a)^2 \left(-N_T \frac{\partial^4 W}{\partial x^4} \right) = -N_T \frac{\partial^2 W}{\partial x^2}. \quad (2.11)$$

Based on Eqs. (2.3b), (2.8) and (2.9), the following relation can be derived:

$$EI \frac{\partial^2 \psi}{\partial x^2} + K A_c G \left(\frac{\partial W}{\partial x} - \psi \right) = 0. \quad (2.12)$$

It can be observed that Eqs. (2.10) and (2.11) are the governing equations. For the hinged boundary condition, the solution of carbon nanotube can be expressed as

$$\begin{aligned} w &= W \sin(\lambda x), \\ \psi &= \psi \cos(\lambda x), \end{aligned} \quad (2.13)$$

Where W and ψ are the amplitudes of the deflection and the slope, $\lambda = k\pi/L$ and k a positive integer which is related to the buckling modes.

Substituting Eq. (2.12) into Eqs. (2.10) and (2.11), we can obtain

$$[(e_0 a)^2 \lambda^2 + 1] \lambda^2 N_T W + \lambda^2 K A_c G W - \lambda K A_c G \psi = 0, \quad (2.14a)$$

$$\lambda K A_c G W - (\lambda^2 EI + K A_c G) \psi = 0. \quad (2.14b)$$

Then, the critical temperature with the nonlocal continuum theory can be derived as

$$T_{cr}^{non} = \frac{\lambda^2 K G I (1-2\nu)}{\alpha [(e_0 a)^2 \lambda^2 + 1] (K A_c G + EI \lambda^2)} \quad (2.15)$$

As a result, the critical buckling temperature can be expressed as the following form [8-9]:

$$P_{cr} = \frac{T_{cr}^{non}}{1/\alpha A_c L^2}$$

3. Results and discussions

In this section, numerical calculations for the thermal buckling properties of carbon nanotube are carried out. The material constants used in the calculation are the Young's modulus $E=1$ TPa, the Poisson's ratio $\nu=0.3$, the shear modulus $G=E/[2(1+\nu)]$, the shear coefficient $k = 10/9$ and the temperature expansion coefficient $\alpha = 1.1 \times 10^{-6}$ K^{-1} which is for the case of the high temperature [10, 11, 12, 13]. It should be noted that according to the previous discussions about the values of e_0 and a in detail, $e_0 a$ is usually considered as the single scale coefficient which is smaller than 2.0 nm for nanostructure [14,15].

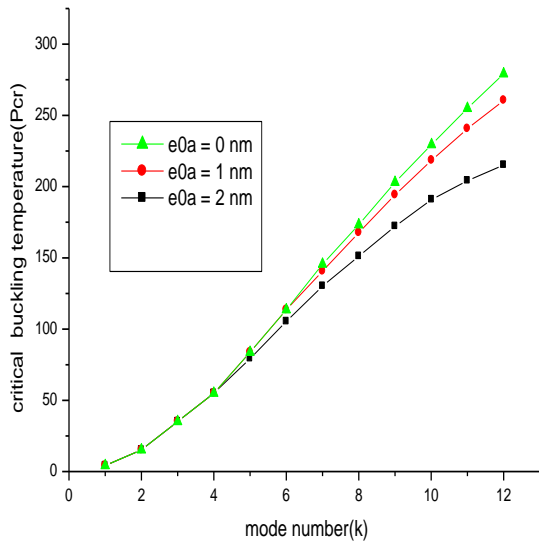


Fig.1. Relation between the critical buckling temperature (P_{cr}) and the mode number (k) with different scale coefficients ($e_0 a$), the value of $L/d=20$.

The relation between the critical temperature (P_{cr}) and the mode number (k) is presented in fig. 1. The ratio of the length to the diameter, L/d is 20. The scale coefficients $e_0 a = 0, 1$ and 2 nm are considered. The most notable feature is that the results based on the two theories are almost the same for small mode numbers. However, the difference becomes obvious with the mode number increasing. The classical elastic (i.e. the local) model, which does not consider the small scale effects, will give a higher approximation for the critical buckling temperature. But the nonlocal continuum theory will present an accurate and reliable result.

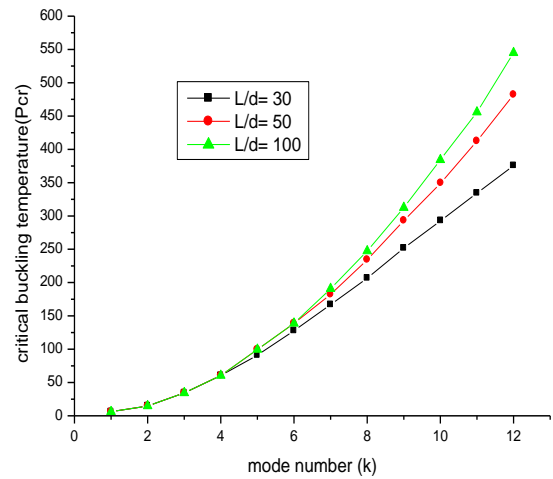


Fig.2. Relation between the critical buckling temperature (P_{cr}) and the mode number (k) with different values of L/d . The scale coefficient $e_0 a = 1$ nm.

The influences of the ratio of the length to the diameter (L/d) on the critical buckling temperature are shown in fig. 2. The scale coefficient is 1 nm. From fig. 2, it can be seen that when the mode number is less than 4, the difference is not obvious. When the mode number is larger than 5, this influence becomes remarkable. Moreover, the critical buckling temperatures for all of the three ratios become larger with the mode number increasing. The larger the ratio of the length to the diameter is, the higher the nondimensional critical buckling temperature becomes. It means that the ratio of the length to the diameter has significant influence on the critical buckling temperature for larger mode numbers.

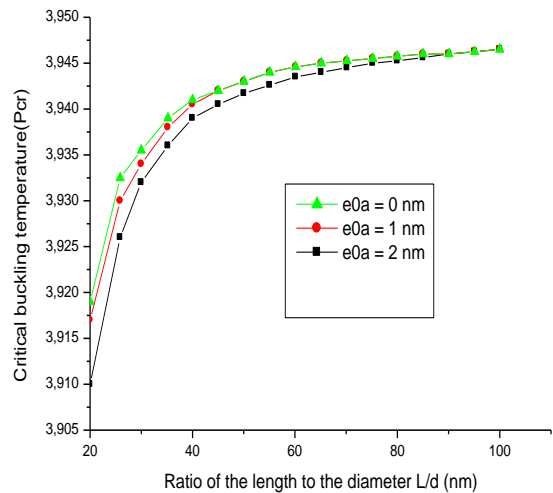


Fig.3.a. Relation between the critical buckling temperature (P_{cr}) and the value of L/d with different scale coefficients ($e_0 a$), $k = 1$.

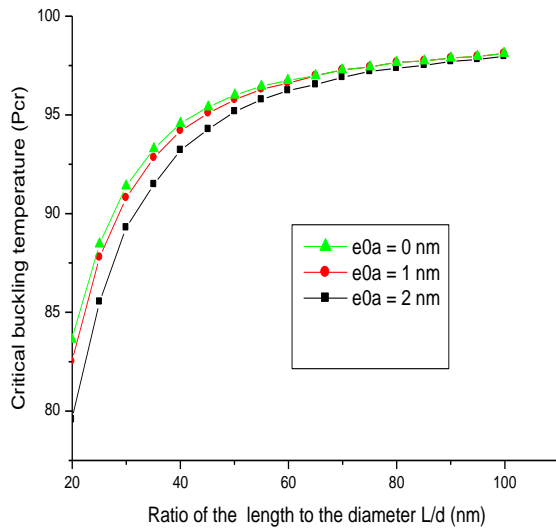


Fig.3.b. Relation between the critical buckling temperature (P_{cr}) and the value of L/d with different scale coefficients (e_0a), $k = 5$.

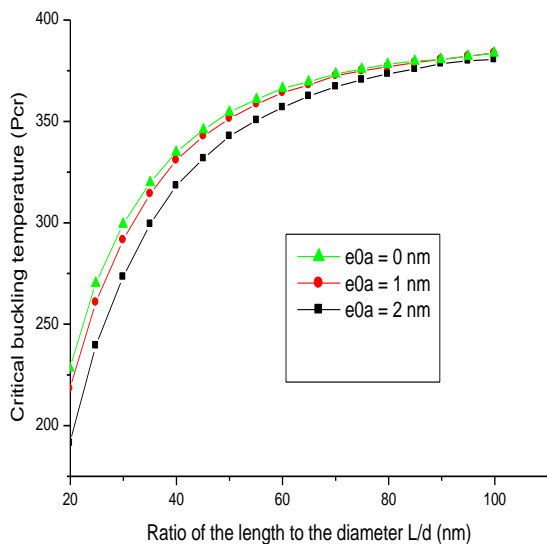


Fig.3.c. Relation between the critical buckling temperature (P_{cr}) and the value of L/d with different scale coefficients (e_0a), $k = 10$.

The relation between the critical buckling temperature and the ratio of the length to the diameter are shown in fig. 3(a)-(c). The scale coefficients $e_0a = 0, 1$ and 2 nm and the mode number $k = 1, 5$ and 10 are considered, respectively. It can be seen that the ranges of the critical buckling temperature for these mode numbers are quite different. In fig. 3(a), the range is the smallest for $k = 1$, but the range is the largest for $k = 10$ in fig. 3(c). It means that

the larger the mode number is, the higher the critical buckling temperature becomes.

Furthermore, it can be observed that when the ratio of the length to the diameter is small, the scale effects are significant. However, the scale effects on the nondimensional critical buckling temperature will diminish with the ratio (i.e. L/d) increasing. It implies that the scale effects on the thermal buckling properties are not obvious for slender carbon nanotube but should be taken into account for short nanotube.

4. Conclusions

In this work, based on the nonlocal continuum theory, the governing equation is presented and the critical buckling temperature of carbon nanotube is derived. The influences of the scale coefficient, the ratio of the length to the diameter, the transverse shear deformation and rotary inertia on the thermal buckling properties are discussed. From the results, it can be concluded that the small scale effects should be considered for the thermal buckling behaviors, especially for higher mode numbers and short carbon nanotube. The critical buckling temperature can be changed by different ratios of the length to the diameter. The influences of the transverse shear deformation and rotary inertia are obvious for higher mode numbers and smaller ratios of the length to the diameter.

References

- [1] S. Iijima, Helical microtubules of graphitic carbon. *Nature*, 354:56 – 58, 1991.
- [2] Y.Q.Zhang, X. Liu, G.R. Liu, *Nanotechnology* 18 (2007) 445701.
- [3] T.Murmu, S.C. Pradhan, *Computational materials Science* 46 (2009) 854.
- [4] A.Tounsi, H. Heireche, H.M. Berrabah, A. Benzair, L. Boumia, *Journal of Applied Physics* 104 (2008) 104301.
- [5] J.C.Hsu, H.L. Lee, W.J. Chang, *Journal of Applied Physics* 105 (2009) 103512.
- [6] H.L. Lee, W.J. Chang, *Physica E* 41 (2009) 1492.
- [7] J.D. Achenbach, *Wave propagation elastic solids*, North-Holland publishing company, Amsterdam, 1973.
- [8] J.C.Hsu, H.L. Lee, W.J. Chang, *Journal of Applied Physics* 105 (2009) 103512.
- [9] H.L. Lee, W.J. Chang, *Physica E* 41 (2009) 1492.
- [10] Y.Q.Zhang, X. Liu, G.R. Liu, *Nanotechnology* 18 (2007) 445701.
- [11] H.L. Lee, W.J. Chang, *Physica E* 41 (2009) 1492.
- [12] X.H.Yao, Q.Han, *Journal of engineering Materials and Technology* 128 (2006) 419.
- [13] M.J. Hao, X.M. Guo, Q. Wang, *European journal of Mechanics A: solids* 29 (2010) 49.
- [14] A.Tounsi, H. Heireche, H.M. Berrabah, A. Benzair, L. Boumia, *Journal of Applied Physics* 104 (2008) 104301.
- [15] Q.Wang, C.M. Wang, *Nanotechnology* 18 (2007) 075702.

Structural and magnetic properties of electrodeposited NiFe alloy on silicon nanowires.

S. Lamrani^{1,2*}, A. Guittoum³, T. Hadjersi¹, S. Bouanik¹, M. Mebarki¹, N. Benbrahim².

1) Centre de Recherche en technologie des Semi-Conducteurs pour l'énergétique, 2 Bd Frantz Fanon, BP 140 les 7 merveilles, Algiers, Algeria.

2) Université Mouloud Mammeri, Tizi Ouzou, 15000 Algeria.

3) Centre de Recherche Nucléaire d'Alger, 2 Bd Frantz Fanon, BP399 Alger-Gare, Algiers, Algeria.

*) E-mail: lamrani.sabrina@gmail.com

Received: 30 April 2014, accepted 26 May 2014

Abstract

Perpendicular Silicon nanowires (SiNWs), having 20 micrometer in length, were fabricated by metal assisted chemical etching of n-type Si(100) wafers in aqueous HF-solution. In a second step, NiFe films were electrodeposited onto these SiNWs. The structure and magnetic properties of as deposited NiFe layers were studied by X ray diffraction (XRD) and vibrating sample magnetometer (VSM). From X-ray diffraction, the FCC NiFe structure was evidenced with a lattice constant, a , equal to 3.5270 Å. From hysteresis curves, we compute the coercive field, H_c , values. We found that the H_c values range from 102 Oe to 236 Oe.

Keywords: Silicon nanowires, NiFe alloy, structure, magnetic properties.

1 Introduction

In recent decades nanomaterials science and nanotechnology is one of the most attractive areas for scientists, both fundamental and technological level, because of the wide range of possible application. The nanowires are part of nanomaterials which have potential applications in the field of optics, electronic components, electronic connectors batteries, solar cells and magnetic recording media ...[1-3].

The nanowires are part of nanomaterials play an important role, in fact they have potential applications in the field of optics, electronic components, electronic connectors batteries, solar cells and magnetic recording media ...[1-3] One of materials most used in magnetism is the permalloy ($\text{Ni}_{80}\text{Fe}_{20}$) due to its high permeability, low coercivity and low magnetic anisotropy. In this work we studied the elaboration of silicon nanowires, and the electrochemical deposition of NiFe on the silicon nanowires. The morphological, structural and magnetic properties were investigated by different characterization techniques.

2 Experimental methods

Before etching, the Si wafers (substrates) were cleaned in trichloroethylene, acetone and ethanol baths in ultrasonic container. Ten wafers were immersed in 10% HF aqueous solution for 5 min at room temperature to remove the native oxide. In this study four samples of silicon nanowires (SiNWs) were elaborated by the metal assisted chemical etching method. The n-type Si (100) wafers were used. Indeed, the cleaned Si samples were dipped into the AgNO_3/HF solution for electroless deposition of Ag nanoparticles (AgNPs) at room temperature ($\sim 20^\circ\text{C}$) for 1min. Subsequently, the AgNP coated Si samples were immersed into the $\text{H}_2\text{O}_2/\text{HF}$ solution for chemical etching for 1 h at room temperature. Finally, the as-etched Si samples were soaked in 69 % HNO_3 to remove the residual AgNPs, cleaned with de-ionized water and dried under azote. These samples were used as a substrate to deposit on a NiFe alloy by electrochemical deposition. The electrolyte used is identical to that reported in the references [4, 5]. All chemicals were of analytical grade and they were used without further purification and mixed in deionized

water. To minimize the oxidation reactions, the solutions were freshly prepared each time before plating.

The deposition was carried out at room temperature, in a three-electrode-cell. A platinum mesh was used as counter electrode and an Ag/AgCl electrode as reference electrode. Different potentials were applied to deposit NiFe alloy on the SiNWs. The structural properties were studied with a Philips X-pert diffractometer in the 2θ scan mode using a Cu $K\alpha$ radiation (1.54056 \AA). The morphology of the samples were investigated by Philips XL 30-FEG scanning electron microscope.

The hysteresis loops were obtained at room temperature using a vibrating sample magnetometer (VSM), with an external magnetic field H applied parallel and perpendicular to the samples surfaces.

3 Results and discussions

Figure 1 shows the cyclic voltammogram of the SiNWs (work electrode) in the plating solution. In the descending potential scan (cathodic branch), it is accurate a deposition of NiFe alloy and the H_2 emission. While the anodic peak arising at positive potentials is the oxidation pic producing a remove of the NiFe deposit [6].

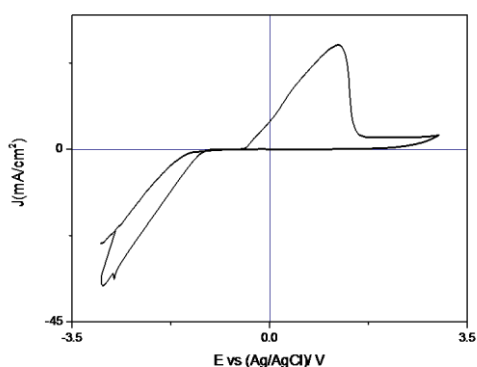


Fig. 1. Cyclic voltammetry scan for silicon nanowires in NiFe electrolyte.

From this XRD spectrum, Fig. 2. (a), we observed that, before removed AgNPs by nitric acid, characteristic peaks of Ag were observed [8].

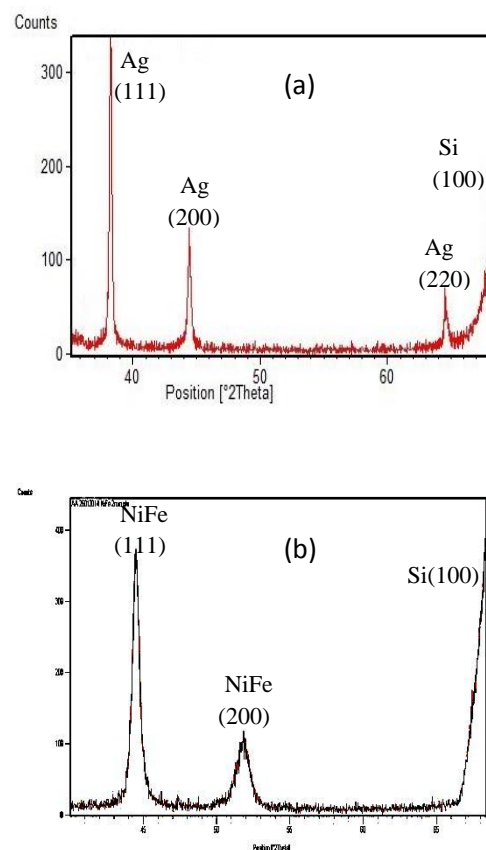


Fig. 2. Example of X-ray diffraction spectra: (a) before remove silver, (b) for NiFe/SiNWs deposit at -2V.

After HNO_3 cleaning, Fig.2. (b) shows characteristic peaks of bcc NiFe alloy. It is also observed that for the NiFe/SiNW a polycrystalline structure is formed. From this spectrum, we calculated the lattice constant, a (\AA), equal to 3.5270 \AA . This value is lower than the bulk value $a_{\text{bulk}}=3.5385 \text{ \AA}$ [7].

The crystallite size of the NiFe/ SiNWs was determined from the widths of the diffraction peaks at half maximum (FWHM) using Scherrer's formula [9]:

$$D = \frac{0.9\lambda}{\beta \cos\theta}$$

Where λ is the wavelength of the Cu $K\alpha$ radiation, θ is the diffraction angle of reflection and β is the FWHM of the diffraction line adjusted by pseudo-Voigt function. For the sample deposit at -2V, D , is equal to 16.4 nm.

The figure 3 shows an example of SEM image of the NiFe/SiNWs deposit at -1.8 V. We observed spherical particles were formed on the surface of the silicon

nanowires. From the section observation, vertical silicon nanowires were observed. Also, it can be seen that some nanowires were broken possible due to the cleavage operation.

The forming process of SiNWs can be described as follow: AgNPs are firstly deposited via Ag^+ reduction in the AgNO_3/HF solution, and then induce the Si at Ag/Si interfaces to be oxidized and then dissolved by HF, leaving pits into Si wafers. Due to the high density of AgNPs, their sinking into silicon substrat lead to formation of SiNWs [11, 10].

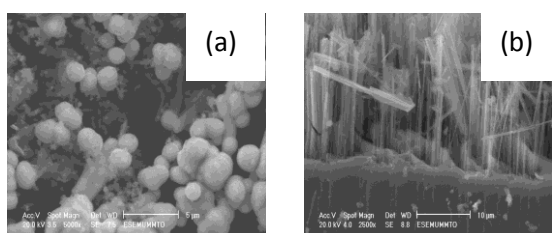


Fig. 3. Plan (a) and cross-sectional (b) view SEM images of NiFe electrochemically deposited onto SiNWs.

In figure 4, we show examples of hysteresis curves for the NiFe/SiNWs with external applied field (H), parallel to the surface of the samples.

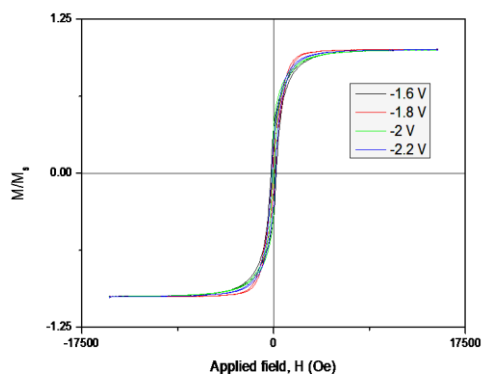


Fig. 4. Normalized magnetization loops as a function of applied magnetic field for NiFe/SiNWs for different applied tensions.

From the hysteresis loops we derived the coercive field (H_c) of the samples. The values of H_c range from 102 Oe to 236 Oe for the tension of -2 V and -1.6 V, respectively. These values are relatively high, in comparison to films [12-14].

4 Conclusion

We elaborated silicon nanowires by metal- assisted chemical etching. NiFe alloy were electrodeposit on these nanowires. The samples presented a polycrystalline structure, having a cell parameter lower than the bulk value. The morphology observed by SEM, shows the formation of spherical particles on the silicon nanowires. The magnetic measurement shows coercivity range from 102 Oe to 236 Oe.

References

- [1] W. Chern, K. Hsu, I.S. Chun, B.P. de Azeredo, N. Ahmed, K.-H. Kim, J.-M. Zuo, N.Fang, P. Ferreira, X. Li, *Nano Lett.* 10 (2010) 1582.
- [2] F. Patolsky, G. Zheng, C.M. Lieber, *Anal. Chem.* 78 (2006) 4260.
- [3] Y. Hea, C. Fanc, S.-T. Lee, *Nano Today* 5 (2010) 282.
- [4] E.R. Spada, L.S. de Oliveira, A.S. da Rocha, A.A. Pasa, G. Zangari, M.L. Sartorelli, *Thin Films of FexNi1-x Electroplated on Silicon (100)*, *J. Magn. Magn. Mater.* 272-276 (2004) E891-E892.
- [5] J.M. Quemper, S. Nicolas, J.P. Gilles, J.P. Grandchamp, A. Bosseboeuf, T.Bourouina, E. Dufour-Gergam, *Permalloy Electroplating Through Photoresist Molds*, *Sensors Actuators A* 74 (1999) 1-4
- [6] S. Sam, G. Fortas, A. Guittoum, N. Gabouze, S. Djebbar, *Surf. Sci.* 601, 4270 (2007)
- [7] T. Yeh, J.M. Sivertsen, J.H. Judy, *IEEE. Trans. Magn.* 23, (1987) 2215
- [8] JCPDS fiche number: 04-0783
- [9] Cullity BD. *Elements of X-ray diffraction*. London: Addison-Wesley, Inc.; 1978.
- [10] O. Fellahi, T. Hadjersi, M. Maamache, S. Bouanik, A. Manseri, *Appl. Surf. Sci.* 257, (2010) 591
- [11] Shao-long Wu, Ting Zhang, Rui-ting Zheng, Guo-an Cheng, *Appl. Surf. Sci.* 258 (2012) 9792- 9799
- [12] A. Guittoum, A. Bourzami, A. Layadi and G. Schmerber, *Eur. Phys. J. Appl. Phys.* 58, issue 02 (2012) 20301
- [13] L. M. Malkinski, R. Eskandari, A. L. Fogel, and S. Min, *J. Appl. Phys.* 111, 07A320 (2012)
- [14] Yuan-Tsung Chen, Chia-Wen Wu, *Intermetallics* 34 (2013) 89-93

The study of the miniaturisation effect on the characteristics of patch antenna using the WCIP method

Toufik Ziar¹, Saida Mellal², Farh Hichem¹, Mourad Zaabat^{2,3} and Chérifa Azizi^{2,3}.

1- Department of MS, Larbi Tebessi University of Tebessa, Algeria.

2- Faculty of SESNV, Larbi Ben M'hidi University of Oum El Bouaghi, Algeria.

3- Materials & active device laboratory LCAM, Larbi Ben M'hidi University of Oum El Bouaghi, Algeria.

Received: 30 April 2014, accepted 26 May 2014

Abstract

The demand of miniature electronic systems has been increasing for several decades. The physical size of systems is reduced due to advancements in integrated circuits. With reduction in size of electronic systems, there is also an increasing demand of small and low cost antennas. Patch antennas are one of the most attractive antennas for integrated RF systems due to their compatibility with microwave integrated circuits. In this paper, the effects of substrate dielectric constant and particularly the miniaturization of the antenna size on the return loss characteristics of patch micro strip antenna (MSPA) have been investigated using the wave concept iterative procedure (WCIP) method. Accuracy of the present results is compared with previous work which has been done theoretically and experimentally.

keywords : Patch antenna ;substrate materials; miniaturization; WCIP method.

1. Introduction

Recently, communication system using electromagnetic waves and especially microwaves became very efficient in many applications such as short range transmission of signals, medical applications, mobiles and laptops where there is a requirement for an antenna which consumes very less space and can be mounted easily in the equipment and still have efficient directive radiation pattern. One such antenna design, which is very famous these days, is micro strip patch antenna MSPA. [1, 2]

Different techniques have been suggested to achieve antenna integration within a single chip. In this paper a simple design by simulation of micro strip patch antenna for microwave applications is proposed by investigating the effects of substrate material nature and antenna size miniaturization on the return loss characteristics of the antenna. Electromagnetic simulations were performed using MATLAB code program which employs the wave concept iterative process method WCIP based on wave concept and fast modal transformation FMT.

2. The theory of the iterative method

The Fast Wave Concept Iterative Process (FWCIP) is introduced firstly in (Azizi et al. 1995; Azizi et al. 1996). It is based on the Definition of transverse waves based on the tangential electric and magnetic fields on some active surface. The same method is denoted in literature as Transverse Wave Formulation - TWF (Wane et al. 2005) and more recently Wave Concept Iterative Procedure - WCIP (Baudrand et al. 2007, Raveu et. al 2007).WCIP compares favorably (Wane and Bajon 2006) with other commercially available software regarding the precision and promises better performance in computation efficiency in structures with very different layer heights.[3]

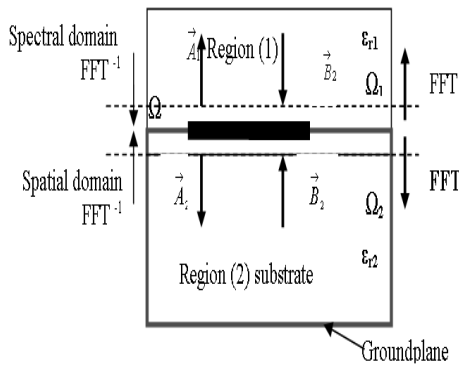


Figure 1. Wave concept iterative procedure definitions

Let Ω be a discontinuity plane inside a metallic box (package) (see figure 1). The regions on both sides are filled with homogeneous electric. The two regions are designated as region 1 (ϵ_{r1} , h_1 , etc.) and region 2 (ϵ_{r2} , h_2 , etc.). Let Ω_i be a surface infinitely close to Ω in region i , n_i the unit vector normal to Ω_i and directed into region i , $i=1$ or 2 (as shown in figure 1)

We define the transverse incident and reflected wave in Ω by the following relation:

$$\vec{A} = \frac{1}{2\sqrt{Z_{0i}}} (\vec{E} + Z_{0i} \vec{J}), \vec{B} = \frac{1}{2\sqrt{Z_{0i}}} (\vec{E} - Z_{0i} \vec{J}) \quad (1)$$

where i indicates the medium 1 or 2, E the tangential electric field, Z_{0i} stands for the characteristic impedance of the same medium, J is the surface current density.

The waves are subject to constraints imposed by the discontinuity (2) and by the reflection over the metallic walls of the box (3).

$$\vec{A} = \hat{\Gamma}_{\Omega} \vec{B} + \vec{A}_0 \quad (2)$$

$$\vec{B} = \hat{\Gamma} \vec{A} \quad (3)$$

A_0 is the incident wave generated by the source in the two regions. Γ and Γ_{Ω} denote the reflection operator on the discontinuity surface Ω and on the metallic walls respectively. The WCIP method solves (2) (3) by an iterative procedure. In (4), (5) k denotes the current iteration and the starting conditions are imposed by the source (6).

$$\vec{A}^{(k+1)} = \hat{\Gamma}_{\Omega} \vec{B}^{(k)} + \vec{A}_0 \quad (4)$$

$$\vec{B}^{(k)} = \hat{\Gamma} \vec{A}^{(k)} \quad (5)$$

$$\vec{A}^{(0)} = \vec{A}_0 \quad (6)$$

Equation (2) is applied in the space domain, while (3) is easily implemented in the modal domain, so a fast modal transform (FMT), based on FFT (N'gongo and Baudrand 1999), can be developed in order to go from (4) to (5) and vice versa through the iterative procedure. While this method found its best applications in the analysis of microwave multilayer structures (Akatiagool et al. 2001, Wane et al. 2005, Wane and Bajon 2006). [4,5,6]

2.1. Design considerations

In its simplest form, the micro strip antenna consists of a sandwich of two parallel conducting layers separated by a single thin dielectric substrate (see figure 2). The lower conductor functions as a ground plane and the upper conductor functions as radiator. The larger ground plane gives better performance but makes the antenna bigger.

Among different shapes of micro strip patch elements such as rectangular, square, dipole, triangular, circular and elliptical for better radiation

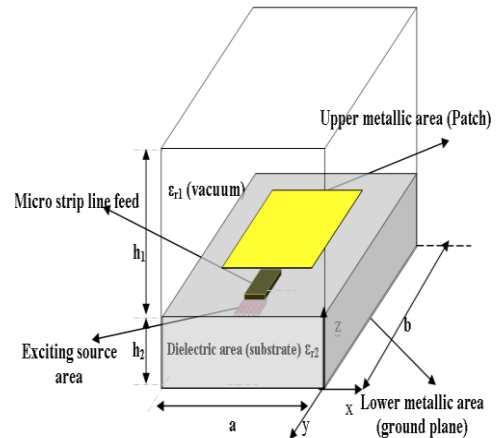


Figure 2- MPA model encapsulated in box

characteristics we use rectangular micro strip patch antenna. In this paper the substrate dimensions taken along X-axis is a mm and along Y-axis is b mm. The substrate thickness along Z-axis is h_2 mm.

The feed location is in the middle of the patch. For good performance, a substrate having a low dielectric constant is desirable since this provides better efficiency, larger bandwidth and better radiation. The design also checks for maximum power transfer by matching the feed line impedance to the impedance of the patch antenna. As an imposed solution we use the Micro strip line feeding technique for impedance matching witch is easier, and feed can be fabricated on some substrate as single layer to provide planner structure. [7]

2.2. simulation results

1. simulations

The Structure Interface used in our study and introduced in our MATLAB code is shown in figure 3.

a-Substrate dielectric constant effect

Figure (1) shows the model for micro strip patch antenna. The different physical parameters simulated by placing them on the proposed model We have chosen the follow simulation parameters values: $a \times b = 10 \times 10 \text{mm}$; $h_1 = 2 \text{mm}$ $h_2 = 1 \text{mm}$; $\epsilon_{r1} = 1$; Nit (iteration number) =300; frequency band [2-250] GHz, Frequency step = 0.1 GHz.

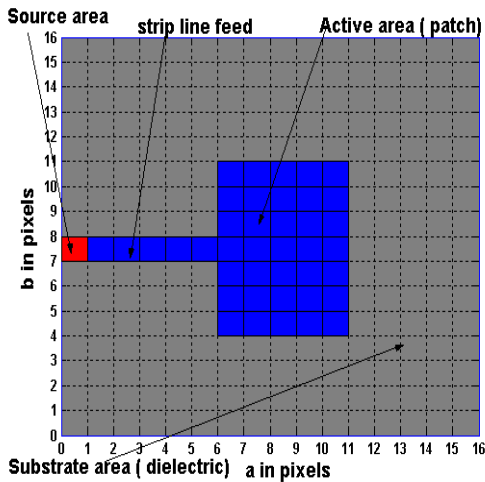


Figure 3. Interface structure

Different substrate materials are considered and the table (1) shows the physical parameters of the different substrate materials used in our simulations

Substrate material	Dielectric constant ϵ_r	Effective Dielectric constant	Loss tangent value
RT-Duroid-5880	2.2	2.1144	0.0011
Neltec NX 9240	2.4	2.3002	0.0010
Benzocyclobuten	2.6	2.4859	0.0010

Table (1) Physical parameters of substrate materials used in our simulations

We launched the simulation program for the same structure by varying only the substrate dielectric constant. We have taken three structure cases: I ($\epsilon_{r2} = 2.2$); II ($\epsilon_{r2} = 2.4$); III ($\epsilon_{r2} = 2.6$).

We obtain results shown in figures 4, 5 and 6.

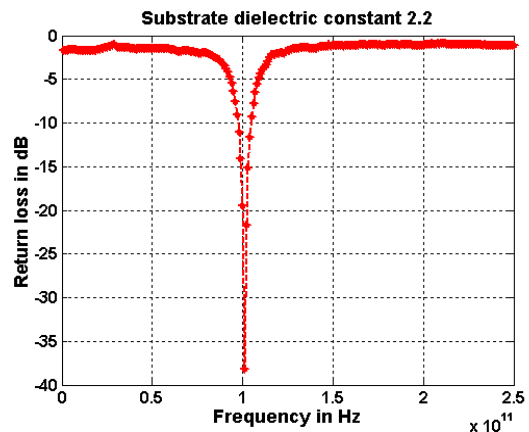


Figure 4. Return loss characteristics for antenna with substrate dielectric constant 2.2

Parameter	Conventional antenna	Antenna N°01	Antenna N°02
Active area 7x5x pixel size in mm ²	22,00	21.33	20.80
Volume of antenna $a \times b \times h_2$ mm ³	100.00	71.30	45.12
Active area reduction in %	/	3	5.40
Volume Reduction in %	/	28.70	54.88

Table 2. Analysis of antenna miniaturization

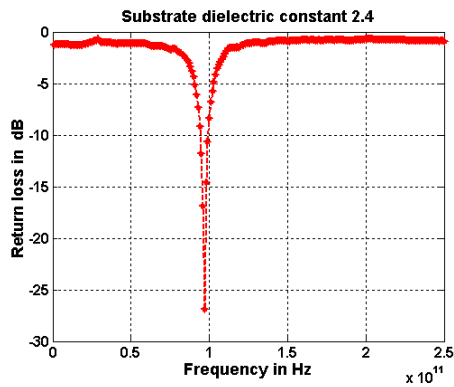


Figure 5. Return loss characteristics for antenna with substrate dielectric constant 2.4

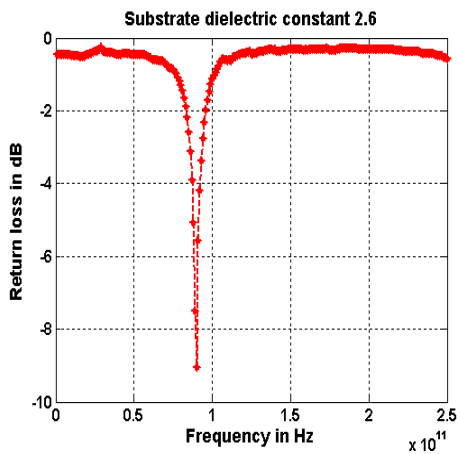


Figure 6. Return loss characteristics for antenna with substrate dielectric constant 2.6

b- Substrate size effect

For an antenna considered as conventional antenna we have chosen the follow simulation parameters values: $a \times b = 10 \times 10 \text{ mm}$; $h_1 = 2 \text{ mm}$ $h_2 = 1 \text{ mm}$ $\epsilon_{r1} = 1$; $\epsilon_{r2} = 4.22$ $N_{it} = 300$; frequency band $[0-250] \text{ GHz}$, frequency step = 0.1 GHz .

We launched the simulation program for two antennas N°1 and N°2 with the same conventional antenna parameters but by varying substrate sizes and also active patch area as it is presented in table 2

For the miniaturization effects we obtain results depicted in figures 7, 8 and 9.

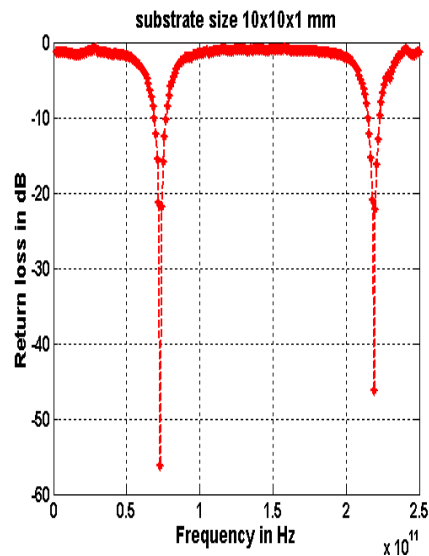


Figure 7. Variation of return loss versus frequency for the conventional antenna.

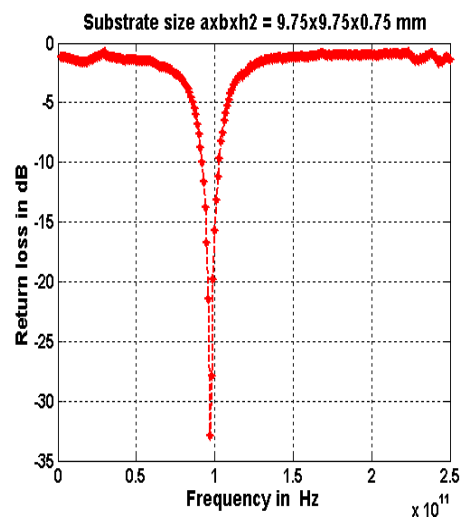


Figure 8. Variation of return loss versus frequency for antenna N°1

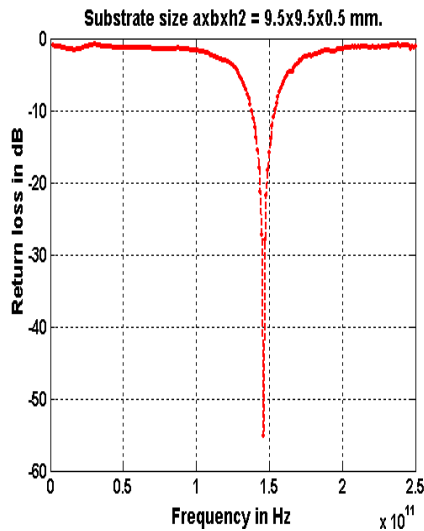


Figure 9. Variation of return loss versus frequency for antenna. N°2

3. Results

The return loss values obtained for different substrate materials with different dielectric constants 2.2, 2.4, 2.6 are -38.5dB, -27 dB -9 dB with resonant frequencies at 105GHz, 96GHz and 90GHz respectively. All the values are having the return loss of <-8dB and bandwidths are everywhere constant

Concerning miniaturization, the return loss characteristics is observed for the conventional antenna configuration and depicted in Figure.7 witch shows two-band of operation in the frequency band [0-250] GHz. The first band is around 75 GHz with -56dB the second band is around 210 GHz with -46dB. Figure 8 gives return loss characteristics for antenna N°1 witch is miniaturized by about 28.70 % in volume compared to the conventional antenna, we observe one band of operation around 95GHz with -37dB and Figure 9 gives return loss characteristics for antenna N°2 (miniaturized by about 54.88 % in volume compared to the conventional antenna) we observe one band of operation around 148GHz with -55dB

4. Conclusion

We conclude that by increasing the dielectric constant of the substrate material gain values are decreased and resonant frequency is shifted left.

Concerning miniaturization we observe that by decreasing antenna volume we have significant fluctuation in gain and resonant frequencies are shifted right.

By using simple relations of the WCIP method without leading to a heavy computing time, we have investigated performances of micro strip patch antenna based on different substrate materials and the effect of miniaturization on these performances. The simulated results obtained by WCIP are, mostly, in good agreement with measurements and the literature.

References

- [1] J.P Bilal Ahmed & “Analytical Study on Effects of Substrate Properties on the Performance of Microstrip Patch Antenna” al International Journal of Future Generation Communication and Networking Vol. 5, No. 4, December, 2012.
- [2] M. Titaouine, A. G. Neto, H. Baudrand, and F. Djahli “Analysis of Frequency Selective Surface on Isotropic/Anisotropic Layers Using WCIP Method” ETRI Journal, Volume 29, Number 1, February 2007
- [3] Ziar, T., Zaabat, M. and Baudrand, H. (2013), The study of packaging miniaturization effect on the characteristics of an active planar circuit by using the iterative method. Int. J. Numer. Model., 26: 521-532. doi: 10.1002/jnm.1858
- [4] N’gongo, R.S and H.Baudrand, A new approach for microstrip active antenna using modal F.F.T algorithm , IEEE APS International yposium Ind . USNC/URSI National Radio Science Meeting, Orlando, USA, jul. 11-16 ,1999.
- [5] Baudrand, H. and R. S. N’Gongo, “Application of wave concept iterative procedure in planar circuits,” Special Issue on Recent Research Developments in Microwave Theory and Techniques, Vol. 1, 187-197, Trans world Research Network, January 1999.
- [6] Azizi. M, Aubert.H.and Baudrand.H., A new iterative method for scattering problems, European Microwave Conference Proceedings, Vol.1, pp. 255-258. 1995
- [7] Kevin Buell & al “A Substrate for Small Patch Antennas Providing Tuneable Miniaturization Factors” IEEE TRANSACTIONS ON MICROWAVE THEORY AND TECHNIQUES, VOL. 54, NO. 1, JANUARY 2006 135and

Morphological and optical properties of sol-gel derived Ni doped ZnO thin film

T. Saidani^{*}, M. Zaabat, A. Benaboud and A. Boudine

Laboratory of active components and materials University Larbi Ben M'hidi Oum El Bouaghi 04000, Algeria

^{*}Tarekfrident@gmail.com

Received: 30 April 2014, accepted 26 May 2014

Abstract

In this work, we are interested in thin films of zinc oxide doped with nickel (Ni), deposited on glass substrates and elaborated by the sol-gel dip coating technique. The effects of the doping concentration in the range of outlet (1%, 3% and 5at%) have been thoroughly studied. The morphological properties of ZnO-Ni films were studied by Atomic Force Microscopy (AFM). The optical properties of the ZnO:Ni thin films were examined by UV-visible spectroscopy and the Tauc method was used to estimate the optical band gap and hall effect for electrical characteristic. Atomic Force Microscopy has indicated that the surface of the ZnO:Ni thin films have uniform and dense ZnO grains. The optical transmittance of ZnO:Ni thin films increased from 86 to about 93% from pure ZnO films to ZnO film doped with 3 wt% Ni and then decreased for 5 wt% Ni, and the optical band gap from 3.297 eV to 3.23eV. The electrical characterization performed using the technique of hall effect, gave a maximum electrical conductivity of $9.3 \cdot 10^3 (\Omega \cdot \text{cm})^{-1}$ obtained for the film doped with 3%Ni.

Keywords: Ni doped ZnO, Thin films ZnO, Optical properties, Sol gel method, dip coating.

PACS: 77.55.hF; 81.20.Fw; 78.20.-e; 07.85.Ne; 68.60.Bs;

1. Introduction

In recent years, thin films of zinc oxide have acquired an increasing interest in many research fields because of its many potential applications. The zinc oxide thin film can be used as a very sensitive sensor in chemical gas sensors, as pressure sensor or in electronic devices such as rectifiers, filters, resonators and for radio communications in the manufacture of varistors. Many deposition techniques were used for the production of ZnO thin films, such as laser ablation [1], spray pyrolysis [2], rf-magnetron sputtering [3], CVD [4], molecular beam epitaxy [5], vapor-liquid-solid (VLC) method [6] and the process sol gel [7,8] etc. In this paper, thin films of ZnO:Ni were deposited by the sol gel method associated to the dip coating technique using a solution of zinc acetate aim of glass substrates. The objective in this work is to study the effect of

nickel doping level by Nickel on the morphological, optical and electrical properties of ZnO:Ni thin films.

2. Experimental part:

2-Methoxyethanol and monoethanolamine (MEA) are used as the solvent and stabilizing agent, respectively. Dihydrate Zinc acetate $[\text{Zn}(\text{CH}_3\text{CO}_2)_2 \cdot 2\text{H}_2\text{O}]$ and dihydrate nickel acetate $[\text{Ni}(\text{CH}_3\text{CO}_2)_2 \cdot 2\text{H}_2\text{O}]$ are dissolved in a mixture of 2-Methoxyethanol and monoethanolamine at room temperature. The concentration of zinc acetate is 0.1 M and the molar ratio of MEA to Zn is maintained at 1.0. ZnO precursor containing Ni-dopants were prepared with different percents (1, 3 and 5at %). The resulting mixture solution was stirred for 3h at 65°C to yield a clear and homogenous solution. The films ZnO:Ni were prepared by dip-coating method at controlled withdrawal speed 50 mm min⁻¹. Each coated

layer was dried at 200°C for 10 min-1, and the films were annealed at 500°C for 2 hours in air.

The surface morphology was observed by atomic force microscope (AFM). The optical properties have been studied by a spectrophotometer and the conductivity of the ZnO:Ni thin films were measured by the Hall Effect technique.

3. Results

3.1. Surface morphology

Fig. 1 shows the AFM micrographs of the surface profile for ZnO :Ni thin films. The Films of pure ZnO and ZnO doped with Ni at different concentration deferens show that the surface is uniform, which contains spherical grains of various sizes. The calculated size of the grains of ZnO films. Neither is given in Table 1 As can be seen, the grain size increases with the concentration of Ni, it goes from 42 nm to 85 nm for pure ZnO and doped ZnO 5at% Ni respectively.

3.2. Optical properties

The optical properties of thin films of ZnO:Ni was determined from the transmission measurement in the range of 300-1100 nm. Figure 2 shows the optical transmission spectra of ZnO:Ni films prepared with different doping levels in Ni. All films show a high transmittance in the UV region of the order of 86-93%. It was observed that the transmittance increases with the increase of Nickel concentration with a maximum value obtained at 3% Nickel. Beyond 5% the transmittance decreases with the increase of the Ni dopant concentration. The transmittance increased to 3 wt% of Ni because the pure ZnO films are porous. Due to doping, nickel atoms occupy vacant sites in ZnO and reduce the dispersion of light and therefore the transmission factor increases with the increase of doping up to 3% of Ni. With an additional increase in the concentration of doping, nickel atoms occupy interstitial sites in the ZnO and increase the absorption of light, and therefore a decrease in transmittance.

The optical energy gap of pure ZnO thin films doped with different rate of nickel doping is given by the following equation [9]:

$$(\alpha h\nu) = A(h\nu - E_g)^{1/2}$$

Where A is a constant and E_g is the gap energy. The value of the gap energy can be determined from the intersection of the curve $(\alpha h\nu)^{1/2} = f(h\nu)$ with the axis of

abscissas [10,11] as is shown in Figure 3. absorption Coefficient α can be calculated from the transmittance of ZnO:Ni film with the formula $\alpha = (1/d) \ln (1/T)$, where d: thickness of films ZnO:Ni and T: the value of transmission. The evolution of the optical gap of the films according to doping is reported in Figure 4.

It can be seen that the optical band gap energy of undoped ZnO film is 3.247 eV. The effect of the Ni doping on films has increased the E_g values from 3.247 to 3.267 and 3.297 eV for 1 and 3 wt% doped films, respectively. Blue shift due to Ni doping has been largely ascribed to the Burstein-Moss effect. DiTrollo et al. have reported a large variation of E_g of ZnO film with increasing Ni doping concentration [12].

3.3. Electrical properties

Figure 5 shows the evolution of the conductivity of the films of ZnO:Ni as a function of the dopant concentration (Ni). This curve shows that the conductivity of the ZnO thin film: Ni increases with the increase of the dopant concentration of Ni and reaches its maximum value of $9.310^3 (\Omega \cdot \text{cm})^{-1}$ doping for 3wt% Ni, then it decreases to $4.210^3 (\Omega \cdot \text{cm})^{-1}$. This increase in conductivity with increasing concentration of doping can be performed by increasing the number of charge carriers (electrons) from the donor ions Ni^{2+} incorporated in substitutional or interstitial sites of Zn^{2+} cation [14]. The reduction of conductivity beyond 3wt% Ni may be due to a decrease in the carrier mobility due to excessive Ni.

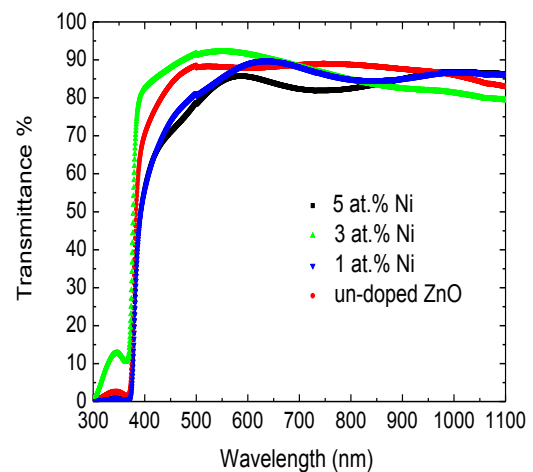


Fig. 2. Transmittance spectra of ZnO:Ni thin films with various Ni doping contents.

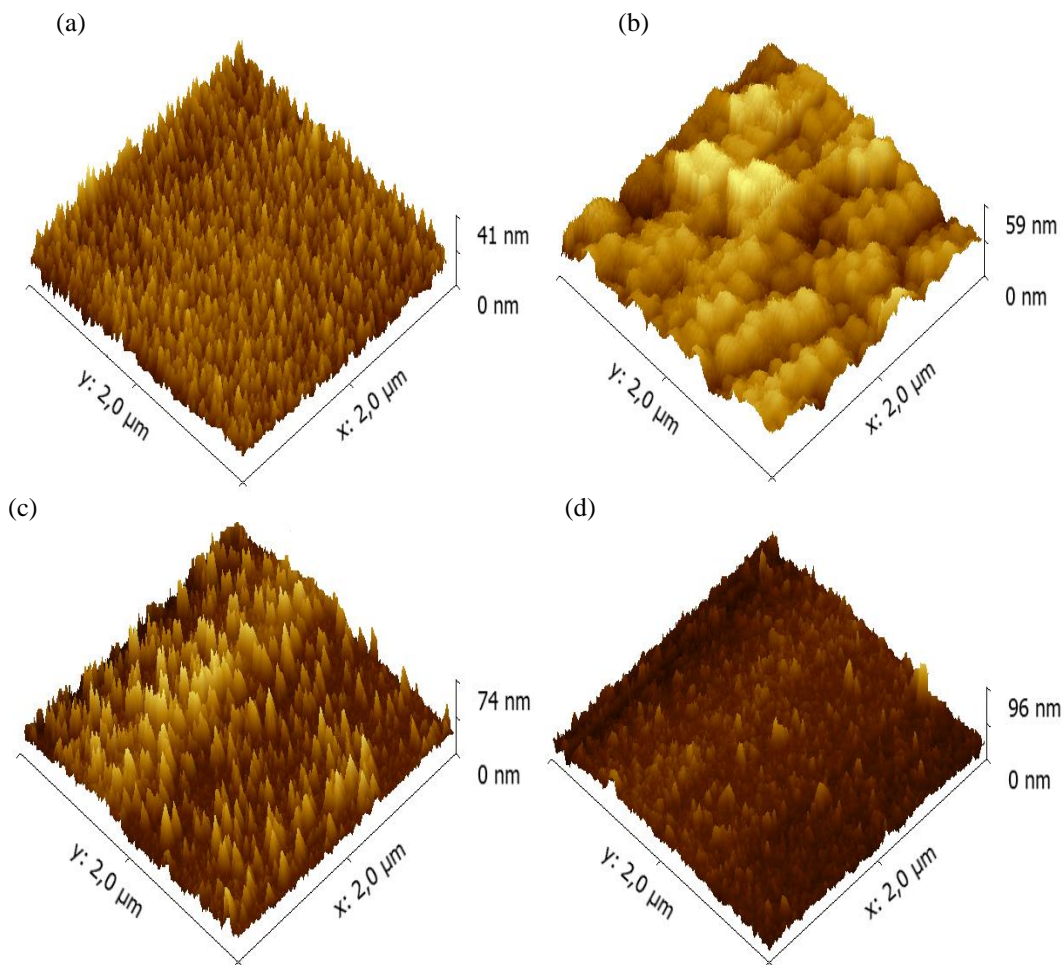


Fig. 1. Three dimensional AFM images of ZnO :Ni thin films at different concentration (a) 0%, (b) 1%, (c) 3% and (d) 5 %

Table 1 Average grain size of the Ni:ZnO thin films with different Ni doping contents.

Samples	Average crystallite size (nm)
Ni content at%	
0	42
1	59
3	71
5	85

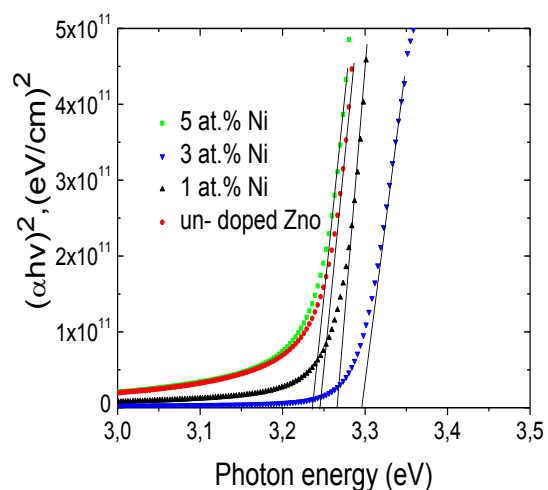


Fig. 3.Plot of $(\alpha hv)^2$ versus $h\nu$ curves of ZnO :Ni thin films.

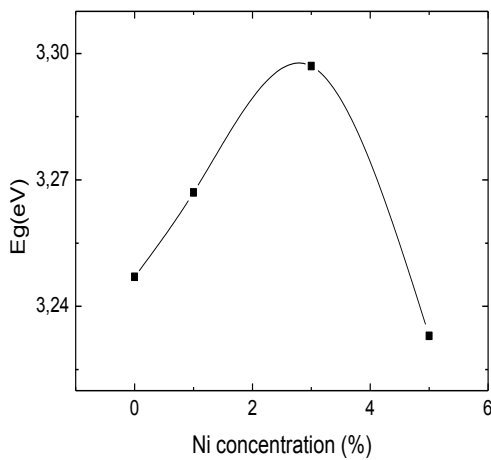


Fig. 4. The optical band gap as a function of Ni doping concentration.

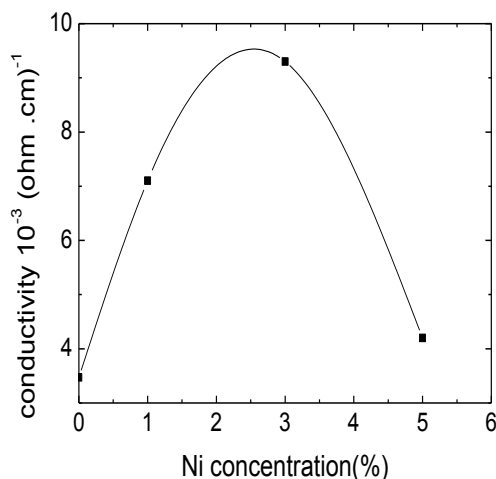


Fig. 5. Electrical conductivity of ZnO :Ni thin films

5. Conclusion

In this work, we have developed and characterised thin films of ZnO doped with pure nickel by sol-gel on glass substrates. The atomic force microscope shows spherical grains of different sizes. The ZnO film:Ni developed showed high transmittance which is greater than 86% in the visible region and the optical gap increases with increasing the concentration of Ni. Furthermore, it was found the increase in conductivity with increasing the concentration of Ni up to 9.3×10^{-3} ($\Omega \cdot \text{cm}$) $^{-1}$ and has a maximum value obtained for films doped 3% Ni.

Reference

- [1] J.A. Sans, A. Segura, M. Mollar and B. Mari; *Thin Solid Films* vol.251, 453-454, 2004.
- [2] - M.N. Kamalasanan, S. Chandra; *Thin Solid Films* 288 (1996) 112.
- [3] Y. Kashiwaba, F. Katahira, K. Haga, T. Sekiguchi, H. Watanabe; *J. Crystal Growth* vol. 221,431 2000.
- [4] F. Paraguay, D. W.Estrada, L.D.R. Acosta, N.E. Andrade, M. Miki-Yoshida; *Thin Solid Films* vol.350,192,1999.
- [5] L.X. Su, Y. Zhu, Q.L. Zhang, M.M. Chen, T.Z. Wu, X.C. Gui, B.C. Pan, R. Xiang, Z.K. Tang, *Appl. Surf. Sci.* 274 (2013) 341-344.
- [6] N. Kouklin, *Adv. Mater.* 20 (2008) 2190-2194.
- [7] H. Liu, J. Yang, Z. Hua, Y. Zhang, L. Yang, L. Xiao, Z. Xie, *Appl. Surf. Sci.* 256 (2010) 4162-4165.
- [8] D. Wang, J. Zhou, G. Liu, J. Alloys *Compd.* 487 (2009) 545-549.
- [9] C.-Y. Tsay, K.-S.Fan, C.-M. Lei, *J. Alloys Comp.* 512 (2012) 216-222.
- [10] Powder Diffraction File Data Card 5-644,3cPDS International Center for Diffraction Data, Swartmore, PA.
- [11] N. Zebbar, M.S. Aida, A .Hafdallah, W. Daranfah, H. Lekiket, and M. Kechouane, *Materials Science Forum* 609, 2009, 133-137.
- [12] A. Di Trolio, E.M. Bauer, G. Scavia, C. Veroli, *J. Appl. Phys.* 105 (2009) 113109.
- [13] Ki-SoekAn, Wontae Cho. ByungKooK Lee, Sun Sook Lee and Chang Gyoum Kim, *Journal of nanoscience and nanotechnology* 8, 2008, 4856-4859.
- [14] X.Y. Li, H.J. Li, Z.J Wang, H. Xia, Z.Y. Xiong, J.X. Wang, B.C. Yang, *Optics Communications*, 2009, 282, 247.

Effect of Al doping on the properties of electrodeposited ZnO nanostructures

Ouidad Baka, Mohamed Redha Khelladi and Amor Azizi

Laboratoire de Chimie, Ingénierie Moléculaires et Nanostructures, Université de Sétif-1, 19000 Sétif, Algeria.

Received: 30 April 2014, accepted 26 May 2014

Abstract

In this study, Al-doped zinc oxide (AZO) nanostructures are prepared on polycrystalline fluorine-doped tin oxide (FTO)-coated conducting glass substrates from nitrates baths by the electrodeposition process at 70 °C. The electrochemical, morphological, structural and optical properties of the AZO nanostructures were investigated in terms of different Al concentration in the starting solution. It was found from the Mott-Schottky (M-S) plot that the carrier density of AZO nanostructures varied between 3.11×10^{19} to 5.56×10^{19} cm^{-3} when the Al concentration was between 0 and 5 mM. Atomic force microscopic (AFM) images reveal that the concentration of Al has a very significant influence on the surface morphology and roughness of AZO thin films. X-ray diffraction (XRD) patterns demonstrate preferential (002) crystallographic orientation having c-axis perpendicular to the surface of the substrate and average crystallites size of the films was about 23–36 nm. As compared to pure ZnO, Al-doped ZnO exhibited lower crystallinity and there is a shift in the (002) diffraction peak to higher angles. ZnO nanostructures were found to be highly transparent and had an average transmittance of 80 % in the visible range of the spectrum. After the incorporation of Al content into ZnO the average transmittance increased and the band-gap tuning was also achieved (from 3.22 to 3.47 eV).

Keywords: Al-doped ZnO ; carrier density ; electrodeposition ; nanostructures ; XRD.

1. Introduction

Metal oxide semiconductor films have been widely studied in recent years due to their optical and electrical properties. ZnO is both transparent in the visible region and electrically conductive especially when doped with appropriate metals such as Ga or Al [1]. Doped ZnO thin films are of technological importance because of their great potential for various applications such as transparent conducting electrodes (TCOs), insulating or dielectric layers, light-emitting diodes (LEDs) and for solar cells [1, 2], etc. Al-doped ZnO thin films are prepared by different techniques such as sol-gel, spray pyrolysis, pulsed laser deposition (PLD), magnetron sputtering, and metal organic chemical vapor deposition (MOCVD) [8-12]. Amongst all other methods as mentioned above, electrochemical deposition is one of the most attractive methods for the synthesis of nanostructures of semiconductors oxides [3, 4]. It provides advantages such as the ability to use a low synthesis

temperature, low costs, and a high purity in the products. Also, electrodeposition allows the stoichiometry, thickness, and microstructure of the films to be controlled by adjusting the deposition parameters.

In the present paper we have prepared Al-doped ZnO nanostructures by electrochemical deposition technique. The effects of Al doping on the electrochemical, morphologies, microstructures, and optical properties of ZnO nanostructures were studied in detail. The growth mechanism of Al-doped ZnO nanostructures is presumed.

2. Experimental Details

2.1. Electrochemical synthesis

The deposition solution, prepared with distilled water, contained 0.1 M $\text{Zn}(\text{NO}_3)_2$, 1 M KNO_3 and between 0.05 and 5mM $\text{Al}(\text{NO}_3)_3$. The deposition parameters of the AZO films were kept the same as

those for the undoped ZnO film. Deposition temperature was 70° C and pH was in the range of 4 to 6. The deposition process was carried out in a three-electrode cell. The counter-electrode was a platinum wire and the reference electrode was a saturated calomel electrode (SCE, +0.241 V vs. SHE). F-doped SnO₂ (FTO, 20-23 Ωsq.⁻¹)-coated transparent glasses were used as a working electrode. The substrates were cleaned ultrasonically in water, acetone and ethanol. They were activated in 45 % HNO₃ for 2 min and finally rinsed with distilled water prior the electrodeposition [5]. The applied potential was -1.7 V vs. SCE. The ZnO nanostructure was deposited in a potentiostatic mode, using a computer-controlled potentiostat/galvanostat (Voltalab 40) as a potential source.

Cyclic voltammetry (CV) was found to offer some note worthy information in the electrodeposition synthesis of zinc oxide thin film. Table 1 shows the bath composition and the electrodeposition conditions employed in the preparation of the thin films.

Table 1: Deposition conditions of samples AZO0-AZO3.

Sample	[Al ³⁺] (mM)	pH	E _s (V/ECS)	N _b (cm ²)
AZO0	0	6.5	-0.42	3.11×10 ²⁰
AZO1	0.05	5.6	-0.37	3.91×10 ²⁰
AZO2	0.5	4.6	-0.64	4.27×10 ²⁰
AZO3	5	3.9	-0.95	5.56×10 ²⁰

2.2. Sample characterization

The Mott-Schottky (M-S) analysis for AZO thin films was carried out by conducting a standard electrochemical measurement at 0.2 kHz frequency in a 1 M KNO₃ solution by scanning the potential from positive to negative direction in 50 mV/s steps. The applied potentials were set in the range of -1.0 to + 0.2 V vs. SCE. The crystallographic structure of the thin films was analyzed by a Rigaku Smartlab diffractometer using Cu Kα₁ radiation at 40 kV (Cu Kα₁, λ = 0.15406 nm). The surface morphology was observed by atomic force microscopy (AFM). The RMS roughness (root-mean-square height deviation) of the samples was obtained directly from the software of the AFM (PicoScan 5.3 from Molecular Imaging). The optical transmittance spectra were obtained with a SHIMADZU 2401PC spectrophotometer in the UV-visible region. The spectra were corrected for glass substrates. All measurements were conducted at room temperature

1. Results

1.1. Electrochemical characterization

The electrodeposition process of ZnO is well-known; first, the reduction of nitrate ions produces nitrite and hydroxide ions at the cathode. This was followed by the interaction of Zn with hydroxide ions forming zinc hydroxide. After dehydration of these hydroxides, ZnO is formed as a final product. This mechanism of electrodeposition is simply described as follows [6],

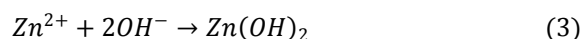
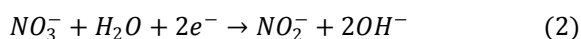


Fig.1 as shown the CV recorded at 70° C in the potential range from +0.2 to -1.4 V vs. SCE in a nitrate solution at 20 mV s⁻¹. An increase of the cathodic current density begins around -0.7 V corresponds to the nitrate reduction (reaction 2) [7]. The next increase around -1.1 V corresponds to the reduction of Zn²⁺ into metallic Zn. During the reverse anodic scan; no anodic currents were observed denoting thus the good stability of the films which present no reoxidation process.

In order to understand the influence of Al³⁺ during the reduction process, voltammetry was also performed at a constant Zn²⁺ concentration, and from 0.05 to 5 mM Al(NO₃)₃ (Fig. 2). For comparison, the curve previously obtained from zinc nitrate solution is also represented on Fig. 2 (curve AZO0). Only the cathodic forward sweeps are shown for the sake of clarity.

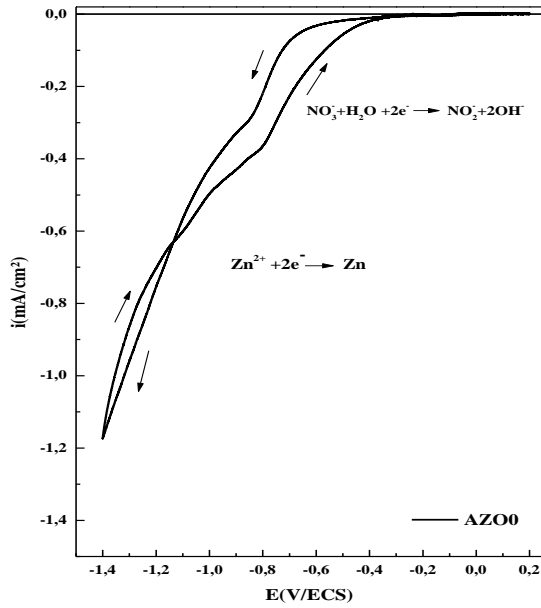


Fig. 1 Cyclic Voltammetry curve recorded for FTO electrode at 70°C in 0.1 M $\text{Zn}(\text{NO}_3)_2$ and 1 M KNO_3 solution. The potential scanning rate was 20 mV/s.

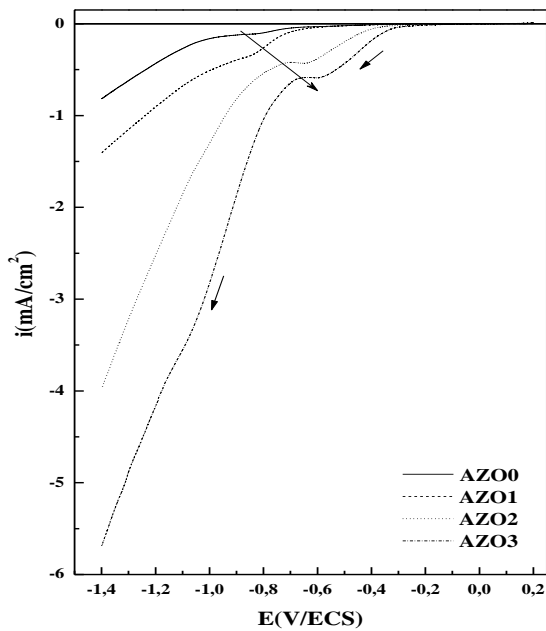


Fig. 2 Cyclic voltammetry curves of the electrolytes used for undoped and Al-doped ZnO growth with different Al^{3+} concentration according to Table 1. The scans were performed at a rate of 20 mV/s on FTO substrates.

All cyclic voltammetry curves show a similar feature. With the presence of Al^{3+} ions in the solution, OH^- ions also react with Al^{3+} ions to form $\text{Al}(\text{OH})_3$, which incorporates Al into ZnO and thus dopes the ZnO film [1]:



It's clear from Fig. 2, the increase in current density from -0.11 to -0.58 mA/cm^2 was observed with

increasing of Al^{3+} concentration from 0 mM to 5 mM in the electrolyte. The fast increase in current density during electrochemical deposition with Al can be interpreted that Al^{3+} accelerated the reduction of NO_3^- . This implies catalytic role of Al^{3+} to the reduction of nitrate [8].

The semiconductor properties such as donor density (N_D) can be measured from the capacitance measurements [9, 10]. In order to determine the effect of the Al concentration on the defects and donor density of the ZnO nanostructures, M-S analysis was performed. The flat band potential (E_{fb}) and the charge carrier density for the semiconductor material (ZnO) can be determined using [11]:

$$\frac{1}{C_{sc}^2} = \frac{2}{q\epsilon\epsilon_0 N_D A^2} \left(E - E_{fb} - \frac{kT}{q} \right) \quad (7)$$

where C is the interfacial capacitance, q the electron charge ($1.6 \times 10^{-19} \text{C}$), ϵ the ZnO dielectric constant ($\epsilon = 8.5$), ϵ_0 the free space permittivity ($8.85 \times 10^{-14} \text{F}/\text{cm}$), A the exposed electrode area ($\approx 1 \text{cm}^2$), E the applied potential across the ZnO space-charge region, E_{fb} the flat band potential and kT/q is the temperature (T) dependent correction term involving the Boltzmann constant k . Flat-band potentials and donor densities were calculated from the intercept and slope of the M-S plots respectively. Fig. 3 shows the M-S plot for all the samples of undoped and Al-doped ZnO (AZO). The positive slope of the M-S plot confirms the n type conductivity of the samples. The carrier concentration of AZO thin films increases from 3.11×10^{20} to $5.56 \times 10^{20} \text{cm}^{-3}$ with the concentration of Al. This range is in agreement with reported carrier concentrations for AZO [12]. It was observed that by increasing the doping concentration, the flat-band potential also changes from -0.42 to -0.95 V vs. SCE.

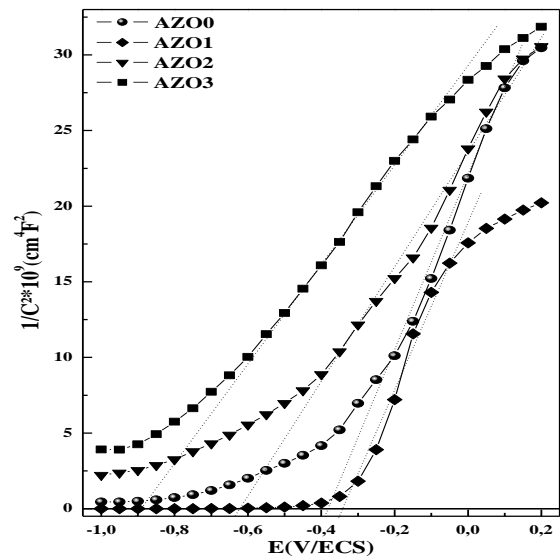


Fig. 3 Mott-Schottky plots of undoped and Al-doped ZnO (AZO) thin films in 1M KNO_3 as the electrolyte. Frequency employed was 0.2 kHz.

1.2. Morphological analysis

The two-dimensional AFM images of the surface morphologies of ZnO and AZO thin films are shown in Fig. 4. It was found that the films grow with microcrystalline structure. From the images it is seen that all the film surfaces are well covered with the variably distributed spherical grains of varying sizes. It is evidently seen that addition of Al changes the morphology of thin films from clusters into well defined spherical grains. Surface roughness is one of the important properties of the AZO thin films for many opto-electronics applications, because the smooth structure can reduce the scattering of incident light, which makes the contribution to increase the transmittance [13]. Effectively, the surface roughness of the deposited layers is determined by AFM. It is found that the surface roughness is strongly dependent on the concentration of Al in the solution. From this figure, when Al concentration increased from 0.05 to 5 mM, the RMS roughness increased from 5 to 34 nm.

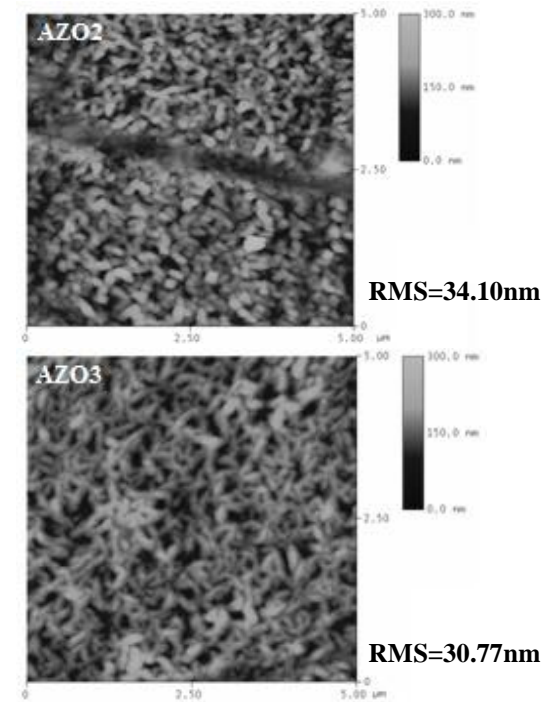
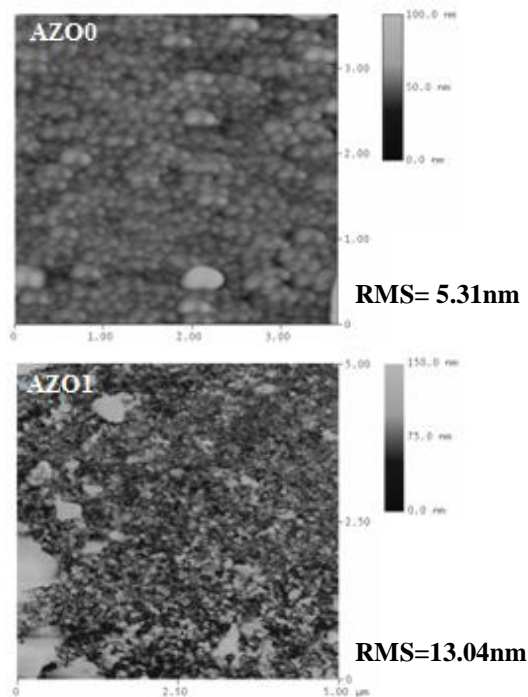


Fig. 4 AFM images of electrodeposited Al-doped ZnO thin films with different Al content.

It should be noted that the maximum value of RMS was observed at $C_{Al} = 0.5$ mM and attributed to the rough surface of the AZO film. After this maximum of RMS, the latter decreased as the aluminum concentrations increased.

1.3. Structural analysis

The XRD patterns of electrodeposited AZO thin films at different Al concentrations are shown in Fig. 5. These patterns are found to have preferred orientation along (002) plane of the wurtzite structure of ZnO with c-axis normal to the substrate surface. Moreover, the peak intensities of those films decreased with increased Al concentrations. This indicates that an increase in doping concentration deteriorates the crystallinity of films, which may be due to the formation of stresses by the difference in ion size between Zn and Al. On the other hand, the peak position of the (002) plane is shifted to the higher value with the increase of Al doping concentration as shown in the table 2.

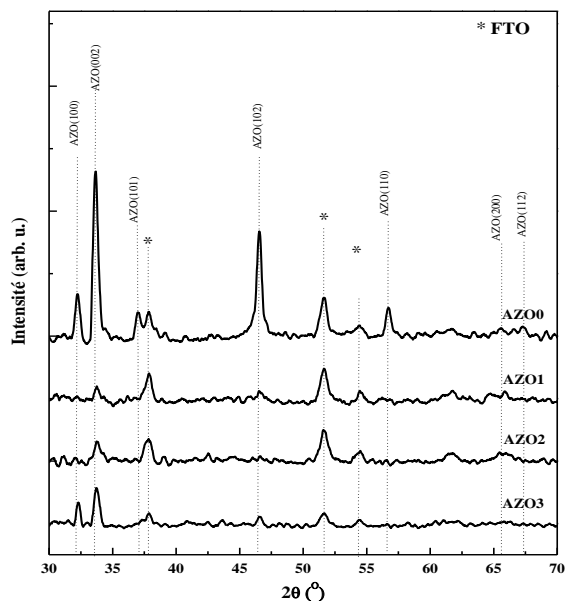


Fig. 5 Typical XRD patterns of the undoped and Al-doped ZnO nanostructures deposited on FTO substrate at different concentrations of Al.

The shift towards the higher angles may be due to the contraction caused by the substitution of Al^{3+} (radius 0.53 \AA) on the Zn^{2+} sites (0.60 \AA) [14]. The average crystallites size can be estimated from the full width at half maximum (FWHM) values of the diffraction peaks. An average size of the crystallites in the direction perpendicular to the plane of the films could be obtained using the Scherrer equation [15]:

$$D = \frac{k\lambda}{\beta \cos\theta} \quad (8)$$

where D is the crystallite size, k is a shape factor and usually takes a value of 0.94, λ is the X-ray wavelength ($\lambda = 1.5406 \text{ \AA}$), β is the FWHM and θ is Bragg angle of the given (002) peak. The calculated values of the lattice parameters and average crystallite sizes for ZnO and AZO were summarised in Table 2. When Al doping concentration was increased, the crystallite size of AZO decreased from 36 to 26 nm. Also, the lattice parameters decreases with the increasing the Al content. The reduction of a and c parameters may be due to smaller ionic radius of Al^{3+} than Zn^{2+} .

Table 2: The effect of the Al doping concentration on the microstructural and optical properties.

Sample	2θ (°)	c (Å)	a (Å)	D (nm)	E_g (eV)
AZO0	33.66	5.320	3.258	36.08	3.22
AZO1	33.73	5.310	3.251	28.70	3.41
AZO2	33.73	5.310	3.254	26.65	3.44
AZO3	33.75	5.307	3.249	31.47	3.47

1.4. Optical characterization

Fig. 6a show the optical transmittance spectra of ZnO and AZO thin films deposited on FTO substrates. The value of transmittance increases from 80 % to 90 % with an increase of the Al concentration from 0 to 5 mM. Optical transmission in the visible range is important for TCO applications such as solar cell windows. From the optical absorption spectra, the optical band gap (E_g) was calculated by using the well-known Tauc relationship [16]:

$$\alpha h\nu = A(h\nu - E_g)^n \quad (9)$$

Where A is a constant, E_g is the band gap of the material, and n depends on the nature of the transition, being $n = 1/2$ for direct transitions [17]. It can be seen that the band gap increases from 3.27 to 3.47 eV with the increasing of the Al content [18].

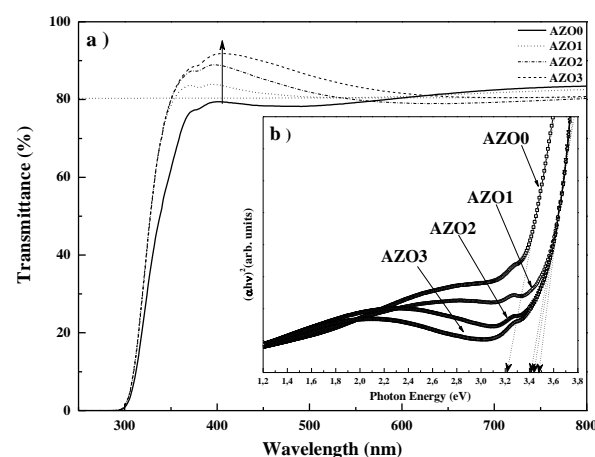


Fig. 6 Transmission spectra of the ZnO and Al doped ZnO (AZO) thin films electrodeposited on FTO.

The optical absorption edge has a blue shift to the region of higher photon energy with an increase in Al concentration. The blue shift behavior in the band gap can be attributed to an increase in the carrier concentration that blocks the lowest states in the conduction band, known as the Burstein–Moss effect [19]; an increase in the carrier concentration in Al doped ZnO will cause the Fermi level to move into the conduction band. Therefore, the low energy transitions are blocked [20, 21]. The filling of the conduction band by electrons generally causes a blue shift in the band gap.

2. Conclusion

Aluminum doped ZnO nanostructures were synthesized by electrochemical method at various Al concentrations. The effects of Al doping on the electrochemical, morphological, microstructural, and

optical properties of ZnO were examined. By addition of Al in the solution, the voltammogram of ZnO shifts the electrodeposition potential in the positive region. Also, the carrier density of the AZO thin film increased from 3.10×10^{20} to 5.60×10^{20} cm^{-3} with increasing Al concentration. The XRD analysis showed that the crystallinity of the AZO thin films deteriorated as compared to that of ZnO film. The average optical transmittances of AZO films in the visible wavelength range were over 80 %. The high transmittance of > 80 % in Al-doped ZnO allow it to be used as a TCO in solar cells. The optical band gap of the ZnO films shifted from 3.22 eV to more than 3.47 eV after doping.

References

- [1] X. Han, K. Han, and M. Tao, ECS Transactions, 25 (2010) 93-102.
- [2] O. Lupan, V.M. Guerin, I.M. Tiginyanu, V.V. Ursaki, L. Chow, H. Heinrich, T. Pauporte, J. Photochem. Photobiol, A: Chem, 211 (2010) 65-73.
- [3] M. R. Khelladi, L. Mentar, A. Beniaiche, L. Makhloufi, A. Azizi, J. Mater. Sci., Mater. Electron. 24 (2013) 153-9.
- [4] S. Laidoudi, A.Y. Bioud, A. Azizi, G. Schmerber, J. Bartringer, S. Barre, A. Dinia, Semicond. Sci. Technol. 28 (2013) 115005.
- [5] S. Haller, J. Rousset, G. Renou, and D. Lincot, EPJ Photovoltaics, 2 (2011) 20401
- [6] Izaki M, Omi T 1996 J. Electrochem. Soc. 143 L53
- [7] M.R. Khelladi, L. Mentar, M. Boubatra, A. Azizi, Mater Lett, 67 (2012) 331-333.
- [8] J.A. Cox, A. Brajter, Electrochim. Acta 24 (1979) 517.
- [9] A. Wolcott, W. A. Smith, T. R. Kuykendall, Y. Zhao, and J. Z. Zhang, Adv. Funct. Mater. 19 (2009) 1849 .
- [10] V. K. Mahajan, M. Misra, K. S. Raja, and S. K. Mohapatra, J. Phys. D: Appl. Phys. 41 (2008) 125307.
- [11] J. Rousset, E. Saucedo, D. Lincot. Chem Mater, 40 (2009) 21534
- [12] A. C. Aragonès, A. Palacios-Adrós, F. Caballero-Briones, F. Sanz, Electrochim Acta 109 (2013) 117- 124.
- [13] I. G. Dimitrov, A. O. Dikovska, P. A. Atanasov, T. R. Stoyanchoy, T. Vasilev, J. Phys. Conf. Ser. 113 (2008) 012044.
- [14] S.C. Navale, V. Ravi, S. Mulla, S. W. Gosavi, S. K. Kulkarni, Sensors and Actuators B126 (2007) 382.
- [15] R. Jenkins, R. L. Snyder, Introduction to X-ray Powder Diffractometry, p. 89, John Wiley & Sons, New York (1996).
- [16] J. Tauc. Optical Properties of Solids 22, F. Abeles, Ed., North Holland Pub, Amsterdam, (1970).
- [17] B. Pejova, I. Grozdanov, J. Solid State Chem, 158 (2001) 49.
- [18] O. Baka, A. Azizi, S. Velumani, G. Schmerber, A. Dinia, J Mater Sci: Mater Electron, 25 (2014) 1761-1769.
- [19] E. Burstein, Physical Review, 93 (1954) 632.
- [20] T.S. Moss, Phys. Soc. Lond. B 67 (1954) 775.
- [21] K. Sakai, T. Kakeno, T. Ikari, S. Shirakata, T. Sakemi, K. Awai, T. Yamamoto, Journal of Applied Physics, 99 (2006) 043508.

Numerical simulation of radiation damage on the device performance of GaAs MESFETs

Y. Beddiafi^a, A. Saadoune^a, L. Dehimi^b

^aLaboratory of Metallic and Semi-conducting Materials, B.P. 145, University of Biskra, Biskra, 07000, Algeria,

^bFaculty of science, University of Batna 05000, Algeria

Corresponding author: a.saadoune@univ-biskra.dz

Received: 30 April 2014, accepted 26 May 2014

Abstract

In this work, the effect of the radiation on the current-voltage characteristics of device GaAs metal Schottky field effect transistors (MESFET) at room temperature is investigated. Numerical Simulation tuned by means of a physics based device simulator. When the substrate of this transistor is subjected to radiations, structural defects, which are created, have undesirable effects and can degrade the performance of the transistors. These defects appear like deep traps. Results showed that in the presence of donor traps the current-voltage characteristics increases. However, acceptor traps have a significant effect on the current-voltage characteristics. In the presence of acceptor traps, the space charge zone in the channel increases, hence, reduces the current drain.

Keywords: Simulation, defects, silvaco, traps, GaAs

I. INTRODUCPION

The GaAs metal Schottky field effect transistors (MESFET) are one of important components used in electronic devices.

Deep traps are believed to be responsible for many parasitic effects in GaAs FETs such as the gate lag and drain lag effects in which a slow transient is observed in the drain current following a voltage applied to the gate or the drain.

The trap properties, energy and cross-section either measured by transient spectroscopy, voltage or optically excited deep level transient spectroscopy (DLTS).

The transistor GaAs MESFETs is simulated for two dimensional on a semi-insulating substrate compensated

by deep levels, and to clarify effect of impurity compensation by deep levels in the substrate [1].

In this work K. Horio et al, they simulate important case, that is, a case of GaAs MESFET on a Cr-doped semi-insulating substrate where deep Cr acceptors compensate shallow donors [1], and the compare the results with those obtained for a case with deep EL2 donors.

The objective of our work is to make modeling GaAs MESFET using Silvaco ATLAS TCAD simulator. We will determine the electrical characteristics $I_{ds}-V_{ds}$, with the influence of traps in low and high-resistivity material for two sample of transistor MESFET presented below.

2. PHYSICAL MODEL

A. Device structure

In this work, we will study two samples of transistors MESFET. As to a model for the semi-insulating substrates, we adopt a two level compensation model as described below.

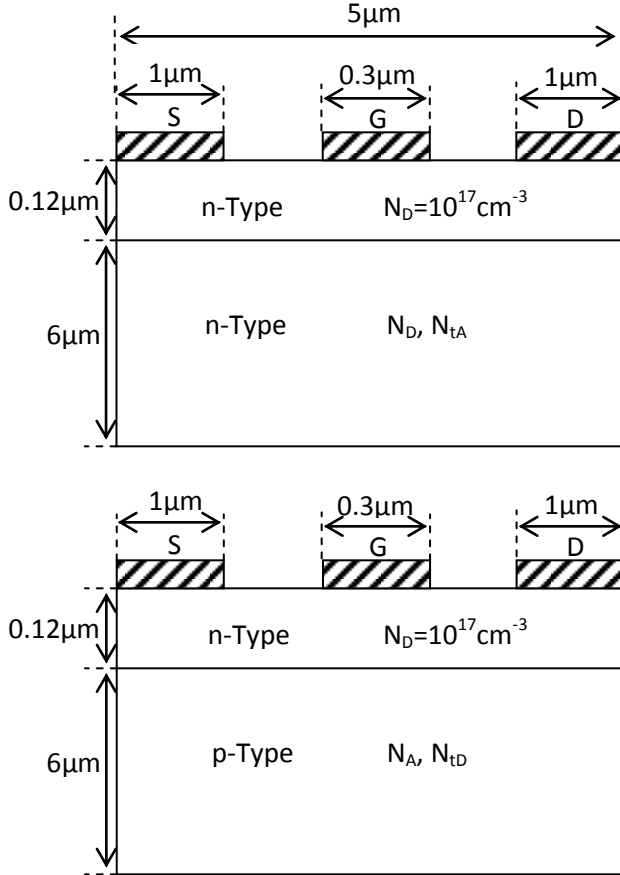


Fig. 1. Devices structures simulated in this study.

In the semi-insulating substrate n-type, we assume that deep acceptors (N_a) compensate shallow donors (N_D). In the p-type semi-insulating substrate, we assume that deep donors (N_D) compensate shallow acceptors (N_a).

B. Numerical simulation

In this work, we used the simulator TCAD-SILVACO (two-dimensional ATLAS) to study the performance of transistors MESFETs GaAs in the presence of deep traps. The important advantage of this type of simulator is

that it gives the ability to visualize physical phenomena inaccessible and therefore observable [2, 3].

The basic equations are the following:

Poisson's Equation relates the electrostatic potential to the space charge density:

$$\frac{\partial^2 \psi}{\partial x^2} = -\frac{q}{\epsilon \epsilon_0} (N_D - N_A + p - n + N_{tD}^+ - N_{tA}^-) \quad (1)$$

Where ψ is the electrostatic potential, $\epsilon \epsilon_0$ is the local permittivity, N_A and N_D are the shallow-acceptor density and shallow-donor density, respectively, p and n are the hole and electron densities, respectively, N_{tA}^+ and N_{tD}^+ are the ionized deep acceptors and deep donor's density, respectively.

The continuity equations for electrons and holes are defined by equations:

$$\frac{\partial n}{\partial t} = \frac{1}{q} \cdot \text{div} J_n + G_n - U_n = 0 \quad (2.a)$$

$$\frac{\partial p}{\partial t} = -\frac{1}{q} \cdot \text{div} J_p + G_p - U_p = 0 \quad (2.b)$$

Where G_e and G_h are the generation rate for electrons and holes, respectively, and U_e , U_h are the recombination for electrons and holes respectively.

By default, ATLAS includes both Eqs. 2.a and 2.b. In some circumstances, however, it is sufficient to solve only one carrier continuity equation.

Derivations based upon the Boltzmann transport theory have shown that a drift-diffusion model may approximate the current densities in the continuity equations. In this case, the current densities are expressed in terms of the quasi-Fermi levels ϕ_n and ϕ_p as:

$$\vec{J}_n = e \mu_n n \nabla \phi_n \quad (3.a)$$

$$\vec{J}_p = e \mu_p p \nabla \phi_p \quad (3.b)$$

Where μ_n and μ_p are the electron and hole mobilities. The quasi-Fermi levels are then linked to the carrier

concentrations and the potential through the two Boltzmann approximations:

$$n = n_i \exp\left(\frac{\psi - \phi_n}{kT}\right) \quad (4.a)$$

$$p = n_i \exp\left(\frac{\phi_p - \psi}{kT}\right) \quad (4.b)$$

Where n_i is the effective intrinsic concentration and T is the lattice temperature. These two equations may then be re-written to define the quasi-Fermi potentials:

$$\phi_n = \psi - \frac{kT}{q} \ln\left[-\frac{n}{n_i}\right] \quad (5.a)$$

$$\phi_p = \psi - \frac{kT}{q} \ln\left[-\frac{p}{n_i}\right] \quad (5.b)$$

By substituting these equations into the current density expressions, the following adapted current relationships are obtain

$$\vec{J}_n = qD_n \nabla n - q\mu_n n \nabla \psi - n\mu_n kT \nabla \ln(n_i) \quad (6.a)$$

$$\vec{J}_p = -qD_p \nabla p - q\mu_p p \nabla \psi + p\mu_p kT \nabla \ln(n_i) \quad (6.b)$$

The final term accounts for the gradient in the effective intrinsic carrier concentration, which takes account of band gap narrowing effects. Effective electric fields are normally defined where by:

$$\vec{E}_n = -\nabla\left(\psi + \frac{kT}{q} \ln(n_i)\right) \quad (7.a)$$

$$\vec{E}_p = -\nabla\left(\psi - \frac{kT}{q} \ln(n_i)\right) \quad (7.b)$$

Which then allows the more conventional formulation of drift-diffusion equations to be written see Eqs. 7.a and 7.b.

$$\vec{J}_n = qD_n \nabla n + q\mu_n n \vec{E}_n \quad (7.a)$$

$$\vec{J}_p = -qD_p \nabla p + q\mu_p p \vec{E}_p \quad (7.b)$$

It should be noted that this derivation of the drift-diffusion model has tacitly assumed that the Einstein relationship holds. In the case of Boltzmann statistics this corresponds to:

$$D_n = \frac{kT}{e} \mu_n \quad (8.a)$$

$$D_p = \frac{kT}{e} \mu_p \quad (8.b)$$

The equations are solved by the Newton method. Several models are activated in the simulation including: Shockley-Read-Hall recombination (SRH Model), electric mobility dependent parallel field (Fldmob model), concentration dependent mobility (Conmob model), and impact ionization (impact of Selb model).

3. RESULTS AND DISCUSSIONS

Activation energies and capture cross sections of the traps used in this work [1, 4, 5].

Table.1

Deep level	Energy (eV)	Capture cross (cm ²)	
		Electron	Hole
Donor EL2	E _c -0.688	4.68×10 ⁻¹⁶	2×10 ⁻¹⁸
Acceptor Cr	E _v +0.755	1.17×10 ⁻¹⁹	5×10 ⁻¹⁷

The density of deep acceptors and deep donors in the substrate are varied from (5 × 10¹³ to 10¹⁶ cm⁻³) [5]

The conditions for high-resistivity material are given by relations following [6]:

For n-type substrate: $N_D > N_A$ then $(N_A - N_D) > (N_D - N_A)$

For p-type substrate: $N_A > N_D$ then $(N_D - N_A) > (N_A - N_D)$

Where N_b and N_a are the concentrations of shallow donors and acceptors, respectively, and N_{db} and N_{da} are the concentrations of deep donors, and acceptors, respectively.

Figs. 1 and 2 show the influence traps donor and acceptor in the substrates on the electrical characteristics (current-voltage).

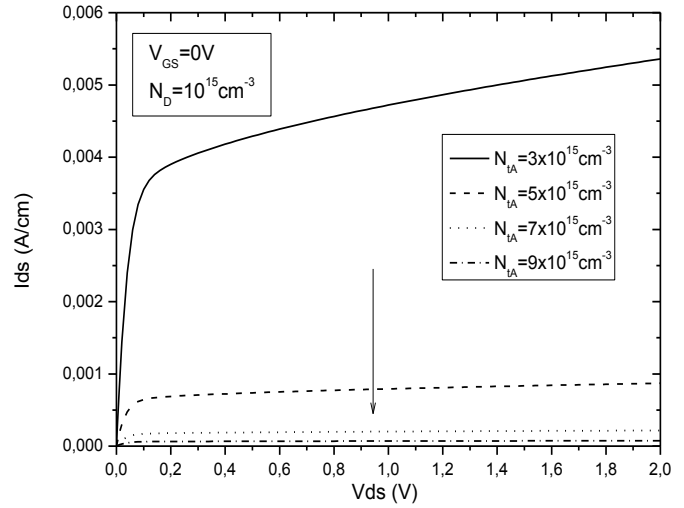
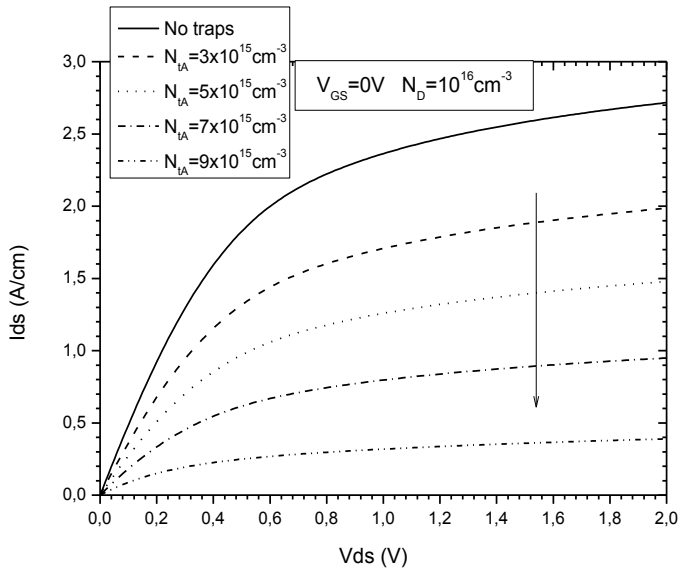


Fig.2. Simulation results of I_{ds} - V_{ds} characteristics for GaAs MESFETs with different deep-acceptor densities in the substrate. (a) low-resistivity material ($N_A < N_D$), (b) high-resistivity material ($N_A > N_D$).

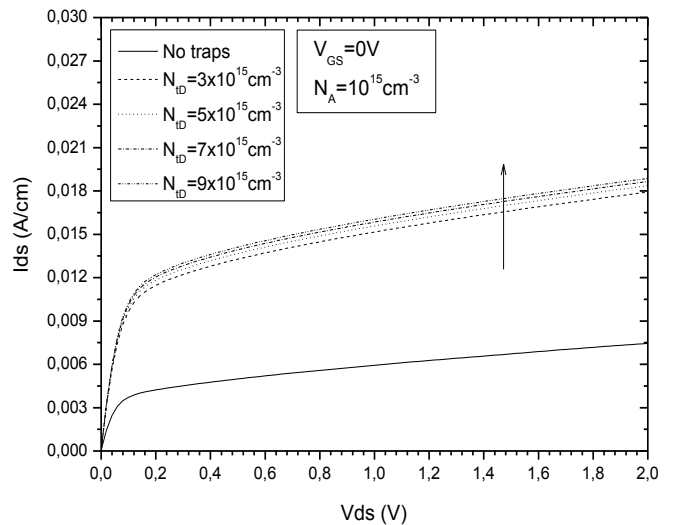
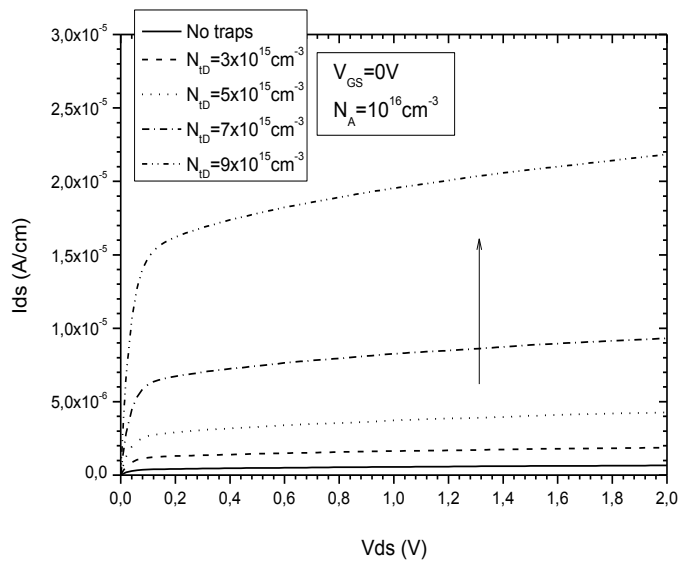


Fig.3. Simulation results of I_{ds} - V_{ds} characteristics for GaAs MESFETs with different deep-acceptor densities in the substrate. (a) low-resistivity material ($N_D < N_A$), (b) high-resistivity material ($N_D > N_A$).

Figs. 2 and 3 shows simulated results I_d - V_d characteristics of GaAs MESFETs on the n-type and p-type substrate, respectively. Two cases with different deep-acceptor densities in the substrate are shown Figs. 2.a and 2.b. The results for a case with deep donors and shallow acceptors in the substrate are shown by Figs. 3.a and 3.b.

for a fixed voltage V_{ds} ($V_{gs} = 0$), the current I_{ds} decreases with increasing density of acceptor traps, this is because of the influence of trap densities acceptors on the area of space charge created in the interface of the substrate channel. The acceptor traps may compensate the shallow donors to reduce the free electron density. They are also negative when they have absorbed a free electron so that they also compensate the space charge.

Figs. 3.a and 3.b shows I_{ds} versus V_{ds} plot at $V_{gs}=0$ with increasing density of donor traps, the current increases because the number of free carriers increases.

4. CONCLUSION

In the present work, the effect of the traps on the Id-Vd characteristics of The GaAs metal Schottky field effect transistors (MESFET) is studied numerically using the simulator TCAD-SILVACO (two dimensions ATLAS). The results showed that in the presence of donor traps the current-voltage characteristics increases because the number of free carriers Increases. However, the acceptor traps have a significant effect on the current-voltage

characteristics. In the presence of acceptor traps, the load space area in the channel Increases, hence, Reduces the current drain.

REFERENCES

- [1] K. Horio, K.Asada, H.Yanai, "Two-dimensional simulation of gaas mesfets with deep acceptors in the semi-insulating substrate" Solid-State Electron. 34 (1991) 335-343.
- [2] B. Kaghouché "Etude par tcad-silvaco d'une structure mos pour la réalisation de capteurs isfet : parametrestechnologiques et electriques" mémoire de magister Université Mentouri - Constantine 2010.
- [3] W. DIB "modelisation des structures photovoltaïques : aspects fondamentaux et appliques" mémoire de Doctorat université Abou bekr Belkid de tlemcen 2011.
- [4] Y. Beddiafi, "Modélisation d'un transistor MESFET en GaAs en utilisant le simulateur atlas-silvaco" mémoire de magister, université de biskra 2013.
- [5] K. Horio, Y. Fuseya "Two-dimensional simulations of drain-current transients in GaAs MESFET's with semi-insulating substrates compensated by deep levels" Electron Devices, IEEE Transactions on
- [6] C. Kokot, C. Stolte, "Backgating in GaAs MESFET's" IEEE Trans. Electron Devices 29 (1982) 1059-1064.

Effect of a buffer layer on the Performance of Thin-film Cu(In,Ga)Se₂ Solar Cells

M. Mostefaoui^{1,2}, H. Mazari², S.Khelifi¹, R.Dabou¹

¹*Unité de Recherche en Energies Renouvelables en Milieu Saharien d'Adrar, Algérie*

²*Laboratoire de Microélectronique Appliquée, Département d'électronique,*

Université Djillali Liabès de Sidi Bel-Abbes, Algérie

Received: 30 April 2014, accepted 26 May 2014

Abstract

Copper indium gallium diselenide (CuIn_xGa_{1-x}Se₂ or CIGSe) solar cells has been considered to be one of the most promising thin-film solar cells and is important for terrestrial applications because of their high efficiency, long-term stable performance and potential for low-cost production. In this work, the CIGS heterojunction solar cell has been numerically simulated using SCAPS-1D tool. We study the influence of a buffer layer on the performance of the CIGSe solar cells. Quantum efficiency, J_{sc}, Voc and efficiency has been calculated in different buffer layer materials (CdS, ZnS, ZnSe, InS). The solar cell optimized shows an efficiency of > 18% under the AM1.5G spectrum and one sun.

Keywords :CIGSe solar cells, buffer layer, simulation, SCAPS-1D.

PACS:

1. Introduction

Solar or photovoltaic cells represent one of the best possible technologies for providing an absolutely clean and virtually inexhaustible source of electricity. Thin film solar-cells with polycrystalline Cu(In,Ga)Se₂ (CIGSe) absorber layers provide a good alternative to wafer based crystalline silicon solar cells, which currently constitute the major share of photovoltaics installed and used worldwide. These compounds are direct bandgap semiconductors which minimize the requirement for long minority carrier diffusion lengths. Such p-type semiconductors with high absorption coefficient are the promising absorbing materials for thin film photovoltaic technology [1].

Buffer layer is an intermediate layer film between the absorber and window layers with two main objectives, to provide structural stability to the device and to fix the electrostatic conditions inside the absorber layer [2].

Cadmium sulphide (CdS) is a prominent candidate to be used a buffer layer in Cu(In,Ga)Se₂ based solar cell. Note that Cadmium (Cd) is a metal that can cause severe toxicity in humans and the environment.

In this work, we present a numerical study of the thin film CIGSe solar cells with SCAPS, is used to calculate PV parameter sunder standard illumination (AM1.5G, 100 mW/cm², 300K).

We study the influence of a buffer layer on the performance of the CIGSe solar cells. Quantum efficiency, J_{sc}, Voc and efficiency has been calculated in different buffer layer materials (CdS, ZnS, ZnSe, InS). The purpose is to replace the CdS by Other materials like Zinc Sulphide (ZnS), Zinc Selenide (ZnSe) and Indium Sulphide (InS).

2. Simulation details

2.1. Program Description

SCAPS is a one-dimensional solar cell device simulator, developed at ELIS, University of Gent, which is freely available to the PV research community [3]. The user can define a solar cell as a series of layers with different properties, such as thickness, doping densities and defect distribution. It is then possible to simulate a number of common measurements: I-V, QE, C-f, and C-V. Several modeling tools such as AMPS-1D, PC1D specific to PV devices have been developed.

SCAPS is used to simulate the J-V characteristics of the CIGSe solar cell under the global spectra AM1.5. We demonstrate the effect of buffer layer on the photovoltaic parameters (J_{sc} , η , V_{oc} and FF).

2.2. Cell Structure

Solar cell structure used in the device simulation consists of an p-CIGSe absorber layer, the buffer layer and a window layer made of n-ZnO:Al. Aluminum (Al) is used as the front contact and Molybdenum (Mo) back contact layers. The cell is illustrated schematically in Fig. 1.

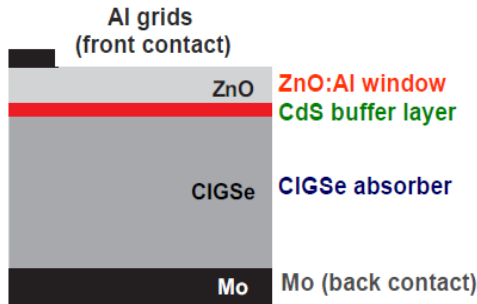


Fig.1: Schematic structure of a CIGS solar cell.

From its earliest development, CIGSe was considered promising for solar cells because of its favorable electronic and optical properties including its direct band gap with high absorption coefficient and inherent p-type conductivity [4].

2.3. Input parameters

Before simulating any device, we have to describe the materials that are used to build the structure. The

parameters used for simulations of a standard CIGSe solar cell are summarized in the following table1.

Table 1. The parameters for the CIGSe solar cell at 300K[5].

parameters	CIGSe	CdS	ZnO :Al
$E_g(\text{eV})$	1.5	2.4	3.5
ϵ_r	13.6	10	9
$\chi(\text{eV})$	4.5	4.2	4.65
$\mu_n(\text{cm}^2\text{V}^{-1}\text{s}^{-1})$	100	100	100
$\mu_p(\text{cm}^2\text{V}^{-1}\text{s}^{-1})$	25	25	25
$N_c(\text{cm}^{-3})$	$2.2 \cdot 10^{18}$	$1.5 \cdot 10^{18}$	$2.2 \cdot 10^{18}$
$N_v(\text{cm}^{-3})$	$1.8 \cdot 10^{19}$	$1.8 \cdot 10^{19}$	$1.8 \cdot 10^{19}$
$V_t(\text{cm/s})$	$1 \cdot 10^7$	$1 \cdot 10^7$	$1 \cdot 10^7$
$V_t(\text{cm/s})$	$1 \cdot 10^7$	$1 \cdot 10^7$	$1 \cdot 10^7$

Other materials such as ZnS, ZnSe, InS were tested with CdS are used for the simulation (Table 2).

Table 2. The parameters for the CIGSe solar cell at 300K.

parameters	ZnS	ZnSe	InS
$E_g(\text{eV})$	0.06	0.08	0.05
ϵ_r	10	10	13.5
$\chi(\text{eV})$	3.5	2.9	2.8
$\mu_n(\text{cm}^2\text{V}^{-1}\text{s}^{-1})$	50	50	400
$\mu_p(\text{cm}^2\text{V}^{-1}\text{s}^{-1})$	20	20	210
$N_c(\text{cm}^{-3})$	$1.5 \cdot 10^{18}$	$1.5 \cdot 10^{18}$	$1.8 \cdot 10^{19}$
$N_v(\text{cm}^{-3})$	$1.8 \cdot 10^{18}$	$1.8 \cdot 10^{18}$	$4.0 \cdot 10^{19}$
$V_t(\text{cm/s})$	$1 \cdot 10^7$	$1 \cdot 10^7$	$1 \cdot 10^7$
$V_t(\text{cm/s})$	$1 \cdot 10^7$	$1 \cdot 10^7$	$1 \cdot 10^7$

3. Simulation results and discussion

The simulation has been carried out by using SCAPS dedicated thin films solar cells. The J-V characteristics are represented in the figure below for CdS buffer layer.

3.1. Current-voltage simulation

Figure 2 shows the simulated characteristics J (V), with the AM1.5 illumination conditions (100mW/cm²), for different buffer layer. The table 3 includes all the photovoltaic parameters (I_{sc}, η, V_{oc} and FF) of the CIGSe solar cell with different buffer layer.

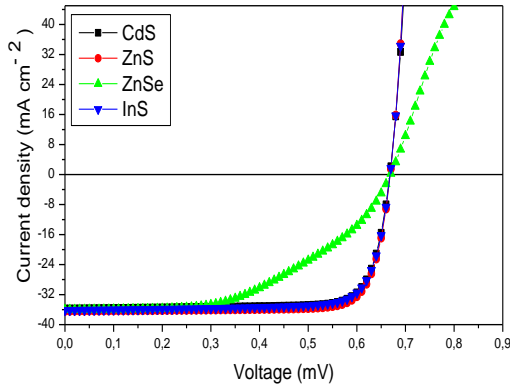


Fig.2: Current-voltage characteristics under AM1.5 illumination for the CIGSe solar cell.

	CdS	ZnS	ZnSe	InS
V _{co} (V)	0.668	0.668	0.669	0.668
J _{sc} (mA /Cm ²)	35.76	36.42	36.02	36.16
FF %	80.48	81.30	50.33	79.58
η %	19.23	19.80	12.13	19.23

Table2. The photovoltaic parameters for the CIGSe solar cell.

From these figures, one can notice that solar cells with CdS, ZnS and InS as buffer layer gives high conversion efficiency. As for the solar cell buffer With ZnSe layer had the least conversion efficiency.

3.2. Spectral response simulation

The quantum efficiency *QE* is the number of carriers collected by the solar cell to the number of photons incident on the solar cell. The short circuit current density can be predicted from the wavelength dependency of quantum efficiency *QE*(λ) and the solar spectrum .

$$J_{sc} = q \int_{\lambda} \phi(\lambda) QE(\lambda) d\lambda \quad (1)$$

Where $\phi(\lambda)$ is the incident photon flux density per unit wavelength band width.

The choice of the buffer layer can also be explained by the drawing of the quantum efficiency which is shown in Figure 3.

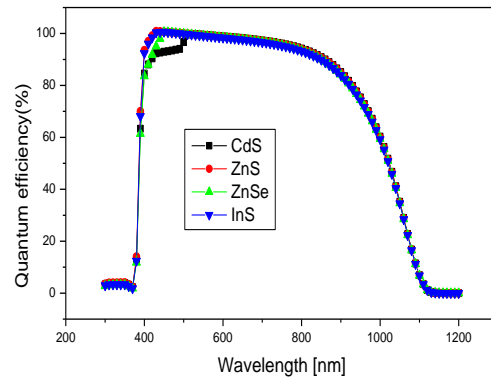


Fig.3: Simulated QE spectrum for different buffer layer.

From Fig. 3, we note that the QE with CdS buffer layer is lower with respect to the ZnS (ZnSe and InS) buffer layer in the wavelength regime of 350nm-900nm.

The solar cell with ZnS, ZnSe and InS buffer shows the increasing spectral response reaches a maximum 100% from the wavelength 370 nm to 900 nm. The steeper slope for shorter wavelength between 400 nm and 500 nm is occurred in CdS buffer of 90% and exhibit a higher response of 98% at the wavelengths larger than 800 nm.

4. Conclusion

In this investigation, we study the performance of the CIGSe solar cells. The CdS buffer layer is replaced by other materials like Zinc Sulphide (ZnS), Zinc Selenide (ZnSe) and Indium Sulphide (InS).

The analysis of all the results shows that the best photovoltaic parameters (J_{sc} , η , V_{oc} and FF) are obtained with ZnSe and ZnS as buffer materials can be compared to CdS buffer.

We concluded that InS and ZnS can be used as alternative material to CdS. As the later presents serious environmental problems.

References

- [1] Byung Tae Ahn, Liudmila Larina, Ki Hwan Kim, and Soong Ji Ahn , Development of new buffer layers for Cu(In,Ga)Se₂ solar cells, *Pure Appl. Chem.*, Vol. 80(200).
- [2] Nawfal Y. Jamil, Suha N. Abdulla, Abid A.K. Muhammed, Design and Fabrication Heterojunction Solarcell of Si-CdS-ZnO Thin Film, proceedings of the international conference nanomaterials: applications and properties, Vol. 1 No 4,(2012)
- [3] Koen Decock , Samira Khelifi, Marc Burgelman, Modelling multivalent defects in thin film solar cells *Thin Solid Films* 519 (2011) 7481-7484.
- [4] Rocheleau R, Meakin J, Birkmire R, *Proc. 19th IEEE Photovoltaic Specialist Conf.*, 972-976(1987).
- [5] Thèse de doctorat, Zacharie Jehl Li Kao, Elaboration of ultrathin Copper Indium Gallium Di-Selenide based Solar Cells,2012.

Fabrication, structural and optical characterization of In doped ZnO thin films prepared by the colloidal method

M. Medjaldi^{1,2}, O. Touil¹, M. Zaabat², B. Boudine¹, O. Halimi¹ And M. Sebaï¹.

¹Laboratoire de Cristallographie, Département de physique, Faculté des Sciences Exactes, Université Constantine 1

²laboratoire composants actifs et matériaux, Département de physique, Faculté des Sciences Exactes, Université Larbi Ben m'hidi OEB Algérie.

Received: 30 April 2014, accepted 26 May 2014

Abstract:

Regarding to the excellent conductivity and high transparency in the visible range, the zinc oxide (ZnO) films have been widely used as transparent electrodes in optoelectronic devices, ZnO is a direct wide band-gap (3.37 eV) semiconductor. The conductivity of ZnO will be largely enhanced by doping little In, but it still keeps high transparency. So, IZO film has been widely investigated and is considered to be a promising possible alternative to ITO films.

This work consist to the fabrication and characterization of ZnO:In thin films. The sample preparation was carried out by the colloidal method. The pure and In doped ZnO thin films were deposited using a dip-coating technique on glass matrix. The optimal condition for samples fabrication has been investigated. The XRD and Raman characterizations show that the ZnO thin film crystallize with a wurtzite structure. The optical properties of ZnO thin films doped In reveal that doping changes the optical gap of ZnO.

Keywords: ZnO thin films; Indium doping; XRD and Raman characterizations.

1. Introduction

ZnO is a n-type compound semiconductor with a large exciton binding energy of 60 meV at room temperature and a wide direct band gap of 3.37eV, and high transmission in the visible range, which provides it the potential application in various optoelectronic applications such as optical sensors and light emitters, etc... [1,2]. During the last years, in ordre to enrich the potential application in devices ZnO has been doped with many different kinds of elements, such as Al, Ga, In, and Sb to enhance the optical/electrical properties [3-5].

In our work, we fabricated two In-doped ZnO samples, which are 0,5 and 1% IZO. Their structures were characterized in this paper. Raman scattering measurements were designed to obtain more detailed information of the structures in In-doped ZnO nanomaterials.

2. Experimental

To prepare a ZnO solution, 1.5g of zinc acetate dihydrate ($Zn(CH_3COO)_2 \cdot 2H_2O$) was dissolved in 30 ml of absolute ethanol at room temperature. When the solution turned milky, an equimolar amount of MEA was added drop by drop to obtain a clear and transparent solution after stirring at 60°C

for 1h. The solutions were deposited by dip coating method on glass substrate. The obtained films were preheated at 100°C for 10min and the heat treatment was carried out at 500°C for 2h.

The crystal structure and phase of the samples were characterized by X-ray diffraction technique using Bruker AXS D8 Discover diffractometer, $CuK\alpha$ ($\lambda=1.54056 \text{ \AA}$), where the angle ranges within 20°-80°. Raman scattering experiments was performed at room temperature using a Raman spectroscope meter (?????) with the ??? nm line. The films transmittance was recorded by Shimadzu 3600 PC double beam UV-VIS-NIR spectrometer.

3. Results and discussion

3.1. Structural analysis

The figure 1 shows the X- rays diffraction pattern of two samples (0,5 and 1% Indium doped zinc oxide), and are vertically normalized for clarity.

The comparison of the observed XRD patterns with the standard JCPDS data N° 36-1451 confirms the formation of crystallites of nanometer size and hexagonal (wurtzite) [6]. No extra peak is noted in Fig. 1, suggesting no secondary phase in wurtzite ZnO.

The all investigated films have adopted a preferred orientation along the direction [002], which indicates that the films have the preferred orientation with the c-axis normal to the substrate. the Bragg position of (002) is at 34.54°, 34.3° for 0.5% and 1% indium doped ZnO respectively, and then a slight angle shift was carefully detected. Others reflection positions (2θ and their angle shifts are listed in table1.

These results are in well agreement with those of literature [7].

It is also found that the peak (0 0 2) is less intense and sharper for 1% In, suggesting that In doping $\geq 1\%$ can reduce the crystal quality, which means that the crystal quality had been improved to a certain extent.

The grain size G is given by the well-known Scherrer's formula [8],

$$G = (0.94 \lambda) / (\beta \cdot \cos \theta) \quad (1)$$

Where β is the full width at half medium of the peak, 2θ is the Bragg angle and λ is X-rays wavelength. The calculated values of G are listed in table1.

Consequently, according to all orientations, indium doping reduces the grain size. Since the radius of In^{3+} ion (0.092 nm) is larger than Zn^{2+} ion (0.083 nm) [9], the indium atoms occupying positions in ZnO lattice lead the expansion of the lattice.

Fig. 2 shows the Raman spectra of In-doped ZnO (0,5 and 1%). No Raman Peak of In_2O_3 appeared in the spectra of the In-doped ZnO, indicating no secondary phase in In-doped samples, which is consistent with the XRD results.

Table 1. X-rays results of pure and indium doped ZnO

(hkl)		Bragg angle 2θ (°)	Angle Shift $\Delta 2\theta$	Grain size (nm)
(100)	ZnO pur	31,79	-	-
	0,5% In	31,81	+0,014	11,37
	1% In	31,69	-0,106	9,7285
(002)	ZnO pur	34,45	-	-
	0,5% In	34,54	+ 0,09	15,69
	1% In	34,3	- 0,15	12,46
(101)	ZnO pur	36,288	-	-
	0,5% In	36,37	+0,082	14,35
	1% In	36,19	-0,098	12,14

The wurtzite ZnO (space group C_{6v}^4) has six first-order optical modes, which are E_2^{low} , E_2^{high} , $A_1(\text{TO})$, $A_1(\text{LO})$, $E_1(\text{TO})$, and $E_1(\text{LO})$ [10]. The two intensive peaks at 99 cm^{-1} and 437,5 cm^{-1} are indicated to be E_2^{low} and E_2^{high} , which are the characteristic bands of the wurtzite ZnO, and the peaks at 380 and 579 cm^{-1} are known to be $A_1(\text{TO})$ and $A_1(\text{LO})$, which are also the first-order optical modes of wurtzite ZnO.

The peak observed at 332 cm^{-1} is attributed to $E_2^{\text{high}}-E_2^{\text{low}}$, which are second order features caused by multi-phonon processes [11].

The board band at 980-1465 cm^{-1} is conjectured to be associated with intrinsic lattice defects and often arise by the doping [12].

The shift of the E2 mode can give the information on stress. Previous investigations have shown the relation between stress and E_2 (high) mode: under a compressive stress the

E_2 (high) up shifts, where as a tensile stress will lead to its downshift [13]. Compared to the E_2 (high) mode of the standard ZnO (437 cm^{-1}), a up shift of 0,5 cm^{-1} was observed for the E_2 (high) mode of the two ZnO:In films. This shift indicates that a slight compressive stress existed in the In doped ZnO films. This shows that doping In atoms into a ZnO films will cause its compressive lattice distortion.

3.2. Optical characterization

Transmission spectra for indium doped ZnO thin films are shown in Fig.3a. The average optical transparency is higher than 90% in the visible region (400-700nm) of spectrum for all the films, which gives the thin ZnO films the character of transparency in the visible region and makes this material a potential candidate for optoelectronic applications.

Figure 1. X-rays pattern of indium doped ZnO (0.5 and 1%), grown by dip coating process within 20°-80°.

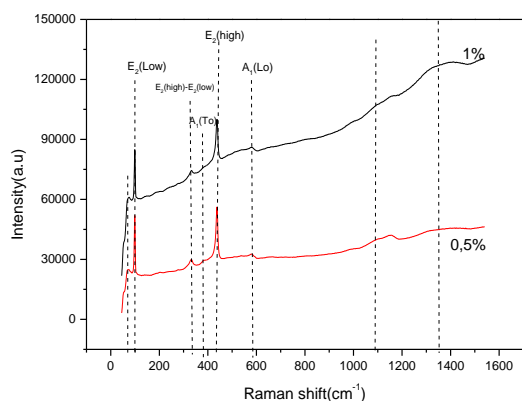


Fig 2. Raman spectra of two samples of In-doped ZnO (0,5 and 1%).

Compared to pure ZnO film, the UV absorption edge is blue-shifted for IZO film, indicating broadening of the optical band gap due to In doping. In general, a blue shift of the absorption edge is associated with an increase in the concentration of carriers blocking the lowest states in the conduction band, known as the Burstein-Moss effect [14]. In doping increases the Fermi level of the films into the conduction band, making the films completely degenerate, which shifts the absorption edge to energies higher than the actual band gap of the material.

For direct-transition semiconductors, the optical band-gap E_g can be calculated according to :

$$(\alpha h\nu)^2 = D(h\nu - E_g)^{1/2} \quad (2)$$

where α is the absorption coefficient, $h\nu$ is the photon energy and D is a constant [15,16]. We assume that $\alpha = (1/d) \ln(1/T)$, where d is the film thickness and T is the transmittance.

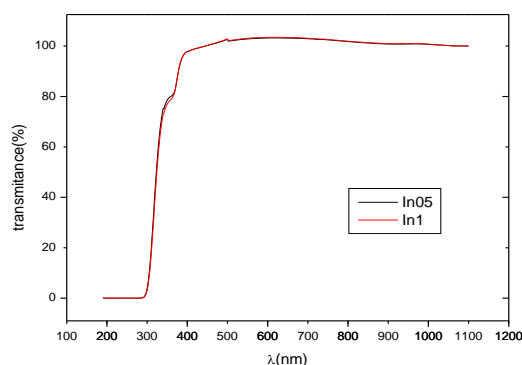


Fig-3.a: transmittance of In doped ZnO (0.5% and 1%) and pure ZnO.

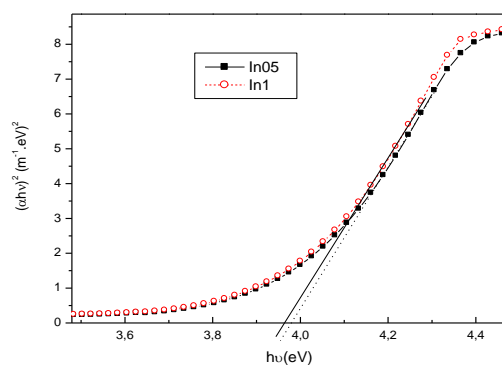


Fig-3.b: UV-visible spectroscopy of In doped ZnO (0.5 and 1%)

A plot of $(\alpha h\nu)^2$ versus $h\nu$ is shown in Fig. 3b. E_g can be determined by extrapolation to the energy axis at $(\alpha h\nu)^2=0$. We obtained E_g values of 3.97 and 3.96 eV for 0,5% and 1% indium doped ZnO thin film; these values are greater than E_g for pure ZnO thin film (3.37 eV).

In figure 3b, it can be seen that the influence of the concentration of Indium on the gap is weak.

This observation is similar to this of Ayouchi et al. [17], who had obtained values of E_g higher than those of stoichiometric massive ZnO and thus observed a decrease of E_g . This phenomenon was attributed to the reduced grains size in the thin layers of ZnO prepared and to the oxygen deficiency.

4. Conclusion

Indium doped ZnO thin films were prepared on glass matrix by colloidal method, with different concentrations. The XRD spectrum of the all thin films have a crystalline structure with the preferential orientation of (0 0 2). The raman spectroscopy result is consistent with the XRD one. UV-visible spectroscopy shows that the In changes the optical gap of ZnO (shift of optical gap to higher energies (blue shift)).

The results obtained by different characterization reveal that the introduced of Indium as a dopant for different ratio (0.5, 1%), who is an isoelectronic with ZnO, have not make a free electron. This results indicated that Indium has formed a composite ZnO/In.

References

- [1] R.F. Service, Science 895, 276 (1997).
- [2] T. Makino, C.H. Chia, T.T. Nguen, Y. Segawa, Appl. Phys. Lett. 77 (2000) 1632-1634.

- [3] W.W. Wang, X.G. Diao, Z. Wang, M. Yang, T.M. Wang, Z. Wu, *Thin Solid Films* 491 (2005) 54.
- [4] X. Yu, J. Ma, F. Ji, Y. Wang, C. Cheng, H. Ma, *Appl. Surf. Sci.* 245 (2005) 310.
- [5] M. Miki-Yoshida, F. Paraguay-Delgado, W. Estrada-Lopez, E. Andrade, *Thin Solid Films* 376 (2000) 99.
- [6] JCPDS Card N° 36-1451 (ZnO).
- [7] A.A. Dakhel, *Materials Chemistry and Physics* 117 (2009) 284-287.
- [8] M. Benhaliliba, C. E. Benouis, M. S. Aida, F. Yakuphanoglu, A. Sanchez Juarez, *J. Sol-Gel Sci. Technol.* 55, 3, (2010) 335-342, doi 10.1007/s10971-010-2258-x.
- [9] B. Wang, M.J. Callahan, C. Xu, et al. *J Cryst Growth* (2007) 304:73-9.
- [10] CA. Arguello, DL. Rousseau, PSP. Porto. *Phys Rev* (1969) 181:1351-63.
- [11] C. Ramon, AL. Esther, I. Jordi, et al. *Phys Rev* 75 (2007) 165-202.
- [12] TC. Damen, SPS. Porto, B. Tell. *Phys Rev* 4 (1966) 142:570.
- [13] Y. Huang, M. Liu, Z. Li, Y. Zeng, S. Liu. *Mater Sci Eng B* (2003) 97-111.
- [14] Z.Q. Xu, H. Deng, Y. Li, H. Cheng, *Mater. Sci. Semicond. Process.* 9 (2006) 132-135.
- [15] K.C. Yung, H. Liem, H.S. Choy, *J. Phys. D Appl. Phys* 42 (2009) 185-200.
- [16] L.H. Xu, X.Y. Li, J. Yuan, *Superlattices Microstruct* 44 (2008) 276-281.
- [17] R. Ayouchi, F. Martin, D. Leinen, J.R. Ramos-Barrado, *Journal of Crystal Growth*, 247 (3) (2003), 497-504.

Channel drop filter based on coupled cavity in photonic crystals

Rahima Bendjelloul, Touraya Bouchemat, Mohamed Bouchemat

Electronics department, Constantine 1 University, Constantine, Algeria

bendjelloulrahima@yahoo.fr

Received: 30 April 2014, accepted 26 May 2014

Abstract

In this paper, a five channel drop filter has been designed in a two dimensional photonic crystal with high dielectric rods in air. Each channel consists of a photonic crystal coupled cavity waveguide with double cavities combined with a line defect waveguide. Desired wavelengths are selected by setting different radii of the two point defects in the photonic crystal coupled cavity waveguides. Defect rods placed at the same channel have an identical radius. The performance of the designed filter has been numerically calculated using the finite difference time domain method. In the designed structure, higher efficiencies in all channels have been achieved.

Keywords: Photonic crystals; channel drop filter; coupled cavity; wavelength; waveguide.

1. Introduction

Photonic crystals (PCs) are envisaged as the main candidates for developing microscale integrated light wave circuits because of their properties for controlling the flow of light on a very small scale [1, 2]. The periodic change in the refractive index of these artificial materials in one, two or three dimension gives rise to photonic band gaps (PBGs) where no electromagnetic waves can propagate inside the crystal. By introducing defects into PCs, it is possible to build waveguides that can channel light along certain paths. It is also possible to construct microcavities that can localize photons in extremely small volumes. Combinations of these defects in photonic crystals structures give rise to a novel phenomena such as the trapping and emission of photons and the tunneling and channeling of photons [3, 4]. These defects are expected to be key building blocks for miniature photonic functional devices and photonic integrated circuits (PICs). Various optical devices can be realized based on PCs such as optical switches [5], band pass filters [6], band stop filters [7], splitters [8], demultiplexers [9], polarizers [10] and directional couplers [11]. In particular, ultra-compact channel drop filters (CDFs) based on resonant coupling between cavity modes of point defects and waveguide modes of line defects have drawn primary interest due

to their substantial demand in wavelength division multiplexing (WDM) optical communication systems.

So far, several structures of channel drop filters based on two dimensional (2D) PCs have been proposed, such as by utilizing the direct coupling between the PC waveguides and microcavities [12, 13]; in which the photons trapped by a resonant cavities are coupled to an in-plane waveguide through direct coupling, can be easily extended to multi-channel drop filters by using a set of microcavities of different sizes, i.e., different resonance frequencies or by changing the shape of the scatterers from a traditional circle to an ellipse [14]. The resonant frequency can be adjusted by altering the orientation angle of the ellipse and the frequency scope can be enlarged by increasing the ratio of the major axis to the minor axis of the ellipse. The concept of in-plane hetero photonic crystals, which consist of a series of connected PC regions with different lattice constants, has also been proposed [15]. Another configuration to consider is a photonic crystal ring resonator (PCRR) in which the CDF is based on the resonant coupling between the ring and the waveguide [16, 17].

Photonic crystal coupled cavity waveguide (PCCCW) [18, 19] has an attractive feature that the slope of guided mode in photonic band gap is smaller than that of PC line defect waveguide (PCLDW),

namely the frequency range of light propagation in PCCCW is narrower than that of PCLDW, and therefore PCCCW is more suitable for designing channel drop filter [20, 21] with narrow bandwidth.

In this paper, a five channel drop filter has been designed in a two dimensional photonic crystal with high dielectric rods in air. Each channel consists of a photonic crystal coupled cavity waveguide combined with a line defect waveguide. The channels are located on both sides of the bus (input) waveguide which is terminated with another channel drop filter in order to use the space more efficiently. The PC based coupled cavity waveguide can be formed by placing two photonic crystal cavities close together. All photonic resonant cavities are obtained by varying the radius of one rod in the photonic crystal structure. The performance of the designed filter has been numerically calculated using the finite difference time domain (FDTD) method with the perfectly matched layer (PML) absorbing boundaries conditions at all boundaries [22]. In the designed structure, higher efficiencies in all channels have been achieved.

2. Design of the channel drop filter

We consider a two dimensional photonic crystal composed of square lattice of rods in an air background with lattice constant $a=0.484 \mu\text{m}$. The refractive index of the rods and the air background is 3.4 and 1, respectively. The radius of rods of perfect PC (with no defects) is $r=0.2a \mu\text{m}$. The dispersion curves of perfect PC are calculated by using plane wave expansion (PWE) method and shown in Fig. 1. The band gap of the perfect PC exists in the frequency ranges of $0.287-0.420 (a/\lambda)$, where λ is the wavelength in free space, which corresponds to wavelength range $1.152-1.686 \mu\text{m}$ for the waves with transverse magnetic (TM) polarization (for which the incident electric field was parallel to the rods).

In general, if an entire row of rods is removed, a single line defect waveguide (SLDW) is obtained. However, if only one of every two or three or n rods of the entire row is removed, a photonic crystal coupled cavity waveguide is formed. Light propagation in PCCCWs is achieved by photon hopping between nearest neighbour cavities because of the overlapping of the modes localized in the defects [23]. The coupling between the strongly localized cavity modes

originates a frequency splitting of the single cavity mode into a number of resonance peaks that depend on the number of coupled cavities.

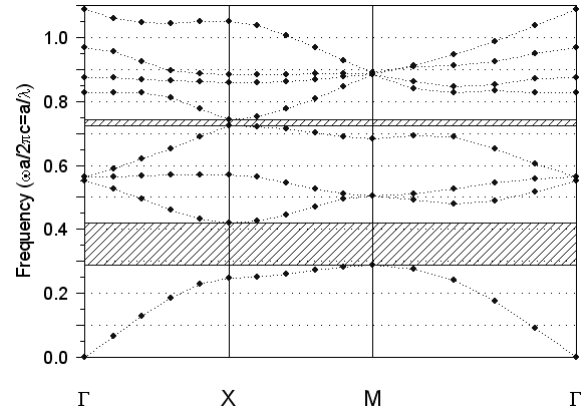


Figure 1. Dispersions curves and band gaps for TM polarization for the photonic crystal structure without defects.

In this paper, we firstly study the PCCCW with double cavities and analyze the effect of changing the distance between cavities on the transmission of it. Fig.2 shows the transmission spectrum of the PCCW for two different distances between the defects. We find from the analysis that when the defects are at close distance from one another, the maximum transmission splits into two peaks, thereby revealing the existence of two different electromagnetic modes (Fig. 2a). However, when the cavity spacing increases, the coupling intensity between neighbouring cavities will become weakened, and a single transmission peak is observed as shown in Fig. 2b.

Based on the above results, we construct a five channel PC drop filter, which is displayed in Fig. 3. The four channels of the CDF are located on the two sides of the bus waveguide. The fifth channel is placed at the end of the bus waveguide. It acts as a channel transmission at its resonance wavelength but works as a reflector for other incident waves at non resonance wavelengths. Each channel consists of a photonic crystal coupled cavity waveguide with double cavities combined with a single line defect waveguide serving as an output waveguide. Desired wavelengths are selected by choosing different radii of point defects in

all channels. Every two cavities placed at the same channel have an identical radius of defect. In order to guarantee the negligible coupling between the cavities or the output waveguides, the separation between the cavities were made larger than $4a$.

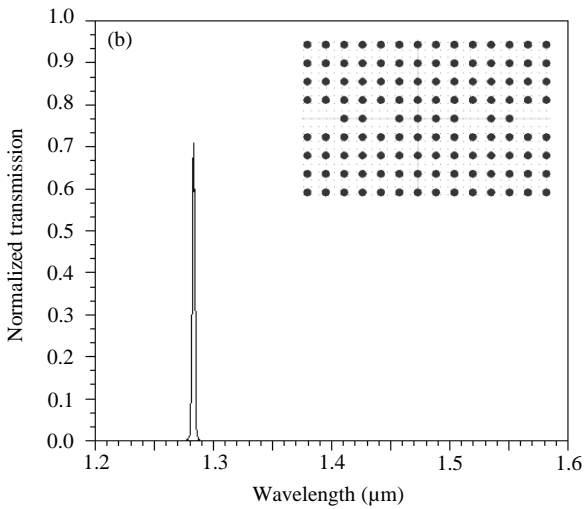
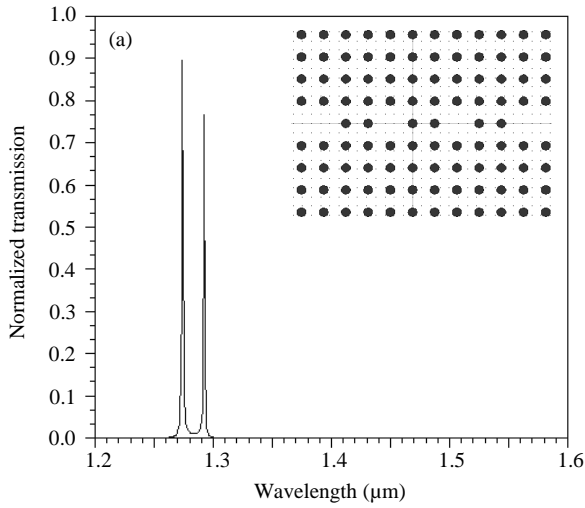


Figure 2. Normalized transmission of the PCCCW with (a) two rods separation, (b) four rods separation. The corresponding waveguide structures are shown in insets, respectively.

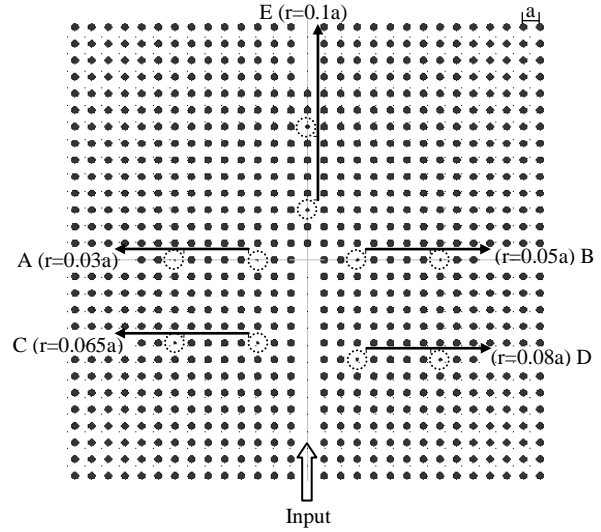


Figure 3. Schematic of the five channel drop filter.

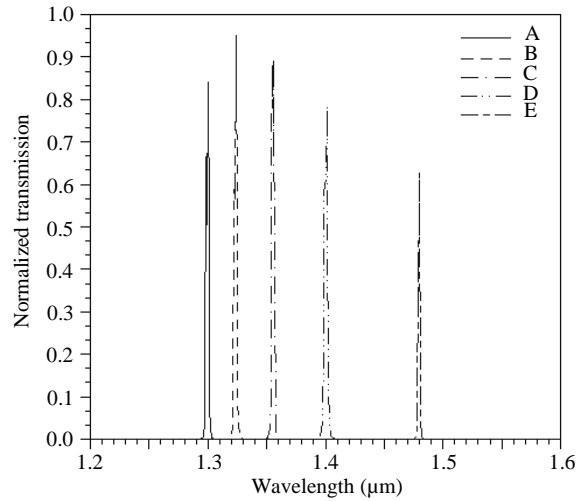


Figure 4. The normalized transmission spectra for ports A ($1.3 \mu\text{m}$), B ($1.3239 \mu\text{m}$), C ($1.3561 \mu\text{m}$), D ($1.4 \mu\text{m}$) and E ($1.48 \mu\text{m}$).

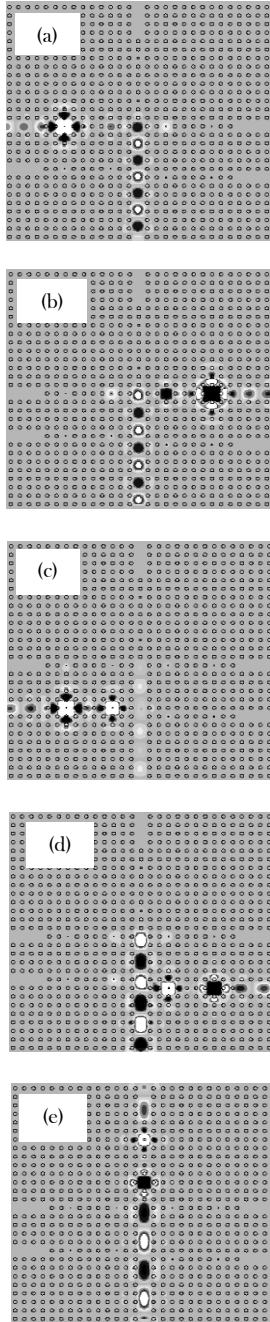


Figure 5. Field distributions at (a) $\lambda=1.3 \mu\text{m}$, (b) $\lambda=1.3239 \mu\text{m}$, (c) $\lambda=1.3561 \mu\text{m}$, (d) $\lambda=1.4 \mu\text{m}$ and (e) $\lambda=1.48 \mu\text{m}$.

3. Simulation and results

The FDTD is one of the most advanced methods today for computation of the field distribution inside the PC based devices which are really optical structures with non uniform dielectric constant distribution.

Different defect cavities are put on the two sides of the bus waveguide to avoid the direct coupling and to reduce the size of the structure. The radius of the defect rods are $r=0.03a$, $0.05a$, $0.065a$, $0.08a$ and $0.1a\mu\text{m}$ for channels A, B, C, D and E, respectively. Location of each cavity is chosen properly in order to get maximum transmission. Fig.4 shows the normalized transmission of the proposed multi-channel drop filter for TM polarization of incident light. The center wavelengths of the five channels are $\lambda=1.3$, 1.3239 , 1.3561 , 1.4 and $1.48 \mu\text{m}$ from outputs A, B, C, D and E, respectively. The normalized transmissions of these wavelengths are 83.5, 96.67, 89.67, 78 and 63.5 %, respectively. It is seen from the results shown in Fig. 4 that the proposed multi-channel drop filter can easily separate the light with five different wavelengths simultaneously with high drop efficiency. In order to demonstrate the filter performance, we simulate the field distributions of this filter at the resonance wavelengths as shown in Fig. 5.

4. Conclusion

We have designed a five channel drop filter based on a two dimensional photonic crystal with a square lattice of dielectric rods in air. It was found that the resonant frequency can be flexibly adjusted by just changing the radius of rod defects in the photonic crystal coupled cavity waveguide. The transmission properties of such structure show that the incident light can be successfully filtered to five different ports and high drop efficiency can be achieved. Such structure may offer promising applications for photonic integrated circuits based on PCs and other nanophotonic structures.

References

- [1] E. Yablonovitch, Phys. Rev. Lett. 58 (1987) 2059.
- [2] S. John, Phys. Rev. Lett. 58(1987) 2486.
- [3] B. S. Song, T. Asano, Y. Akahane, S. Noda, Phys. Rev. B. 71 (2005) 195101.

-
- [4] S. Noda, A. Chutinan, M. Imada, *Nature* 407 (2000) 608.
- [5] Q. Wang, Y. Cui, J. Zhang, C. Yan, L. Zhang, *Optik*, 121 (2010) 684.
- [6] M. Djavid, A. Ghaffari, F. Monifi, M. S. Abrishamian, *J. Appl. Sci.* 8 (2008) 1891.
- [7] F. Monifi, M. Djavid, A. Ghaffari, M.S.Abrishamian, *Proceedings of Progress In Electromagnetics Research Symposium*, July 2-6, 2008, Cambridge, USA.
- [8] A. Ghaffari, F. Monifi, M. Djavid, M.S. Abrishamian, *J. Appl. Sci.* 8 (2008) 1416.
- [9] M. Djavid, F. Monifi, A. Ghaffari, M.S. Abrishamian, *Opt. Commun.* 281 (2008) 4028.
- [10] V. Zabelin, L. A. Dunbar, N. Le Thomas, R. Houdré, M. V. Kotlyar, L. O'Faolain, T. F. Krauss, *Opt. Lett.* 32(2007) 530.
- [11] M. K. Moghaddam, A.R.Attari, M. M. Mirsalehi, *Phot. Nano-Fund. App.* 8 (2010) 47.
- [12] L. Li, G.Q. Liu, Y.H. Chen, F.L. Tang, K. Huang, L.X. Gong, *Optik* 124 (2013) 2608.
- [13] H. Ren, C. Jiang, W. Hu, M. Gao, J. Wang, *Opt. Express* 14 (2006) 2446.
- [14] F. Shuai, W. Yi-Quan, *Chin. Phys. B*, 20 (2011) 104207.
- [15] B. S. Song, S. Noda, and T. Asano, *Science* 300 (2003) 1537.
- [16] M. Djavid, M. S. Abrishamian, *Optik* 123 (2012) 167.
- [17] M. Y. Mahmoud, G. Bassou, A. Taalbi, Z. M. Chekroun, *Opt. Commun.* 285 (2012) 368.
- [18] P. Sanchis, J. Garcia, A. Martinez, F. Cuesta, A. Griol, J. Marti, *Opt. Lett.* 28 (2003) 1903.
- [19] A. Martínez, A. García, P. Sanchis, J. Martí, *Josa A* 20 (2003) 147.
- [20] B. K. Min, J. E. Kim, H. Y. Park, *Opt. Commun.* 237 (2004) 59.
- [21] M. Notomi, A. Shinya, S. Mitsugi, E. Kuramochi, H. Y. Ryu, *Opt. Express* 12 (2004) 1551.
- [22] A. Taflove, S.C. Hagness, *Computational Electrodynamics: The Finite-Difference Time-Domain Method*, 3rd ed., Artech House, Norwood, MA, 2005.
- [23] M. Bayindir, B. Temelkuran, E. Ozbay, *Phys. Rev. B* 61 (2000) 855.

Copper oxide thin films deposition by spray pyrolysis

M. Lamri Zeggar*, M. S. Aida and N. Attaf

Laboratory of Thin Films and Interfaces Faculty of Science University of Constantine, Algeria,

Received: 30 April 2014, accepted 26 May 2014

Abstract

CuO thin films have been grown on heated glass substrates by varying substrate temperatures from 280 to 400°C. The effect of the pyrolysis on structural, optical and electrical properties of CuO films has been investigated in the present work. Phase analysis was carried out using Micro-Raman scattering. The optical properties were studied by means of UV-visible and near infrared spectroscopy. The conductivity was measured by the electrical D.C transport. The structural analysis indicates the presence of a single CuO phase with a monoclinic structure. The optical transmittance spectra show a high absorption of all films in the visible region. The electrical characterization indicates a maximal electrical conductivity of $1,03 \times 10^6$ ($\Omega \cdot \text{cm}$)⁻¹.

Keywords: Copper oxide, solar cells, Spray pyrolysis.

1. Introduction

In recent years, copper oxide (CuO) thin films have attracted great interest due to their important applications in many technological fields. This is due, firstly, to the low cost, the non-toxicity and the availability of copper in the nature, secondly to the simplicity of the deposition process of its components. Copper oxide is known to have two stable forms, namely CuO and Cu₂O with different properties. CuO is a p-type semiconductor with a monoclinic structure; it has a relatively low band gap of 1,2-1,9 eV [1,2]. Furthermore, Cu₂O materials, in general, is a p-type semiconductor which crystallizes in cubic structure with a large direct band gap of 2 et 2,6 eV [3]. These two phases were mainly used in the fields of electronics and optoelectronics such as: high T_c superconductors [4], lithium batteries [5], for magnetic storage [6], gas sensors [7] and absorbers layers in solar cells [8]. Various techniques have been used for CuO thin films deposition namely: sol-gel [9] chemical vapor deposition [10], plasma evaporation [11] and electrodeposition [12].

Among these techniques, spray pyrolysis is a very attractive and versatile technique; it has been largely used to produce adherent, homogenous and stoichiometric films. The main goal of the present work is to produce CuO thin films with good optoelectronic properties by optimizing the substrate temperature while keeping constant the others operating parameters.

2 Experimental

Copper oxide thin films have been prepared on glass substrates by ultrasonic spray pyrolysis. The precursor solution was prepared by dissolving 0.05 M copper chloride (CuCl₂·2H₂O) in distilled water. Then, the precursor solution sprayed in fine droplets of 40 μm in diameter, by an ultrasonic generator on heated glass substrate. Films were formed by pyrolytic reaction. During deposition, the substrate temperature is kept at 280, 300, 350, 400 °C for four different runs. The deposition time for each run is 20 min.

The films crystalline phases are analyzed by micro-Raman measurements performed at room temperature using the 514.5 nm line of an argon ion laser as the excitation source (Renishaw). The UV-Visible transmittance of the films is performed by Shimadzu UV-3101 PC spectrophotometer within the wavelength range of 200-1800 nm. The values of films thickness and refractive index were derived from optical transmission measurement. The electrical characterization of the films was carried out using the electrical D.C transport to measure the conductivity in dark and at room temperature.

3 Results and discussion

3.1 The deposition rate and the refractive index

In Figure.1 we have reported the variation of deposition rate and the refractive index of CuO thin films as a function of substrate temperatures. The deposition rate is estimated from the ratio of the layer thickness on the deposition time, fixed at 20 minutes. As can be seen the deposition rate decreases with increasing of substrate temperature, it is maximal

($V_d=275.15\text{nm/min}$) at substrate temperature equal to 280° and minimal ($V_d=216.32\text{nm/min}$) for the sample prepared at 400°C . The reduction of deposition rate can be explained by the phenomenon of densification. The rise in substrate temperatures yields to an increase in the formation energy of the material by the pyrolytic reaction on the surface, which influence on the growth kinetics and produces denser film. This result is in good agreement with the increase of the refractive index from 1,53 to 1,65 which is a clear indication of films densification.

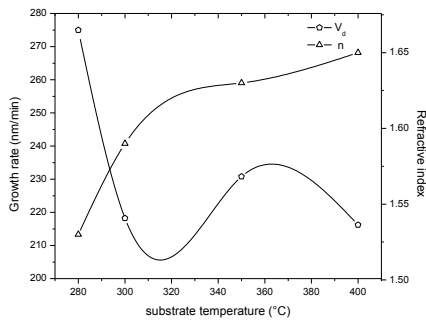


Figure 1: Variation of deposition rate and refractive index as a function of substrate temperatures

3.2. Structural properties

Figure.2 shows the Raman spectra of the as-prepared CuO thin films with diverse substrate temperatures. The Raman spectra are composed with three main phonon modes (Ag and 2Bg) located at 297 , 334 and 608 cm^{-1} which are assigned to a single phase CuO with a monoclinic structure. These peaks are largely reported in the literature [13-15]. No other secondary phase modes are present as Cu_2O [16].

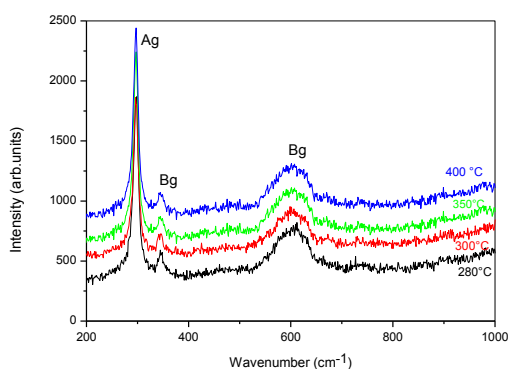


Figure 2: Micro Raman spectra of CuO deposited with various substrate temperatures.

3.3 Optical properties

The transmittance spectra in UV-Visible region of CuO films prepared with different substrate temperatures are shown in figure.3. The

measurements were performed in the UV-visible, corresponding to the wavelength range: $200 - 1800\text{ nm}$. It was determined that all films behaved as transparent materials in the $800-1100\text{ nm}$ wavelength range located in infrared field. On the other hand, in the visible region films transmittance values decreases sharply in the wavelengths range less than 800 nm due to their highly absorbing properties. This wavelength range represents the material fundamental absorption region. Films optical band gap have been estimated, as show in Fig.4 from the plot $(\alpha h\nu)^2$ as a function of photon energy ($h\nu$), according to Tauc formula for direct band gap semiconductors [17]:

$$(\alpha h\nu)^2 = B (E_g - h\nu)$$

Where α is a absorption coefficient, B is a constant, h is Planck constant, E_g is the energy band gap and ν is incident photon frequency.

The obtained optical gaps increase with substrate temperature increasing from 1.44 eV to 1.76 eV

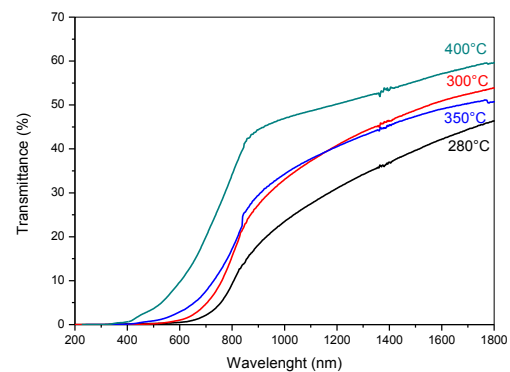


Figure 3: UV-Visible transmittance spectrum of CuO thin films deposited spectra at different substrate temperatures.

which is in good agreement with CuO band gap values reported by Gopalakrishna et al. [18]. They found optical band gap values laying between 1.8 eV and 1.2 eV for substrate temperature ranged from 250 to 400°C . However, film prepared at 280°C have an optical band gap close to 1.44 eV , this value is required for solar cells since it matches well with solar spectrum.

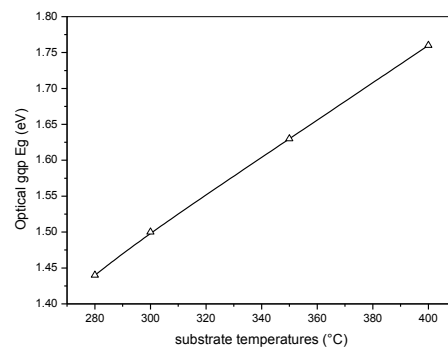


Figure 4: Variation of optical band gap of CuO films with substrate temperature

3.4. The electrical properties

The electrical conductivity variation, measured in the dark and at room temperature, with different deposition temperatures is shown in Figure.5. From this figure we observe that the conductivity increases from 7.11×10^{-8} to 1.03×10^{-6} ($\Omega \cdot \text{cm}$)⁻¹ for substrate deposition temperature increase from 280°C to 350 ° C, while at 400 °C the conductivity decreases by one order of magnitude.

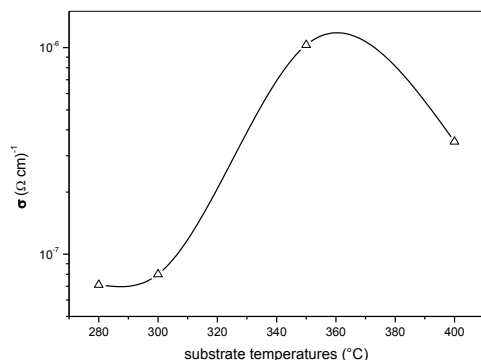


Figure 5: Variation of the conductivity versus the substrate temperatures.

4. Conclusion

CuO thin layers were deposited by ultrasonic spray on glass substrates. The influences of the substrate temperature on structural, optical and electrical properties were studied. The films prepared at different temperatures showed the presence of a single phase CuO with a monoclinic structure. The optical characterization showed a strong absorbance in the visible range with values of optical gap varied from 1.44 to 1.76 eV. All the deposited films exhibit p-type conductivity with a relatively high conductivity. Film deposited at 350°C seems to have suitable optical and electrical properties for efficient thin film solar cell fabrication.

References:

- [1] M. Yin, C.-K.Wu, Y. Lou, C. Burda, J.T. Koberstein, Y. Zhu, S. O'Brien, J. Am. Chem. Soc. 127 (2005) 9506.
- [2] M.K. Wu, J.R. Ashburn, C.J. Torng, P.H. Hor, R.L. Meng, L. Gao, Z.J. Huang, Y.Q. Wang, and C.W. Chu, Phys. Rev. Lett. 58 (1987) 908.
- [3] S. C. Ray, Sol Energy Mater Sol Cells, 68, 307 (2001)
- [4] X.G. Zheng, C.N. Xu, Y. Tomokiyo, E. Tanaka, H. Yamada and Y. Soejima, "Observation of Charge Stripes in Cupric Oxide", Phys. Rev. Lett. 85, 5170 (2000).
- [5] X.P. Gao, J.L. Bao, G.L. Pan, H.Y. Zhu, P.X. Huang, F. Wu, D.Y. Song, J. Phys. Chem. B 108 (2004) 5547-5551.
- [6] R.V. Kumar, Y. Diamant, A. Gedanken, Chem. Mater. 12 (2000) 2301-2305.
- [7] A. Chowdhuri, V. Gupta, K. Sreenivas, R. Kumar, S. Mozumdar, P.K. Patanjali, Appl. Phys. Lett. 84 (2004) 1180-1182.
- [8] K. Han, M. Tao, Sol. Energy Mater. Sol. Cells 93 (2009) 153.
- [9] A. Y. Oral, E. Mensur, M. H. Aslan, E. Basaran, Mater Chem Phys, 83(1), 140 (2004).
- [10] T. Maruyama, Jpn. J. Appl. Phys. 37(1998) 4099-4102.
- [11] K. Santra, C. K. Sarker, M. K. Mukherjee, B. Ghosh, Thin Solid Films, 213, 226 (1992).
- [12] E.R. Kari, K.S. Brown, Choi, Chem. Commun. (2006) 3311-3313.
- [13] D.P. Volanti, D. Keyson, L.S. Cavalcante, A.Z. Simões, M.R. Joya, E. Longo, J.A. Varela P.S. Pizani and A.G. Souza, J. of Allo. and Comps. 459 (2008) 537
- [14] H. Fan, B. Zou, Y. Liu, S. Xie, Nanotechnology 17 (2006) 1099.
- [15] T. Yu, C.-H. Sow, A. Gantimahapatruni, F.-C. Cheong, Y. Zhu, K.-C. Chin, X. Xu, C.-T. Lim, Z. Shen, J.T.-L. Thong, A.T.-S. Wee, Nanotechnology 16 (2005) 1238.
- [16] K. Reimann, K. Syassen, Phys. Rev. B 39 (1989) 11113.
- [17] J.J. Tauc, Amorphous and Liquid Semiconductors, Plenum, London, 1974.
- [18] D. Gopalakrishna, K. Vijayalakshmi, C. Ravidhas, J Mater Sci: Mater Electron DOI 10.1007/s10854-012-0866-7 (2012).

Two-dimensional Modelling and Simulation of CIGS thin-film solar cell

S. Tobbeche^{1*} and H. Amar¹

¹Laboratoire des matériaux semi-conducteurs et métalliques, Faculté des Sciences et de la Technologie,
Département de Génie-Electrique, Université de Biskra, B.P 145, Biskra 07000, Algérie.

Received: 30 April 2014, accepted 26 May 2014

Abstract: 2 D Silvaco Atlas software is used for the study of a CIGS thin film solar cell in the configuration: ZnO(200 nm)/n-type CdS(50 nm)/ p-type CIGS(350 nm)/Mo. The cell performance is evaluated by implementing the defects created at the grain boundaries of the polycrystalline CdS and CIGS material and at the interface CdS/CIGS. The J-V characteristics and the external quantum efficiency EQE are simulated under AM 1.5 illumination. The conversion efficiency η of 20.35% is reached and the other characteristic parameters are simulated: the short circuit current density J_{sc} equals 35.62 mA/cm², the open circuit voltage V_{oc} is of 0.69 V and the fill factor FF is of 82.7 %. The calculated external parameters of the solar cell are in good agreement with the measured characteristics. The simulation results also showed that the rise of the CdS thickness decreases all output parameters and the external quantum efficiency while the rise of the CIGS thickness improves all photovoltaic parameters and the external quantum efficiency. The highest efficiency of 21.08 % is reached for the CIGS thickness of 5 μ m.

Keywords: Computer modelling - Silvaco Atlas - CIGS solar cell - solar cell parameters.

1. Introduction

Thin film solar cells have the potential for low-cost and large-scale terrestrial photovoltaic applications. A number of semiconductor materials including polycrystalline CdTe, CIGS and amorphous silicon (a-Si) materials have been developed for thin-film photovoltaic solar cells. The CIGS based solar cells exhibit an excellent outdoor stability and irradiation hardness [1, 2]. They are attracting considerable interest for space applications, because proton and electron irradiation tests of CIGS and CdTe solar cells have proven that their stability against particle irradiation is superior to Si or III-V solar cells [3]. CIGS is an excellent material for high efficiency thin-film solar cells because it is a suitable energy band gap semiconductor with a high optical absorption coefficient in the visible spectrum of incident sunlight. The absorption coefficient of CIGS films in the visible spectrum is 100 times larger than silicon material. The best performance of CIGS is due to its tunable bandgap to match well the solar spectrum. When alloying the CuInSe₂ (CIS) with Ga to form CIGS thin films, the wider band-gap energy of the CIGS absorber layer can potentially better match the solar spectrum, as well as increase the open circuit voltage of the fabricated cells. The maximum efficiency for the best CIGS cell grown on stainless steel substrates is 17.5 % under AM1.5G illumination [4]. The device structure consists of MgF₂/ITO/ZnO/CdS/CIGS/Mo/stainless steel substrates. The CIGS cell with a Ga composition $x=0.3$ which corresponds to a bandgap energy range of 1.1-1.2 eV fabricated on sodalime glass substrates has an efficiency of 20% [5] AM1.5G, as reported by the NREL (National Renewable Energy Laboratory) research team. In recent years, progress has showed that the best thin-film CIGS solar cells by using thin film CIGS of thickness between 2.5 and 3 μ m, and a band gap in the range 1.2 to 1.3 eV

have surpassed the 20% efficiency barrier for CIGS solar cells and have reached a new world record efficiency of 20.3% [6]. It was established numerically [7], by using AMPS-ID simulation tool that the maximum efficiency obtained numerically for a simple CdS/CIGS solar cell was 19 %. An increase in efficiency is expected mainly using denominated tandem, triple, and multi-junction solar cells, consisting of layers with different band gaps in order to exploit different energy regions of the solar spectrum.

The numerical simulation is a powerful tool and many parameters can be varied to model the observed phenomenon. It can also offer a physical explanation of the observed phenomenon since internal parameters such as the recombination rate and the free carrier densities can be calculated. In this work we have used Silvaco Atlas software on the design and the study of a CIGS solar cell. It makes it possible to design and predict the performance of semiconductor-based devices and solar cells. This work contributes to obtain a better understanding and insight in CIGS solar cells. In this study, we have investigated the thickness effect of the absorber layer CIGS and the buffer layer CdS on the photovoltaic parameters of the solar cell.

2. CIGS solar cell structure

A solar cell structure used in an experimental work [6] was simulated. The cell setup was described as follows: soda-lime glass (3 mm), sputtered molybdenum (500-900 nm), CIGS (2.5-3.0 μ m), chemical bath deposited CdS buffer layer (40-50 nm), sputtered undoped ZnO (50-100 nm), sputtered aluminium doped ZnO (150-200 nm) and nickel/aluminium-grid. CIGS solar cells with an efficiency of 20.3 % were produced with varying composition (Ga/(Ga+In)) from 0.30 to 0.35. Our simulated solar cell structure is formed by a p-type doped CIGS absorber and an n-type doped CdS buffer. A transparent contact of ZnO layer is deposited on the top of the structure to achieve a low series resistance. The solar cell structure is completed

by molybdenium rear metallization contact. The Ga composition is about 0.30, corresponding to a band gap energy of 1.15 eV [7, 8]. Baseline case parameters are shown in Table 1.

3. Physical models and input parameters

Most numerical simulators use the Shockley-Read-Hall (SRH) model to describe carrier recombination currents. We considered two Gaussian deep acceptor (donor) defect distributions for the CdS(CIGS) layer. The position of the recombinative defect states is in a narrow distribution close to the middle of the band gap. A surface recombination at the CdS-CIGS interface which effectively recombines minority carriers that reaches the interface. Absorption coefficients of ZnO, polycrystalline CdS and CIGS are defined in Silvaco database.

We modeled CIGS solar cell with the parameters defined in Table 1. The purpose was to see if it is possible to obtain a reasonable simulation which could be compared with experimental results and other simulation calculations.

Table 1. The solar cell parameters used in the simulation

Parameter and units e, h for electrons and holes, respectively	CdS	CIGS
Thickness (nm)	50	350
Permittivity	10	13.6
Electron affinity (eV)	4.5	4.8
Band gap (eV)	2.4	1.15
Effective conduction band density (cm^{-3})	10^{19}	10^{19}
Effective valence band density (cm^{-3})	10^{19}	10^{19}
Electron mobility ($\text{cm}^2 \text{V}^{-1} \text{s}^{-1}$)	140	140
Hole mobility ($\text{cm}^2 \text{V}^{-1} \text{s}^{-1}$)	25	25
Acceptor concentration (cm^{-3})	0	10^{16}
Donor concentration (cm^{-3})	10^{17}	0
Gaussian density of states (cm^{-3})	10^{15}	10^{15}
Distribution width (eV)	0.1	0.1
Capture cross-section for e (cm^2)	10^{-17}	5×10^{-13}
Capture cross-section for h (cm^2)	10^{-13}	10^{-15}
Recombination velocity at CdS/CIGS interface for e (cm/s)	10^5	10^5
Recombination velocity at CdS/CIGS interface for h (cm/s)	10^5	10^5

4. Simulation results and discussion

Fig. 1 shows the variation curve of the current density J with the applied voltage V , the solar cell's top surface is subjected to AM 1.5 with a power density of 100 mW/cm^2 .

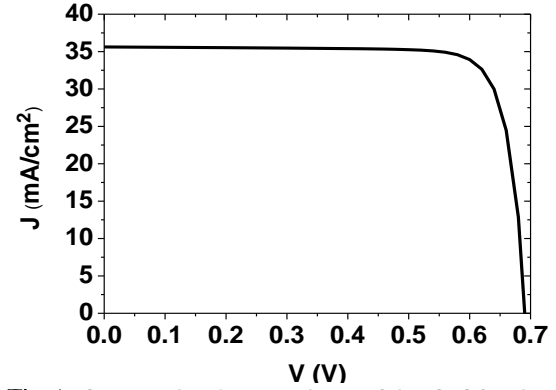


Fig. 1 Current density vs. voltage of the CIGS solar cell.

The photovoltaic parameters of the solar cell obtained by simulation and experiment [6] such as J_s , V_{oc} , FF and η are illustrated in Table 2. These simulation results are in good agreement with those measured. The efficiency is equal to the high record efficiency 20.3% observed experimentally.

Table 2. Simulation and experiment parameters of CIGS solar cell

	J_s (mA/cm^2)	V_{oc} (V)	FF (%)	η (%)
Simulation	35.62	0.69	82.7	20.35
Experiment	35.4	0.74	77.5	20.3

The external quantum efficiency spectrum is illustrated in Fig. 2. This shows a peak response of nearly 86% and falls off in the range below $0.6 \mu\text{m}$ due to the absorption and recombination in the CdS layer.

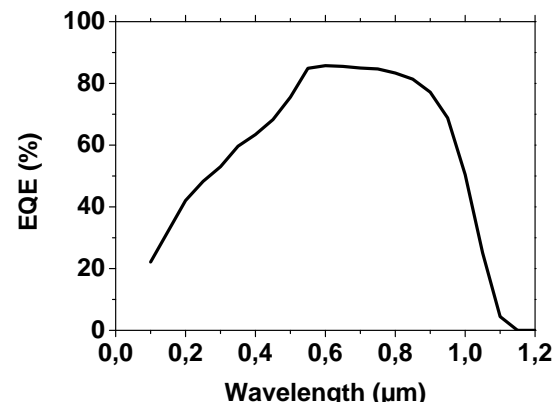


Fig. 2. The external quantum efficiency of the CIGS cell.

4.1. Impact of thickness of the CdS layer

In the simulation, the CdS layer thickness was varied from 10 nm to 100 nm while the CIGS layer thickness remained constant (350nm). Fig.3.(a) shows the effect on

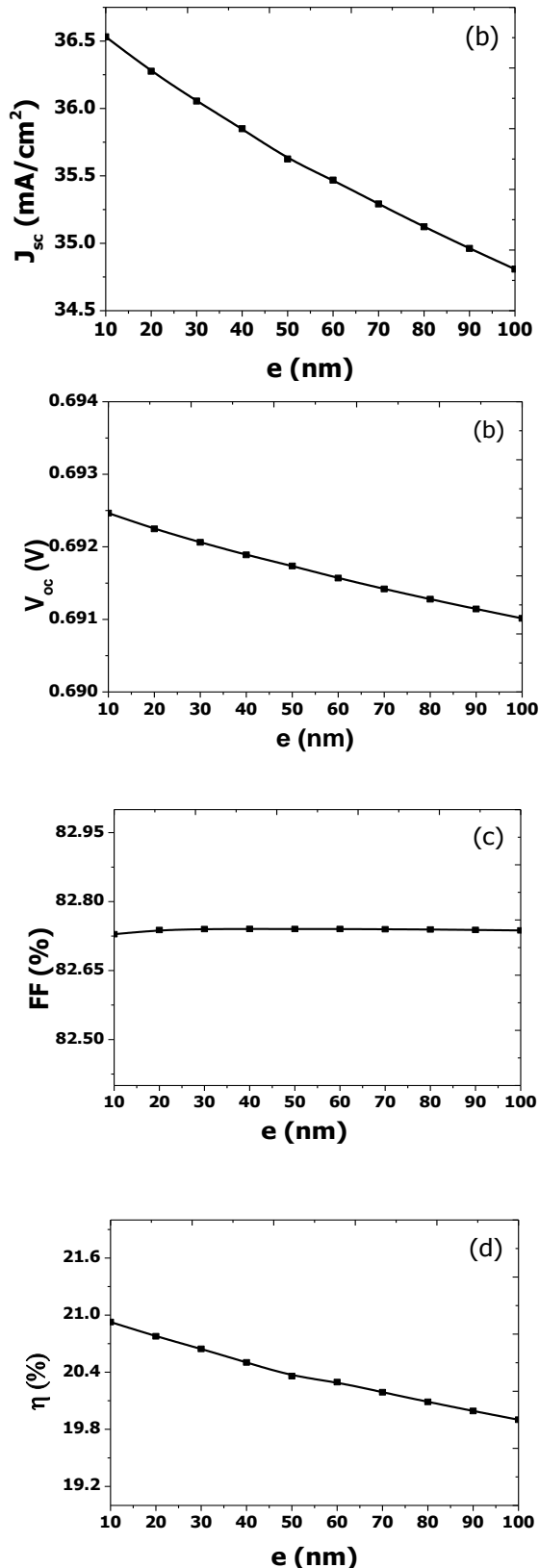


Fig.3. Relationship between CIGS solar cell parameters and CdS layer thickness

the short circuit current, this latter decreases with the increase of the thickness. In fig.3.(b) we displayed the influence on the open circuit voltage, it is clear that the thickness does not have much effect on V_{oc} . In fig.3. (c), the fill factor is nearly constant with the increase of the CdS thickness. It can be seen in fig.3.(d) that the efficiency decreases with the increase the CdS thickness. This is obviously due to the fact that with a thinner CdS layer, most of the photogenerated carriers are collected. When the thickness increases, the photons of short wavelengths are absorbed at a further distance of the CdS/CIGS junction. Though the CdS layer is characterized by defect states which act as recombination centres reduce the lifetime of the minority carriers (holes) and consequently the photogenerated carriers recombine before reaching the junction. Therefore, there's a drop of the short circuit current, the open circuit voltage and the efficiency with the increase of the CdS thickness. These observations are fairly in agreement with simulation in [9]. Generally the thickness of the optimum CdS buffer layer should be within 50 nm and 60 nm [10].

The effect of the CdS layer thickness on the external quantum efficiency spectrum is illustrated in fig. 4. As mentioned earlier, when the thickness increases, more photons with shorter wavelength can be lost in the CdS layer. As expected, the higher the CdS thickness, the lower the external quantum efficiency. The external quantum efficiency for a thicker CdS layer is much lower for wavelengths below 0.6 μm .

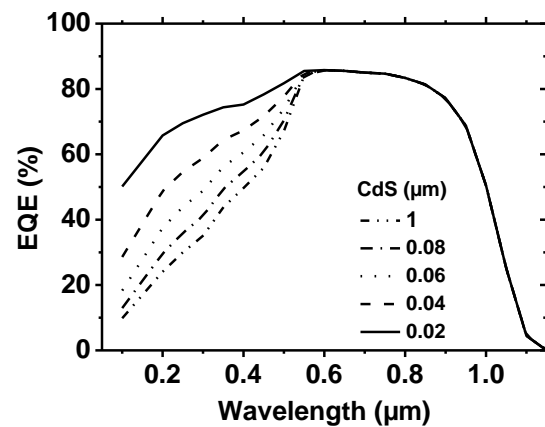


Fig.4. The external quantum efficiency for different thicknesses of CdS layer.

4.2. Impact of thickness of the CIGS layer

The photovoltaic parameters in terms of J_{sc} , V_{oc} , FF and η were simulated for the CIGS thicknesses varying from 0.5 μm to 5 μm and the CdS thickness is constant (50 nm) (fig.5). We observe an increase of these parameters with the CIGS layer thickness. For the thickness equal to 0.5 μm , the efficiency is 13.64%. The highest efficiency of 21.08% is reached for the thickness of 5 μm . The increase in the conversion efficiency is mainly due to the increase of the CIGS thickness. A possible explanation is that more the thickness increases, more photons with longer wavelengths can be collected in the CIGS layer. Therefore,

this will contribute to more generation of electron-hole pairs which

will increase the short circuit current, the open circuit voltage and the efficiency. A very thin CIGS layer means physically that the backcontact and the depletion region are very close. This effect more promotes the electron recombination at the back contact. This type of recombination is detrimental to the cell performance because it affects J_{sc} , V_{oc} and η . These observations are in good agreement with simulation in [9, 11]. The external quantum efficiency also increases as the thickness of the CIGS layer increases (fig. 6). As mentioned previously when the thickness increases, more photons are absorbed, especially the long wavelengths of the illumination. Thus a greater number of electron-hole pairs would be produced from the absorbed photons. Therefore and as illustrated, the higher the CIGS thickness, the higher the external quantum efficiency for wavelengths above $0.55\mu m$.

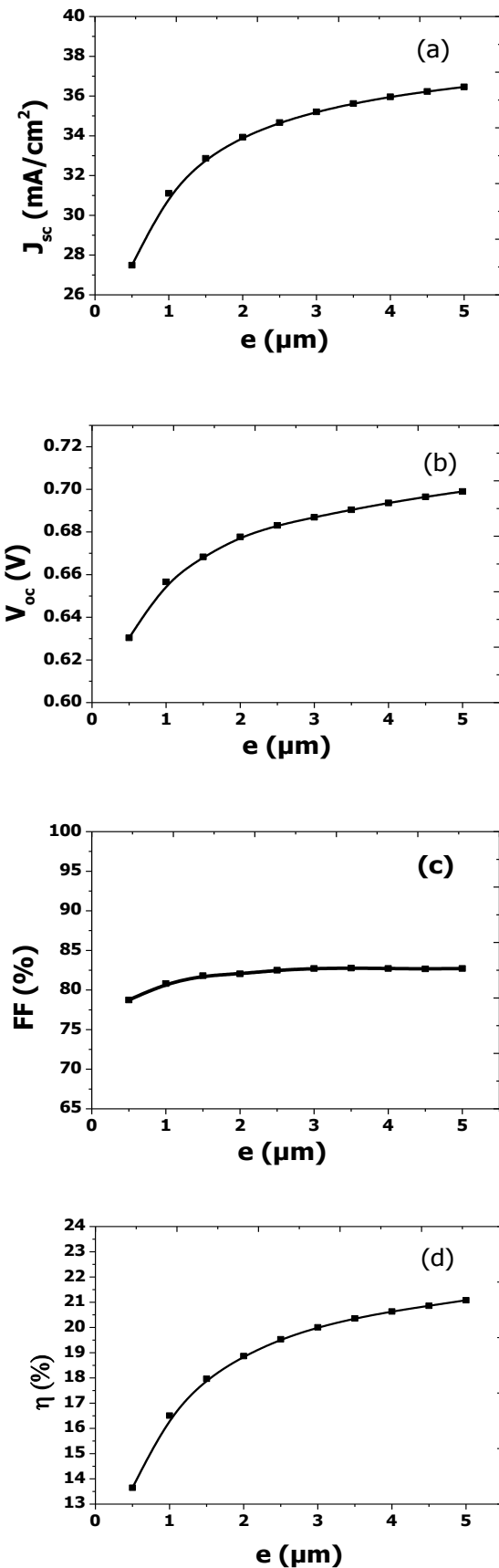


Fig.5. Relationship between CIGS solar cell parameters and CIGS layer thickness.

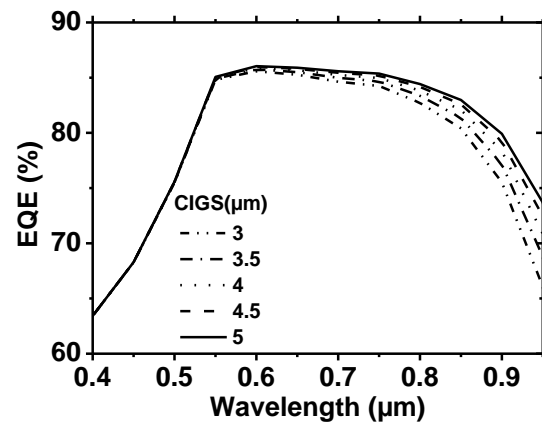


Fig.6. The external quantum efficiency for different thicknesses of CIGS layer.

5. Conclusion

Silvaco Atlas software was used in the simulation of the CIGS solar cell operating under AM1.5. It was shown that the numerical simulation is an important tool for understanding and achieving high efficiency CIGS solar cells. The numerical calculations provide not only a good understanding but they also allow us to predict ways to improve the efficiency. The simulation of the CIGS solar cell gives an efficiency of 20.35 % in good agreement with the experimental high record efficiency of 20.3 % in the CIGS solar cell [6]. The effect of the CdS and CIGS thicknesses on the photovoltaic parameters and the external quantum efficiency were studied. It was found that the rise of the CdS thickness decreases all output parameters and the external quantum efficiency while the rise of the CIGS thickness improves all photovoltaic parameters and the external quantum efficiency. The highest efficiency of 21.08 % is reached for the CIGS thickness of 5 μm .

References

[1] Ullal HS, Zweibel K, Von Roedern B, Proc. 26th IEEE Photovoltaic Specialists Conf., Anaheim, CA, USA; 1997, p. 301.

- [2] Yamaguchi M., J. Appl. Phys. **78** (1995)1476.
- [3] Bätzner DL, Romeo A, Terheggen M, Döbeli M, Zogg H, Tiwari AN, Thin Solid Films 451-452 (2004) 536-543.
- [4] Tuttle JR, Szalaj A, Keane J, Proceedings of the 28th IEEE Photovoltaic Specialists Conference, Anchorage, 2000; 1042-1045.
- [5] I.Repins, S. Glynn, J. Duenow, T.J. Coutts, W. Metzger, and M.A. Contreras, Conference Paper NREL/CP-520-46235, juin 2009.
- [6] P. Jackson, D. Hariskos, E. Lotter, S. Paetel, R. Wuerz, R. Menner, W. Wischmann and M. Powalla, Prog. Photovolt. Res.Appl.19(2011)894-897.
- [7] K. Ramanathan, M.A. Contreras, C.L. Perkins, S. Asher, S.F. Hasoon, J. Keane, D. Young, M. Romero, W. Metzger, R. Noufi, J. Ward, A. Duda, Prog. Photovolt: Res. Appl 11 (2003) 225.
- [8] M.A. Contreras, B. Egaas, K. Ramanathan, J. Hiltner, A. Swartzlander, F. Hasoon, R. Noufi, Prog. Photovolt: Res. Appl 7 (1999) 311.
- [9] Puvaneswaran Chelvanathan, Mohammad Istiaque Hossain, Nowshad Amin, Current Applied Physics 10 (2010) S387-S391.
- [10] Yamamoto, Y. Saito, K. Takahashi, M. Konagai, Sol. Energy Mater. Sol. Cells 65 (2001)125-132.
- [11] Nowshad Amin, Puvaneswaran Chelvanathan, M. Istiaque Hossain and Kamaruzzaman Sopian, Energy Procedia 15 (2012) 291 - 298.

Effect of solvents on the properties of ZnO thin layers obtained by sol gel dip coating process

Chahra Boukaous^{a,b}, Azzedine Telia^a, David Horwat^c, Salah Ghanem^a and Patrice Miska^c

^a *Laboratoire Microsystème et Instrumentation, Département d'électronique, Université de Constantine1, route d'Ain El Bey 25000 Constantine, Algérie.*

^b *Laboratoire Microstructure et Défauts dans les Matériaux, Département de physique, Université de Constantine1, route d'Ain El Bey 25000 Constantine, Algérie.*

^c *Université de Lorraine, Institut Jean Lamour, Département CP2S, UMR CNRS 7198, Parc de Saurupt, Nancy F-54011, France*

Received: 30 April 2014, accepted 26 May 2014

Abstract

Undoped Zinc Oxide (ZnO) thin films have been grown on glass substrates by sol gel process associated with dip coating using two different solvents, ethanol and 2-methoxyethanol. The effects of these solvents on structural and optical properties of ZnO thin films have been studied. Crystallinity and surface morphology of the ZnO films were analyzed using X-ray diffractometry (XRD), Raman microscopy and atomic force microscopy (AFM). The optical properties were determined by means of photoluminescence spectroscopy (PL) and Fourier transform infrared spectroscopy (FTIR). The experimental results revealed a better crystalline quality and ultraviolet emission performance and a higher surface roughness for ZnO thin films prepared with 2-methoxyethanol.

Keywords: ZnO thin films; Sol-gel; FTIR; Photoluminescence; Raman; Spectroscopy, XRD.

1. Introduction

Zinc oxide (ZnO) is an oxidic compound naturally occurring as the rare mineral zincite, which crystallizes in the hexagonal wurtzite structure $Pb\bar{3}mc$ [1]. ZnO is n-type semiconductor material with a wide band gap of 3.3 eV and a large exciton binding energy of 60 meV [2], in addition it has specific properties such as low costs, non toxicity, high transparency in VIS/near IR spectral region [3]. These numbers of properties give ZnO increasing attention in the research community such as varistors, light-emitting diodes (LEDs), optoelectronic devices and conductive gas sensors [4-7]. Many techniques have been used to synthesize ZnO thin films, such as pulsed laser deposition, atomic layer deposition, RF magnetron sputtering, chemical vapor deposition, plasma-assisted molecular beam epitaxy (MBE) and sol-gel process [7-13]. Among them, the sol-gel technique offers the possibility of preparing a small at low cost for technological applications. The usual starting materials

of the sol-gel process are metal alkoxides that are hydrolyzed to form a sol, solvents such as 2-methoxyethanol, ethanol and isopropanol, stabilizers can also be added like monoethanolamine (MEA), diethanolamine (DEA) and triethanolamine (TEA). It is also well known that the properties of ZnO films deposited by sol-gel technique change depending on the nature of the starting materials mentioned previously. However, few studies have been devoted to the study of the influence of solvent upon films properties [14-15].

In this work, ZnO films grown on glass substrates using sol-gel method were fabricated and the effects of solvent on the structural and optical properties of the films were intensively investigated.

2. Experimental procedure

In order to deposit undoped ZnO thin films on glass substrates using sol-gel process, the precursor solutions were prepared from zinc acetate dehydrate

(Zn(CH₃COO)₂·2H₂O), solvent (2-methoxyethanol (C₃H₈O₂, 99.5%) or ethanol) and stabilizer (Diethanolamine (DEA)). The sols were prepared by dissolving of zinc acetate dehydrate in 2-methoxyethanol or absolute ethanol, in which DEA was subsequently added to obtain a transparent solution and to keep the solution stable for dip-coating process. The molar ratio of DEA to zinc acetate was 1.0 and the zinc acetate concentration was 0.7M. Then the resultant solution was magnetic stirred at 60°C for 2h until it become clear and homogeneous to serve as the coating solution after aging for more than 24 hours at room temperature. Undoped ZnO thin films were deposited on pre-cleaned glass substrates using the dip-coating technique at a speed of 3cm/min. These substrates were cleaned ultrasonically initially by ethanol then by acetone and finally with de-ionized water. Between each deposition process, the substrates were dried at 300°C in the case of 2-methoxyethanol and 60°C in the case of ethanol for 10 minutes in air. This process was repeated eight times to obtain the desired thickness. Finally, the samples were annealed at 500°C in air for 2 hours.

The crystalline structures of the samples were analyzed by an X-ray diffractometer (XRD, Bruker D8 Advance) with Cu K α radiation. During the measurement, the current and voltage of XRD was maintained at 20 mA and 40 kV, respectively. The surface morphology was evaluated by Atomic Force Microscopy (Pacific Nanotechnology Advancing Nanotechnology). Raman spectra of the samples were recorded on a Bruker Raman spectrometer using a 523 nm wavelength YAG laser.

The optical properties of the deposited films were investigated using FTIR and photoluminescence. FTIR measurements were performed in the spectral region 400-4000 cm⁻¹ using a Fourier transform infrared spectrometer Jasco (FT/IR-6300). PL spectra were collected in the wavelength region of 300-850 nm. The samples were excited by Hg arc lamp using 315 nm as the excitation source.

3. Results and discussion

3.1. XRD (X-ray diffraction)

The crystallinity of sol-gel derived ZnO thin films were identified by X-ray diffraction. Fig.1 shows the XRD patterns of ZnO thin films prepared by different solvents (2-methoxyethanol and ethanol). These patterns correspond to three diffraction peaks of polycrystalline ZnO at (100), (002) and (101) planes. The result reveals that ZnO gel films annealed at 500°C have a hexagonal wurtzite structure. The intensity of the (002) peak is higher than others peaks, so the predominant orientation is (002) in the two cases.

Table1 summarizes the intensities of different peaks for ethanol and 2methoxyethanol.

The average crystallite size D is obtained using the Debye-Scherrer formula [16]

$$D = \frac{0.94\lambda}{\beta \cos\theta}$$

Where: $\lambda = 0.15406$ nm is the wavelength of X-ray, β is the full width at half maximum (FWHM) of the peak and θ is the Bragg's angle. The crystallite sizes corresponding to preferred orientation of crystalline thin films are reported in table1.

We remark that the crystallite size value in the case of the ZnO films prepared with ethanol is smaller than those prepared with 2-methoxyethanol.

Solvent	(hkl)	2 θ (degree)	Intensity (a.u.)	FWHM (degree)	Crystallite size (nm)
2 Methoxy- ethanol	(002)	34.72	90.12	0.26	33.1
Ethanol	(002)	34.78	42.72	0.37	22.9

Table1. hkl, 2 θ , intensity, FWHM and crystallite size values for the ZnO thin films

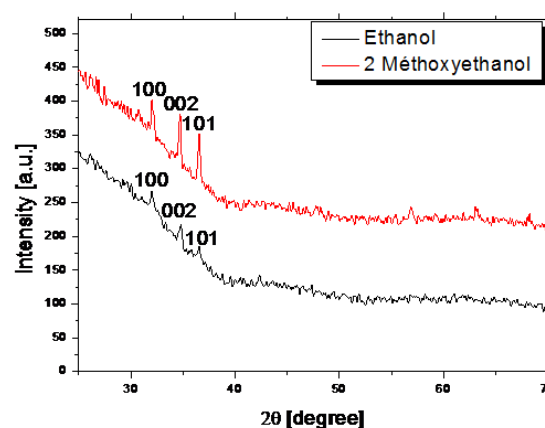


Fig.1. XRD patterns of ZnO thin films annealed at 500°C for 2h

3.2. AFM (Atomic Force Microscopy)

Fig.2 shows the three dimensional surface morphology images of ZnO thin films prepared from different solvents. The scanning area is 0.78×0.78 μ m². We can remark for these images that we have obtained a fine grains in the two cases, whereas the surface is roughness in the case of 2-methoxyethanol. The root mean square (RMS) roughness is 7.86 nm and 2.17 nm in the case of 2 methoxyethanol and ethanol, respectively.

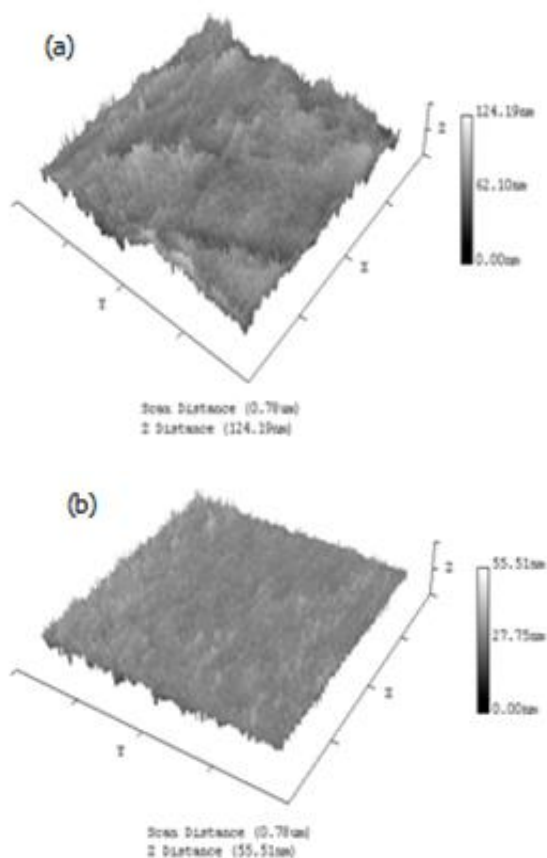


Fig.2. AFM images of ZnO thin films prepared with: (a) 2-Methoxyethanol (b) Ethanol

3.3. Raman spectroscopy

Fig.3 shows the Raman spectrum of undoped ZnO thin films, Wurtzite-type ZnO belongs to the space group $P63mc$, the zone center optical phonons can be classified according to the following irreducible representation: $\Gamma_{opt}=A_1+E_1+2E_2+2B_1$, where B_1 modes are silent, A_1 and E_1 are polar modes, both Raman and infrared active, while E_2 modes (E_2 low and E_2 high) are non polar and Raman active only.

In the two cases we have observed the first peak located around 99 cm^{-1} , it is related to the E_2 (low) phonon frequency of the ZnO wurtzite structure [17-18]. The second one is the LO mode at 560 cm^{-1} , which is contributions from both the A_1 (LO) and E_1 (LO) modes (LO scattering mode) due to random crystallite orientation [19]. Whereas another vibration band is observed in the case of 2-methoxyethanol located at 438 cm^{-1} correspond to E_2 (high) mode is predominately associated with vibrations of oxygen sublattice, is typical for ZnO hexagonal structure [20]. The presence of this mode indicate the crystallinity of the thin films prepared

with 2-methoxyethanol is better, which confirm the results observed by XRD analysis [21].

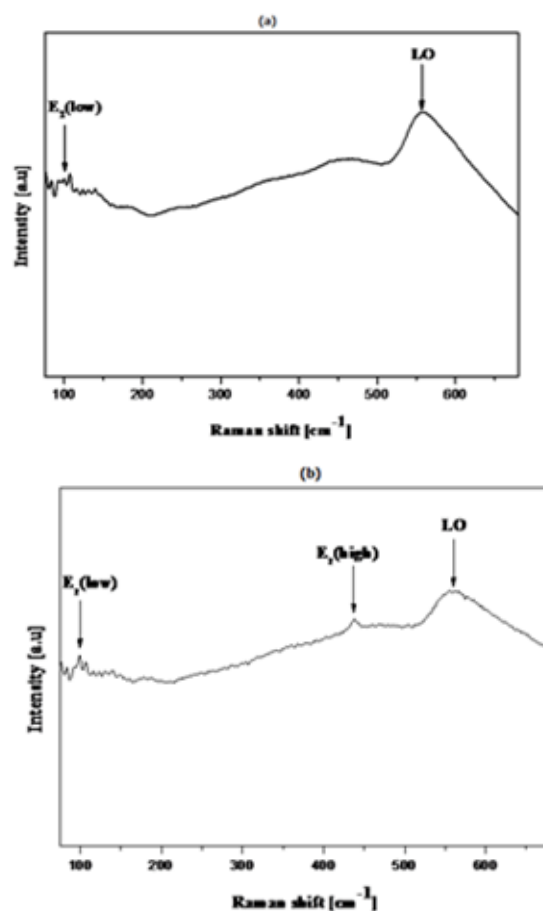


Fig.3. Raman spectrum of undoped ZnO thin film prepared with: (a) Ethanol (b) 2-Methoxyethanol

3.4. FTIR (Fourier transform infrared spectroscopy)

The FTIR analysis of ZnO thin films synthesized with different solvents are shown in Fig.4.

The FTIR spectrum for the undoped ZnO thin films shows no characteristic functional groups in the low frequency region except a weak absorption around 2350 cm^{-1} [22-23]. This weak absorption is probably due to an existence of CO_2 molecules in air. Another strong peak is observed at 890 cm^{-1} is observed, this peak is resulting from C-O vibrations [23]. The feature appearing between 520 and 770 cm^{-1} , which comprises of several peaks, are attributed to the stretching modes of Zn-O [23-25]. In the two cases, we have obtained the same peaks but there is a slight shift due to the change in the morphology of these films

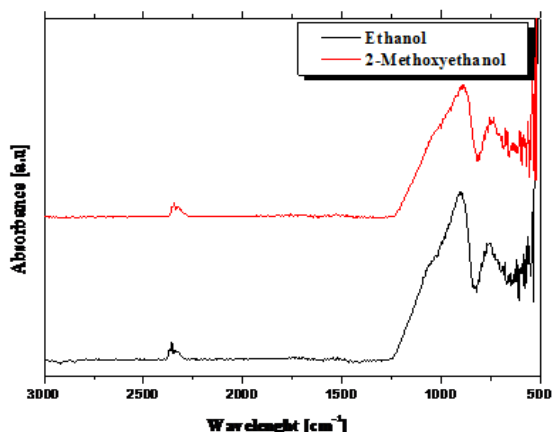


Fig.4. FTIR spectra of ZnO thin films annealed at 500°C for 2h

3.5. PL (Photoluminescence spectroscopy)

Photoluminescence is a powerful tool to identify surface, interface, and impurity levels and to evaluate alloy disorder and interface roughness. The intensity of the photoluminescence signal provides information on the quality of surfaces and interfaces by the determination of optical active defects and relaxation pathways of excited states [26-27]. The luminescence spectrum of ZnO thin films prepared by sol-gel method is shown in Fig.5. The PL spectra in all samples exhibit two emission peaks, an intense near band-edge (NBE) emission located at 380 nm, due to free exciton emission, and a broad band one around to 530 nm related to the green emission. The origin of the green luminescence is usually attributed to emission related to grain boundary defects and other interior defects such as oxygen vacancy (VO) and impurities [28]. The intensities of these peaks are higher in case of 2-methoxyethanol than those in case of ethanol, giving good ZnO quality with 2-methoxyethanol.

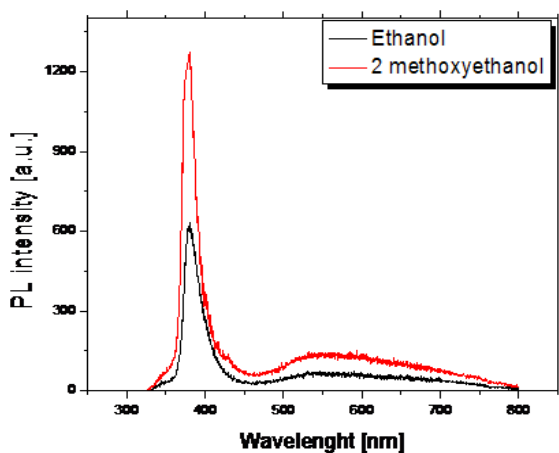


Fig.5. PL spectrum of ZnO thin films annealed at 500°C for 2h

4. Conclusion

Transparent and high quality undoped ZnO thin films were deposited on glass substrate using sol-gel dip coating method. We have carried a comparative study of structural and optical properties of ZnO thin films prepared from two different solvents. XRD spectra indicate that all films exhibit wurtzite hexagonal crystal structure with preferred orientation growth along (002) plane. AFM surface analysis revealed that films surface is smoother in sample deposited with ethanol as solvent than in that prepared with 2-methoxyethanol. The presence of E_2 (high) mode indicate the better crystallinity of thin films prepared with 2-methoxyethanol. Photoluminescence spectra of these films exhibit two peaks due to free exciton emission and to oxygen vacancies in ZnO.

References

- [1] G. Haacke, New figure of merit for transparent conductors, *Appl. Phys. Lett*, 47 (1976) 4086-4089.
- [2] C. Klingshirn, *Phys. Status Solidi*, B 71 (1975) 547.
- [3] E. Klaus, K. Andreas, R. Brend, *Transparent Conductive Zinc Oxide Springer Series in Material Science*, 104 (2008) 446.
- [4] T.R.N. Kutty, Raghu N, *Appl. Phys. Lett.* 54 (1989) 1796.
- [5] H. Kim, J.S. Horwitz, W.H. Kim, A.J. Mäkinen, Z.H. Kafafi, D.B. Chrisey, *Thin Solid Films*, 420/421 (2002) 539.
- [6] A.N. Gruzintsev, V.T. Volkov, E.E. Yakimov, *Semiconductors*, 37 (2003) 259.
- [7] S. Chunqiao Ge, C. Xie, S. Cai, *Materials Science and Engineering*, B 137 (2007), 53 E. Klaus, K. Andreas, R. Brend, *Transparent Conductive Zinc Oxide Springer Series in Material Science*, 104 (2008) 446.
- [8] S. Yata, Y. Nakashima, T. Kobayashi, *Thin Solid Films*, 445 (2003) 259
- [9] J. Ma, F. Ji, D.H. Zhang, H.L. Ma, S.Y. Li, *Thin Solid Films*, 357 (1999) 98-101.
- [10] Ko H D, Tai W P, Kim K C, Kim S H, Suh S J, Kim Y S, *J. Cryst. Growth* 277 (2005) 352-356.
- [11] J. Park, C. Lee, I. Kim, S. Jang, B. Lee, *Thin Solid Films* 517 (2009) 4432-4435.
- [12] M.S. Kim, T.H. Kim, D.Y. Kim, G.S. Kim, H.Y. Choi, M.Y. Cho, S.M. Jeon, J.S. Kim, D.-Y. Lee, J.-S. Son, J.I. Lee, J.H. Kim, E. Kim, D.-W. Hwang, J.-Y. Leem, *J. Cryst. Growth*, 311 (2009) 3568.
- [13] Y.S. Kim, W.P. Tai, S.J. Shu, *Thin Solid Films*, 491 (2005) 153.
- [14] C.-Y. Tsay, K.-S. Fan, Y.-W. Wang, C.-J. Chang, Y.-K. Tseng, C.-K. Lin, *Ceramics international*, 36 (2010) 1791.
- [15] M. Popa, R.A. Mereu, M. Filip, M. Gabor, T. Petrisor Jr, L. Ciontea, T. Petrisor, *Materials Letters*, 92 (2013) 267.
- [16] B.D. Cullity, S.R. Stock, *Element of X-ray Diffraction*, Prentice-Hall, Inc., New Jersey, 2001
- [17] Aurangzeb Khan, *J Pak Mater Soc*, 4(1) (2010).

- [18] H. Benelmadjat, N. Touka, B. Harieche, B. Boudine, O. Halimi, M. Sebais *Optical Materials*, 32 (2010) 764-767
- [19] C. Roy, S. Byrne, E. McGlynn, J.P. Mosnier, E. de Posada, D. O'Mahony, J.G. Lunney, M.O. Henry, B. Ryan, A.A. Cafolla, *Thin Solid Films*, 436 (2003) 273.
- [20] R. Jothilakshmi, V. Ramakrishnan, R. Thangavel, J. Kumar, A. Sarua, M. Kuball, J. Raman Spectrosc, 40 (2009) 556.
- [21] Z. Pan, P. Zhang, X. Tian, G. Cheng, Y. Xie, H. Zhang, X. Zeng, C. Xiao, G. Hu, Z. Wei, *Journal of Alloys and Compounds*, 576 (2013) 31-37.
- [22] M. Arshad, A. Azam, A.S. Ahmed, S. Mollah, A.H. Naqvi, *Journal of Alloys and Compounds*, 509 (2011) 8378.
- [23] Q. Shi, J. Zhang, D. Zhang, C. Wang, B. Yang, B. Zhang, W. Wang, *Materials Science and Engineering*, B 177 (2012) 689.
- [24] K. Balachandra Kumar and P. Raji, *Recent Research in Science and Technology*, 3(3) (2011) 48-52.
- [25] R N Gayen, K Sarkar, S Hussain, R Bhar and A K Pal, *Indian Journal of pure & Applied Physics*, 49 (July 2011) 470-477.
- [26] A.A.M. Farag, M. Cavas, F. Yakuphanoglu, F.M. Amanullah, *Journal of Alloys and Compounds*, 509 (2011) 7900
- [27] S. Mandal, M.L.N. Goswami, K. Das, A. Dhar, S.K. Ray, *Thin Solid Films*, 516 (2008) 8702.
- [28] S. Hwangbo, Y.-J. Lee, K.-S. Hwang, *Ceramics International*, 34 (2008) 1237.

Modeling and simulation of the structure based on the semiconductor III-V for solar cell application

A. Aissat^a, W. Bellil, R. Bestam, J.P. Vilcot^{a,b}

^aLaboratory LASICOM, Faculty of Sciences, University of Blida 1, Alegria

^bInstitut d'Electronique, de Microelectronique et de Nanotechnologie, UMR CNRS 8520,

Received: 30 April 2014, accepted 26 May 2014

Abstract

This work focuses on modeling and simulation of structure based semiconductors III-V for solar cell application. We first studied the influence of the concentration of indium on the various parameters of the alloy and GaInAsSb on GaAs substrate. Indeed, the increased density of indium decreases the bandgap energy of the alloy, which is very interesting to absorb maximum solar spectrum. We can obtain this structure by gap energy less than 1 eV. The study includes graphs showing the variations of the different factors affecting the conversion efficiency as a function of indium concentration and the thickness of the semiconductor layer. The most appropriate structure for this work is GaInAsSb because it has improved performance.

Keywords: strain quantum wells - GaInAsSb/GaAs ; semiconductor III-V ; solar cells

1. Introduction

The consequences of the use of fossil fuels require finding alternative sources of supply. Among the choices that meet the cost, durability and environmentally friendly, renewable energy appear to be a good compromise. They are inexhaustible energy provided by the sun, wind, falling water, the heat of the earth ... etc. Their exploitation does not generate polluting emissions. Among these energies of the future, solar photovoltaic that can convert sunlight directly into electricity occupies an important place in research, and is growing increasingly important since 1990. This research is focused on two main axis, which may seem opposite (increase cell efficiency, and reducing the cost of production) [1]. This development is mainly through the control of materials used in the design of components. Most of these materials are obtained by standard alloy on substrates. They could in principle cover a wide range of compositions and therefore application. This study is oriented towards the study and simulation of structures based on GaInAsSb / GaAs, for photovoltaic and improving the efficiency of this structure. The development of systems of photovoltaic conversion in the last thirty years has led to significant improvements in terms of cost and performance. To

date the best photovoltaic conversion efficiencies are obtained with solar concentration systems using multi cell junctions based semiconductors III-V materials. The world record in this area is currently owned by the Spire with a yield of 42.3% measured on a multi-junction type GaInP / GaAs / InGaAs bifacial and a concentration factor of solar radiation 406 cell. Previously in 2009, the company Spectrolab (USA) had a return of 41.6% with cells GaInP/GaInAs/Ge [3].

2. Theory

Compounds containing bore, aluminum or nitrogen fall into this category, they generally have little interest in fast electronics, which requires semiconductors with high carrier mobility or for optoelectronics or a direct band gap structure is necessary for the optical transitions are effective. At the other end, the heavy elements such as bismuth or thallium-based compounds give Gallium (GaAs, GaSb) or indium (InP, InAs, InSb) whose properties are very interesting. Table (1) summarizes some parameters for different materials of the III-V [4].

Semiconductor III-V	E_g (eV)	m^*/m_0	μ (cm ² /VS)	a (Å)
GaP	2,26	0,82	110 5	5,4512
GaAs	1,42	0,067	8500	5,6533
InP	1,35	0,077	4600	5,8686
GaSb	0.812	0.046	-	6.096
InAs	0,36	0,023	33000	6,0584
InSb	0.235	0.016	-	6.479

Table 1. Parameters of the main binary compounds.

The lattice constant is estimated from Vegard's law [5], i.e for a quaternary alloy type $A_xB_{(1-x)}C_yD_{(1-y)}$ is expressed by:

$$a(x, y) = x \cdot (1 - y)a_{AD} + (1 - x) \cdot y \cdot a_{BC} + x \cdot y \cdot a_{AC} + (1 - x) \cdot (1 - y)a_{BD} \quad (1)$$

a_{AC} , a_{AD} , a_{BC} and a_{BD} are the lattice constants of the binary compounds constituting the alloy.

Epitaxy of two semiconductors of the same crystalline structure but of different lattice parameter initially, causes strain (Figure. 1). The material constituting the layer of greater thickness imposes its lattice parameter adjacent to each other of the contact interface, so for sufficiently thin layers, the lattice parameter of epitaxy material and elastically deforms according to the parameter of the layer epitaxy is smaller or larger than that of the substrate, the deformation or elongation is "relaxation layers" or narrowing "compression layer". For a description of the effect of strain on the band structure model and Van De Walle and Krijin formalism are used [6].

In the absence of stress, the bands of heavy holes and light holes are degenerated and isotropic in the center of the Brillouin zone, and the strip-splitting spin holes is located at an energy Δ_0 below these two bands. The center of gravity of the valence band average energy $E_{v, moy}$ is therefore $\frac{\Delta_0}{3}$ below the top of the valence band at $k = 0$.

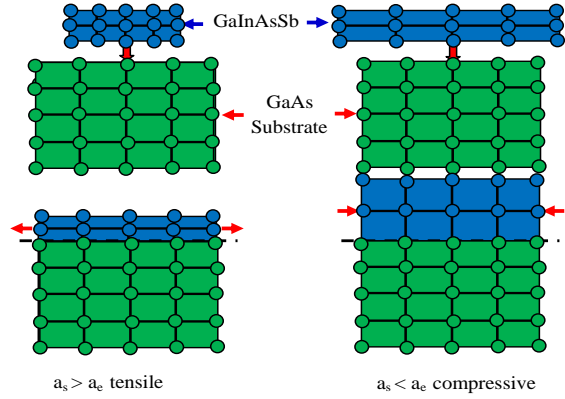


Figure 1. Two types of deformation, (a) layer in compression $a_s < a_e$. (b) layer relaxation $a_s > a_e$.

The effect of strain on the valence and conduction band can be decomposed into two parts:

- The hydrostatic stress, due to deformation along the axis of growth, causes a shift of the center of gravity of the valence band and the center of gravity of the conduction band.
- The Shear stress, which lifts the degeneracy of the energy states of the heavy hole and light hole in $k = 0$.

For an epitaxial layer subjected to a bi-axial compressive strain, the hydrostatic component increases the gap between the valence band and the conduction band, and the shear stress makes the valence bands strongly anisotropic. The band highest energy becomes heavy according to k_{\perp} and light according to k_{\parallel} (hh band). The lower energy band becomes slightly according to k_{\perp} and heavy according to k_{\parallel} (lh band).

Energy shifts of the centers of gravity of the valence band and the conduction band in $K = 0$ induced by the hydrostatic stress, vary proportionally with stress [6]. Expression of the gap energy with duress band is given by:

$$E_g^{cont} = E_c - E_v = E_g(x, y) + \Delta E_c^{hyd} - \Delta E_{v, moy}^{hyd} - \max(\Delta E_{hh}^{cisa}, \Delta E_{lh}^{cisa}) \quad (2)$$

$\Delta E_{v,heavy}^{hyd}$, $\Delta E_{v,light}^{hyd}$, ΔE_{lh}^{cisa} and ΔE_{hh}^{cisa} are the offset of the conduction bands of strain and valence heavy holes and light holes, respectively.

In case the strained layer is a solid solution of quaternary form $A_x B_{1-x} C_y D_{1-y}$, these parameters can be determined by linear interpolation, except for E_c energies are determined qui $\Delta_0/3$ by the following expression:

$$E_g(x, y) = (1 - x) \cdot y \cdot E_{BC} + (1 - x)(1 - y) \cdot E_{BD} + x \cdot y \cdot E_{AC} + x(1 - y)E_{AD} - x(1 - x) \cdot y \cdot C_{ABC} - x \cdot y(1 - y) \cdot C_{ACD} - (1 - x) \cdot y(1 - y) \cdot C_{BDC} - (1 - x) \cdot x \quad (3)$$

During the passage of light in the active layer of the photovoltaic cell, a photon can be absorbed by this layer to produce an electron-hole pair called exciton [7]. The absorption coefficient α for photon energy greater than the energy E of the gap is given by the following relationship:

$$\alpha = \alpha_0 \frac{\sqrt{E - E_g}}{E} \quad (4)$$

With α_0 is constant.

3. Results and discussion

Figure 2 shows the variation of the lattice mismatch as a function of the indium (In) and antimony (Sb) concentration of the structure $Ga_{(1-x)}In_{(x)}As_{(1-y)}Sb_{(y)}/GaAs$. Note that the indium and antimony concentrations cross deformation of the structure but the influence of the indium concentration is more important than the effect of the antimony concentration. Figure.3 shows the effect of the antimony concentration in the valence band. The incorporation of Sb on GaInAs structure gives a breakdown in valence band into two bands E_{hh}^+ , E_{hh}^- and E_{lh}^+ , E_{lh}^- heavy and light holes, respectively. This phenomenon affects the bandgap energy. Figure. 4 shows the evolution of the gap energy of heavy holes and light holes depends on the In and Sb concentration of band. It is found that the indium and antimony concentration significantly reduces the energy bandgap $E_{g,hh}$ and $E_{g,lh}$. If a couple is taken (In = 14%, Sb = 10%) the gap $E_{g,hh} = 1$ eV for the pair (In = 34%, Sb = 10%) the gap is 0.79eV $E_{g,hh}$ was a decrease $\Delta E_g = 0.21$ eV. Figure.5 shows the variation of the

absorption of the structure according to the coefficient of In and Sb concentrations. Note that the absorption coefficient increases with increasing of both of In and Sb concentrations. So indium and antimony cross absorption GaInAsSb/GaAs structure.

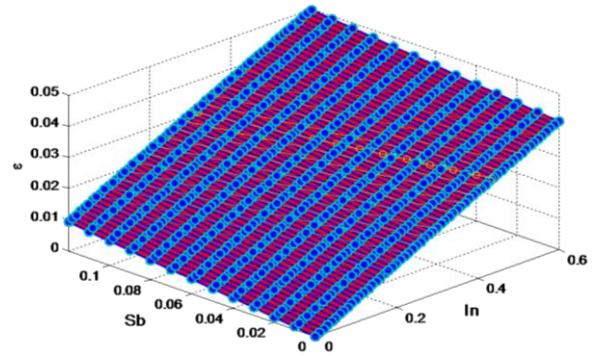


Figure 2. Variation of deformation as a function of the indium and antimony concentrations.

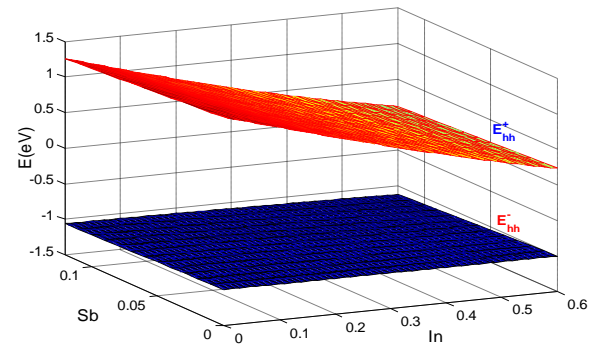


Figure 3. Variation of the energy of the valence band of heavy holes in function of the In and Sb concentrations.

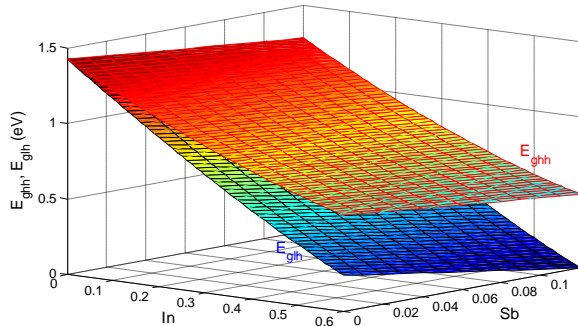


Figure 4. Variation of the gap as a function of the indium and antimony concentrations.

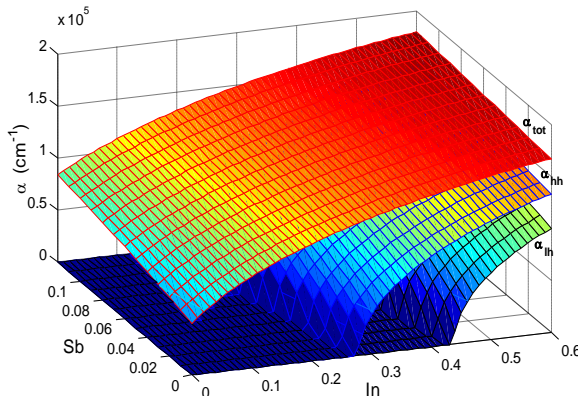


Figure 5. Variation of absorption of the different transitions electrons heavy holes and light holes in total based on In and Sb concentrations.

4. Conclusion

In this work we modeled and simulated the structure based on GaInAsSb on GaAs substrate. We took into account the effect of In and Sb concentrations on the strain the energy in the valence subband, the bandgap energy and the absorption coefficient. In and Sb concentrations decreased significantly the bandgap energy is giving us a very significant increase in the absorption coefficient of the structure GaInAsSb/ GaAs. This study allows us to enhance the efficiency of light conversion .We can use this new material as one of the layers of a multi-junction solar cell.

References

- [1] L. Bailly , "Cellules Photovoltaïques Organiques", l'Université Bordeaux, (2010).
- [2] D. Bordel, "Développement de Nouveaux Substrats", Ecole Centrale deLyon, (2007).
- [3] M. PETIBON Stéphane, "Nouvelles architectures distribuées de gestion et de conversion de l'énergie pour les applications photovoltaïques",doctorat de l'université de Toulouse, (2009).
- [4] L.J.J. Tan, J.P.R. David, Jo Shien Ng, 'Dark Current Mechanism in Bulk' GaInNAs Lattice Matched to GaAs, IEEE Transactions on Electron devices, VOL. 58, Vol. 58, No. 1, (2011) 103 - 106 .
- [5] S. Dhar, N. Halder, J. Kumar, et B.M. Arora, Observation of a 0.7 eV electron trap indilute GaAsN layers grown by liquid phase epitaxy, Appl. Phys. Lett. 85, 964 (2004).
- [6] EbruBakir, "Investigation of Long-wavelength (GaInNAs 2.3 μm) Indium Rich Highly Strained Quantum Wells on InP Substrates", Seminary, (2006).
- [7] Alexandre ARNOULT, "Dopage par modulation d'hétéro structures de semi-conducteurs II-VI semimagnétiques en épitaxie par jets moléculaires', Université Joseph Fourier, (1998).

Optical transitions in quantum dots

A. Benahmed^a, A. Aissat^a, M. Bouzaki^b, R. Bestam^a, S. Chaouchi^a, W. Bellil^a

^a Saad Dahlab Blida University-Faculty of Science Lab "FUNDAPL" Algeria

^b Aboubekr Belkaid Tlemcen University, Faculty of Science "URMER" Algeria

Received: 30 April 2014, accepted 26 May 2014

Abstract

The analysis of the electronic states of a quantum dot of InAs grown on a GaAs substrate has been studied for different geometries. We did the calculation with each type of geometry we based on the Schrödinger equation for stationary particle and we used "Comsol" for calculations. We calculated energy values as a function of each of the parameters: length, width and thickness of the wetting layer where other parameters are held constant.

Keywords: *hétérostructures InAs / GaAs, the Schrödinger equation, simulation, COMSOL.*

1. Introduction

There are several ways to make quantum dots among these techniques include the method known as Stranski-Krastanov, which is the one used for the growth of quantum dots. An important point is that this growth process results in the formation of a two-dimensional layer of InAs based uppermost islets called wetting layer, and acting as a reservoir of electrons scattered over a continuum of power levels.[1, 2, 3]. The objective of this work is to grow hetero structure from two semiconductor materials (InAs/ GaAs). We make calculations by "Comsol" with each type of geometry (rectangular,sphericaland conical) at the same height and the same radius. To get a better idea of how energy changes indicates that we vary one of the parameters of the function (3). The energy level values obtained are listed in the table (01).

2. Method

We detail the theoretical model that we used to determine the wave functions and energy Eigen statesof electrons and holes through the resolution of the Schrödinger equation [1,2]

$$E \psi = H \psi \quad (1)$$

$$i \frac{\hbar}{2\pi} \frac{\partial \psi}{\partial t} = H \psi \quad (2)$$

The equation can be simplified to a stationary Schrödinger equation:

- The parameters of the equation are:
- \hbar ($\approx 6,626.10^{-34}$ J.s) is Planck's constant.
- μ is the reduced mass.
- V is the potential energy.
- E is the valueofenergy.
- Ψ is the quantum mechanical wave function.

$$-\nabla \cdot \left(\frac{\hbar^2}{8\mu\pi^2} \nabla \Psi \right) + V\Psi = E\Psi \quad (3)$$

results in the modification of some parameters such as the radius, quantum dot height and thickness of the wetting layer. Indeed, the solutions of equation (3) where $l = 0$, which are transition energies depicted in Figures (4, 5 and 6). The energy electron-heavy hole transition is written by:

$$\Delta E_{e-hh} = E_e + E_{hh} + E_{g_{InAs}} \quad (4)$$

To resolve this problem, use the form PDE interface coefficient. The model solves for an eigenvalue / eigenvector. Electronvolt is used as an energy and nanometer length units of the geometry unit.

3. Result and discussion:

3.1. The electronic states of a quantum dot InAs with each type of geometry:

The first step we choose is the realization of three different geometric structures shown in Figure

(1),(2)and (3).We make calculations with Comsol each type of geometry with the same dimensions (height, radius, and thickness of the layer of wetting. The energy levels are listed in Table 01, and we see that the highest energy states are obtained for the conical quantum dot; we find that the energy is inversely proportional to the size of quantum dot.

geometry types	E_0 (eV)
conical	1.05
elliptic	0.95
rectangular	0.91

Table 01: The energy levels for each geometry in the ground state E_0 (eV)

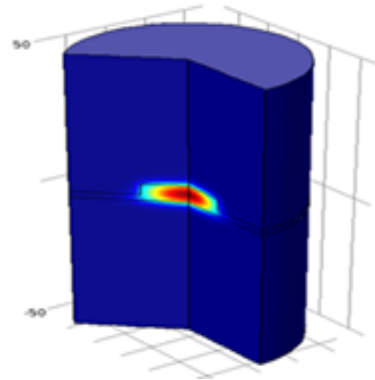


Figure 03: The energy values for conical structure ($E=0.91$ eV)

3.2. Changes in the parameters of the quantum dot:

Among the three geometries, we have chosen the conical structure and we have made changes on the radius of the quantum dot "r" between (50Å and 250Å), the thickness and layer wetting and we obtained the results shown in the figures (4,5 and 6) respectively which correspond to energy levels of optical transition. The analysis of these figures shows that the transition energy is strongly dependent on the size of the quantum dot. Indeed, these energies are inversely proportional to the dimensions of the dot and to the thickness of the wetting layer.

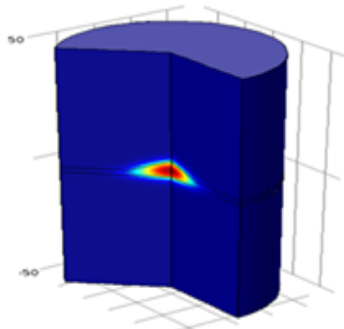


Figure 01: The energy values for conical structure ($E=1.05$ eV)

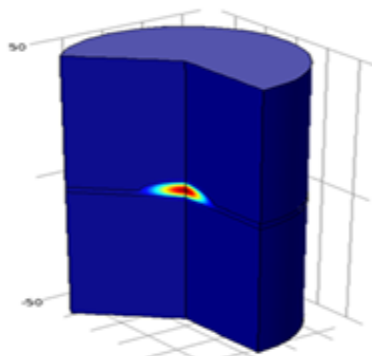


Figure 02: The energy values for elliptical structure ($E=0.95$ eV)

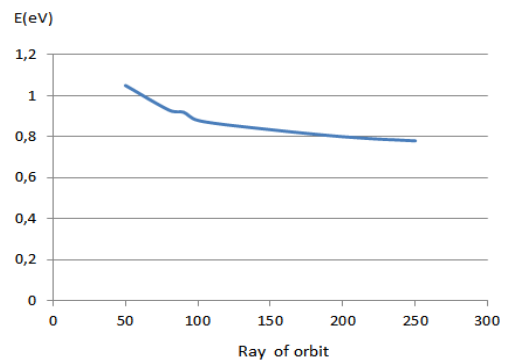


Figure 04: The energy values for changes in the ray of orbit

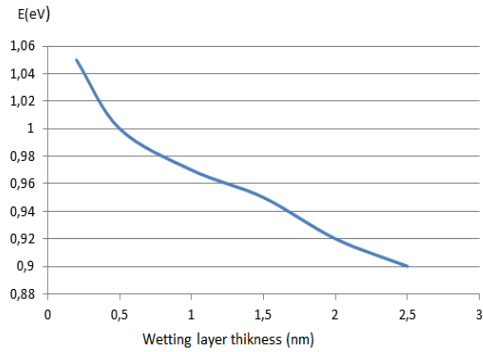


Figure 05: The energy values for Changes in thickness of the quantum dot.

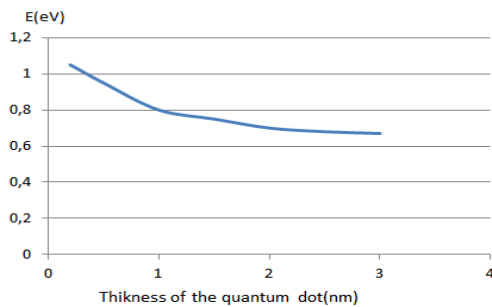


Figure 06: The energy values for Changes in the wetting layer thickness.

There is an offset of the energy of transitions to higher energies because of the change in the

confinement energy when reduces the size of the structures [4, 5].

4. Conclusion:

Our results obtained by studying a single quantum dot, where we use Comsol software and by simulation of elliptic, conical and rectangular nano-crystals InAs shows that the energy associated with the ground level depends on the shape and volume of quantum dots.

References:

- [1] COMSOL Multiphysics Model Library copyright 1998–2008 by COMSOL AB. All rights reserved.
- [2] RF Module User's Guide. 1998–2012 COMSOL-Protected by U.S. Patents 7,519,518; 7,596,474; and 7,623,991. Patents pending.
- [3] R. Chau, B. Doyle, S. Datta, J. Kavalieros and K. Zhang, Integrated nanoelectronics for the future, Nature Materials 6 (2007) 810.
- [4] P. M. Petroff, K. H. Schmidt, G. Medeiros-Ribeiro, A. Lorke et J. Kotthaus, Size quantization and zero dimensional effects in self assembled semiconductor quantum dots, Jpn. J. Appl. Phys. 36, Part 1, 4068 (1997).
- [5] U. Banin, Y. Cao, D. Katz et O. Millo, Identification of atomic-like electronic states in indium arsenide nanocrystal quantum dots, Nature 400, 542 (1999).

Optical and Structural Characterization of Fluorine-Doped SnO₂ Thin Films Prepared by Spray Ultrasonic

Soumaia Abbas^{1,2}, Atman Ben Haoua^{1,2}, Boubaker Ben Haoua² And Achour Rahal^{2,3}

¹Faculty of Mathematics & Materials Sciences, Univ Ouargla, 30000, Algeria.

²Laboratory VTRs, Univ El Oued, 39000, Algeria.

³Material Laboratory Department, Faculty of Sciences, Univ Biskra 07000, Algeria.

Email: abbes_soumia@yahoo.fr

Received: 30 April 2014, accepted 26 May 2014

Abstract

In this work, Fluorine-doped tin dioxide (FTO) films were prepared with spray ultrasonic technique using SnCl₂ and NH₄F as sources of SnO₂ and fluorine dopant, the films were deposited on MICROSCOPE SLIDES (REF 217102) used as glass substrates. The optical and structural properties of the films for different doping concentration (for 3-18 wt% NH₄F) were studied. The optical properties of the films were studied by UV-vis spectroscopy. Optical transmittance spectra of the films showed high transparency of about 72.8-83.5% in visible region which increases with increases F-doping. The optical gap for F-doped SnO₂ films was found in the range from 4.31 to 4.37 eV. The structure and topography of the ultra sonic deposited films were characterized by X-ray diffraction (XRD) and scanning electron microscopy (SEM). X-ray diffraction studies showed that the SnO₂: F films were polycrystalline and have preferential orientations along (2 0 0) planes and grain sizes in the range of 14-30 nm. SEM studies reveal the same observation on the effect of the fluorine doping.

Keywords: Spray Ultrasonic, FTO, UV-Visible Spectroscopy, X-ray diffraction (XRD);

1. Introduction

Transparent conductive oxides (TCO) are interesting materials in several applications, their important properties both electrical conductivity and transparency in the visible region, make them ideal candidates for optoelectronics, photovoltaic and catalytic applications. Among the different transparent conductive oxides, SnO₂ films doped with fluorine seem to be the most appropriate for use in many applications, owing to its low electrical resistivity and high optical transmittance. Non-toxicity and abundance of its components on Earth make it an ideal candidate for applications listed above. SnO₂ is available material and easy to deposit in thin films by using Ultrasonic Spray technique [1, 2]. Thin films of SnO₂ can be prepared by many techniques, such as chemical vapor deposition [3], sol-gel [4], pulsed laser deposition [5] and spray pyrolysis [6]. Among these techniques, new Ultrasonic Spray method is the most convenient technique because it is simple, low cost, easy to add doping materials and promising for high rate and mass production capability of uniform large area coatings in industrial applications [1, 2]. However, the preparation method affects on thin film structural

properties, which play an important role in the optical and electrical properties of the film material. Doping with fluorine (F), antimony (Sb), cobalt (Co), Cerium (Ce), iron (Fe), palladium (Pd), niobium (Nb), molybdenum (Mo) and indium (In) has been achieved to improve tin oxide (SnO₂) property [7-13]. Among these dopants, fluorine has been shown to be the most effective and achieved commercial use due to its low cost and simplicity. A survey of literature reveals that most research works focus on the fluorine doped SnO₂ films used ammonium fluoride (NH₄F) as a fluorine precursor.

In the present work, SnO₂: F thin films were prepared by Ultrasonic spray technique on glass substrates using SnCl₂ and NH₄F as sources of SnO₂ and fluorine dopant. The aim of this work is to study the effect of the doping levels on some physical properties of SnO₂: F thin films such as optical transmittance, crystal structure and surface morphology. The results obtained are compared and discussed with the specified results by several researchers.

2. Results and discussion

2.1. Optical properties

Fig.1 shows UV-Vis transmittance spectra of F-doped SnO₂ thin films with various fluorine concentrations. The transmittance of all samples was more than 70% in the whole visible-light region (400 to 800nm), this transmittance value of fluorine doped tin oxide films are in good agreement with [14, 15]. The films doped with fluorine show increase in transmittance with increasing fluorine concentration, transmittance values are 72.8%, 76.2% and 83.5%, respectively for 6 wt. % F, 9 wt. % and 15 wt. % F. The increase in transmittance is attributed to the well-crystallized films [16]. A slight decrease in the optical transmittance at 18 wt. % (T= 76.8%) could be attributed to an excess free electrons in the films [17].

The comparison of transmittance, absorbance and reflectance of fluorine doped SnO₂ thin film (6 wt. %) is shown in Fig. 2.

Fig.3 shows the optical band gap E_g of SnO₂: F thin films. E_g can be deduced from transmission measurements using Tauc's relation Eq. 1[18]:

$$(\alpha h\nu)^2 = A(h\nu - E_g) \quad (1)$$

Where $h\nu$ is the photon energy, E_g is the optical band gap, A is a constant which does not depend on $h\nu$. E_g values calculated from the optical transmission were in the range of 4.31 ~ 4.37 eV (Table 1). The optical band gap values are higher than the value of $E_g = 3.57$ eV reported for single crystal SnO₂ [19] and are comparable to the value of $E_g = 4.3$ eV reported for F: SnO₂ films [20-23]. This increase in band gap can be attributed to an increase in carrier concentration of the films due to F doping. Similar

optical band gap values were reported for the SnO₂: F films [20, 21] The optical band gap decreases from 4.37 eV at 6 wt. % F to 4.31 eV at 15 wt. % with increasing fluorine concentration then it increases to 4.35 eV with 18 wt. % F doping.

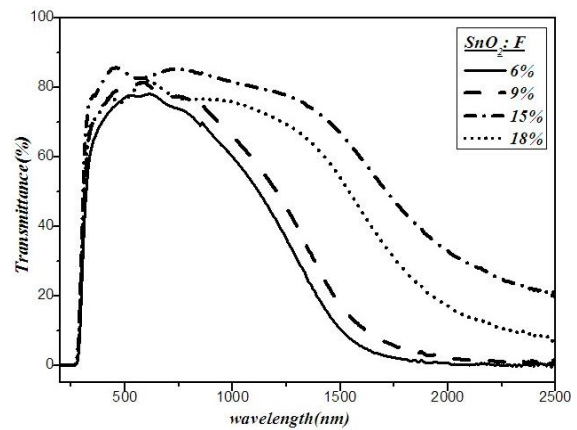


Figure 1: Transmittance spectra of SnO₂: F thin films as a function of Wavelength for different fluorine doping concentration (wt. %).

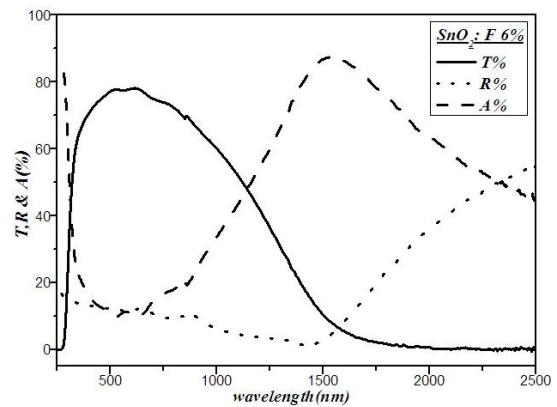


Figure 2: Transmittance, Reflectance and Absorbance spectra of F-doped SnO₂ thin film (6 wt. %)

The thickness of the film t is calculated from transmittance spectra using the following relation Eq. 2 [24, 25]:

$$t = \frac{\lambda_1 \lambda_2}{2(n_1 \lambda_2 - n_2 \lambda_1)} \quad (2)$$

Where n_1 and n_2 are the refractive indexes at the two adjacent maxima (or minima) at λ_1 and λ_2 . The thickness of the films was determined to be between 365 nm and 712 nm; results are listed in Table 1 [26].

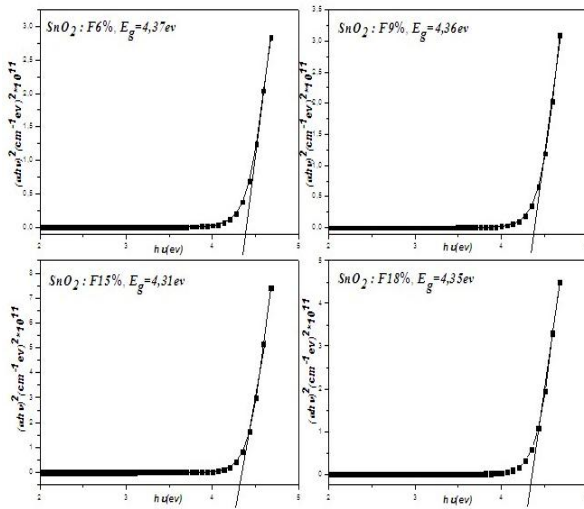


Figure 3: Optical band gap calculations of SnO₂:F thin films for different fluorine doping concentration (wt. %).

Table 1: Films thickness and optical gap values of SnO₂:F thin films for different fluorine doping concentration (wt. %).

F-doping wt. %	6 wt. %	9 wt. %	15 wt. %	18 wt. %
Films thickness (nm)	712.75	639	365.5	489.16
E _g (eV)	4.28	4.37	4.33	4.33

2.2. Structural analysis

The X-ray diffraction patterns of the SnO₂ films deposited by ultrasonic spray with different fluorine concentrations are shown in Fig. 4. For all deposited films, major peaks corresponding to the tetragonal SnO₂ (JCPDS No. 41-1445) were observed. It can be seen that all the films are polycrystalline and contain SnO₂ Tetragonal structure (P₄/mm (136)), and no phase corresponded to fluorine was observed.

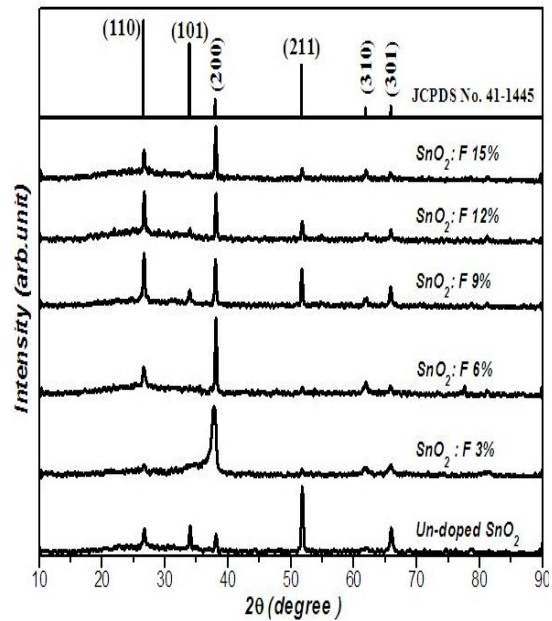


Figure 4: XRD patterns of F-doped SnO₂ films for different fluorine doping concentration.

The XRD results of SnO₂:F thin films prepared by Ultrasonic Spray exhibited five peaks at 2θ equal to 26.58°, 33.86°, 38.12°, 51.85° and 66°, according to the (110), (101), (200), (211) and (301) planes, respectively. It is perceptible from the figure that the un-doped SnO₂ films grow along the preferred orientation of (2 1 1). The intensity of the plane (2 0 0) found increased with increasing fluorine doping concentration. In addition, after fluorine doping the peaks shift slightly to the less value of the Bragg angle [27]. In order to evaluate the preferred orientation of the SnO₂:F films, the texture coefficient T_{hkl} can be calculated from Eq. 3 [28]:

$$T_{hkl} = \frac{I_{hkl} / I_{0hkl}}{\frac{1}{N} \sum_M I_{hkl} / I_{0hkl}} \quad (3)$$

Where T_{hkl} is the texture coefficient of the plane (h k l), I_{hkl} is the measured intensity, I_{0hkl} is the corresponding standard intensity given in the ASTM cards (No. 41-1445), and N is the number of reflections. If the film had no preferred orientation, presumably the T_{hkl} would be one for all peaks. If the value of T_{hkl} is larger, the films may possess the (h k l) preferred orientation. The texture coefficients T_{hkl} of the films are listed in Table 2. It is indicated that all the SnO₂ films doped with 3, 6 and 15 wt. % F exhibit a preferred orientation with (200) plane whereas films doped with 9 and 12 wt. % F had no preferred orientation [29].

Table 2: Texture coefficients of SnO₂: F thin films for different fluorine doping concentration (wt. %).

	I_{110}	I_{101}	I_{200}	I_{111}	I_{301}	T_{hkl}
ASTM	100	75	21	57	15	-
Un-doped	27	30	21	69	28	1.27
3 wt. %	13	/	72	9	14	3.11
6 wt. %	31	/	80	11	12	3.14
9 wt. %	57	20	51	41	23	0.53
12 wt. %	53	16	51	23	15	0.58
15 wt. %	33	12	57	15	11	3.13

The crystalline sizes of SnO₂: F films given in the Table 3 are calculated according to the Scherrer's formula Eq. 4 [30]:

$$D = \frac{0.9\lambda}{\beta \cos\theta_\beta} \quad (4)$$

Where D is the crystallite size, β is the full width at half-maximum (FWHM) of the most intense diffraction peak, λ is the X-ray wavelength (1.5404 Å) and θ_β is the Bragg angle. A broad size distribution of about 27.53 nm was found for the un-

doped film. However, for doped film at 9 wt. % Scherrer's equation applied to the most intense (1 1 0), (2 0 0) and (2 1 1) diffraction lines. A broad size distribution ranging from 27.28 nm to 30.35 nm whereas for doped films at 12 wt. % the average crystalline size calculated to (1 1 0) and (2 0 0) diffraction lines it ranging from 26.96nm to 29.45nm. In addition, the calculated sizes were in the range of 14 nm, 28.56 nm and 26.82 nm for 3 wt. %, 6 wt. % and 15 wt. %, respectively.

The lattice constants a and c , for the tetragonal phase structure is determined from XDR results using Eq. 5 [30]:

$$\frac{1}{d_{hkl}^2} = \frac{h^2 + k^2}{a^2} + \frac{l^2}{c^2} \quad (5)$$

Where d_{hkl} is the inter-planar distance, (h k l) are the Miller indices and a and c are the lattice constants. The calculated lattice constants a and c are given in Table 3. All the values were marginally larger than those of the standard SnO₂ with tetragonal structure in JCPDS card, which was caused by the F^- (substitution) of O^{2-} [26, 27].

Table 3: XRD analysis results of F-doped SnO₂ films for different fluorine doping concentration.

F-doping wt. %	Grain size D (nm)	Lattice Parameter a (Å)	Lattice Parameter c (Å)
Un-doped film	27.53	4.725	3.184
3 wt. %	14.03	4.763	3.141
6 wt. %	28.56	4.708	3.322
9 wt. %	27.28–30.35	4.725	3.184
12 wt. %	26.69–29.45	4.725	3.184
15 wt. %	26.289	4.742	3.200

The surface morphology of F: SnO₂ thin films deposited on glass substrate by ultrasonic spray for different fluorine doping concentration (3 wt. %; 6 wt. % and 12 wt. %), is shown in Fig. 5.

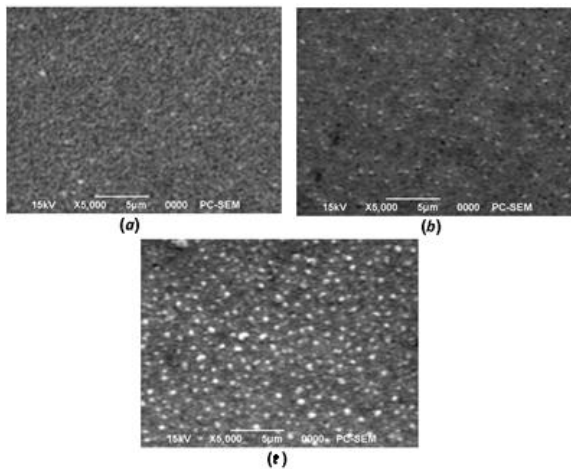


Figure 5: SEM micrographs of SnO₂: F films for various F-content (wt. % in film): (a) 3 wt. %, (b) 6 wt. %, and (c) 12 wt. %.

SEM micrographs show polycrystalline SnO₂ thin films with homogeneous distribution. From the SEM image, it is seen that the substrate is well covered with large number of fine grains and film surface is uniform. The films are continuous and consists inter-granular regions appearing darker [20, 29].

3. Conclusions

Thin films of fluorine doped tin oxide SnO₂ were successfully prepared on glass substrates by Ultrasonic spray technique. The effects of doping levels on the optical and structural properties of SnO₂: F thin films were experimentally investigated. The optical transmittance of the films found increased with increasing fluorine doping concentrations. The average visible transmittance of all samples was more than 70% in the visible region with an optical band gap of about 4.37-4.31 eV and thickness between 365 nm and 712 nm. X-ray diffraction studies revealed that all the films are polycrystalline with tetragonal structure. The preferred orientation of SnO₂: F films was found varying on doping level variation. The films show a preferred orientation along (2 1 1) for un-doped film whereas the films doped with 3, 6 and 15 wt. % F exhibit a preferred orientation with (2 0 0) plane. The grain size D was also found in the range of 14-30 nm. The results showed that this technique is superior to

the conventional technique for both improving the film thickness uniformity and film transparency. In addition, the obtained results suggest that the deposited films can be used as transparent electrodes in solar cells applications.

References

- [1] A. Rahal, S.Benramache, and B.Benhoua, *Journal of Semiconductors* 34(8)083002 (2013) 1-4.
- [2] A. Rahal, S.Benramache, and B.Benhoua, *Journal of Semiconductors* 34(9)083002 (2013) 1-5.
- [3] J. Szuber, G. Czempik, R. Larciprete, B. Adamowicz, *Sensors and Actuators B* 70 (2000) 177-181.
- [4] H. Köse, A.O. Aydin and H. Akbulut, *Acta Physica Polonica A* 121(2012) 227-229.
- [5] Ch.J. Lee, J.H. Lee, J.J. Kim, J.Y. Lee and H.Y. Lee, *Integrated Ferroelectrics* 115 (2010) 34-40.
- [6] K. Murakami, K. Nakajima, S. Kaneko, *Thin Solid Films* 515 (2007) 8632-8636.
- [7] Ch.M. Wang, Ch.C. Huang, J.Ch. Kuo and J.L. Huang, *Surface & Coatings Technology* 231 (2013) 374-379.
- [8] G. Korotcenkov, I. Boris, V. Brinzari, S.H. Han and B.K. Cho, *Sensors and Actuators B* 182 (2013) 112-124.
- [9] Z. Jiang, Z. Guo, B. Sun, Y. Jia, M. Li and J. Liu, *Sensors and Actuators B* 145 (2010) 667-673.
- [10] B. Zhu, Ch. Yin, Z. Zhang, Ch. Tao and Liu Yang, *Sensors and Actuators B* 178 (2013) 418-425.
- [11] G. Turgut, E.F. Keskenler, S. Aydın, E. Sönmez, S. Dogan, B. Düzgün and M. Ertugrul, *Superlattices and Microstructures* 56 (2013) 107-116.
- [12] E. Zampiceni, E. Bontempi, G. Sberveglieri and L. E.Depero, *Thin Solid Films* 418 (2002) 16-20.
- [13] L. Francioso, A. Forleo, S. Capone, M. Epifani, A. M. Taurino and P. Siciliano, *Sensors and Actuators B* 114 (2006) 646-655.
- [14] S. Chaisitsak, *Sensors* 11 (2011) 7127-7140.

- [15] E. Elangovan, K. Ramamurthi, *Applied Surface Science* 249 (2005) 183-196.
- [16] D. Tatar and B. Düzgün, *Indian Academy of Sciences* 79 No 1 (2012) 137-150.
- [17] H. Kim and H.H Park, *Ceramics International* 38S (2012) S609-S612.
- [18] J. Tauc, *The optical properties of solids*, Éd. J. Tauc, New York: Academic Press (1966).
- [19] R. Summit, J.A. Marley and N.F. Borrelli, *J. Phys. Chem. Solids* 25 (1964) 1465.
- [20] A.A. Yadav, E.U. Masumdar, A.V. Moholkar, K.Y. Rajpure and C.H. Bhosale, *Physica B* 404 (2009) 1874-1877.
- [21] H. Khallaf, Ch.T. Chen, L.B. Chang, O. Lupan, A. Dutta, H. Heinrich, F. Haque, E. del Barco and Lee Chow, *Applied Surface Science* 258 (2012) 6069-6074.
- [22] Stjerna, E. Olsson, C.G. Granqvist, *J. Appl. Phys.* 38 (1967) 3767.
- [23] H. Kim, R.C.Y. Auyeung and A. Pique, *Thin Solid Films* 516 (2008) 5052.
- [24] J. C. Manificier, M. De Murcia and J. P. Fillard, *Thin Solid Films* 41 (1977) 127-135.
- [25] M. Jubault, *Doctorate Thesis*, University of Pierre and Marie Curie, France (2009).
- [26] D.R. Acosta, E.P. Zironi, E. Montoya and W. Estrada, *Thin Solid Films* 288 (1996) 1-7.
- [27] Q. Gao, Q. Liu, M. Li, X. Li, Y. Liu, Ch. Song, J. Wang, J. L. Ge Shen and G. Han, *Thin Solid Films* 544 (2013) 357-361.
- [28] I. Yang, H. Zhao, Q. Chen, Sh. Liu, H. Sha and F. Zhang, *Thin Solid Films* 520 (2012) 5691-5694.
- [29] A. Muthukumar, G. Giusti, M. Jouvart, V. Consonni and D. Bellet, *Thin Solid Films* 545 (2013) 302-309.
- [30] S. Sujatha Lekshmy, G. P. Daniel and K. Joy, *Applied Surface Science* 274 (2013) 95-100.

FTIR and AFM studies of the Ge on Porous Silicon/Si substrate hetero-structure obtained by molecular beam epitaxy

S. Gouder^a, R. Mahamdi^a, M. Aouassa^b, S. Escoubas^b, L. Favre^b, A. Ronda^b and I. Berbezier^b

^aElectronics Department, University Hadj Lakhdar Batna (05000), Algeria

^bIM2NP Aix-Marseille Universités, UMR CNRS n°7334,

Faculté des Sciences St-Jérôme - Case 142, 13397 Marseille Cedex 20 France

Received: 30 April 2014, accepted 26 May 2014

Abstract

The single crystal Ge layers have been deposited by molecular beam epitaxy on porous silicon (PSi) substrate, with different thicknesses (40 nm and 80 nm) at the growth temperature of 500°C and 600°C. During deposition, the pore network of PSi layers has been filled with Ge. Fourier transformed infrared spectroscopy (FTIR) and Atomic force microscopy (AFM) have been applied for investigation of vibrational modes and morphological properties of the Ge on PSi layers. AFM investigation showed the surface roughness and pyramid like hillocks. It also confirmed the nanometric size of the crystallites. FTIR absorption measurements showed different vibrational modes present in the Si_{1-x}Ge_x structures. The observed vibrational frequencies depend strongly on the growth temperature.

Keywords: Germanium, porous Silicon, molecular beam epitaxy, AFM, nanocrystals, FTIR.

1. Introduction

The interest in porous silicon (PSi) is increased considerably by the observation of its room temperature visible photoluminescence (PL) [1] and electroluminescence [2, 3]. PSi shows different features in comparison to the bulk silicon such as shifting of fundamental absorption edge into the short wavelength and PL in the visible region of the spectrum. Analyses of PSi show that this material presents interesting properties [4-6] necessary for a wide area of potential applications such as waveguides [7], thermal [8] and optical [9-12] applications or for Silicon on insulator (SOI) technology [13]. However, PSi has good compatibility with existing silicon technology.

Many microelectronic devices incorporate Ge containing layers such as Si_{1-x}Ge_x [14]. To provide increased device performance, it is advantageous to have a relatively high Ge content in the Si_{1-x}Ge_x layer. Nevertheless, greater amounts of Ge increase the amount of strain which is due to the lattice mismatch (4.2 %) between Ge and Si. This problem is partially overcome by growing a relaxed SiGe buffer layer, called virtual substrate [15, 16], on top of which the active layers (Ge or Si) are deposited. PSi is a spongy material and could partially relax the epitaxial strain caused by the heteroepitaxy of SiGe layers because of the large density of pores. Then, it could be used as a stressor layer with Ge epitaxial layer grown on. This process has the advantage of low cost thin film solar

cells. Especially, when filling the pore network of a PSi with Si or Ge.

In our previous work [17], we reported the use of PSi as sacrificial layer to grow epitaxial planar and fully relaxed Ge membranes. The Ge layers were grown on PSi by molecular beam epitaxy (MBE) in ultra high vacuum atmosphere. The resulted Ge thin films could be used as relaxed pseudo-substrate in conventional microelectronic technology. However, further characterisation is needed to address the issue of the use of these samples on optoelectronic technology. In this study, we report the studies of morphological properties and vibrational modes of Ge layers grown on PSi as a function of the growth temperature and deposited thickness.

2. Experimental procedure

The main The Ge layers were grown on PSi substrate by MBE, in order to fill the pore network of a PSi layer with Ge. In this work, we used two samples with different Ge thicknesses $h=40$ nm and $h=80$ nm elaborated at 600°C and 500°C respectively. The fabrications of the PSi and Ge layers grown on PSi have been described in our previous work [17].

The surface morphology and roughness of prepared samples was obtained by Atomic Force Microscope (AFM), type PSIA XE-100, in the tapping mode.

Absorption FTIR spectra of the samples were measured using a Nicolet-Avatar-360 spectrophotometer. This technique can be used to evaluate the evolution of the chemical bond with growth temperature.

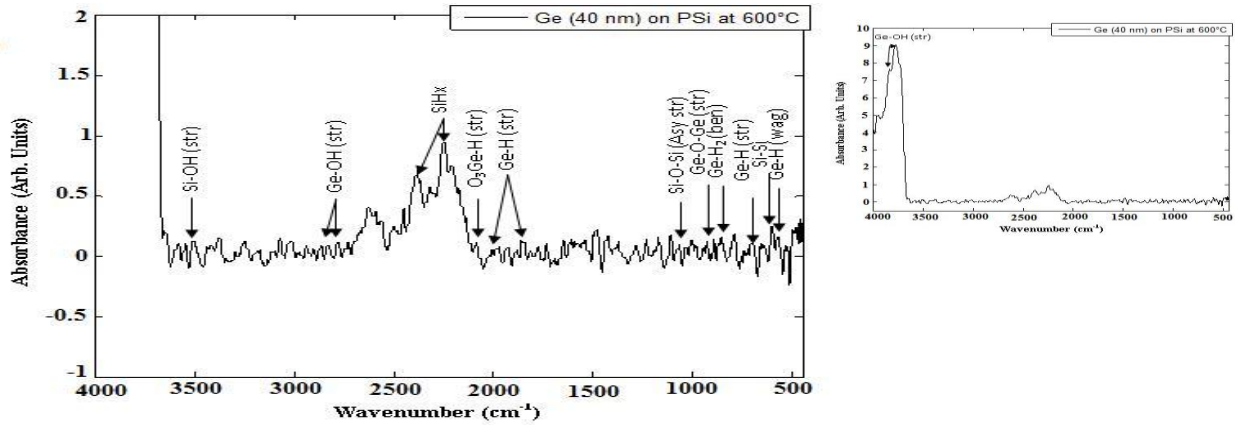


Fig. 1 FTIR absorption spectra obtained from Ge grown on PSi at 600°C for h=40 nm. Inset: FTIR spectra on large scale.

3. Results

The internal surface chemical composition of as-prepared PSi was characterized using FTIR technique. The different bonds are resumed in our work submitted and accepted for another conference [18], where a combined analysis of FTIR spectroscopy and PL spectra were applied to characterize the Ge/PSi structures.

The surface composition of Ge/PSi structures were characterized by FTIR absorbance analysis. The results are depicted in Fig. 1 and 2. FTIR absorption measurements on the Ge/PSi structures showed replacement of the Si-OH modes with Ge-OH related modes. Specifically, Ge-OH stretching modes at 2780, 3770 and 3830 cm^{-1} for 40 nm thick Ge grown at 600°C and at 2789, 2838, 2918, 3836 and 3305 cm^{-1} for 80 nm thick Ge grown at 500°C appeared in FTIR spectra [19, 20, 21, 22]. The FTIR absorbance spectra characteristic of the hybride-terminated surface, which consists of Si-H stretching modes at 2254 and 2351 cm^{-1} [23] for 40 nm thick Ge and at 2250 cm^{-1} for 80 nm thick Ge [23]. However, the peak at 3520 cm^{-1} is in general attributed to the stretching signal of the Si-OH bond [24]. The characteristic asymmetric stretching signals of Si-O-Si bridges between 1066 and 1184 cm^{-1} [25] and at 1070 cm^{-1} [23] are too weak. Also, we noticed the presence of the stretching points of O₂Ge-H and O₂Ge-H at 2035 and 2065 cm^{-1} [19]. In addition, Si-Si bonds are obtained at 609 and 613.5 cm^{-1} [23] for 40 nm thick Ge and 80 nm respectively. The above results indicate that FTIR spectra of

Ge/PSi samples contain vibrational modes arising from chemical compound of Ge, O and H.

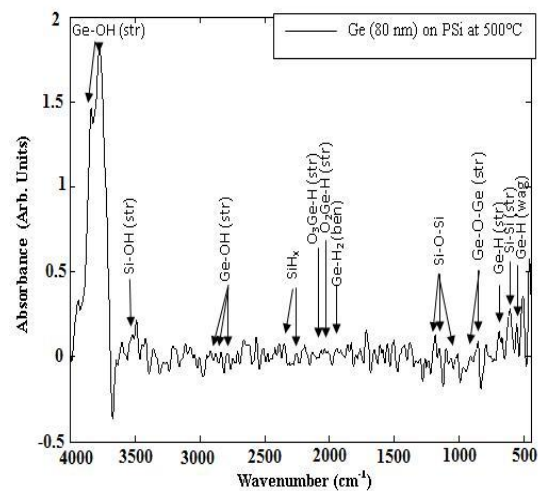


Fig. 2 FTIR absorption spectra obtained from Ge grown on PSi at 500°C for h=80 nm.

However, we display in fig. 1 and 2 a low presence of SiH_x for a 80 nm thick Ge, compared to the other sample grown at 600°C. Some authors correlated the presence of SiH_x with the strain of PSi materials [26, 27], this explanation is supported by our results obtained from FTIR spectra with in addition the results reported in our previous work [17] obtained by high resolution X-ray diffraction.

Figure 3 shows the 2D and 3D views of different samples. From the AFM measurements, we find that the root mean square (RMS) roughness decreases with the deposited thickness from RMS= 15.2 nm for h=40 nm to RMS=3 nm for h=80 nm, and is estimated to be 2 Å for PSi [17]. From fig. 3, the formation of pores can be clearly seen in 3D images, it is observed that there is a condensation point which forms the skeleton of PSi and pyramid like hillocks surfaces. These can

be regarded as a condensation point to form skeleton clusters which play an important role for the strong visible luminescence. The lateral sizes of the nanocrystals are found to be in the range of 3-5 nm. Despite this, it is difficult to differentiate nanocrystals sizes but it is expected that their sizes are smaller for a 80 nm thick Ge which leads to an intense PL, especially since we found that Ge thicknesses have no effect on PL properties [18].

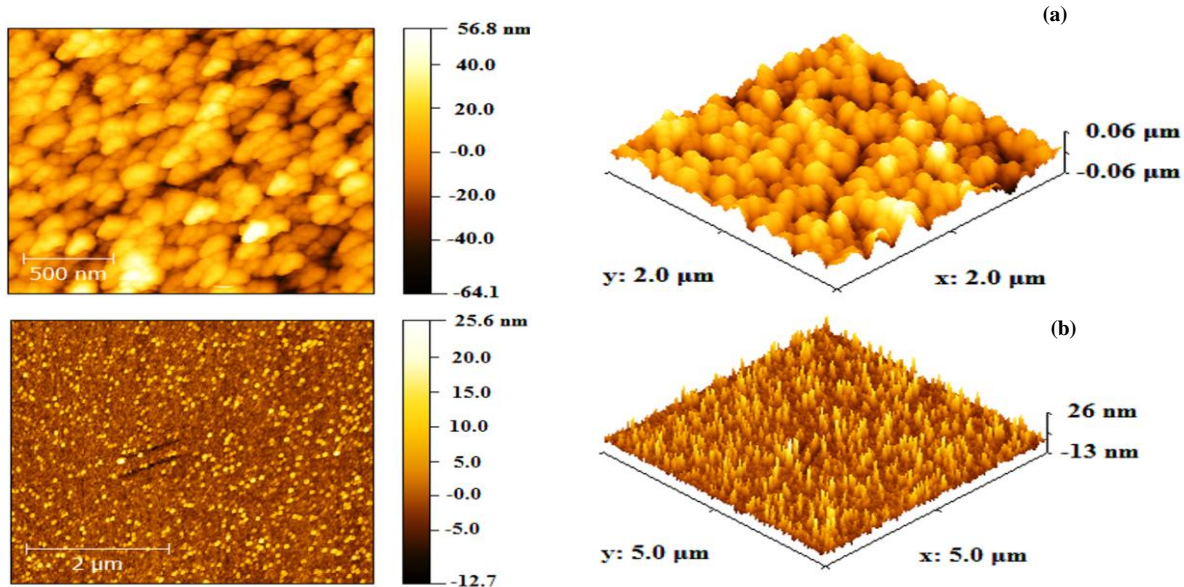


Fig. 3 AFM images of Ge grown by MBE on PSi for; (a) h=40 nm at 600 °C and (b) h=80 nm at 500 °C

4. Conclusion

A combined study of FTIR and AFM was conducted on PSi and Ge/PSi structures with different thicknesses and growth temperature. The AFM investigation shows the rough Si and Ge/PSi surfaces, which can be regarded as a condensation point for small skeleton clusters which play an important role for the PL. Also, we have deduced the size of Si nanocrystals from AFM measurements. Furthermore, FTIR absorption results of the Si_{1-x}Ge_x layers depend on the growth temperature and show the emergence of Ge-O-Ge, Ge-H and Ge-OH stretching modes.

Acknowledgement

The authors are grateful to the laboratory STM for providing the PSi samples.

References

- [1] L.T. Canham, *Appl. Phys. Lett.* 57 (1990) 1046.
- [2] H. Mimura, T. Matsumoto, Y. Kanemitsu, *Solid-State Electronics*, 40 (1996) 501.
- [3] K. D. Hirschman, L. Tsybeskev, S. P. Duttagupta, P. M. Fauchet, *Nature* 384 (1996) 338.
- [4] M. Voos, P. Uzan, C. Delalande, G. Bastard, A. Halimaoui, *Appl. Phys. Lett.* 61 (1992) 1213.
- [5] G. Bomchil, A. Halimaoui, I. Sagnes, P.A. Badoz, I. Berbezier, P. Perret, B. Lambert, G. Vincent, L.

- Garchery, J.L. Regolini, *Appl. Surf. Sci.* 65 (1993) 394.
- [6] A.G. Nassiopoulou, S. Grigoropoulos, L. Canham, A. Halimaoui, I. Berbezier, E. Gogolides, D. Papadimitriou, *Thin Solid Films*. 255 (1995) 329.
- [7] H.F. Arrand, T.M. Benson, A. Loni, R. Arens-Fischer, M.G. Krueger, M. Thoenissen, H. Lueth, S. Kershaw, N.N. Vorozov, *J. Luminescence*, 80 (1999) 119.
- [8] M.G. Berger, M. Thonissen, R. Arens-Fischer, H. Munder, H. Luth, M. Amtzen, W.Theiss, *Thin Solid Film*. 255 (1995) 313.
- [9] H. P. Maryska, F. Namavar, N. M. Kalkhoran, *Appl. Phys. Lett.* 61 (1992) 1338.
- [10] P. Pirasteh, J. Charrier, A. Soltani, S. Haesaert, L. Haji, C. Godon, N. Errien, *Appl. Surf. Sci.* 253 (2006) 1999.
- [11] A. Loni, L.T. Canham, M.G. Berger, R. Arens-Fischer, H. Munder, H. Luth. H. Arrand, T.M. Benson, *Thin Solid Film*. 276 (1996) 143.
- [12] G. Maiello, S. La Monica, A. Ferrari, G. Masini, V.P. Bondarenko, A.M. Dorofeev, N.M. Kazuchits, *Thin Solid Film*, 297 (1997) 311.
- [13] J. Charrier, C. Lupi, L. Haji, C. Boisrobert, *Mater. Sci. Semicond. Proces.* 3 (2000) 357.
- [14] M. Oehme, J. H. Werner, E. Kasper, M. Jutzi, M. Berroth, *Appl. Phys. Lett*, 89 (2006) 071117.
- [15] F.K. LeGoues, B.S. Meyerson, J.F. Morar, *Phys. Rev. Lett.* 66 (1991) 2903.
- [16] E. Kasper and K. Lyutovich, *Solid-St Electron.* 48 (2004) 1257.
- [17] S. Gouder, R. Mahamdi, M. Aouassa, S. Escoubas, L. Favre, A. Ronda, I. Berbezier, *Thin Solid Films* 550 (2014) 233.
- [18] R. Mahamdi, S. Gouder, M. Aouassa, S. Escoubas, L. Favre, A. Ronda, I. Berbezier, Fifth International conference on NANOstructures SELF-Assembly NANOSEA 2014 Marseille 7th-11thJuly 2014 (Communication Accepted).
- [19] P. Tolstoy, V. Chernychova, A. Skryshevsky, A John Wiley & Sons, INC., Publication, 2003.
- [20] P. Hollins, *Surf. Sc. Reports*, 16 (1992)51.
- [21] R. Ryberg, *Phys. Rev.* B40 (1989) 8567.
- [22] X. L. Wu, G. G. Siu, Y. Gu, N. Tang, T. Gao, X. M. Bao, *Appl. Phys. Lett.* 74 (1999) 827.
- [23] M.A. Vasquez-A., G. Aguila Rodriguez, G. Garcia-Salgado, G. Romero-Paredes, R. Pena-Sierra, *Revista Mexicana De Fisica*, 53 (2007) 431.
- [24] W. Jaimes Salcedo, J. Francisco, R. Fernandez, E. Galeazzo, *Brazilian Journal of Physics*, 27 (1997) 158.
- [25] A. Bragaru, M. Simion, M. Miu, T. Ignat, I. Kleps, V. Schiopu, A. Avram, F. Craciunoiu, *Romanian J. of Information*, 11 (2008) 379.
- [26] H. Sugiyama, O. Nittono, *J Cryst. Growth*, 103 (1990) 156.
- [27] D. Buttard, D. Bellet, G. Dolino, *J Appl Phys*, 79 (1996) 8060.

Optoelectronic properties of nanosized GaAs

T. Eloud , A. Gueddim and N. Bouarissa

Materials Science and Informatics Laboratory, Faculty of Science and Technology, University of Djelfa, Algeria.

Received: 30 April 2014, accepted 26 May 2014

Abstract:

Quantum dots (QDs) represent an interesting topic in the controlled modification of optical, electronic and thermoelectric properties of semiconductor materials. Applications in optoelectronic and other devices have been theoretically proposed due to its easy tuning properties by means of controlling size, shape, and density of QDs.

Gallium Arsenide (GaAs) nanostructures are being a popular subject of research since last three decades because of its fascinating properties and potential for nanoelectronic devices which is the trend of miniaturization nowadays. Gallium Arsenide nanoclusters have a significant change of electronic properties from the bulk. This has been the favor in the fabrication of nano-electronic devices for example, optoelectronic devices and transistors. The electronic band structure and optical properties of a GaAs quantum well have been investigated using the pseudopotential approach.

Keywords: *Quantum dot; GaAs; Optical and electronic properties ; pseudopotential method.*

1. Introduction

In recent years, there has been increasing interest in III-V semiconductors as materials for optoelectronic devices [1]. Gallium arsenide (GaAs) is a compound comprising the elements gallium and arsenic. It is a III-V semiconductor, and is used in the manufacture of devices such as microwave frequency integrated circuits, monolithic microwave integrated circuits, infrared light-emitting diodes, laser diodes, solar cells and optical windows. In addition, it is often used as the substrate material for epitaxial growth of other III-V semiconductors, including InGaAs and GaInNAs [1]. It is technologically very important and is the most studied compound semiconductor material [1, 2].

Many of the band structure parameters of bulk GaAs are known with a greater precision than those for any other compound semiconductor ([3] and references therein; [4–9]). However, the new class of materials formed by semiconductor nanostructures has a large and mostly unexplored ensemble of possible applications. The discovery of the nano-solid of various shapes, and its assemblies, has been quite surprising and has thus generated enormous and ever-increasing interest, paving the way for scientific insights and technological thrusts ([10] and references therein). Experimentalists are now able to grow nanostructures of high quality from diverse semiconductor materials [11, 12], with the ability to dope them [13–20]. New physical and chemical properties have been found to occur in such systems, arising from the large fraction of low-coordinated atoms at the surface and the confinement of electrons to a rather small volume [10]. Semiconductor compounds, owing to the tunability of their electronic and optical properties by the three-dimensional confinement of carriers, have attracted considerable interest as technologically important materials. Thus, the

study of quantum confinement in these semiconductors is one of the promising concepts that may lead to a greater understanding of the solid state.

In this paper, we study the electronic and optical properties of nanostructured GaAs in the zinc-blende structure by using the pseudopotential method (PM). The objective of this work is to show the extent to which the quantum confinement effects can modify the electronic and optical properties of bulk GaAs. Although in most cases the PM approach cannot replace the first-principles methods, one must acknowledge a weak connection between state-of-the-art *ab initio* calculations and experimental achievements in the realm of nanostructures [11]. The reason is that nanostructures are small in size, but large in the number of atoms constituting them. Besides, their relevant observables are accessible only through a proper treatment of excitations [11]. Nevertheless, even at the nanoscale the PM has been shown to give accurate results [11, 21]. Moreover, the computational effort needed by this approach is much smaller than that needed by *ab initio* methods.

The paper is organized as follows. Section 2 briefly describes the computational method used in the calculation. The results regarding the effects of quantum confinement on the Optoelectronic properties are presented and discussed in section 3. Finally, the conclusion drawn from the present study is presented in section 4.

2. Computational details

The current calculations are mainly based on the PM (see e.g. [22]). In the PM, the one-electron Schrödinger equation is replaced by a pseudo-wave equation:

$$\left(\frac{p^2}{2m} + V(r)\right) \varphi_k(r) = E_k \varphi_k(r) \quad (1)$$

With $\varphi_k(r)$ denoting the pseudo-wave function and $V(r)$ the pseudopotential. This equation can be used to calculate the physical properties of semiconductors, which are dependent on the valence and conduction electrons only.

The effective potential $V(r)$ is expanded as a Fourier series in reciprocal lattice space. For a binary compound, the expansion is written in two parts, which are symmetric and antisymmetric with respect to an interchange of two atoms about their midpoint. Because of cancellation between the kinetic and potential energies in the vicinity of atomic cores, only a few Fourier terms suffice.

The PM involves the fitting of the atomic form factors $V_a(G)$, which are treated as adjustable parameters, to experiment. Adjustments to the specific pseudopotential form factors, on which the band structure calculation depends, are made using a nonlinear least-squares fitting procedure [23]. More details of the procedure can be found in [24]. In the present work, three band energy level spacings are used for bulk GaAs, namely $\Gamma - \Gamma$, $\Gamma - X$, and $\Gamma - L$. The experimental band-gap energies for GaAs at $\Gamma - L$ and L high-symmetry points fixed in the fits are 1.42 [25], 1.81 [25] and 1.72 eV [25], respectively. The final adjusted pseudopotential form factors of bulk GaAs are found to be $V_s(3) = -0.239833$, $V_s(8) = 0.0126$, $V_s(11) = 0.059625$, $V_A(3) = 0.060536$, $V_A(4) = 0.05$ and $V_A(11) = 0.01$.

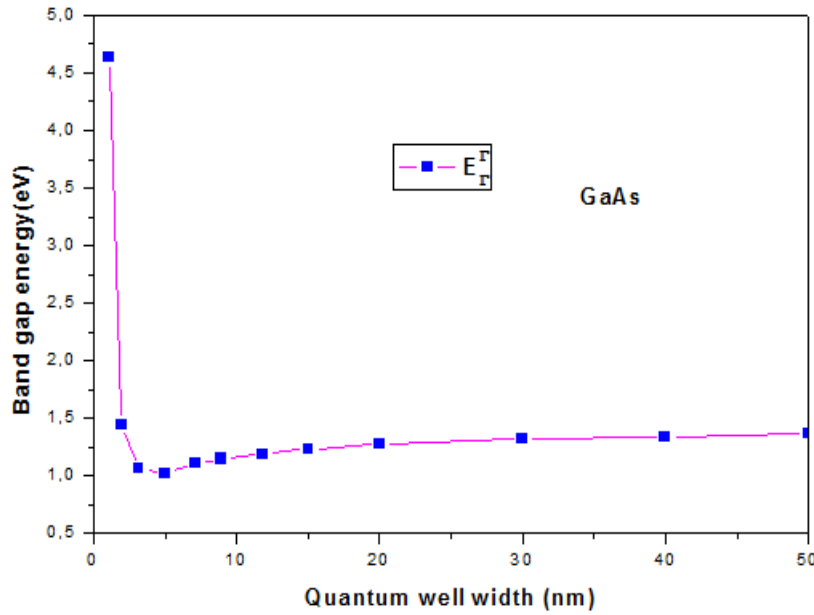


Figure 1. Direct band-gap energy (E_r^Γ) in nanostructured GaAs as a function of quantum well width

The confinement effect on the energy band gap of a quantum well of width a is calculated using the expression [26, 27]

$$E_g = E_g^0 + \frac{\hbar^2 \pi^2}{2a^2} \left[\frac{1}{m_e^*} + \frac{1}{m_h^*} \right] - \frac{1.8e^2}{\epsilon a} \quad (2)$$

where E_g is the band gap of the nanostructure, E_g^0 is its corresponding bulk band-gap energy, ϵ is the effective dielectric constant, and m_e^* and m_h^* are the electron and heavy hole effective masses for bulk GaAs, respectively.

By using equation (2), the band-gap energies for GaAs nanostructures at the Γ , X , and L high-symmetry points in the Brillouin zone have been determined. The results

of calculations are used in the fitting procedure so as to adjust the pseudopotential form factors for each quantum well width a being considered here. The final adjusted pseudopotential form factors for selected quantum well widths of GaAs are given in table 1.

The carrier effective masses m_e^* and m_h^* have been determined for bulk GaAs using a procedure similar to that of Bouarissa [28], where m_e^* and m_h^* are calculated at the Γ valley in the conduction band minimum and the valence band maximum, respectively.

Table 1. Symmetric ($V_S(G)$) and antisymmetric ($V_A(G)$) pseudopotential form factors for selected quantum well widths of GaAs.

Quantum Wellwidth(nm)	Form factors (Ry)					
	$V_s(3)$	$V_s(8)$	$V_s(11)$	$V_A(3)$	$V_A(4)$	$V_A(11)$
3	-0.084025	0.551957	0.001769	-0.705132	0.05	-0.163124
9	-0.216466	0.0126	0.048521	0.58.086	0.05	0.01
15	-0.228204	0.0126	0.053313	0.072672	0.05	0.01
20	0.231214	0.0126	0.054797	0.069643	0.05	0.01
50	-0.237359	0.0126	0.057940	0.062556	0.05	0.01
100	-0.238903	0.0126	0.058860	0.061441	0.05	0.01

3. Results and discussion

The variation of the direct band-gap energy E_r^r (taken as the transition between the top of the valence band state and the lowest conduction band state at the Brillouin zone centre) as a function of the quantum well width in zinc-blende nanostructured GaAs is shown in figure 1. We observe that as the quantum well width increases from 1 to 3 nm, E_r^r decreases rapidly. Going from a quantum well width of 3 to 5 nm, the decrease becomes weak. Beyond a quantum well width of 5 nm, E_r^r increases slightly and then it becomes almost constant in the well width range 20–50 nm. Thus, the quantum confinement effects are expected to open the band gap when the well width is below 4 nm. The band-gap energy due to a quantum confinement effect becomes much larger than the unconfined or bulk band-gap energy for small quantum well widths (in the well width range 0–2 nm).

The computed electron energy band structures of bulk GaAs (solid curves) and GaAs quantum wells with a well width of 3 nm (dotted curves) along several symmetry points in the Brillouin zone are shown in figure 2. The zero energy reference is taken to be at the top of the valence band for both cases considered here. The valence band maximum is formed by the triply degenerate hybridized Ga(4p,3d)–As(4p)-like orbitals in an antibonding manner. The upper valence bands are derived from the p orbital of As and with some admixture of the p orbital of the cation Ga. The bottom of the valence state is a singlet originating from the bonding Ga(4s)–As(4s)-like orbitals that exhibit a weak dispersion. The As states contribute preferably to the bottom of the valence band, while a substantial number of Ga states contribute to the highest valence band. The behaviour of conduction band states is much more complicated than that of valence band states. The

conduction bands are more delocalized and more ‘free-electron-like’ than the valence bands. The free electron behaviour results in more dispersion bands and band crossing. This trend is generally common for III–V semiconductors [29–31]. The first conduction band at Γ is predominantly of cationic s character. The higher conduction states arise from the hybridization of the Ga(4p,3d)- and As(4p,4d)-like orbitals. For bulk GaAs, the minimum conduction band is at the zone centre Γ . Hence, bulk GaAs is a direct-gap semiconductor as is well known. When moving from the bulk to a GaAs quantum well (nanostructure) with a well width of 3 nm (dotted curves, figure 2), one can note that the electronic band structure is generally affected without changing the shapes of the bands. Practically all the bands are shifted. The shift is not constant and depends on the k -point and energy. The L -point conduction-band minimum moves down relative to the valence-band maximum in such a way that the lowest conduction band occurs at the L high-symmetry point instead of Γ (in the case of bulk GaAs). Therefore, nanostructured GaAs becomes an indirect (Γ - L) band-gap semiconductor. The bottom of the valence state in the case of nanostructured GaAs is shifted upwards, thus suggesting a de-enhancement of the full valence band width. This in turn is an indication of the change in the crystal ionicity when moving from bulk to nanostructured GaAs. It has been reported in the literature that the antisymmetric gap (the gap between the first and the second valence bands at the X point) is related to the ionicity of the semiconductor [32, 33] in such a way that it grows with increasing ionicity. As can be seen from figure 2, when moving from bulk to nanostructured GaAs, this gap decreases, thus suggesting the decrease in ionicity of GaAs. Based on quantum confinement theory [10], the effect of quantum confinement on the electronic properties may be explained as due to the Coulomb potential and kinetic energies of electron-hole pairs (usually called excitons),

which are responsible for the photoluminescence blueshift of nanometric semiconductor; the photoluminescence blueshift is dictated by the joint effect of the intrinsic band gap expansion and electron-phonon coupling. On the other hand, the higher-conduction states are also affected when moving to the

nanometric scale. This is an indication of the change in the transport properties when one goes from bulk to nanostructured GaAs. The effect of quantum confinement on the transport properties can be traced back to the confinement of the charge carriers, which results in a change in the carrier's effective masses.

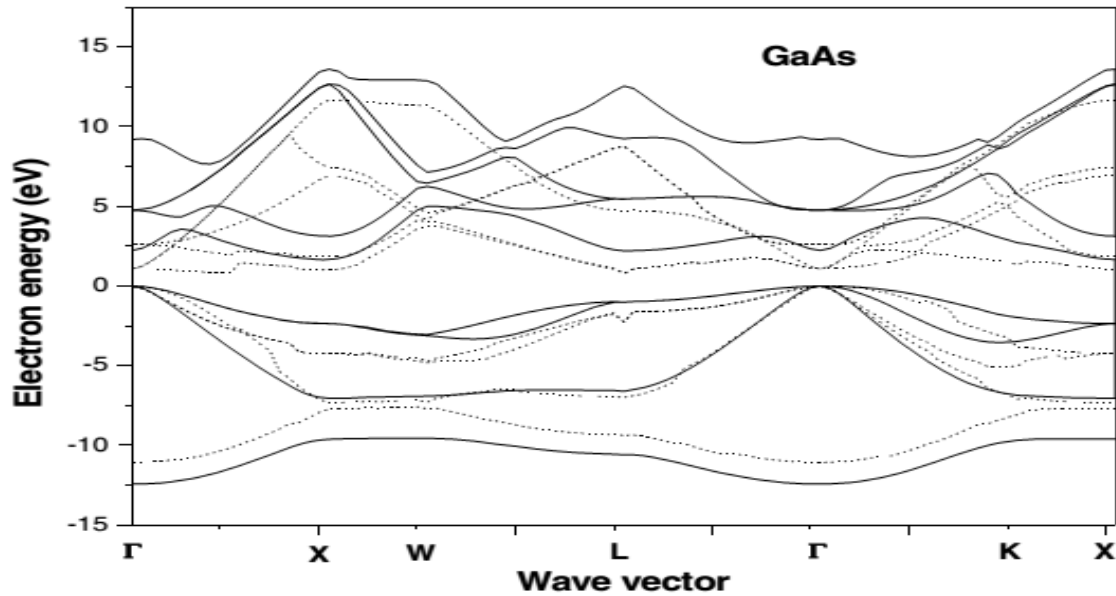


Figure 2. Electronic band structures for bulk GaAs (solid curves) and GaAs quantum wells with a quantum well width of 3 nm (dotted curves).

The study of dielectric properties is concerned with the storage and dissipation of electric and magnetic energy in materials. It is important to explain various phenomena in electronics, optics and solid-state physics. The transverse effective charge e_T^* is a basic parameter characterizing the dielectric properties of solids. Its value is dynamic and reflects the effects of covalency with respect to some reference ionic value [34]. The definition of the charge depends critically on what physical quantity is assumed to be measured. In this paper, e_T^* has been calculated using a relation similar to that used previously in [29], i.e.

$$e_T^* = \frac{\Delta z}{2} + \frac{4\alpha_p}{1+\alpha_p^2} \quad (3)$$

In our case, $\Delta z = -z_{\text{Ga}} + z_{\text{As}}$, where z are the valences. The variation in e_T^* as a function of GaAs quantum well width is depicted in figure 3. From an inspection of this figure, one can note that with increasing the quantum well width up to 50 nm, e_T^* decreases rapidly. However, when the quantum well width goes beyond the value of 50 nm up to 100 nm, the de-enhancement of e_T^* becomes slow and it tends to be constant. This suggests that e_T^* in nanostructured GaAs is larger than that in bulk GaAs. We may then conclude that the effect of confinement in GaAs leads to an increase in e_T^* .

The dielectric constant is an essential piece of information when designing capacitors and in other circumstances where a material might be expected to introduce capacitance into a circuit. In polar materials atomic displacements create dipoles. The long-range macroscopic electric field accompanying these displacements is determined by a non-analytical contribution to the dynamical matrix [35, 36], consisting of the tensors of the Born effective charges and of the high-frequency dielectric constants. Nevertheless, in the zinc-blende structure (like in our case here), those tensors are isotropic [37, 38]. Thus, the high-frequency dielectric constant (ϵ_∞) is a scalar and can be derived from the expression

$$(\epsilon_\infty = n^2) \quad (4)$$

where n is the refractive index. The latter has been calculated using the Ravindra et al [39] model

$$n = \alpha + \beta E_g \quad (5)$$

where E_g is the fundamental energy band gap, $\alpha = 4.084$ and $\beta = -0.62 \text{ eV}^{-1}$. The model has been chosen because it is found to show better agreement with the known data for n in III-V semiconductors [40]. The dependence of ϵ_∞ on the GaAs quantum well width is shown in figure 4. We observe that ϵ_∞ decreases monotonically and nonlinearly with increasing

the quantum well width up to 100 nm. Since materials with high-dielectric constants are useful in the manufacture of high-value capacitors, the behaviour of ϵ_∞ with respect to the quantum well width suggests an enhancement in the ability of nanostructured GaAs to

store electrical potential energy under the influence of an electric field. In other words, the dielectric capacity of nanostructured GaAs becomes stronger and hence the material becomes a good insulator.

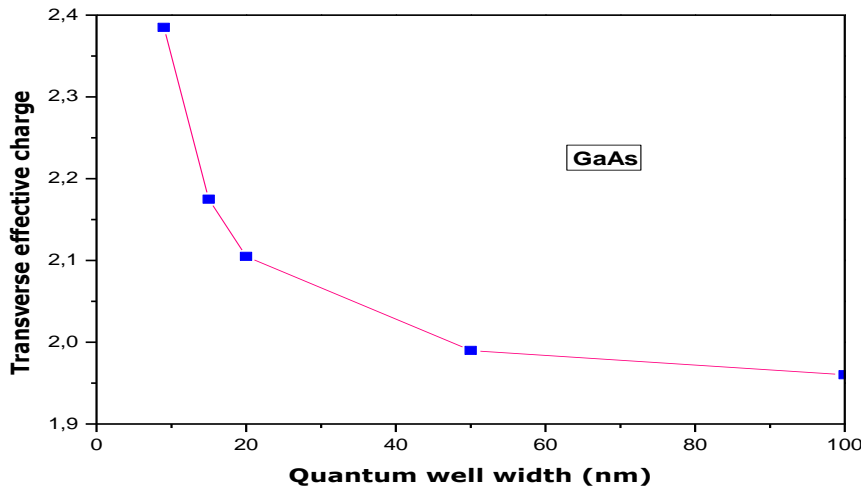


Figure 3. Transverse effective charge in nanostructured GaAs as a function of quantum well width

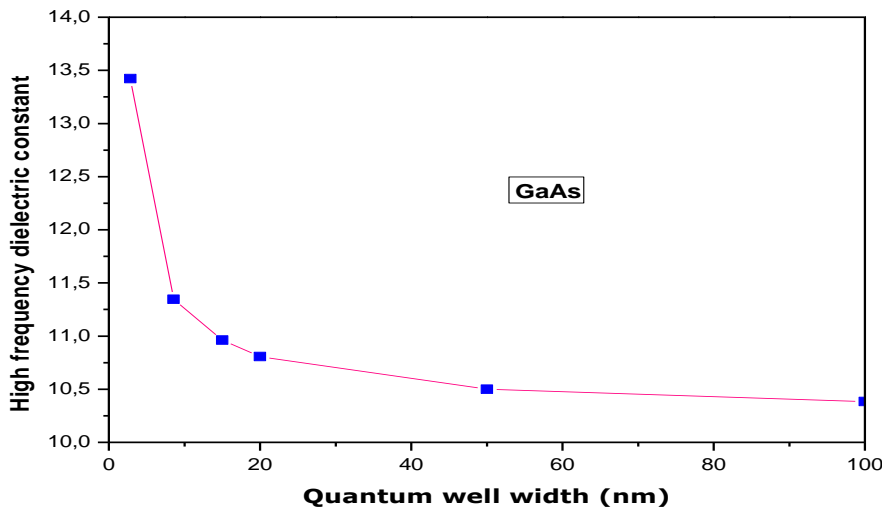


Figure 4. High-frequency dielectric constant in nanostructured GaAs as a function of quantum well width.

The calculations are extended to include the static dielectric constant (ϵ_0).

In this respect, ϵ_0 has been determined using the relation that holds between ϵ_0 and ϵ_∞ [41],

$$\frac{\epsilon_0 - 1}{\epsilon_\infty - 1} = 1 + v \tag{6}$$

where v is given by

$$v = \frac{\alpha_p^2 (1 + 2\alpha_c^2)}{2\alpha_c^4} \tag{7}$$

and α_p is the polarity that was obtained using the Vogl definition [42]

$$\alpha_p = -\frac{V_A(3)}{V_S(3)} \tag{8}$$

Here, $V_S(3)$ and $V_A(3)$ are the symmetric and antisymmetric pseudopotential form factors at G(111), respectively, whereas α_c is the covalency of the material in question that was estimated from the relation

$$\alpha_c = \sqrt{1 - \alpha_p^2} \tag{9}$$

In figure 5, ϵ_0 is plotted against the GaAs quantum well width. Note that ϵ_0 decreases monotonically with increasing the quantum well width. The trend of ϵ_0 seems to be similar to that of ϵ_∞ . Both trends indicate the enhancement of the ability of nanostructured GaAs to store electrical potential energy under the influence of an electric field. On the other hand, it should be

mentioned that for a quantum well width of 100 nm, the value of ϵ_0 is found to be 11.40. This is consistent with the fact that ϵ_0 for bulk GaAs is 11.21 (according to our results) and with the behaviour of ϵ_0 , which shows a decrease with increasing the quantum well width, i.e. beyond a quantum well width of 100 nm, ϵ_0 goes from 11.40 (nanostructured GaAs) to 11.21 (bulk GaAs).

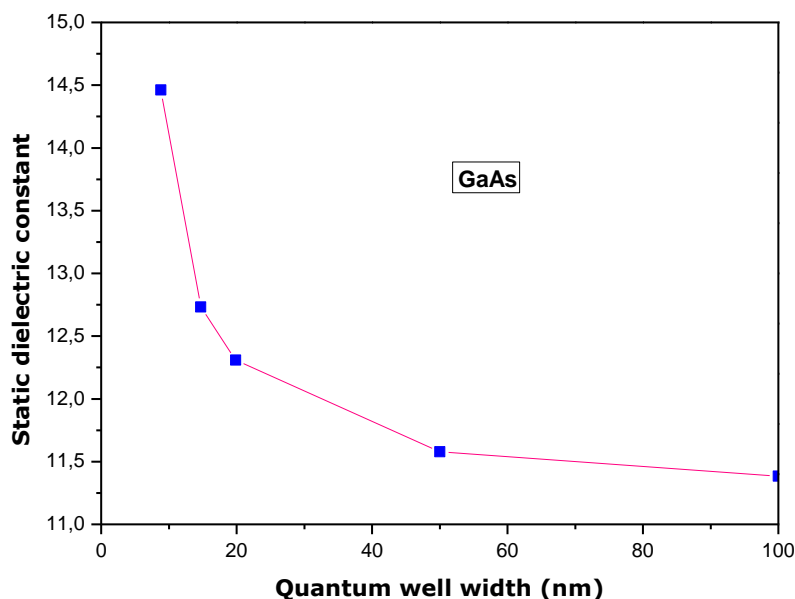


Figure 5. Static dielectric constant in nanostructured GaAs as a function of quantum well width.

4. Conclusion

Based on the pseudopotential approach, the effect of quantum confinement on electronic and optical properties of a GaAs quantum well has been investigated. The quantum well width was taken to be in the range 1-100 nm. The direct band-gap energy E_g^r was found to vary non-monotonically with the quantum well width. An inspection of the electronic band structure showed that quantum confinement has an important effect on the electronic and transport properties. In addition, for a quantum well width of 3 nm, it is found that nanostructured GaAs becomes an indirect ($r-L$) band-gap semiconductor. As far as the dielectric properties are concerned, our results showed that the effect of confinement in GaAs leads to an increase in the transverse effective charge, high-frequency dielectric constant and static dielectric constant, thus indicating that the dielectric capacity of nanostructured GaAs becomes stronger and hence the material of interest becomes a good insulator. The present study may help in the discovery of new desired properties when moving from bulk to nanostructured GaAs.

References

- [1] Vurgaftman I, Meyer J R and Ram-Mohan L R 2001 J. Appl. Phys. 89 5815
- [2] Adachi S 1994 GaAs and Related Materials: Bulk Semiconducting and Superlattice Properties (Singapore: World Scientific)
- [3] Blakemore J S 1983 J. Appl. Phys. 53 R123
- [4] Lautenschlager P, Garriga M, Logothetidis S and Cardona M 1987 Phys. Rev. B 35 9174
- [5] Shen H, Pan S H, Hang Z, Leng J, Pollak F H, Woodall J M and Sacks R N 1988 Appl. Phys. Lett. 53 1080
- [6] Grilli E, Guzzi M, Zamboni R and Pavese L 1992 Phys. Rev. B 45 1638
- [7] Levinstein M, Rumyantsev S and Shur M (ed) 1999 Handbook Series on Semiconductor Parameters vol 2 (Singapore: World Scientific)
- [8] Boucenna M and Bouarissa N 2004 Mater. Chem. Phys. 84 375
- [9] Saib S and Bouarissa N 2006 Solid State Electron. 50 763
- [10] Sun C Q 2007 Prog. Solid State Chem. 35 1

- [11] Bester G 2009 *J. Phys.: Condens. Matter* 21 023202
- [12] Yoffe A D 2001 *Adv. Phys.* 50 1-208
- [13] Celebi C, Koenraad P M, Silov A Y, Van Roy W, Monakhov A M, Tang J M and Flatté M E 2008 *Phys. Rev. B* 77 075328
- [14] Yakunin A M et al 2007 *Nature Mater.* 6 512
- [15] Kudelski A, Lemaitre A, Miard A, Voisin P, Graham T C M, Warburton R J and Krebs O 2007 *Phys. Rev. Lett.* 99 247209
- [16] Fernandez-Rossier J and Brey L 2004 *Phys. Rev. Lett.* 93 117201
- [17] Leger Y, Besombes L, Maingault L, Ferrand D and Mariette H 2005 *Phys. Rev. Lett.* 95 047403
- [18] Besombes L, Leger Y, Maingault L, Ferrand D, Mariette H and Cibert J 2004 *Phys. Rev. Lett.* 93 207403
- [19] Leger Y, Besombes L, Fernandez-Rossier J, Maingault L and Mariette H 2006 *Phys. Rev. Lett.* 97 107401
- [20] Erwin S C, Zu L J, Haftel M I, Efros A L, Kennedy T A and Norris D J 2005 *Nature* 436 91
- [21] Kent P R C, Bellaiche L and Zunger A 2002 *Semicond. Sci. Technol.* 17 851
- [22] Cohen M L and Chelikowsky J R 1988 *Electronic Structure and Optical Properties of Semiconductors* (Berlin: Springer)
- [23] Kobayashi T and Nara H 1993 *Bull. Med. Sci. Tohoku Univ.* 2 7
- [24] Bouarissa N and Boucenna M 2009 *Phys. Scr.* 79 015701
- [25] Aspnes D E, Olson C G and Lynch D W 1976 *Phys. Rev. Lett.* 37 766
- [26] Kayanuma Y 1988 *Phys. Rev. B* 38 9797
- [27] Ragan R 2002 PhD Thesis California Institute of Technology, CA
- [28] Bouarissa N 2006 *J. Phys. Chem. Solids* 67 1440
- [29] Bouarissa N 1998 *Phys. Lett. A* 245 285
- [30] Bouarissa N 2002 *Phys. Status Solidi b* 231 391
- [31] Bouarissa N 2002 *Eur. Phys. J. B* 26 153
- [32] Chelikowsky J R, Wagener T J, Weaver J H and Jin A 1989 *Phys. Rev. B* 40 9644
- [33] Bouarissa N 2007 *Physica B* 399 126
- [34] Lee K-W and Pickett W E 2003 *Phys. Rev. B* 68 085308
- [35] Giannozzi P, de Gironcoli, Pavone P and Baroni S 1991 *Phys. Rev. B* 43 7231
- [36] Wagner J-M and Bechstedt F 2000 *Phys. Rev. B* 62 4526
- [37] Saib S, Bouarissa N, Rodríguez-Hernández P and Muñoz A 2007 *J. Phys.: Condens. Matter* 19 486209
- [38] Saib S and Bouarissa N 2009 *Diamond Relat. Mater* 18 1200
- [39] Ravindra N M, Auluck S and Srivastava V K 1979 *Phys. Status Solidi b* 93 k155
- [40] Bouarissa N 2006 *Mater. Lett.* 60 2974
- [41] Davydov S Yu and Tikhonov S K 1998 *Semiconductors* 32 947
- [42] Vogl P 1978 *J. Phys. C: Solid State Phys.* 11 251

Study of light propagation in TiO_2 multilayer DBRs

K. Zellagui, A. Dekhira, O. Ouamerali

*Laboratoire de Chimie Théorique computationnelle et Photonique
Faculté de chimie USTHB, BP 32 El Alia Bab Ezzouar, Alger, Algeria*

Received: 30 April 2014, accepted 26 May 2014

Abstract

This work take for objective to develop an efficient simulation code to determine the optical properties of some photonic materials based on TiO_2 , namely DBRs. Basing on the Transfer matrix method (TMM), we have implemented an algorithm which calculates the reflectance and the transmittance of multilayered photonic materials and plots the corresponding spectra.

1. Introduction

During the 21st century, manipulation of photons has become the core study of area of the photonics. Photons are fast and unlimited natural sources that could replace the role of electronics. A novel class of materials referred to as “photonic crystals” is synthesized to manipulate light.

Photonic crystals [1, 2] are structures which dielectric constant is periodically changed on length scale in one, two or three dimensions (*1D*, *2D* and *3D*) with periodicity comparable to the light wavelength [3]. As analogous to electrons in an atomic crystal, the propagation of electromagnetic waves in periodic dielectric structures can be forbidden in certain directions and within a certain frequency range [4],

[5]. Because of this similarity, this frequency range, in which photonic crystals exhibit strong reflection, is called as photonic. The one-dimensional multilayered structure is the simplest photonic crystal.

Distributed Bragg reflectors (DBRs) are periodic structures with a unit cell of two dielectric layers having different refractive indices and thicknesses. They can be considered as unidimensional photonic crystals and are used in a wide variety of optoelectronic devices including semiconductor lasers, solar cells and so on.

In this work, we developed an efficient simulation code to determine the optical properties of two DBRs, such as TiO_2/air and $\text{TiO}_2/\text{SiO}_2$ (1D).

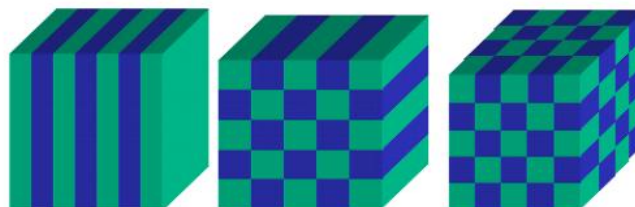


Figure 1: Samples of photonic structures *1D*, *2D* and *3D*

2. Theoretical background

Photons that are propagating into a photonic crystal are analogous to electrons moving into a conventional crystal “semiconductor”. That photon-electron analogy is due to the analogy between the equation of Helmholtz, derived from Maxwell equations [6], and the equation of Schrödinger.

$$\nabla^2 \Psi(\vec{r}) = -\frac{2m}{\hbar^2} (U - V(\vec{r})) \Psi(\vec{r}) \quad (1)$$

$$\vec{\nabla} \times [\vec{\nabla} \times \vec{H}(\vec{r})] = \left(\frac{\omega}{c}\right)^2 \epsilon(\vec{r}) \vec{H}(\vec{r}) \quad (2)$$

As there is similarity between electronic semiconductors and photonic crystals, the concepts of solid state crystals, viz, reciprocal space, Brillouin zones, dispersion relations, Bloch wave functions [7], etc; can also be applied to photonic crystals. That is why it is logical to call the periodic dielectric structures photonic crystal.

3. Algorithm and validation

Basing on the Transfer matrix method (TMM) [8], we have implemented an algorithm which calculates the reflectance and the transmittance of multilayered photonic materials and plots the corresponding spectra.

We have used a technique that is basing on the finite differences in frequency domain, and chosen the real space instead the space of Fourier to build the transfer matrix of each layer of the photonic structure. The calculation of transfer matrix is done by a recursive algorithm. The code developed using MATLAB 2009 can calculate the reflectance and the transmittance of any one-dimensional photonic crystal as well as their Bloch modes via the determination of eigenvalues of the transfer matrices.

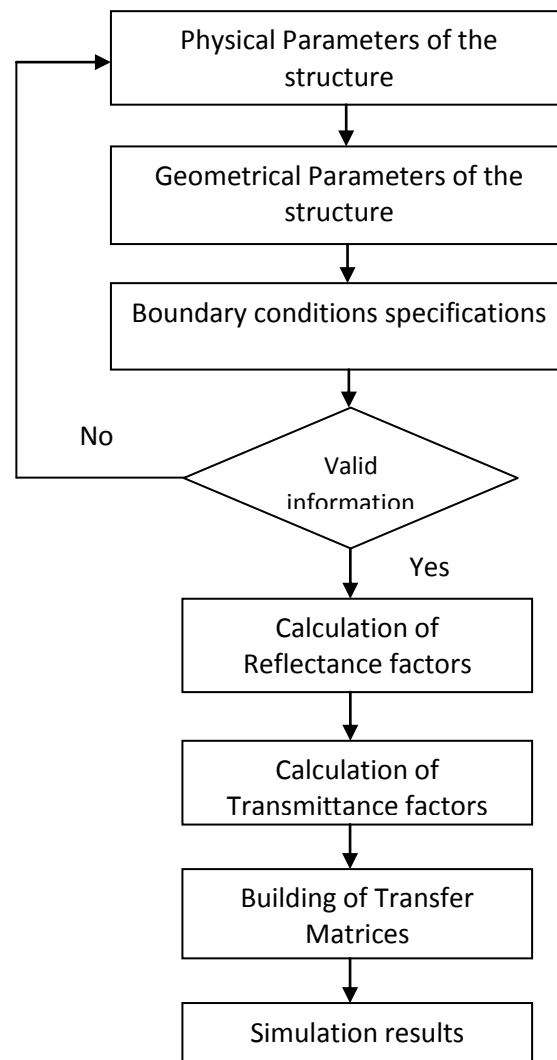


Figure 2: the algorithm flowchart

The reflectance and the transmittance of a TiO₂-SiO₂-based DBR were calculated in order to validate the efficiency of our code. The results are in

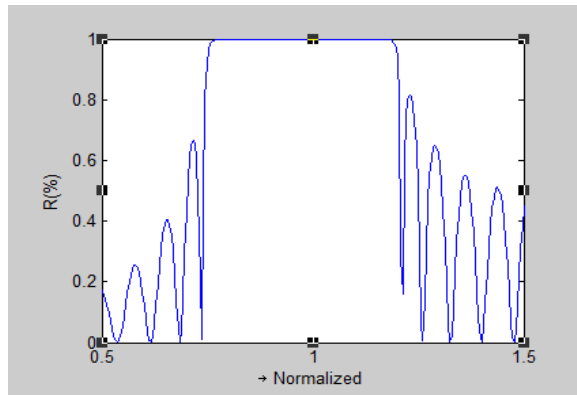


Figure 3: Reflectance spectrum of TiO₂-SiO₂ DBR

good agreement with those found in literature as well as those obtained by other methods.

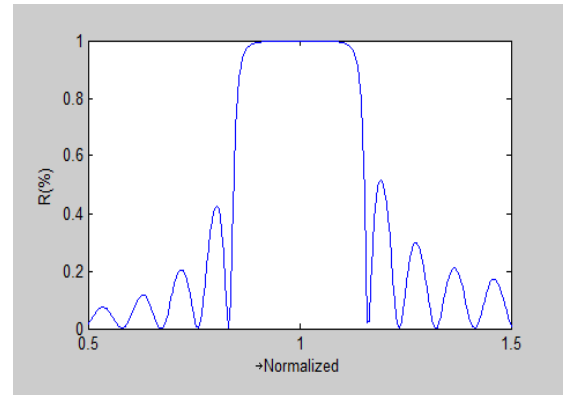


Figure 4: Reflectance spectrum of TiO₂-air DBR

4. Conclusion

In this work, the development of an algorithm and a computer code to calculate the optical properties (reflectance and the transmittance) of multilayered 1D photonic crystals is presented. The algorithm developed is based on the transfer matrix method TMM in the frequency domain. We have described briefly the algorithm and presented the flowchart related to.

References

- [1] E. Yablonovitch, Inhibited spontaneous emission in solid-state physics and electronics, *Phys. Rev. Lett.* 58, p. 2059, 1987.
- [2] S. John, Strong localization of photons in certain disordered dielectric superlattices. *Phys. Rev. Lett.* 58, 2486–2489, 1987.
- [3] Nagpal, Y., Sinha, R. K., Modeling of Photonic Band Gap Waveguide Couplers, *Microwave Opt. Technol. Lett.*, vol. 43, pp. 47-50, 2004.

- [4] Ozbay, E., Temelkuran, B., Reflection Properties and Defect Formation in Photonic Crystals, *Appl. Phys. Lett.*, vol. 6, pp. 69, 1996.

- [5] Arriaga, J., Knight, J. C., Russel, P. St. J., Modeling The Propagation of Light in Photonic Crystals Fibers,

Physica D, vol. 189, pp. 100-106, 2004.

- [6] JOANNOPOULOS J.D., MEADE R.D. & WINN N.J. Photonic Crystal - Molding the Flow of Light. Princeton Univeristy Press. 1, 407, 1995.

- [7] H.Miguez, C.Lopez, F.Meseguer, A.Blanco, L.Vasquez, R.Mayoral, M.Ocana, V.Fornés et A.Mifsud, "Photonic cristal properties of packed ubmicrometric SiO₂ spheres", *Applied physics Letters*, 71, p 1148-1150, (1997). 3, p.53-66, 2002.

- [8] D. Felbacq and E. Centeno, *Optique Communication* 199, pp 39-45, 2001.

Analysis of Pulse Width Modulation DC-DC Chopper -On/Off Control via a second order filter-

Souad Belhour⁽¹⁾, Abdelouahab Zaatri⁽²⁾

⁽¹⁾Département de Physique, Faculté des Sciences,

⁽²⁾Département de Mécanique, Faculté des Sciences de l'Ingénieur,
Laboratoire des Applications de Technologie Avancées (LATA), Constantine,
Université 1, 2500 Constantine, Algérie

Email : souad_belhour1@yahoo.fr

Received: 30 April 2014, accepted 26 May 2014

Abstract

*This paper presents the analysis of a nonlinear on/off control system including a filter of a second order in the closed loop for compensating the fluctuation of the irradiation as well as the variations of the load. The proposed system is capable of generating a pulse width modulation which is used to design and built up a *PWM* (Pulse Width Modulation) chopper dedicated to regulate fluctuating power supplies (photovoltaic, wind, etc.). The study essentially focuses on determining the relationship between the pulse duration with respect to system parameters and technological requirements. The theoretical study is followed by a simulation of a *DC – DC* chopper.*

Keywords: on/off control, pulse width modulation, chopper design, optimal control

1-Introduction

In recent years, renewable energy regains serious interest in most developed countries. Indeed, these energies are renewable, non-polluting, distributed through space and can be collected and converted by means of converters. Among renewable energy sources that have experienced great development, include solar photovoltaic, wind energy and biomass. However, one of the major problems concerning the spread of renewable energy is to further reduce system cost while increasing performance.

But if the first challenge relates to the manufacturing technology, there is another problem concerning the adaptation of this energy for use in various applications such as pumping water, controlling electric motors, lighting, battery charging, etc. [1, 2]. This concerns in particular the regulating devices which are *DC/DC* converters (choppers) and *DC/AC* (inverters). The interest in this problem is that the performance of these devices directly influences the overall performance of the energetic system as a whole. Research in the field of *DC – DC* converters and *DC – AC* revealed for more than a decade the importance of on-off power supplies. Indeed, the use of power transistors (bipolar and *VMOS*) as fast static switches in the power amplifier reduces the consumption. Also, it enables sufficiently high cutting frequencies to

facilitate the filtering of harmonics and consequently reducing the weight, size and cost of the converter. In this respect, switching converters based on the technique of pulse width modulation (*PWM*) were imposed as a viable system for the case of low power [3, 4, 5, and 6].

In a previous work [7], we have designed and built up an experimental *DC / DC* converter based on an on/off element with a feedback via a first order filter. The load was outside the loop. As a consequence, the system was able to regulate the output voltage w.r.t to the fluctuations of the solar energy. But did not regulate the output voltage w.r.t the variation of the load.

The work proposed in this article is an extension of [7]. It concerns the study of an *on – off* control system using a feedback via a second order filter including the load. In principle; this system enables the compensation of both variations stemming from the irradiation and of the load. The proposed model can also be analyzed in terms of time optimal control and can therefore be studied under the theory of "maximum principle" as established by [5]. This system is operated in the context of power converters which are dedicated to renewable energy sources (photovoltaic, wind, etc.) [8, 9, and 10], especially for the design and realization of a chopper.

Such a system is capable of generating a Pulse Width Modulation (*PWM*) which is used for the design and realization of a chopper. This study essentially aims to determine the relationship between the switching frequency according to system settings and related technological parameters. The theoretical study led to the establishment of conditions that determine the system performance based on the parameters chosen. It is followed by the simulation and the realization of an experimental chopper.

2-System Modeling Overview

The proposed control system is shown schematically in Figure (1). It can be reduced to the study of an *on-off* control system. It comprises the direct forward path a nonlinear $+/-$ symmetric element

denoted N . This nonlinear element is characterized by its threshold width h and its *on-off* level which equals $+E$ and $-E$. It also comprises a linear second order filter denoted W . In the feedback system path includes a matching element denoted k of the output to the set point value. The quantities involved are:

- f_0 : the set point signal.
- $X(t)$: the control signal.
- $U(t)$: the controlled signal.
- $Z(t)$: the feedback signal.
- $V(t)$: the output signal.

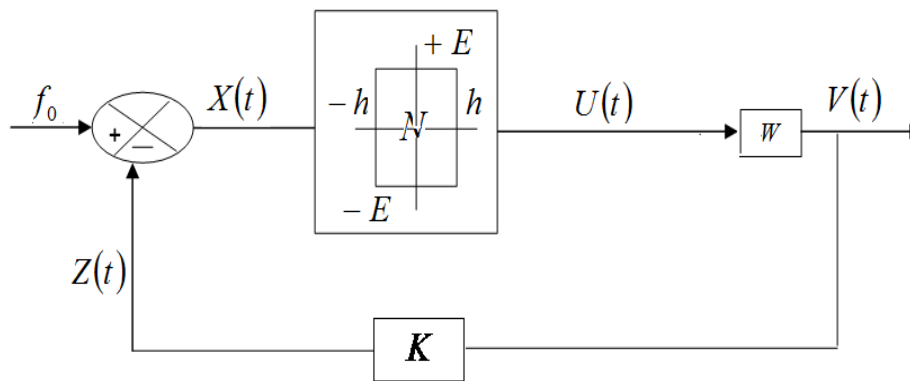


Figure (1): Scheme of the control system

The reference variable f_0 is compared with the controlled quantity $Z(t)$. The set point signal f_0 assumed constant in the case of a chopper. The resulting error is the control variable $X(t)$ which acts as input to the nonlinear N element. The signal $U(t)$ at the output N is converted by a linear second order W filter. This provides the output $V(t)$ to be used by the actual load. The inclusion of the filter W in the servo is used to regulate the output voltage vis-à-vis fluctuations (radiation, wind speed ...) and load variations. Note also that this system corresponds to the case of the optimal time control as developed by. [5]

The correspondence between the previous study and the envisioned *PWM DC-DC* is interpreted as follows. E Corresponds to the voltage provided by

the solar panel. It is thus, in general fluctuating and needs to be regulated before being able to feed the loads. $U(t)$ is the controlled voltage at the output of the *PWM* modulator. $V(t)$ is the output voltage which effectively supplies the load (engine; pump, battery, etc.)

2.1. the behavior of the non-linear element N

For simplicity, we assume that the input voltage $X(t)$ is triangular and can cross the threshold values $(+/-h)$ at specific instants. As a result, the output $U(t)$ will be a succession of constant pulses of amplitude E with alternating sign. The duration and the *on-off* intervals are variables. The instants during which the signal jumps are called the switching instants. These instants are determined by the following conditions

$$\begin{aligned}
 &si \quad X(t) > +h \quad et \quad \frac{dx(t)}{dt} > 0 \quad \Rightarrow U(t) = -E \\
 &si \quad X(t) < -h \quad et \quad \frac{dx(t)}{dt} < 0 \quad \Rightarrow U(t) = +E
 \end{aligned}
 \tag{1}$$

The evolution of the output signal in correspondence with the input signal is shown in **Figure (2)**

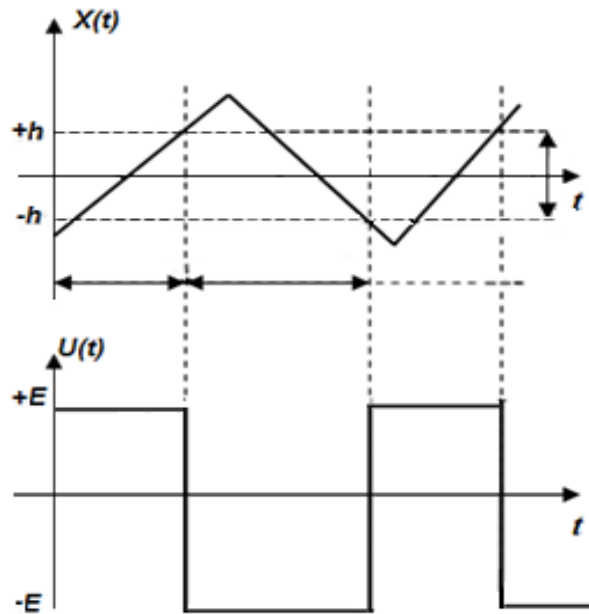


Figure (2): Input $X(t)$ and output $U(t)$ of the nonlinear element

II.2- Signal Analyze of the second order filter

The feedback is performed after the output of a linear element; the second filter order as show in Figure (3) consists of an inductor L , its internal resistance r ; a capacitor C , and the working load

R . The input V_{in} and output V_{out} of this filter. When negligent the internal resistance r of the coil w.r.t the load resistance R of use, the input-output relation of the filter is given by the differential equation of second order

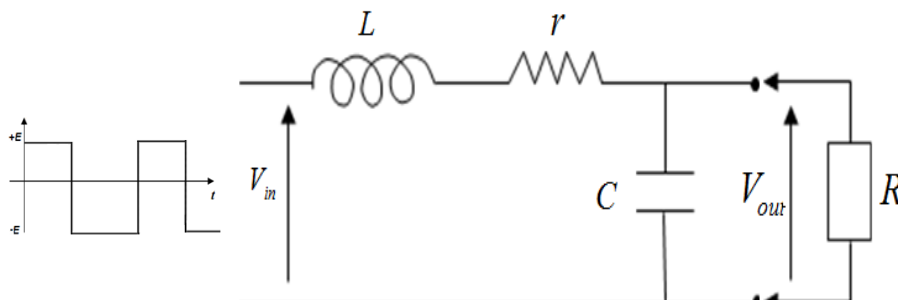


Figure (3): low pass filter of 2nd order

$$V_{in} = (-1)^k E = V_{out} + RC \frac{dV_{out}}{dt} + LC \frac{d^2V_{out}}{dt^2} \quad (2)$$

The transfer function of this filter is:

$$\frac{V_{out}}{V_{in}} = F(s) = \frac{\omega_n^2}{s^2 + 2\xi\omega_n s + \omega_n^2} = \frac{\omega_n^2}{s_1 - s_2} * \left[\frac{1}{s - s_1} - \frac{1}{s - s_2} \right] \quad (3)$$

where

s : Is the Laplace variable.

ω_n, ξ : The angular frequency and dumping coefficient of the system

$$\omega_n = \frac{1}{\sqrt{LC}} \quad \xi = \frac{R}{2} * \sqrt{\frac{C}{L}}$$

3. Determination of Pulse Durations

3-1 General case

The determination of pulse duration is a fundamental problem in the analysis of *on-off* non linear systems. In the general case, obtaining an analytical solution is extremely, even impossible. And only graphical techniques or simulation can help to analyze this type of problems. The determination of analytical expressions of period of self-oscillation in case $f_0 \neq 0$ is difficult. Nevertheless, an analytical solution has been found for $f_0 = 0$ and is presented in this section.

For $f_0 = 0$, the input signal V_{in} of the second order filter is a square wave defined by

$$V_{in}(s) = X(s) = \frac{2E}{s} th \frac{Ts}{4} \quad (4)$$

By considering the characteristic equation (3) of the second order filter:

$$s^2 + 2\xi\omega_n s + \omega_n^2 = 0 \quad (5)$$

We can distinguish three cases with respect to the damping factor ξ , according to the two roots. s_1 and s_2 .

➤ for $\xi > 1 \Rightarrow$ we get two real roots which are ;

$$s_{1,2} = -\xi\omega_n \pm \omega_n \sqrt{\xi^2 - 1}$$

➤ for $\xi < 1 \Rightarrow$ we get two imaginary roots which are .

$$s_{1,2} = -\xi\omega_n \pm j\omega_n \sqrt{1 - \xi^2}$$

The system can generate oscillations,

➤ For $\xi = 1 \Rightarrow$ we get a double root:

$$s_{1,2} = -\omega_n$$

The output of the filter as an open loop

$$Y(s) = F(s) * X(s) \quad (6)$$

This can be rewritten.

$$Y(s) = \frac{2E}{s} * th \frac{Ts}{4} * \frac{\omega_n^2}{s_1 - s_2} * \left[\frac{1}{s - s_1} - \frac{1}{s - s_2} \right] \quad (7)$$

The switching condition according to the residue theorem is given by the closed loop condition:

$$Y(t_i) = 2E \oint \frac{1}{s} th \frac{Ts}{4} \left[\frac{\omega_n^2}{s_1 - s_2} \right] \left(\frac{1}{s - s_1} \right) e^{-st} ds + 2E \oint \frac{1}{s} th \frac{Ts}{4} \left[\frac{\omega_n^2}{s_1 - s_2} \right] \left(\frac{1}{s - s_2} \right) e^{-st} ds = h \tag{8}$$

It can be written as follows

$$\frac{1}{s_1} th \frac{Ts_1}{4} - \frac{1}{s_2} th \frac{Ts_2}{4} = \frac{h}{2E\omega_n^2} (s_1 - s_2) \tag{9}$$

This expression is the core of our analysis. We notice that the period of auto oscillation T depends on the parameters of the nonlinear element (E, h) as well as from the parameters of the second order filter (ω_n, ξ).

$$\frac{th \frac{T}{4} (-\xi\omega_n + \omega_n \sqrt{\xi^2 - 1})}{-\xi\omega_n + \omega_n \sqrt{\xi^2 - 1}} - \frac{th \frac{T}{4} (-\xi\omega_n - \omega_n \sqrt{\xi^2 - 1})}{-\xi\omega_n - \omega_n \sqrt{\xi^2 - 1}} = \frac{h}{E\omega_n} \sqrt{\xi^2 - 1} \tag{10}$$

We notice that the period of auto oscillation depends from the parameters of the nonlinear element (E, h) as well as from the parameters of the second order filter (ω_n, ξ).

$$\frac{-\xi \sin\left(\frac{T}{2} \omega_n \sqrt{\xi^2 - 1}\right) + \sqrt{\xi^2 - 1} sh\left(\frac{T}{2} \xi \omega_n\right)}{ch\left(\frac{T}{2} \xi \omega_n\right) + \cos\left(\frac{T}{2} \omega_n \sqrt{\xi^2 - 1}\right)} = \frac{h}{2E} (1 + 2\xi^2) \sqrt{\xi^2 - 1} \tag{11}$$

And the presence of oscillatory functions that complicates the solution of this equation

c- Third case:

This is a border line case which corresponds to a double root, the expression (9) becomes

$$\frac{-\omega_n T + 4sh \frac{\omega_n T}{2}}{2\omega_n \left(1 + ch \frac{T\omega_n}{2}\right)} = \frac{h}{E\omega_n^2} \tag{12}$$

3-2 -Analyze of the auto-oscillation period w.r.t damping factor

a- First case:

In the first case where the two roots are real, the expression (9) becomes

b- Second case:

In the second case $\xi \ll 1$, we imaginary conjugate roots, the expression (9) becomes:

4. Simulation Results

4-1 Simulation Scheme

Beside that we have found out the analytical expressions that links the auto-oscillation period w.r.t the damping factor, it remains difficult to found out the roots of such equations (10, 11, and 12). As a consequence, we proceed to determine these roots by simulation and to draw the relationship. We illustrate some cases by simulation with Simulink (Figure 4).

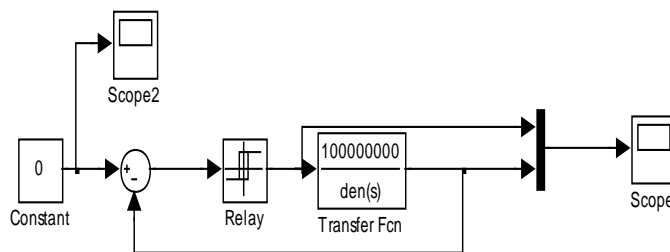


Figure (4): scheme of the 2nd order system with Simulink

The simulations cases have been performed with the following values; $f_0 = 0 V$ $\omega_n = 10000 rd/s$, $h = 0.1 E = 12$.

Somme examples of simulation for different values of ξ are presented below (Fig5). The period of self-oscillation is measured from the graphical representation of the output as provided by Simulink :

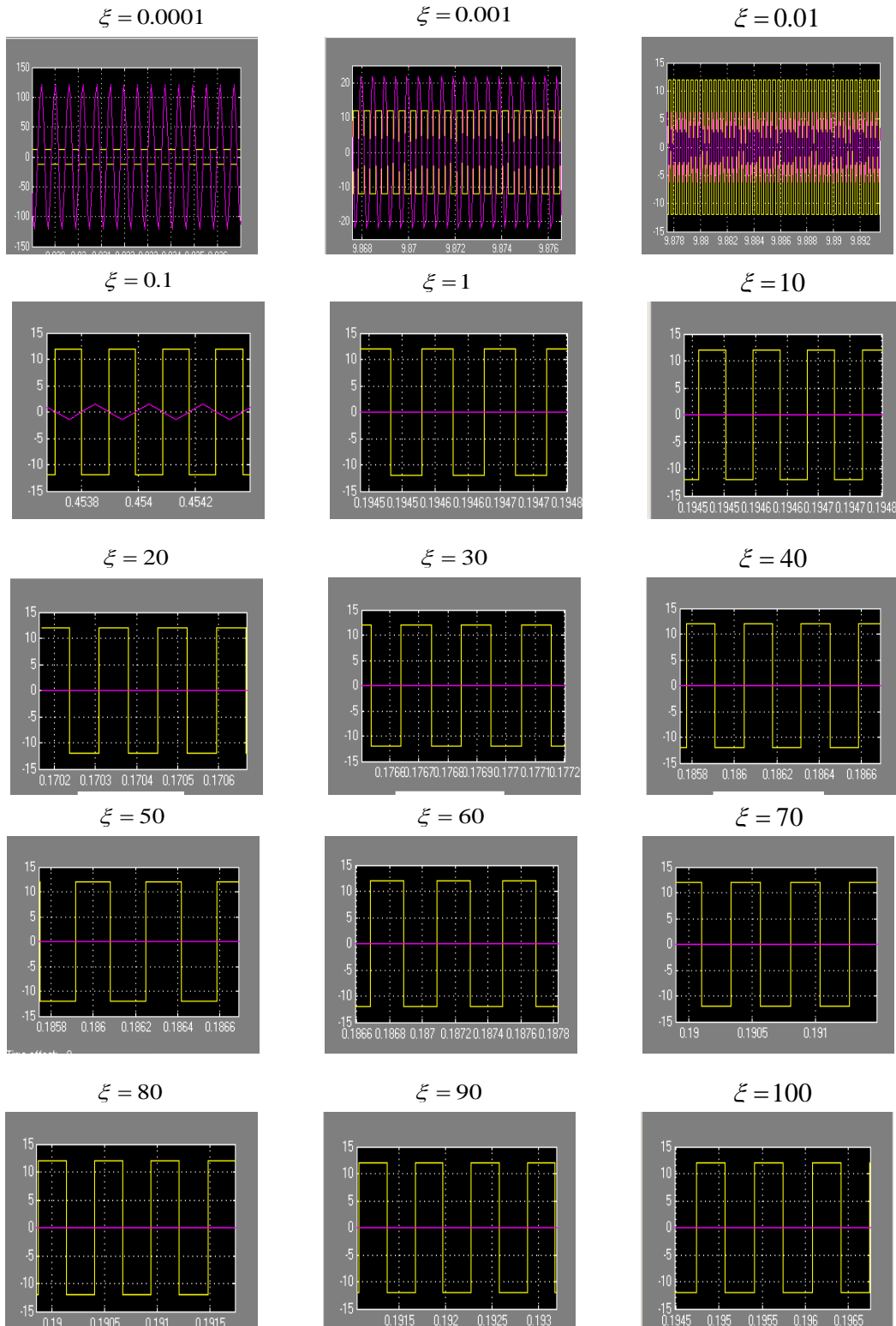
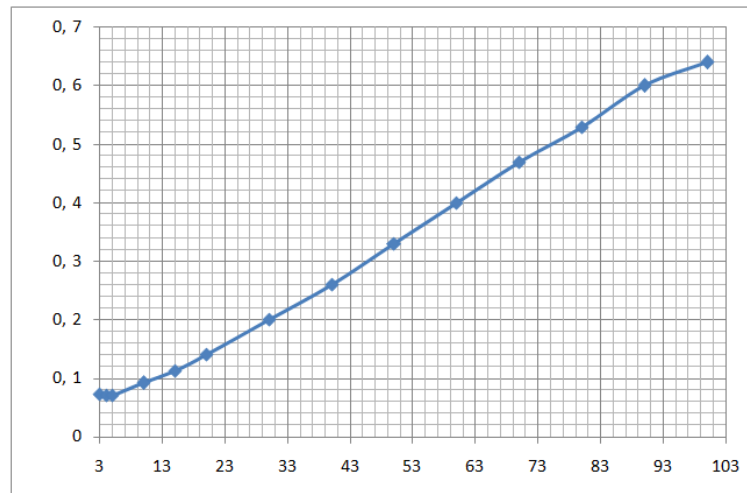


Figure.5. Input and output Signals for different values of ξ

4-2 The variation of T with respect to ξ

The variation of pulse durations (T) with respect to ξ have obtained through the simulation and the results are presented on **Figure (6)**.

$T * 10^{-4}$ (s)



ξ

This curve shows that the variation of $T = f(\xi)$ increases linearly. We notice a minimal value of T ($T = 10 \mu s$) that corresponds to ξ approaching unity. For $\xi < 1$ the system becomes unexplainable. This relationship is the basic for dimensioning and optimizing the PWM choppers under consideration.

5. Conclusion

We have presented detailed study fan *on-off* feedback system via a second order filter. Such a system is capable of generating a *PWM* of varying duration and duty cycle and is used for the design and realization of choppers. This system is designed to enable the compensation of both variations stemming from the irradiation and of the load.

This theoretical study essentially aims to determine the relationship between the switching frequency according to system settings and related technological parameters. However, the determination of pulse duration is a fundamental problem in the analysis of *on-off* non linear systems. In the general case, obtaining an analytical solution is extremely difficult, even impossible. And only graphical techniques or simulation can help to analyze this type of problems. Nevertheless, an analytical solution of $T = f(\xi)$ is given for $f_0 = 0$ involving the parameters of the on-off system and of the second order filter.

Given the complexity of the expressions obtained for self oscillation ($f_0 = 0$), we have used graphical representation of simulation to determine graphically the relationship $T = f(\xi)$. Moreover; experiments to validate this analysis are under course.

References:

- [1] Huang J., Padmanabhan K. and Collins O. M., 2011. The sampling theorem with constant amplitude variable width pulses. *IEEE Transactions on Circuits and Systems* **58**, 1178-1190.
- [2] Rodriguez J., Jih S. L. and Fang Z. P., 2002. Multilevel inverters: a survey of topologies, controls, and applications. *Industrial Electronics, IEEE Transactions on* **49** (4), 724-738
- [3] Andrews M. and Boys J. T., 1993. Improvements in estimating the spectra of random PWM waveforms. *Electronics Letters* **29**(21), 1822-1823.
- [4] Gow J. A. and Manning C. D., 2000. Photovoltaic converter system suitable for use in small scale stand alone or grid connected applications. *IEE Proceedings-Electric Power Applications* **147**(6), 535-543.

- [5] Hausmair., Katharina., Chi S., Singerl P. and Vogel C., 2013. Aliasing-free digital pulse-width modulation for burst-mode RF transmitters. *IEEE Transactions on Circuits and Systems* **60** (2), 415-427
- [6] Maksimovic D., Jang Y. and Erickson R., 1996. Nonlinear-carrier control for high-power-factor boost rectifiers. *IEEE Trans. Power Electron* **11**(4), 578-584
- [7] Sun J. and Chen M., 2008. Nonlinear average current control using partial current measurement. *IEEE Trans. Power Electron* **23**(4), 1641-1648
- [8] Krzysztof G., 2009. Non-linear average electrothermal models of buck and boost converters for SPICE. *Microelectronics Reliability* **49**, 431-437.
- [9] Subrata B., Dinkar P. and Jayanta P., 2007. Design, implementation, and testing of a single axis levitation system for the suspension of a platform. *ISA Transactions* **46**, 239-246.
- [10] Sun, J., 2002. Small-signal modeling of variable-frequency pulse-width modulators. *IEEE Trans. Aerosp. Electron. Syst* **38**(3), 1104-1108

Monte Carlo model to study $\text{Al}_x\text{Ga}_{1-x}\text{N}$ nanostructure under an electron beam. Influence of aluminum mole fraction

L. Leghrib and A. Nouri

Material Sciences Department, University of Oum-El-Bouaghi, Oum-El-Bouaghi, 04000, Algeria
Nouri_kader@yahoo.fr

Received: 30 April 2014, accepted 26 May 2014

Abstract

In the present paper, a Monte Carlo calculation model of $\text{Al}_x\text{Ga}_{1-x}\text{N}$ nanostructure is presented in order to describe the influence of different parameters such as the accelerating energy and primary current of electron beam as well as the influence of aluminum mole fraction. The carrier excess generated during the collision of the incident electron with the atoms of the material (random walk) is calculated as a function of depth. The radiative recombination of electron hole pairs can be collected as a light (CL signal). Numerical results obtained are compared with experimental data.

Keywords: Gallium nitride, Monte Carlo, Cathodoluminescence, nanostructure, quantum well.

1. Introduction

In the last few years the technology of group III nitride epitaxy has shown great progress on modern materials and electronic devices as well as on high electron mobility transistors (HEMTs), Light emitting diodes (LED) and photovoltaic solar cell, etc [1,11].

Cathodoluminescence (CL) has been used with success in studying luminescence properties of semiconductors[6-8]. Cathodoluminescence (CL) simulation was carried out to study the heter structure of GaAs[10].

Light emitted from a specimen in response to electron-beam irradiation. The electrons and the holes recombine radiatively[13].

The Al mole fraction is a critical parameter which determines the emission wavelength in AlGa_N light-emitting diodes [11,12].

2. Model

2.1 Electron-Matter Interaction

The electron-matter interaction during SEM analysis may result in a range of effects on incident electrons, which can be divided into two primary types of electron scattering: elastic and inelastic [2]. The e-h pair produced during the random walk process of the incident electrons within the sample. The simulation was performed with the following steps: (1) defining

numerous random pathways s of the incident electrons in the sample (2) dividing the sample into several zones; (3) calculation of carrier excess Δn (e-h pair) within each zone based on Monte Carlo method (random walk) taking into account the conditions of the incident electron beam (e.g., accelerating voltage E_0 , primary current I_0). The radiative recombination of carrier excess results cathodoluminescence signal. More detailed calculation procedures and explanations are available in Aouati *et al.* [9].

2.2 Penetration depth

The penetration depth of an incident electron can be given by:

$$R_e(\mu\text{m}) = \left(\frac{0.0276 \cdot A}{\rho \cdot Z^{0.889}} \right) \cdot E_0^{1.75} \quad [3]$$

$$R_e(\mu\text{m}) = \left(\frac{0.0398}{\rho} \right) \cdot E_0^{1.7} \quad [4]$$

$$R_e(\mu\text{m}) = \left(\frac{25.6}{\rho} \right) \cdot \left(\frac{E_0}{30} \right)^{1.7} \quad [5]$$

Where ρ is the density of material, Z is the atomic number, A is atomic mass and E_0 is the accelerating energy

But in our model, the penetration depth is calculated by a numerical method based on the random walk [9].

2.3 Cathodoluminescence signal (I_{CL})

The cathodoluminescence signal I_{CL} can be calculated by integration of minority carrier excess taking into account the absorption phenomenon:

$$I_{CL} \propto \int_0^{\infty} \Delta n(z) e^{(-\alpha z)} dz$$

Where Δn is the minority carrier excess (for a p-type semiconductor), α is the absorption coefficient.

In our case, the integral becomes summation because the numerical calculation procedure:

$$\begin{aligned} I_{CL} &= \sum_{i=1}^n \Delta n_i e^{-\alpha z_i} \\ &= \Delta n_1 e^{-\alpha z_1} + \Delta n_2 e^{-\alpha z_2} + \dots + \Delta n_n e^{-\alpha z_n} \\ &= CL_1 + CL_2 + \dots + CL_n \end{aligned}$$

Where Δn_i is the minority carrier excess inside the zone i after the random collisions.

Table 1. Some bulk material parameters for GaN and Al_xGa_{1-x}N used in our calculation. [14]

Parameter	GaN	Al _x Ga _{1-x} N
Crystal density g (g/cm^3)	6.15	6.15-2.92x
Energy band gap E_g (eV)	3.43	$x^2 - 2.43x + 3.43$

3. Results and conclusion

The first main result of this work is

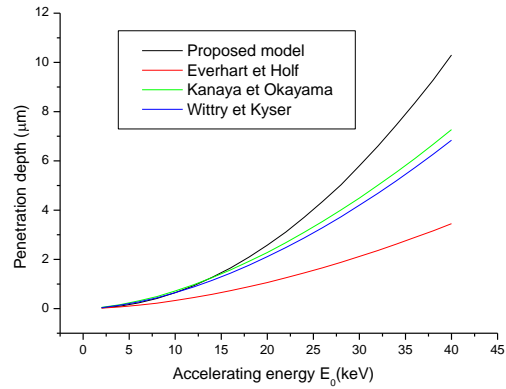


Fig.1. Penetration depth of electrons in GaN as a function of accelerating energy

The maximum electron depth is proportional to the accelerating energy.

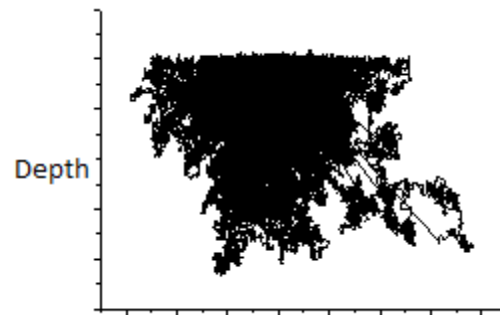


Fig.2. Monte Carlo simulations of the penetrated electrons paths into GaN

Fig.2. shows 100 simulated electron trajectories for a 20-keV electron beam.

The Al composition of Al_xGa_{1-x}N layers was estimated by assuming the Vegard's law. The band gap of ternary compound depends on composition fraction x is given by:

$$E_{g_{AlGaN}}(x) = x^2 - 2.43x + 3.43 \text{ eV (hexagonal) [14].}$$

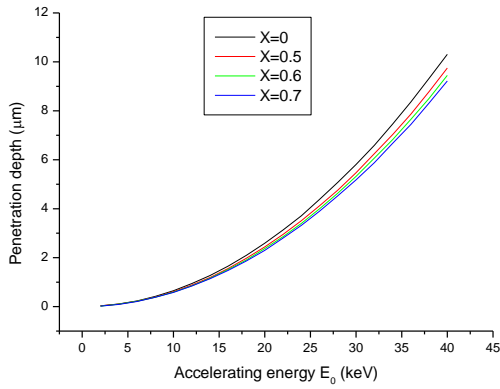


Fig.3. Penetration depth of electrons in AlGaN for different values of content X

At the beam energies between 0 and 40 keV, the electrons penetrate into GaN on a depth of about 0-10 μm, but in AlGaN the penetration depth is smaller, that depends on Al mole fractions X (Fig.3)

The Cathodoluminescence signal decreases when the aluminum percentage increases, this decreasing may be explicated by the increasing in band gap energy (the possibility of recombination decreasing) (Fig.4).

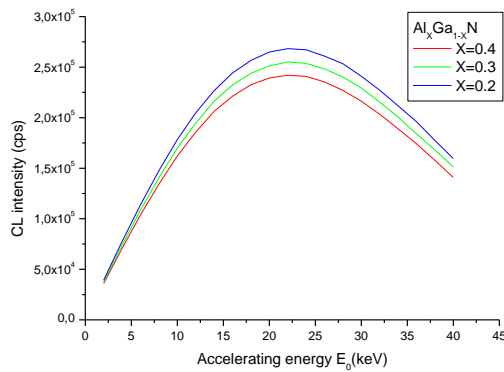


Fig.4. Cathodoluminescence signal as a function of accelerating energy for different values of content X

Figures 5 and 6 show the variation of minority carrier excess as a function of depth. The general form is Gaussian. The quantity of carrier excess depends on aluminium fraction.

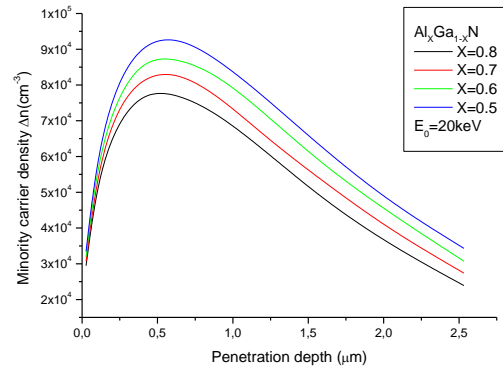


Fig.5. Minority carrier excess as a function of depth in AlGaN for different values of content X

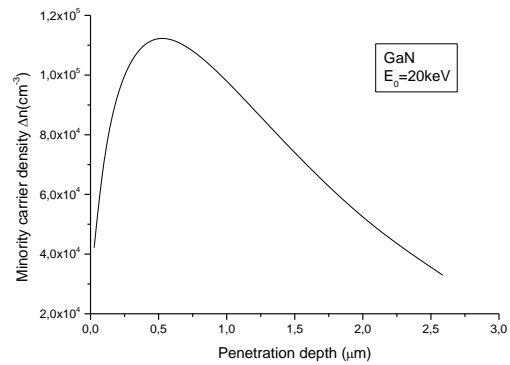


Fig.6. Minority carrier excess as a function of depth in GaN

4. Conclusions

The dependence of the cathodoluminescence signals on aluminum mole fraction is calculated and shows the cathodoluminescence signals decreases when the aluminum mole fraction increases.

A process of varying the elemental components of the semiconductor alloy in a controlled way to achieve a desired band gap that can emit a desired wavelength of radiation.

Finlay, the Al mole fraction is a critical parameter which determines the emission wavelength in AlGaN light-emitting diodes.

The band gap energy can be tailored to get desired visible light radiation.

References

- [1] T.D. Moustakas "Nitride Semiconductors: Why they work in optoelectronic devices?", ECS Transactions, 41 (6) 3-11 (2011).
- [2] B. G. Yacobi, D.B. Holt, "Cathodoluminescence Microscopy of Inorganic Solids", Edition Plenum Press, New York, 1990.
- [3] K. Kanaya, S.Okayama, J. Phys. D: Appl. Phys. 5, pp. 43, 1972.
- [4] T. E. Everhart and P. H. Hoff, J. Appl. Phys., Vol. 42, No. 13 (1971) 5837.
- [5] D. B. Wittry and D. F. Keyser, J. Appl. Phys., 38,375, 1967.
- [6] C. Klein, J. Appl.Phys. 39(4), 2029, 1968.
- [7] J.1. Pankove and E.R. Levin "Scanning electron microscopy studies of GaN", J. Appl. Phys., Vol. 46, No.4, April 1975.
- [8] Nouiri, A., Chaguetni, S., Belabed, N., 2006. "Monte Carlo model of the temperature rise at a GaAs surface under an electron beam", Surface and Interface Analysis 38, 1153-1157.
- [9] Aouati, R., Nouiri, A., "Monte Carlo Calculation for cathodoluminescence of AlGaAs/GaAs nanostructure", International Journal of Nanoscience Vol. 10, No. 3 (2011) 373-379.
- [10] A. Nouiri, R. Aouati, "Monte Carlo model of cathodoluminescence characterization of AlAs/GaAs/AlAs laser diode", Physica E 40 (2008) 1751-1753.
- [11] H.X. Jiang et J.Y. LIN, "AlGa_xN and InAlGa_xN alloys - epitaxial growth, optical and electrical properties, and applications" Opto-Electron. Rev., 10, no. 4, (2002).
- [12] M. GODLEWSKI *et al* "In-depth and in-plane profiling of light emission properties from semiconductor-based heterostructures", Opto-Electron. Rev., 12, no. 4, (2004).
- [13] K. Fleischer *et al* "Depth profiling of GaN by cathodoluminescence microanalysis", Appl. Phys. Lett., Vol. 74, No. 8, 22 February (1999).
- [14] Abdelkader Hamdoune, Université Abou-Bakr Belkaïd-Tlemcen

Spectroscopic Ellipsometry characterization of thin films deposited on silicon substrate

S. Benzitouni^a, A. Mahdjoub^b, M. Zaabat^a.

Faculty of Exact Sciences and Natural and Life Science

^aActive Devices and Materials Laboratory, Larbi Ben M'hidi University, Oum El Bouaghi 04000 Algeria

^bMaterials and Structures Laboratory, Electronic Systems and Reliability, Larbi Ben M'hidi University, Oum El Bouaghi 04000 Algeria

Received: 30 April 2014, accepted 26 May 2014

Abstract

In this work we used spectroscopic ellipsometry to study the optical properties of thin films deposited on silicon substrates. Analysis of the ellipsometric spectra allows determining the thickness of the deposited films and the dispersion of their optical indices. The proposed method is to develop a theoretical model to calculate the ellipsometric angles as function of the wavelength of the incident light. The theoretical model is based on the theory of propagation of electromagnetic waves in a stratified medium and effective medium approximation of Bruggman. The theoretical ellipsometric spectrum will be adjusted to the measured spectrum to determine the optical characteristics of the deposited films. In the case of silicon oxynitride thin films this analysis allows among others to determine the chemical composition of the deposited film and to detect any index gradient in the layer.

Keywords: *thin film, ellipsometry, silicon oxynitride, optical properties.*

1. Introduction

Spectroscopic ellipsometry is one of the most accurate and reliable optical techniques to characterize a large variety of materials and thin films on any substrate. Because today's devices such as solar cells[1, 2], light emitting devices[3, 4] and thin film transistors[5] are formed by complex multilayers structures, the correct use of ellipsometry requires appropriate models for data analysis. The Principle of modeling is to adjust the parameters of a theoretical model to minimize the difference between the measured and calculated spectra. Most of the problems encountered in the analysis of ellipsometric spectra are related to inadequate choice of the model rather than the quality of measurements.

In this work, we proposed a mathematical model based on the theory of propagation of electromagnetic waves in stratified media. The optical indices dispersion is described by the Bruggman approximation of effective media. This model was used to analyze ellipsometric spectra measured on thin films of silicon oxynitrides deposited on silicon substrate.

Oxynitrides are particularly interesting compounds, intermediate between silica and nitride, they encompass mechanical and dielectrical qualities of silica, and present the advantage of serving as a diffusion barrier to impurities, like nitrides. These qualities give them opportunities in the field of microelectronics or to achieve antireflection which improves the performance of solar cells[6-15].

2. Theoretical model

Ellipsometry is a method of optical analysis based on the change of polarization state of light upon reflection on a flat surface. We send to the sample a polarized light and the change of polarization introduced by the sample is analyzed. These changes can be represented by two Fresnel coefficients r_s and r_p (Eq.1) [16-18], acting on each of the field components (Fig. 1). The report of these coefficients is defined in Eq.2:

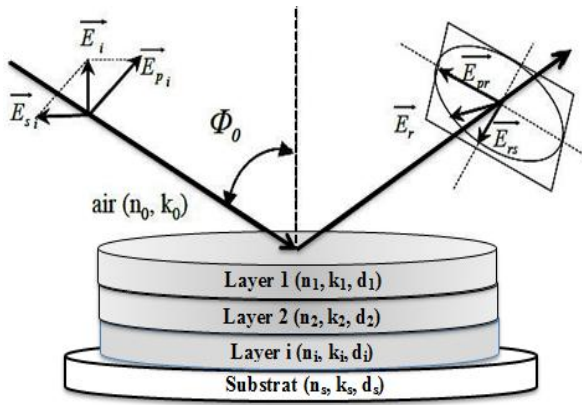


Fig. 1. Schematic view of an ellipsometric measurement, using multilayer optical system.

$$r_p = \frac{E_p^r}{E_p^i} = \frac{\left| \frac{E_p^r}{E_p^i} \right| e^{i(\delta_p^r - \delta_p^i)}}{\left| \frac{E_p^r}{E_p^i} \right|} = \left| r_p \right| e^{i\delta_p}$$

$$r_s = \frac{E_s^r}{E_s^i} = \frac{\left| \frac{E_s^r}{E_s^i} \right| e^{i(\delta_s^r - \delta_s^i)}}{\left| \frac{E_s^r}{E_s^i} \right|} = \left| r_s \right| e^{i\delta_s} \quad (\text{Eq. 1})$$

$$\rho = \frac{r_p}{r_s} = \tan \psi e^{i\Delta} \quad (\text{Eq. 2})$$

The measurable of ellipsometry are the phase and the light amplitude changes upon reflection which are denoted as ψ and Δ .

$$\tan \psi = \left| \frac{r_p}{r_s} \right| \quad \text{And } \Delta = \delta_p - \delta_s \quad (\text{Eq. 3})$$

Ellipsometry is an indirect method; it does not give direct access to the physical parameters of the sample (optical thickness and the optical indices dispersion). It is necessary to use a model for describing the optical response of a sample. i.e. to calculate the reflection coefficients r_p and r_s and then find the Ψ and Δ angles. To calculate the optical response of a stratified media, we used the matrix representation of Abeles [19] which represents each stratum by a matrix:

For S mode:

$$\begin{pmatrix} E_0^- \\ E_0^+ \end{pmatrix} = \frac{1}{2} \begin{pmatrix} 1 & -\frac{1}{N_0 \cos \theta_0} \\ 1 & \frac{1}{N_0 \cos \theta_0} \end{pmatrix} \prod_{j=1}^L \begin{pmatrix} \cos \beta_j & \frac{i \sin \beta_j}{\tilde{N}_j \cos \theta_j} \\ i \tilde{N}_j \cos \theta_j \sin \beta_j & \cos \beta_j \end{pmatrix} \begin{pmatrix} 1 \\ \tilde{N}_s \cos \theta_s \end{pmatrix}$$

And for P mode:

$$\begin{pmatrix} E_0^- \\ E_0^+ \end{pmatrix} = \frac{1}{2} \begin{pmatrix} 1 & -\frac{\cos \theta_0}{N_0} \\ 1 & \frac{\cos \theta_0}{N_0} \end{pmatrix} \prod_{j=1}^L \begin{pmatrix} \cos \beta_j & \frac{i \sin \beta_j \cos \theta_j}{\tilde{N}_j} \\ i \tilde{N}_j \sin \beta_j / \cos \theta_j & \cos \beta_j \end{pmatrix} \begin{pmatrix} 1 \\ \tilde{N}_s / \cos \theta_s \end{pmatrix}$$

Where

$$\beta_j = \frac{2\pi \tilde{N}_j d_j}{\lambda} \cos \theta_j$$

β_j the phase shift due to the layer is calculate from θ_j the incidence angle, \tilde{N}_j the complex optical index and d_j the layer thickness.

To model the optical indices of silicon oxynitrides we used the effective media approximation of Bruggman (BEMA) (Eq.4) [20]. In this approximation, the deposited layers are considered as combinations of homogeneous mixtures of silicon nitride Si_3N_4 and SiO_2 silica. The optical indices are then calculated from the volume fractions f of SiO_2 and Si_3N_4 and their optical indices published by Palikin his handbook [21].

$$\sum_{n=1}^L f_n \frac{\varepsilon_n - \varepsilon}{\varepsilon_n + 2\varepsilon} = 0 \quad (\text{Eq.4})$$

For minimizing the difference between measured and calculated spectra, quantified by the quadratic error χ^2 , we used the simplex method [22].

$$\chi^2 = \frac{1}{2M} \sum_{i=1}^M \left((\tan \psi_{ex}^i - \tan \psi_{th}^i)^2 + (\cos \Delta_{ex}^i - \cos \Delta_{th}^i)^2 \right) \quad (\text{Eq.5})$$

The proposed model allowed highlighting the effect of the thickness and the chemical composition (volume fractions) of the films on the ellipsometric spectra. The confrontation of calculated spectra to ellipsometric measures taken on real structures allowed the validation of the theoretical model.

3. Results and discussions

The proposed model is used first to describe the optical indices dispersion of SiO_2N_x using the effective media approximation of Bruggman, and then to study the influence of the chemical composition and the film thickness on the ellipsometric angles. Finally the proposed model was validated by the confrontation between calculated and experimental spectra.

3.1. Optical indices calculated

The effective media approximation of Bruggman permits to have a good description of the optical indices dispersion depending from chemical composition of the deposited films. It thus enables to distinguish between the optical behavior of silica-rich and silica-poor films.

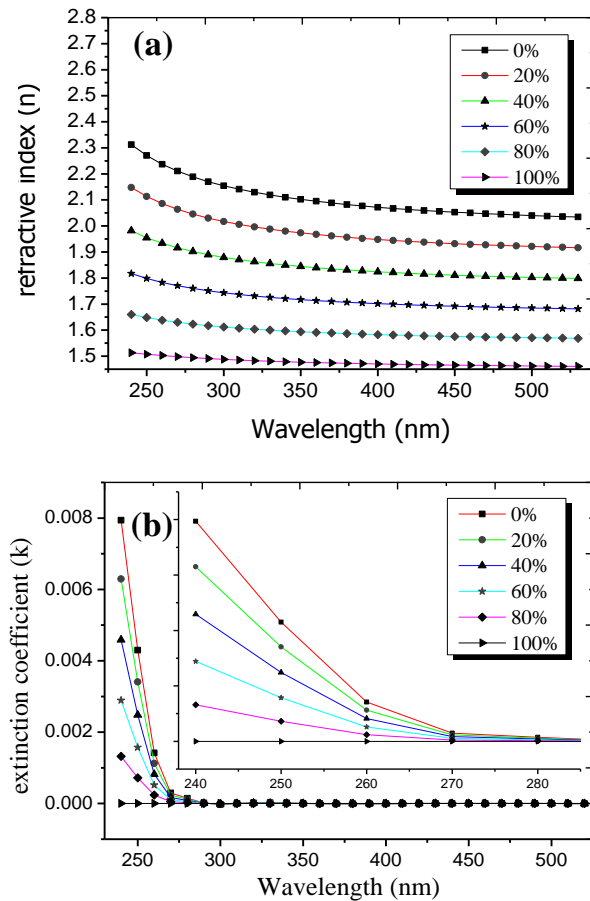


Fig. 2. (a) Calculated refractive index n , and (b) extinction coefficient k of SiO_xN_y thin films as a function of the volume fraction of SiO_2 .

In Figure 2 both n and k decrease with increasing the proportion of SiO_2 , which explain the dependence between the optical indices and the chemical composition of SiO_xN_y . (b) Shows a strong absorption above to 6 eV which corresponds to a direct photo-excitation process and a total transparency in the visible and near infrared ranges.

Ellipsometric spectra

Using the proposed theoretical model, ellipsometric spectra were calculated for homogeneous films of oxynitrides containing 20% silica. The thickness varies from 150 nm to 350 nm. The incidence angle was taken equal to 70° in agreement with experiment.

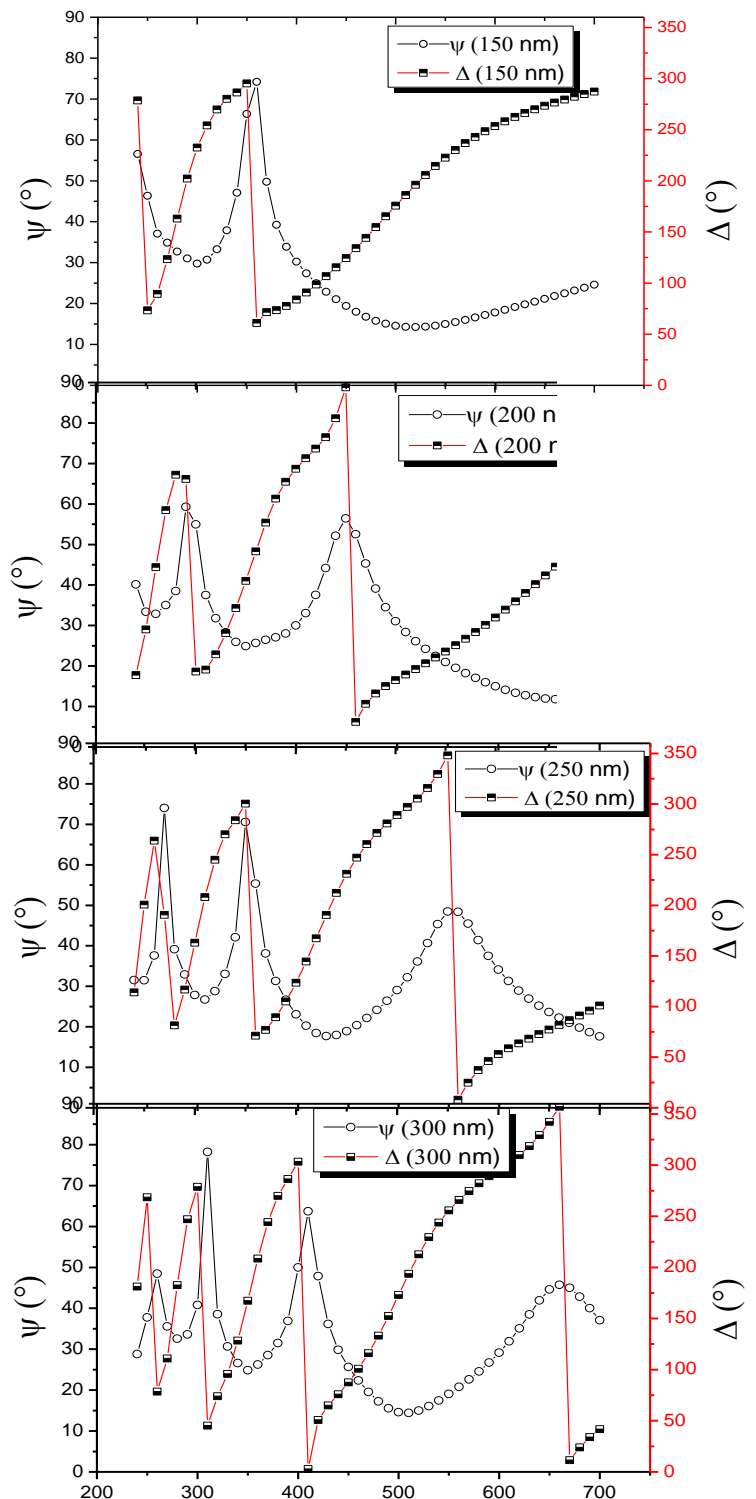


Fig. 3. Ellipsometric spectra calculated for variable thickness of SiO_xN_y containing 20% silica.

In Figure 3 we observe a pseudo-periodic variation in ellipsometric spectra depending on the wavelength. This

variation is due to interferences resulting from reflections at the two interfaces Air / film and film / Substrate. It is noted that when the film thickness increases the number of oscillations increases accordingly.

3.2. Analysis of Measured spectra

To validate the model two samples were used, the first sample presents an oxynitride film deposited using variable precursors flow while the second film is deposited at constant flow.

Ellipsometric spectra recorded between 250nm and 825nm for the two samples were compared with those calculated by the proposed model. The adjustment is done using progressively models with an increasing number of strata (monolayer, bilayer and trilayer models).

The trilayer model gives the best agreement between calculation and measurements, for the two samples (Fig.4). The optical thickness and volume fraction of SiO₂ of each sample are reported in Table 1. Both deposited films are silica-rich, and this is probably due to the high reactivity of oxygen

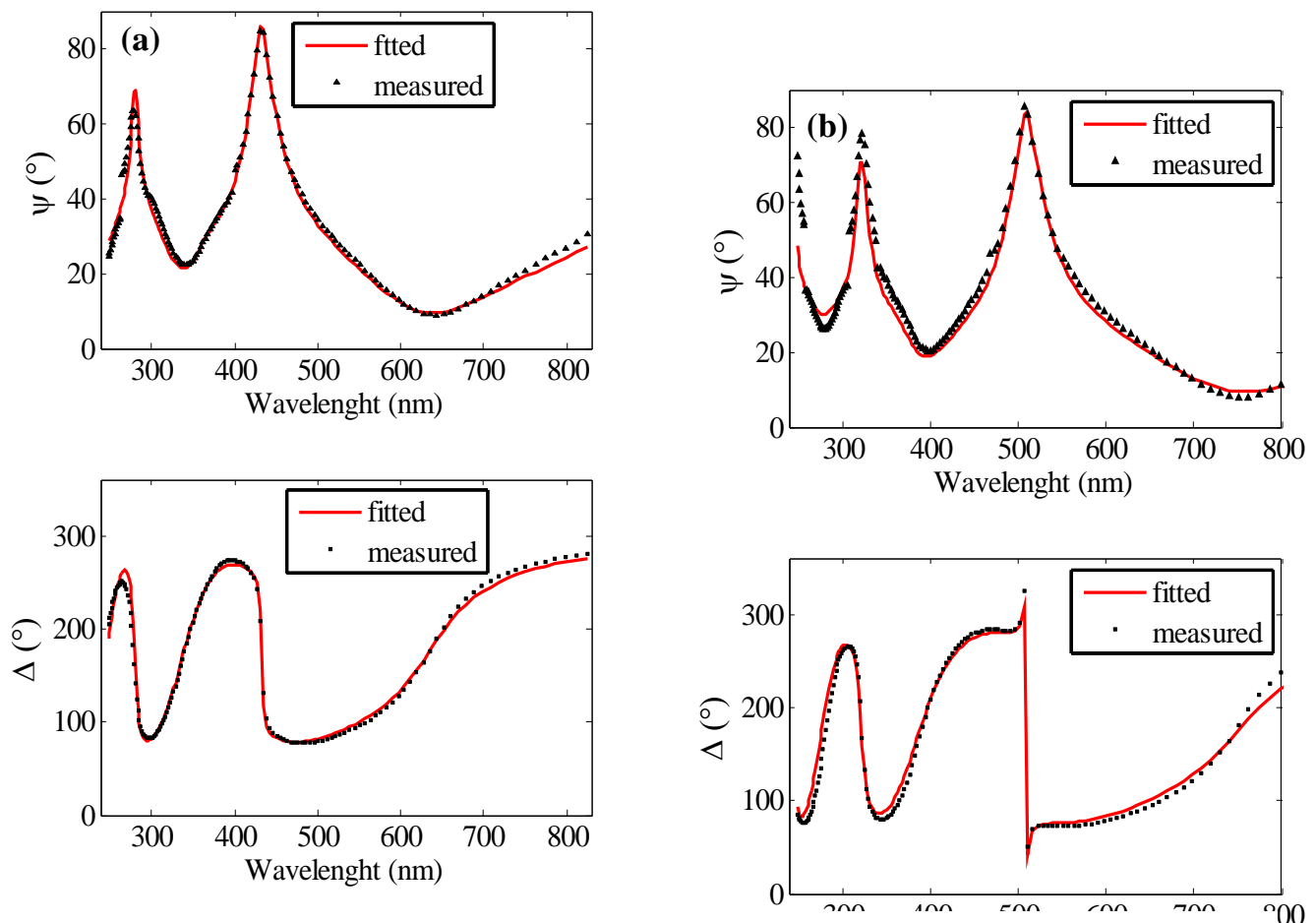


Fig. 4. Experimental and fitted spectra of ψ and Δ angles, corresponding to two samples of SiO_xN_y thin films: (a) 259 nm, (b) 306 nm.

Table 1; Ellipsometric analysis				
sample	Sample 1		Sample 2	
	Thickness (nm)	f_{SiO_2} (%)	Thickness (nm)	f_{SiO_2} (%)
Layer 1	115	98	3	80
Layer 2	104	78	138	85
Layer 3	42	50	164	88

The analysis of measured ellipsometric spectra reported in table 1 shows that for sample 1 the volume fraction of SiO₂ is gradually decreasing from the air to the substrate which means that the deposited film is inhomogeneous in depth. Contrary to this, for sample 2, the volume fraction of SiO₂ is almost constant, which indicates the homogeneity of the deposited thin film. These results are in accordance with the sample conditions of preparation.

The quadratic error χ^2 shown in figure 5 represents the mean deviation between the experimental and that calculated spectrally by different proposed optical systems such as monolayer, bilayer and trilayer. We can clearly see that for the sample 1, more the number of layers increases more the error decreases and the adjustment with multilayer system becomes better. Such a compartment confirms the results of Table 1 (inhomogeneous deposited film). While for the sample 2, the quadratic error is almost constant indicating that the monolayer modelling system is sufficient. This confirms the results of Table 1 (comparable volume fraction of SiO₂ in the depth of deposited film).

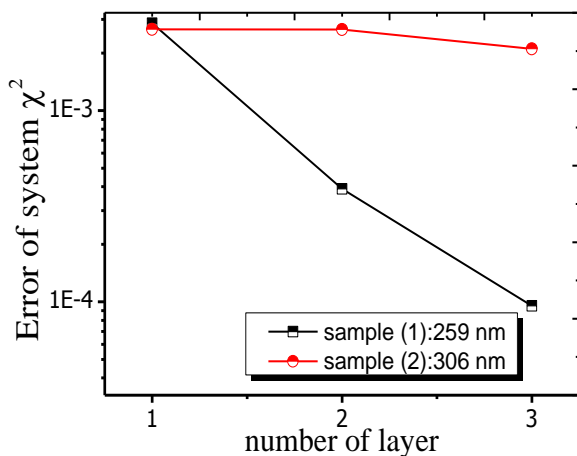


Fig. 5. Quadratic error χ^2 for three optical systems proposed for analysing ellipsometric spectra of sample S₁ and S₂

4. conclusion

We have investigated the optical properties of thin films of silicon oxynitride by spectral ellipsometry. The good agreement between calculated and measured spectra indicates that the proposed model correctly simulates such optical systems. It is clear that the results obtained by the multilayer system in the case of inhomogeneous samples indicate that more the proposed system is complex, more the adjustment is successful and this appears directly on the values of the error function, which decreases rapidly. For homogeneous film, a monolayer model is sufficient to analyze the ellipsometric spectra. Ellipsometric analysis shows that both deposited films are silica-rich probably because of the high reactivity of oxygen with silicon.

References

- [1] S. Engmann, V. Turkovic, H. Hoppe, and G. Gobsch, *J. Phys. Chem. C*, volume 117, issue 47, (2013) 25205.
- [2] L. Remache, A. Mahdjoub, E. Fourmond, J.L. Dupuis, M. Lemiti, *J. Physica status solidi (c)*, Volume 8, issue 6, (2011) 1893.
- [3] I. Tsuda, N. Nabatova-Gabain, *Encapsulated organic light emitting diode devices characterization by spectroscopic ellipsometry*, Horiba Document Japan, (2008).
- [4] W. Xie, Yi Zhao, J. Hou and S. Liu, *J. Appl. Phys.*, volume 42 (2003) 1466.
- [5] C. Eypert, application scientist-thin film division, characterization of pentacene-based thin film transistors using the MM-16 spectroscopic ellipsometer, *Horiba Document Japan* (2005).
- [6] X. Xiangdong, Z. Lianghang, H. Long, *J. Non-crystalline solids A*, volume 358, issue 1, (2012) 99.
- [7] R. Mahamdi, M. Boulesbaa, L. Saci, F. Mansour, C. Mollet, M. Collet, P. Temple-Boyer, *J. Nanosci Nanotechnol*, volume 11, issue 10, (2011) 9118.
- [8] S. Zhou, W. L. Changlong, *J. Thin film physics and applications*, Proceedings of SPIE, the International Society for Optical Engineering A. (2011) 7995.
- [9] A. M. Wu, H. Y. Yue X. Y., Zhang, *J. Materials science forum A*, volume 654, issue 2, (2010) 1712.
- [10] L. M. Schäde, *J. Thin solid films A*, volume 518, issue 7, (2010) 1830.
- [11] M. F. Saenger, J. Sun, *J. Thin solid films A*, volume 518, issue 7, (2010) 1830.
- [12] F. Rebib, E. Tomasella, V. Micheli, *J. Optical materials (Amsterdam) A*, volume 31, issue 3, (2009) 510.
- [13] A. Zhang and K. T. Chan, *J. Appl. Phys. Lett.* 83, (2003) 2524.
- [14] M. Faryad, A. Shoji Hall, G. D. Barber, T.E. Mallouk, *J. Optical society of America, JOSA B*, volume 29, issue 4, (2012) 704.
- [15] B. I. Akca, V. D. Nguyen, J. Kalkman, N. Ismail, G. Sengo, F. Sun, A. Driessen, T. G. Van Leeuwen, M. Pollnau, K. Wörhoff, and R. M. de Ridder, *J. Selected topics in quantum electronics*, volume 18, issue 3, (2012).
- [16] R. M. A. Azzam et Bashara, *Ellipsometry and polarized light*, North-Holland edition (1986).
- [17] M. Losurdo and K. Hingerl, *Ellipsometry at the Nanoscale*, Springer, Berlin, (2013).
- [18] M. Born and Wolf, *Principles of optics*, Pergamon Press Oxford (1970).
- [19] F. Abeles, *Thin Solid Films*, 34, (1976) 291.
- [20] D.A.G. Bruggeman, *Ann. Phys. (Leipzig)* 24 (1935) 636.
- [21] E.D. Palik, *Hand book of optical constants of solids*, Academic Press Handbook Series, Orlando, (1985).
- [22] J. A. Nelder and R. Mead, *Computer Journal*, 7(1965) 308.

Theoretical approach by the ADF-Band of electronic properties in oxides. Part I: ZnO

Fahima Boudjada, Hocine Chorfi and Abdelghani Djebli

Laboratoire de Cristallographie, Département de Physique, Faculté des Sciences Exactes, Université Constantine 1,
Route Ain El Bey 25000, Constantine -ALGERIE-

Received: 30 April 2014, accepted 26 May 2014

Abstract:

The ADF-Band (Amsterdam Density Functional), based on the Density Functional Theory (DFT), which is one of the most common methods used in ab-initio calculations in periodic systems such as polymers, thin films and crystals. Modeling of crystalline oxides state, at the nanoscale, through optimization of the crystalline structure. Computational calculation by the ADF-Band provides the opportunity to confirm the crystal structure and determine their electronic properties such as: the Energy gap (E_g), the Fermi level (E_f), the structure of the bands in the first Brillouin zone, the character and the nature of (B.C), (B.V) bands and the charge transfer in the oxides.

Keywords: ADF-Band, Energy gap, Fermi level, optimization, electronic bands, charge transfer.

1. Introduction

Among the oxides, ZnO has gained substantial interest in the research community. It is a II-VI binary compound semiconductor, n-type and crystallize in either cubic zinc blende or hexagonal wurtzite structure where each anion is surrounded by four cations at the corners of tetrahedron. A tetrahedral coordination is typical of sp^3 covalent bonding. The ionicity of ZnO resides at the borderline between covalent and ionic semiconductor. ZnO is economical and has technical applications such as Photo-catalytic, the sensitive thin layer gas, varistors, LED diodes, spintronics components, nanolasers...[1].

In our work, the ZnO crystal, with wurtzite hexagonal structure [2], was modeled by using the ADF-Band program [3-4-5-6]. We have employed the density-functional theory (DFT) using two different approximations, namely, the local-density approximation (LDA) and the generalized gradient approximation (GGA), in the exchange-correlation function to calculate the total energy and electronic structure of ZnO. Computational calculations allowed to:

- (i) Optimize the geometry of the structure.
- (ii) Represent the electronic bands, the first Brillouin zone, the nature and character of the bands.
- (iii) Plot the density of electronic states (DOS) with the Fermi level energy and Gap band.
- (iv) View the charge transfer, which reveals partial character in the oxide.

2. Computational details

2-1- Optimization of ZnO Crystalline Structure

a)-Creation of a unit cell: the structure selected has a hexagonal wurtzite unit cell with two lattice parameters $a=3.24 \text{ \AA}$ and $c=5.21 \text{ \AA}$, in the ratio of $c/a=\sqrt{8/3}=1.63$, and belongs to the space group of $P6_3mc$. The value of the parameter u (defined as the length of the bond parallel to the c axis in units of c) is 0.375 in an ideal wurtzite structure and deviation from that is probably due to lattice stability and ionicity such as zinc antisites and oxygen vacancies [7].

b) - Geometrical optimization: after optimization, we obtain the energy formation as a function of the number of unit cell. A new values of unit cell parameters are calculated at the equilibrium cohesive energy.

2-2-Electronic bands structure

a)-Bands diagram :the diagram is constituted by the plot of $E(k)$ where the wave vector (k) takes its values on the first Brillouin zone (Fig.1).

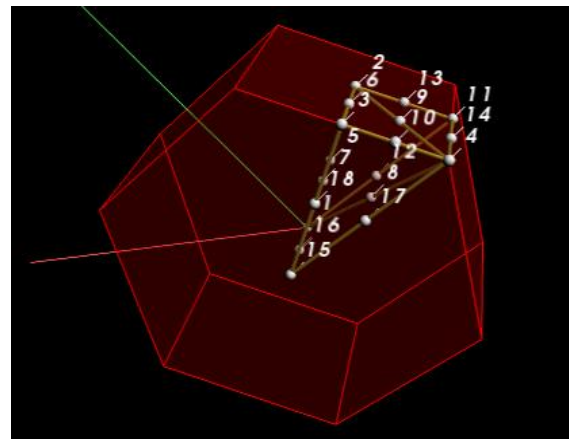


Fig.1: Path visualization of the First Brillouin Zone with k -points numbers of wurtzite structure.

b)-Bands nature: Fermi level is represented by a redline. The bands bellow E_f form the valence band (B.V) and whose above it form the conduction band (B.C)

c)-Bands character:With the function 'Double Isosurface (+, -)' we select the lowest and the highest energy band (occupied state) and the lowest energy band (unoccupied /virtual state).

2-3- Electronic density of state

a)-With 'DOS'function, we obtain the plot of the density of states in terms of energy.

b)-To view the contribution to the bands, we use 'addgraph'subfunctionand select Oxygen or Zinc atom.

2-4-Charges transfer

The charges transferis determined by the 'density deformation'functionand represented by'cuts plane (+/-)'subfunction.

3. Results and Discussions

3-1) By using a convergence criterion equal to 0.001 (example) for one unit cell and teen unit cell, we obtainthe plot of energy formation. The optimized energy appears as -0.5747 a.u and -0.5787a.u as it is shown in the figure1 and figure2 respectively.

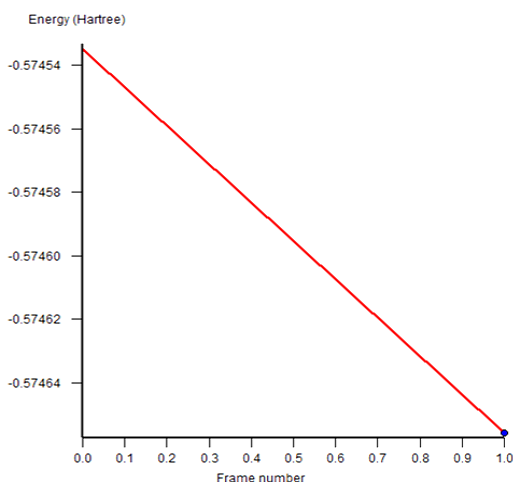


Fig.2: Energy of formation forone unit cell.

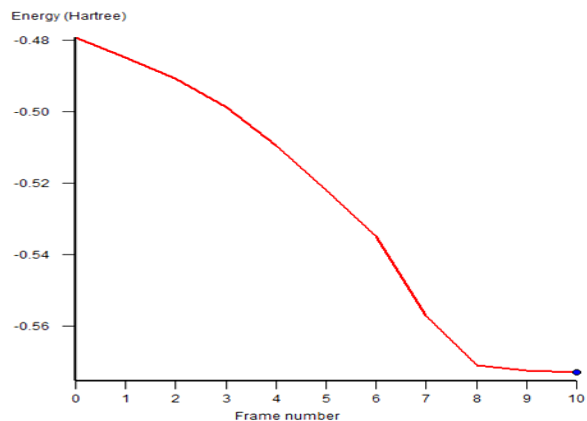


Fig.3: Energy of formation for a fragment (ten unit cells).

3-2) The bandwhose energies are between the values $E_f \pm 0.75$ a.u are represented with a number of energy values equal to 300.

The diagram band (Fig.4) shows that:

-ZnO material is n-type semiconductor, anisotropic and with a direct gap.

-The valence band is constituted by nine bands (which come from the occupied orbital) double degenerate at unique k-point1 ($\Gamma/k=0,0,0$).

-The conduction band is constituted by five bands, which come from the unoccupied / virtual orbitals.

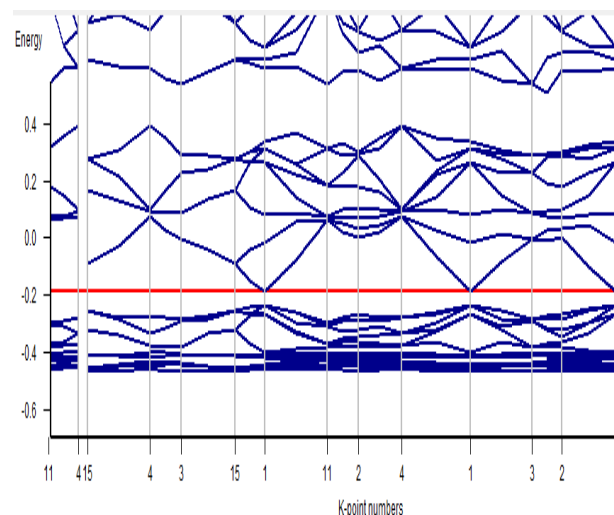


Fig.4 :Diagram band of zinc oxide (ZnO).

-To visualize the character of the valence band, we select the lowest band of occupied state $k=(0,0,0)$ (Fig.5) and highest band of occupied state $k=(0,0.8,0.8)$ (Fig.6). For the conduction band, we select only the lowest band of unoccupied/virtual state $k=(0,0,0)$ (Fig.7).

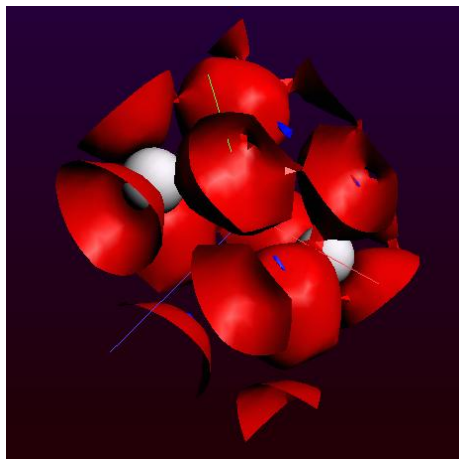


Fig.5: 2s-orbital of Oxygen atom.

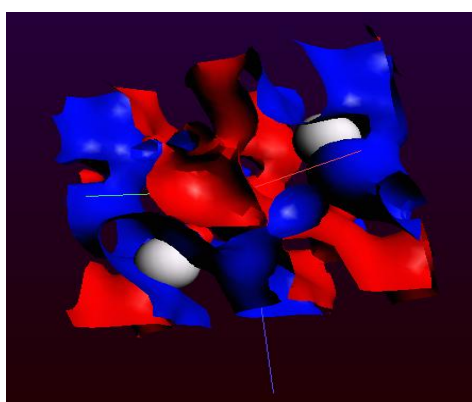


Fig.6: 2p-orbital of Oxygen atom.

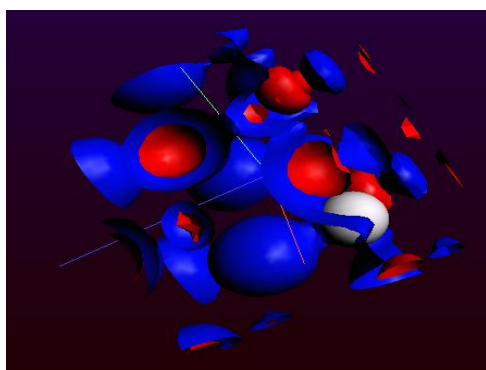


Fig.7: 4s-orbital of Zinc atom.

3-3) From the band gap information (fig.4):

The standard LDA(VWN) and GGA(BLYP-D) calculations underestimate the ZnO band gap to be as low as $E_g^{LDA}=1.304\text{eV}$ and $E_g^{GGA}=1.550\text{eV}$, as opposed to $E_g^{exp}=3.37\text{eV}$. This is due to the fact that the d-electrons are in the valence band and are properly taken into account and is in good agreement with the literature [7].

The plot of the density of states in terms of energy is shown by Fig.8.

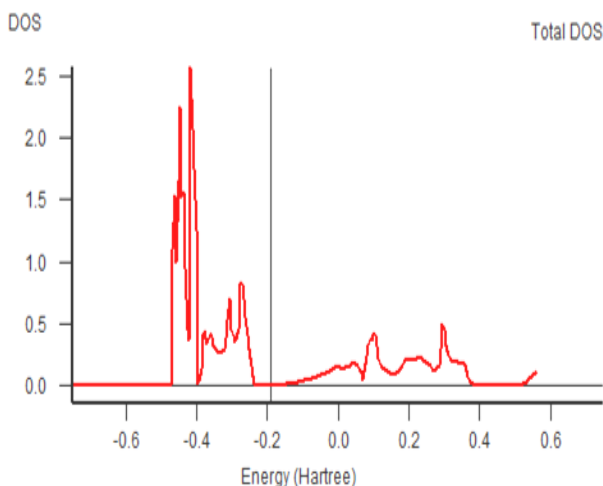


Fig.8: Total density of states In ZnO bulk.

To view the contribution to the bands (Fig.8), we select the Oxygen atom and obtain the Figure 9, which shows that the major contribution to conduction band (C.B) comes from Zinc atoms and the major contribution to valence band (B.V) from Oxygen atoms.

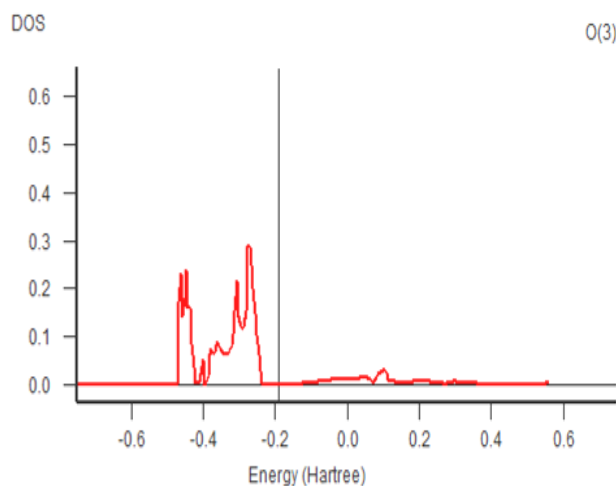


Fig.9: Density of States of Oxygen atoms in ZnO bulk.

3-4) The Fig(III-4-1) -Charge transfer in ZnO (Fig.10) shows that a charge is added (blue color) near the Oxygen and removed (red color) from the Zinc atom.

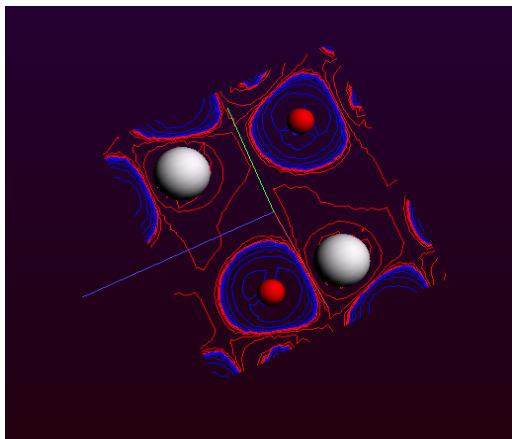


Fig.10: Charge map of the charge density in ZnO.

The amount of charge is only about 0.33. This is of course due to the fact that the 2p-Oxygen orbital overlaps quite significantly with the Zinc region (Fig.11).

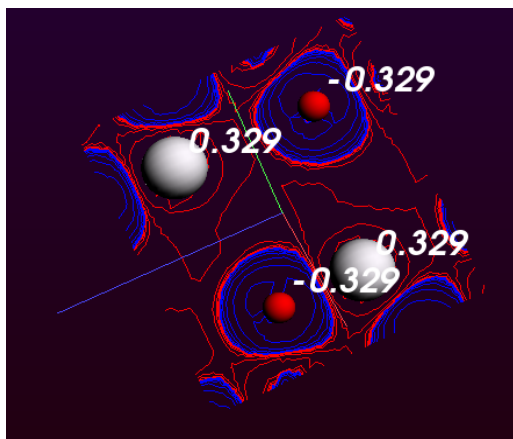


Fig.11: Amount of charge in ZnO.

4. Conclusion:

In addition to the agreement between the experimental values and geometric confirmation [9-10], the underestimation of the ZnO band gap with standard LDA and GGA methods indicate that the function used is not suitable. However, they tell us about the character and nature of the valence band (B.V) and the conduction band (B.C) and the charge transfers. In the

case of ZnO, the valence band (B.V) come from 2p-orbital of Oxygen atoms and the conduction band (B.C) from 4s-orbital of Zinc atoms. The charge transfer is only partial. The ADF Band offers also the possibility of doping, by insertion or substitution, with various proportions using the procedure of fragmentation.

Acknowledgment

This work was accomplished in the 'Laboratoire de cristallographie - Université Constantine1-'Algeria and supported by the 'CNEPRU'.

References

- [1] S.J.Chen, Y.C.Lui, H.Jiang, Y.M.Lu, J.Y.Zhang, D.Z.Shen, X.W.Fan, Journal of Crystal Growth, Vol285(2005).
- [2] A.Rivaton, B.Mailhot, J.Soulesin, H.Varghese, J.L.Gardette, Euro.Polym.J, 38, 1349(2002).
- [3] F.Tran, and P.Blaha. Physical Review Letters 102, 226401(2009).
- [4] V. I. Asimov, F. Aryasetiawan, and A. I. Lichtenstein, Journal Physics: Condensed Matter 9, 767(1997).
- [5] M. Kuisma, J. Ojanen, J.Enkovaara, and T. T. Rantata. Physical Review B 82, 115106(2010).
- [6] J. P. Perdew, A. Ruzsinsky, G. I. Csonk, O. A. Vydrov, G. E.Scuseria, L.A.Constantin, X.Zhou and K. Burke. Physical Review Letters 100 136406(2008).
- [7] U. Ozgur, Ya. I. Alivov, C. Liu & al. Journal of Applied Physics 98, 041301 (2005).
- [8] S. N. Steinmann, and C. Corminboeuf, Journal of Theory and Computation 132, 3567 (2011).
- [9] D. Alfe, Computer Physics Communications 180, 2622 (2009).
- [10] S. Grimme, S. Ehrlich, and L. Goerigk Journal of Computational Chemistry 32, 1457 (2011).

Modeling of surface tempering by a pulsed laser beam: Study of the material type's influence

Nadir Boutalbi¹, Mohamed Najib Bouaziz² and Hamza Ali Agha^{1,2}

¹Department of Mechanics Engineering, University of Abderrahman MIRA BEJALA
boutalbinadir@yahoo.fr

²Laboratory of Biomaterials and Transport Phenomena, U.Y.F. Medea, BP 164, 26000, Medea

Received: 26 April 2014, accepted 19 June 2014

Abstract

In recent years, laser technology has become one of the bases of modern technology thanks to its importance and its effectiveness to achieve what other classical energy sources are unable to do, especially in the process of surface tempering of materials. During the current industrial competitiveness, it is too hard to realize products that would stay intact, resistant to corrosion, and preserve by time their mechanical, electrical, optical or thermal properties. Laser surface tempering of materials can be introduced more quickly, in the sense of reaching high accuracy, requires a control of processes. The latter has not provided experimentally a proper solution, which encouraged researchers to develop several mathematical models. Moreover, mathematical modeling reduces the experimental cost and predicts the best parametric data and their influence on the optimization of the processing operation.

In this work, we suggest a semi-analytic solution for the equation of heat conduction resulting from laser surface tempering of semi-infinite material, in 1D, with a convective boundary condition and receiving a pulsed laser beam on its lateral face. A Semi-analytical approach, based on GAVER-STEHFEST algorithm for the inversion of the solution in real domain is adopted. And the effect of the material's types on the temperature is obtained and discussed.

Keywords: Surface tempering, pulsed laser beam, modeling:

1. Introduction

With the ever more precise answers they provide to increasingly diverse and demanding industrial situations, the laser surface tempering has become essential due to its extreme power and energetic localization. It allows obtaining more preferment structures that are difficult or impossible to obtain by classical energetic sources, and helps most of the time solving problems related to the optimization of surface properties[1-2]. Surface Tempering by laser can be more quickly introduced in a sense to reach an enhanced precision using a command control of the process. However, the control of the spatial and temporal evolution of temperature in the material is essential during the operation. [3]

In the field of metallurgy, particularly in surface tempering of metals by the laser technique, the problem of the process control has not yet found an adequate solution through experimental measures

which encouraged researchers to develop several analytical, numerical and mathematical models[3-9], based on simplified and realistic hypothesis in accordance with a description of the probable induced effects and phenomena which govern heat treatment. Mathematical modeling reduces the

experimental cost and enhances the understanding of the implied physical processes. [4]

The main problem mentioned by several authors, concerns the adoption of the boundary conditions while using the time-dependent laser source which explains the limited works in this sense. The experience shows that the use of periodic laser pulses allows getting several forms resulting from the evolution of the transitory temperature's profile that develops inside the material during the treatment. This makes it possible to modify the action's period of the thermal process, this is on one hand. On the other hand, the reached temperature is higher than the temperature of structural transformation related to the processed material's type, without reaching very high surface temperatures and with a better use of energy. [10]

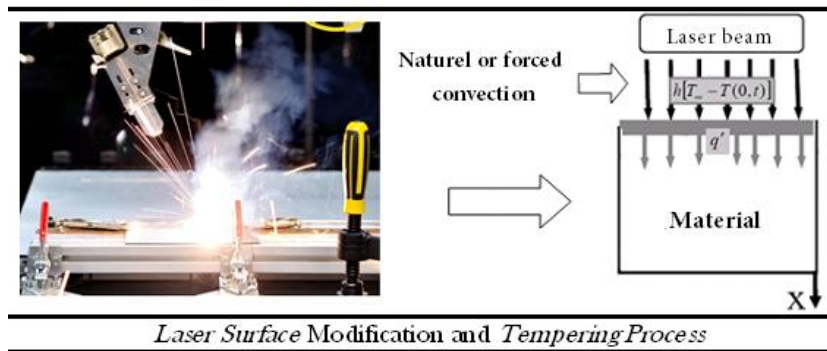
The temperature profile of surface hardening for material considered as semi-infinite medium, with a convective boundary condition and receiving a laser source of periodic pulses on its lateral face cannot be simulated directly by the analytical formulations. Among the mathematical models which have received particular attention are those of Zubair and Chaudhry [6], are reported and discussed in this paper. It is on the basis of this development that a semi-analytical model is developed. And the effect of

material type's on the temperature profile is also obtained and discussed.

the critical temperature of the structural change, and slightly lower than its melting point. The Cooling of the treated zone is done by quenching towards the core of the piece.

2. Mathematical analysis

Surface tempering consists of heating locally and rapidly the material to a temperature superior to



The phenomena of this process for a semi-infinite, homogeneous and isotopic body receiving on its lateral facing a laser beam depending on time is given by the following differential equation:

$$\left\{ \begin{aligned} \rho C_p \frac{\partial T}{\partial t} &= k \frac{\partial^2 T}{\partial x^2} + \dot{I}_0(t)(1-R)\mu \exp(-\mu x) f(t) \\ f(t) &= \begin{cases} 1 & t \leq \tau \dots \text{heating_phase} \\ 0 & t > \tau \dots \text{cooling_phase} \end{cases} \end{aligned} \right. \tag{1}$$

The initial and boundary conditions are modeled as follows:

$$\left\{ \begin{aligned} T(x,0) &= T_0 \\ -k \frac{\partial T(x,t)}{\partial x} \Big|_{x=0} &= h[T_\infty - T(0,t)] \\ \frac{\partial T(\infty,t)}{\partial x} &= 0 \end{aligned} \right. \tag{2}$$

• **The analytical solution proposed by Zubair-Chaudhry**

The solution for equation (1) of the heating phase in the Laplace domain is obtained by the Laplace transform then by analytical inverse transform, the solution in the real field is given by the following compact solution:

$$\theta(x,t) = (T_\infty - T_0) \left[\operatorname{erfc} \left(\frac{x}{2\sqrt{\alpha t}} \right) - E \left(\frac{hx}{k}, \frac{\alpha t}{x^2} \right) \right] - \frac{\mu(1-R)}{\rho C_p} \left[\frac{\left(\mu + \frac{h}{k} \right)}{\frac{h}{k}} \times \left\{ \operatorname{erfc} \left(\frac{x}{2\sqrt{\alpha t}} \right) - E \left(\frac{hx}{k}, \frac{\alpha t}{x^2} \right) \right\} * \left\{ \frac{\partial}{\partial t} [\exp(\alpha \mu^2 t) * \dot{I}_0(t)] \right\} - \left\{ \exp(-\mu x + \alpha \mu^2 t) * \dot{I}_0(t) \right\} \right] \tag{3}$$

3. Critic:

The analytical solutions obtained by **Zubair and-Chaudhry** are limited to simple variable laser sources, "details are shown in [6]", because of the inability to perform a simplification of the compact solution due to the convolution product(*).

Concerning periodic pulses of laser signals, which are recognized in the field of material processing, having a complicated mathematical formulation in the real field, such as laser beam of triangular pulses, **Table1**, this complexity is due to the summation

Table 1 : Representation of the laser periodic signal, type triangular

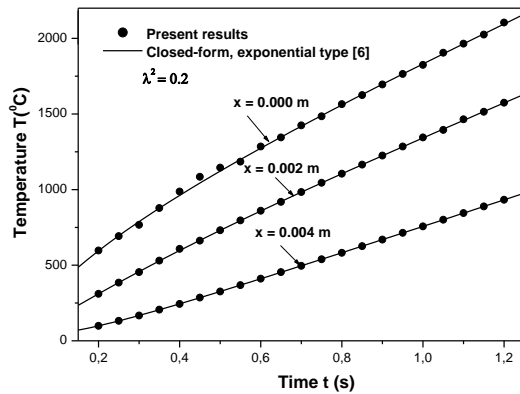
<i>Graphics representation</i>	<i>Governance equation</i>
	$i_0(t) = \sum_{n=0}^{\infty} I_0 \frac{t}{a} (-1)^n [u(t - na) - u(t - (n+1)a)]$

4. Validation of the model

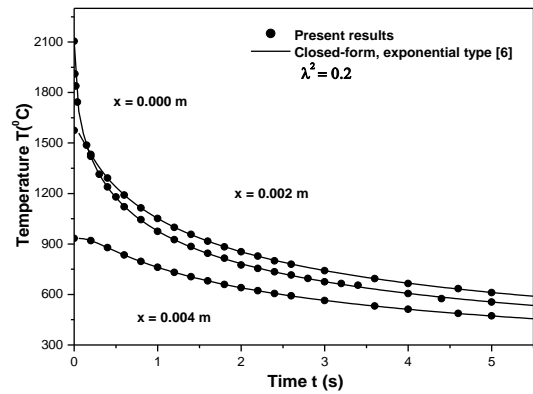
Extension of the procedure:

In this work, we solve the problem with a semi-analytical approach. The basis of our approach is based on the Laplace transform; the compact

the most practical one for the inversion is that of **GAVER-STEHFEST** [11] it is used to solve equation (3) for a triangular laser signal type in real time, following a FORTRAN program. The results



Heating phase



Cooling Phase

Validation of the proposed semi-analytical solution with the analytical solution of **Zubair - Chaudhry** [6] for the laser source type exponential $i_0(t) = I_0 \exp(\lambda^2 t)$

solution in this field is given by **Zubair-Chaudhry**.

To avoid the problem discussed due to the analytical inversion, we can use numerical methods;

are collected for four types of materials **Table 2**, aiming at studying their influence on the temperature's profile.

Table 2 : Thermo-physical properties of materials used in the simulation

Material	C_p [J / KgK]	k [W / mK]	ρ [Kg / m ³]	α [m ² / s] $\times 10^{-6}$	μ [1 / m] $\times 10^7$	Melting point [°K]
Steel	460	80.3	7880	22.15	6.16	1800
Nickel	447	90.3	8900	22.696	6.75	1726
Copper	383	386	8954	112.5576	6.7	1356.6
Chrome	450	94	7190	29.0527	6.7	2130

5. Results and discussion :

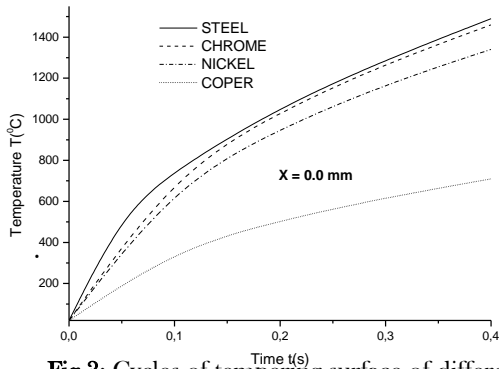


Fig 3: Cycles of tempering surface of different materials

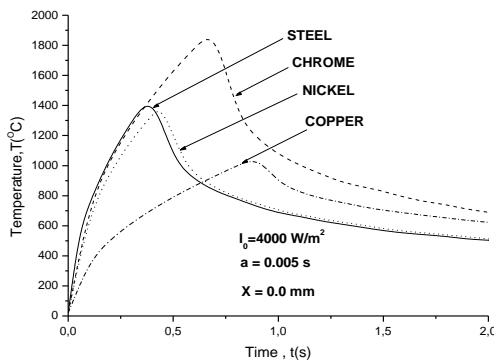


Fig 4: Temperature profile evolution in the Heating phase for different materials

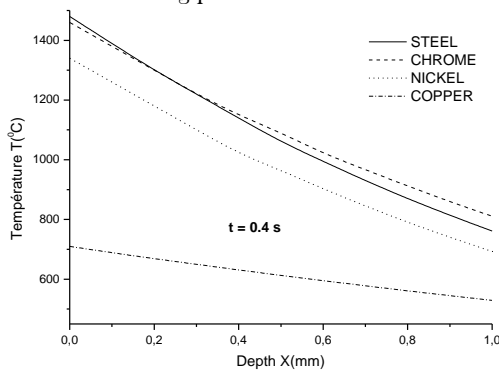


Fig 5: Evolution of temperature in depths for different materials in heating phase at $t=0.4s$

fig3 shows that the evolution of temperature profiles differ from one material to another, however, all these materials are kept in the same processing conditions, a simple comparison (Fig.4) reveals that the material with the lowest coefficient of absorption and thermal diffusivity (Table 2) shows the most advanced profile of surface temperature in the following order, Steel, Chrome, Nickel and finally Copper. On the other side, **fig5** shows that temperature gradient for the different materials becomes increasingly important in the sense of the decrease in thermal conductivity (Table 2), while the effect of temperature penetration into the different materials becomes also important in the following order, copper, Chrome, Nickel and finally steel, in the sense of the increase in thermal conductivity. So

for these reasons, it is preferable to use the powerful lasers in the surface tempering of materials which have an important thermal conductivity in order to avoid material hardening in volume.

6. Conclusion:

The surface tempering process of a semi-infinite body in 1D, with a convective boundary condition, receiving a periodical laser source pulses on its lateral surface cannot be simulated directly by analytical formulations.

A semi-analytical approach based on GAVER-STEHFEST algorithm for the inversion of the solution in the real field is adopted. The effect of the material's types on the temperature profile during the heating phase is also noted and discussed for four different kinds of materials.

Nomenclature

τ : Time interaction laser-material in the heating phase [s], λ^2 : Parameter of the laser pulse [1/s], R : coefficient of Reflectivity, T_0 : initial temperature of material, T_∞ : environment temperature [$^\circ K$], $i_0(t)$: Power of the laser source [W/m^2], $\theta = T - T_0$

$$E\left(\frac{hx}{k}, \frac{\alpha t}{x^2}\right), \text{ a known complex function [6]}$$

Bibliographical References

- [1] PANTELIS D., EngineerTechnics, Vol. MD2, No. M1240, S(1993).
- [2] DESALOS Y. and LESTART F., EngineerTechnics, Vol. MD1, No. M1205, (1996).
- [3] J. BESSROUR andtal, Int. J of thermal science, 41 (2002), pp.1055-1066.
- [4] YILBAS. S. B. and KALYON. M., International Journal of Heat and Mass Transfer, Vol.45, (2002), pp. 1571-1582.
- [5] BLACKWELL B.F., ASME J. Heat Transfer, Vol.112, (1990), p. 567-571.
- [6] ZUBAIR. S. M and CHAUDHRY. M.A., Int. J. Heat Mass Transfer. Vol. 39, No. 14, (1996), pp. 3067 -3074.
- [7] YILBAS. S.B. and SAMI M., Int. Comm. Heat Mass Transfer. Vol. 24, No. 6, (1997), pp. 785 -791.
- [8] BOUAZIZ M. N., BOUTALBI N., International Journal of Thermophysics, Vol. 32, No. 5, (2011), pp.1047-1059.
- [9] GUSTAVO G. and TIEN-CHEN J., International Journal of Heat and Mass Transfer, Vol.43, (2000), pp.2177-2192.
- [10] SHUJA S.Z., doctoral thesis, king FAHD university of petroleum and minerals, Dhahran SAUDI ARABIA, (June 1998), pp.319.
- [11] H. STEHFEST., Communications of the ACM, Vol.13, (1970), pp.47-49

Phosphorus profile optimization for conventional crystalline silicon solar cells emitters

H. Ghembaza^a, A. Zerga^a and R. Saïm^b

^aResearch Unit in Materials and Renewable Energy (URMER), Tlemcen University, Po Box 119 Tlemcen, 13000 Algeria

^bLaboratoire Energétique et Thermique Appliquée (ETAP), Tlemcen University, Po Box 119 Tlemcen, 13000 Algeria

Received: 11 February 2014, accepted 15 June 2014

Abstract

The basic mechanisms of dopants diffusion in silicon are translated from Fick's laws. Their resolutions led us to determine the distribution of impurities versus time. This distribution is described mathematically by a Complementary Error Function in a first step and a Gaussian redistribution in a second time. The best approach is designed using a numerical analysis and simulation. To do this, we are interested in simulating the phosphorus diffusion by the Silvaco® Simulation Code. The first results obtained led us to initiate a reflection on the influence of diffusion parameters on the electrical characteristics of solar cells. Thus, various simulations were conducted to show the influence of temperature and diffusion time on the shape of diffusion profiles, and this while maintaining a surface concentration of phosphorus in constant close to the solubility limit of this dopant in silicon. Controlling the formation of emitters by the variation of the diffusion parameters is therefore an effective way to improve the quality of emitters and an opportunity to increase the performance of mc-Si conventional solar cells by about 2.5% absolute.

Keywords: Solar Cell, Crystalline Silicon, Diffusion, Emitter, Passivation

PACS:

1. Introduction

The emitters of the industrial silicon solar cells formed by POCl₃ diffusion is well known and largely used in the photovoltaic industry. During the diffusion, the phosphorus oxychloride (POCl₃) reacts with oxygen to form the Phosphorus Silicate Glass (P.O.) which is deposited on the silicon surface and releases the phosphorus which can then diffuse far in the silicon to form the p-n junction. This diffusion can be obtained in a conventional furnace under atmospheric pressure, but this technique present the difficulty to ensure the homogeneity of the formed emitter. However, another diffusion technique allows phosphorus doping under low pressure starting from a liquid source; the POCl₃. This allows an increase in the kinetic of gases which offer a better uniformity on the solar cells and a good reproducibility.

Several types of emitters can be obtained with the variation of the diffusion parameters, namely:

temperature, time, pressure, surface concentration as well as, the addition of a possible pre-oxidation step. This latter is an enough method for the control of the presence of the electrically active phosphorus. In our study we are interested to the low sheet resistance emitter which is necessary for a good ohmic contact by screen-printed method. The numerical simulation code (Silvaco®) is used in order to show the effects of the phosphorus diffusion parameters on the performances of the crystalline silicon.

2. Modeling

To model the phosphorus diffusion profile in crystalline silicon, we have based on the PLS model included in Silvaco Athena® Code for an emitter with initial boron doping of 10¹⁶ cm⁻³ under a furnace pressure of 0.2 bars.

The diffusion of phosphorus in silicon is based on the Fick's laws, which stipulates that the diffusion

profile follows initially a Complementary Error Function and a Gaussian function in a second stage. However, an experimental phosphorous diffusion profile was used to validate our numerical simulation results.

This experimental profile was obtained with phosphorus diffusion in crystalline silicon at 825°C during 30 minutes. The sheet resistance of emitter was about 40Ω/sq. The phosphorous profile was determined by the Secondary Ion Mass Spectroscopy (SIMS).

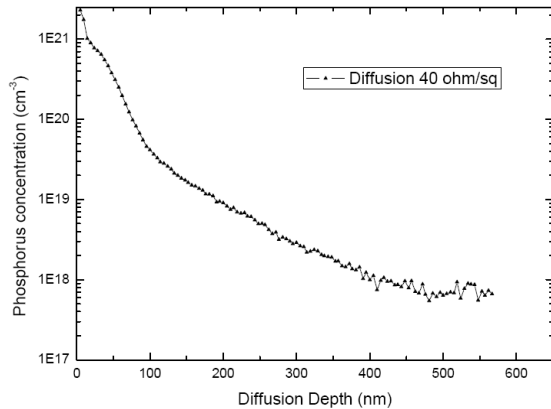


Figure 1 SIMS phosphorus diffusion profile.

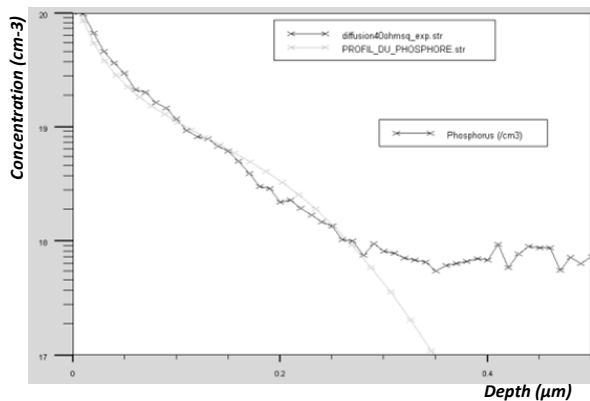


Figure 2 Experimental phosphorus diffusion profile modeling.

By using the Silvaco simulation code we can adjust the adequate profile to model the SIMS experimental profile (figure 2).

In other hand, we varied the diffusion parameters for a thorough study of the diffusion profiles:

2.1. Influence of temperature

The figure below show the variation of phosphorous profile with different diffusion temperature. As the temperature increases, doping increases, and the formed junctions are deeper. This behavior is explained by the variation of the coefficient diffusion and the limit of solubility with the

temperature. In addition, we observe a reduction in the sheet resistance of the emitter when the temperature increases, as well as a lengthening of the formed junction. We present the following profiles for a 45 min diffusion times.

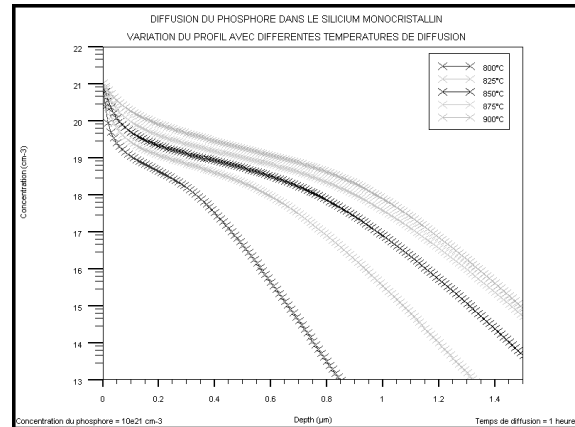


Figure 3 Variation of phosphorus diffusion profile versus temperature

The temperature is the key parameter for the phosphorus diffusion in silicon, a range of 800 to 850°C is allowed for acceptable sheet resistances in photovoltaic industry.

2.2. Influence of diffusion time

Solving Fick's equations, leads us to two cases for doping distribution: pre-deposition and the drive-in steps. One could however, easily to note that the influence of the diffusion time is more important for a fixed pre-deposition time and a variable drive-in time, since the quantity of phosphorus deposited at the pre-deposition time is the infinite source of the doping agents for the redistribution.

A longer drive-in time allows a lengthening of the concentration profile which brings amount of phosphorus introduced into silicon. The following figure illustrate an increase in the junction depth, and a decrease in the sheet resistance, at 800°C:

2.3. Influence of surface concentration

When the flow of POCl_3 is higher, doping increases consequently, since when the doping concentrations is lower, the quantity of phosphorus is insufficient to obtain uniform phosphorus glass. When the surface concentration increases, a strong non-linearity are observed on the profiles

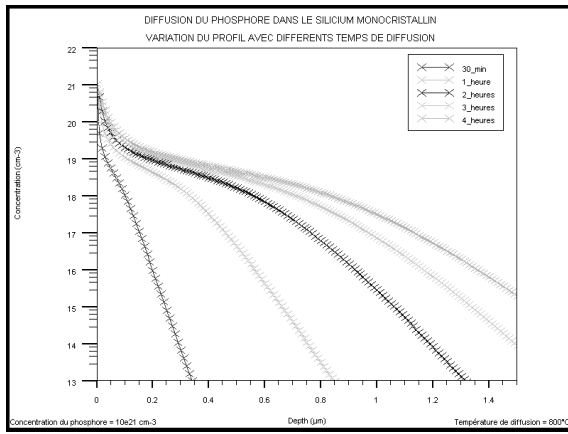


Figure 4 Variation of phosphorus diffusion profile versus diffusion time

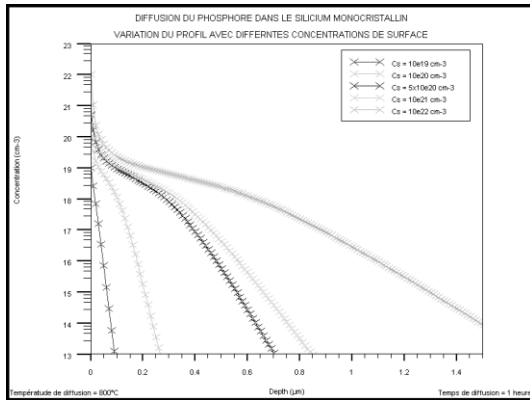


Figure 5 Variation of phosphorus diffusion profile versus phosphorus concentration

3. Results and discussion

3.1. Optimization of the emitter formation - evaluation of the dead layer

At high phosphorus concentrations, the emitter has an increased sensitivity to recombination. This is manifested by the creation of a zone called the “dead layer” which characterizes the presence electrically inactive phosphorus, due to the formation of precipitates.

The optimization of the emitter formation leads to the minimization of the formed dead zone. This area can be evaluated directly from the diffusion profile of phosphorus (SIMS profile) and the intersection with solid solubility and the charges concentration.

3.2. Effect of the diffusion parameters on the electric characteristics of the solar cell

Several studies have shown the effect of doping on the sheet resistance of the emitter, which will influence the parameters of the solar cell in the industrial processes.

We varied the concentrations of phosphorus and we obtained the following values for the emitter’s sheet resistances:

TABLE 1

Emitter sheet resistance versus phosphorus doping

Surface concentration (cm ⁻³)	Sheet resistance (ohm/sq)
5×10^{20}	159.48
6×10^{20}	138.63
7×10^{20}	133.56
8×10^{20}	136.06
9×10^{20}	135.97
10^{21}	147.64

We studied the influence of the variation of the diffusion parameters of the emitter on the solar cells characteristics. In the following table, we combine our results:

TABLE 2

Variation of the solar cells characteristics with the diffusion parameters

Parameters	Conventional solar cell	Simulated solar cell	Units
Isc	4.9	6.5	A
Voc	0.6	0.6	V
Vmax	0.5	0.5	V
Imax	4.7	6.1	A
Pmax	2.7	3.3	W
FF	82.9	82.1	%
η	13.6	15.73	%

When the new distribution of phosphorus is taken into account, we note a change of each electric performance (short-circuit current I_{sc} , tension in open circuit V_{oc} , fill factor FF and efficiency η).

Indeed, control of phosphorus diffusion by the variation of the diffusion parameters proved to be effective means to improve the emitter quality, since a variation of about 2.5% absolute in solar cell efficiency was observed.

4. Conclusion

In the case of conventional solar cells a high doping concentration of emitter ensure a better metallization by screen printing, but the front surface passivation is limited and it cause more losses by Auger recombination. Beyond these recombination, the

characteristic of the profile obtained with a high phosphorus concentration, is that when the surface concentration exceeds the limit solubility, the atoms of phosphorus in excess are incorporated in the form of precipitates. In this zone, the life time is significantly reduced, so the area containing the precipitates is often called dead layer, this translates into a low spectral response of the solar cells.

The collection of charges is reduced and the saturation current of the emitter is achieved by these recombination. These two factors, influence respectively on the short circuit current and open circuit voltage. The reduction in the emitter doping thus seems a solution to limit the losses by recombination. However, a weak doping involves an increase in the resistive losses. The doping of the emitter has opposite effects on the characteristic of the solar cell. His profile should be optimized to reduce the series resistance while minimizing recombination.

In this work we have presented an optimization of the diffusion process by an innovating technique at low pressure furnace in order to control the emitter formation of solar cells while ensuring a good passivation and a better electrical collection.

Our result proves that we can target certain electrical properties only by the manipulation and optimization of POCl_3 doping profile. It is shown that an efficiency increase of about 2% absolute can be obtained with these manipulations.

References

- [1] B. Bazar Bachi, Thèse de doctorat, INSA Lyon, 2010.
- [2] A. Bentzen, Phosphorus diffusion and gettering in silicon solar cells. PhD thesis, University of Oslo, 2006.
- [3] J. C. C. Tsai, Proceeding of the IEEE, Vol. 57, N° 9, 1969.
- [4] M. Sasani, Semiconductor Physics, Quantum Electronics & Optoelectronics, Vol. 7, N° 1, 2004.
- [5] S. Solmi and al., Dopant and carrier concentration in Si in equilibrium with monoclinic SiP precipitates. Physical Review, 1996.
- [6] Scotten W. Jones, « Diffusion in silicon », IC Knowledge LLC, 2008
- [7] F. Boucard, Thèse de Doctorat, Université Louis Pasteur - Strasbourg I, 2003
- [8] D. Mathiot, « Dopage et diffusion dans le silicium », Cours DEA, InESS Strasbourg, disponible sur : www-iness.c-strasbourg.fr/~mathiot/ressourceDopageDiff.pdf
- [9] E. M. Bazizi, Thèse de Doctorat, Université de Toulouse, 2010.
- [10] A. Cuevas and al., Proceedings of the 19th IEEE Photovoltaic Specialists Conference, 1987.
- [11] A. S. Bouazzi, Cours de technologie des CI, Chapitre 6 : Dopage et diffusion, ENIT, 2007.
- [12] M. J. Kerr, PhD Thesis, Australian National University, 2002.
- [13] A. Zerga, et al., in Proc. of the 21st EPVSEC, Dresden, Germany, 2006.

GC/MS Analysis and Antioxidant Activity of the Essential Oil leaves *Thymus numidicus* Poiret. growing in Mila

¹Zellagui Amar*, ¹Boutellaa Saber, ¹Arab Yasmine and ²Gherraf Noureddine

Laboratory of Biomolecules and Plant Breeding, Life Science and Nature Department, Faculty of Exact Science and Life Science and Nature, University of Larbi Ben Mhidi Oum El Bouaghi, Algeria.

² Process Engineering Department, Larbi ben M'hidi University, Oum Elbouaghi 04000, Algeria.

Received: 17 May 2014, accepted 26 June 2014

Abstract

Essential oil components of the leaves of *Thymus numidicus* growing in Mila have been studied by gas chromatography mass spectrometry GC/MS to afford 60 Sixty compounds representing 94.0 % of the total oil and mainly represented by oxygenated monoterpenes,. The main constituents of the essential oil from the leaves were thymol (41.2%), β -cymene (12.9%), chlorocresol (11.2%), β -linalool (10.7%) and methyl thymol ether (3.3%). The antioxidant activity was evaluated by spectroscopic method, used for that free radical compound (DPPH) and in comparison with vitamin C as a standard. The essential oil showed a moderate activity against free radical compound (DPPH) 17.4% at 1M.

1. Introduction

The genus *Thymus* L., belonging to the Lamiaceae family represented by around 350 species of perennial, aromatic herbs and subshrubs predominantly found in Mediterranean region, Asia, Southern Europe and North Africa [1], and comprised in Algeria over 12 species [2].

Thymus species are considered as medicinal plants due to their pharmacological and biological properties. In native medicine, flowering parts and leaves of *Thymus* species have been extensively used as herbal tea, tonic, carminative, antitussive and antiseptic, as well as for treating colds [1,3,4,5]. Recent studies have shown that, thyme have strong antibacterial, antifungal, antiviral, antiparasitic [6,7,8,9], sedative, antispasmodic [10,11], antioxidant [8,12,13] and antiaflatoxinogenic [14] activities.

Thymus species as well as many other aromatic plants biosynthesize variable amounts of volatile compounds known as essential oil; therefore, chemical classification of *Thymus* species was based on the main essential oil components and their chemical polymorphism, moreover, numerous chemotypes have been defined, such as carvacrol and thymol, γ -terpineol, thujone, geraniol, linalool and others [15]. Hence the main objectives of this study were:

- (i) determine the chemical composition of hydrodistilled oils of the leaves of *Thymus numidicus* Poiret. (End. W. Alg. Tun.) growing in Mila - Algeria by gas chromatography/mass spectrometry (GC/MS).
- (ii) Evaluate the antioxidant capacity of the plant essential oils.

2. Material and Methods

2.1 Plant material

The Leaves of *Thymus numidicus* Poiret. were collected at the end of April 2012 (flowering stage) from Grarem wilaya Mila (North Eastern Algeria). The plant was identified by Pr. Zellagui Amar, Oum El Bouaghi University. A voucher specimen was deposited at Laboratory of Biomolecules and Plant Breeding, Life Science and Nature Department under the code number ZA 140.

2.2 Extraction

Essential oils were obtained by hydrodistillation of 100 g of dried leaves using a Clevenger-type apparatus for 3 h. The oil was stored in sealed vials protected from the light at +4°C before analyses. The oil sample was subsequently analyzed by GC-MS.

2.3 Gas chromatography/mass spectrometry (GC/MS)

Analyses were performed with a Varian CP-3800 gas chromatograph equipped with a DB-5 capillary column (30m × 0.25 mm; coating thickness 0.25 μm) and a Varian Saturn 2000 ion trap mass detector. Analytical conditions: injector and transfer line temperatures 220 and 240°C, respectively; oven temperature programmed from 60°C to 240°C at 3°C/min; carrier gas helium at 1 mL/min; injection 0.2 μL (10% n-hexane solution); split ratio 1:30. Identification of the constituents was based on comparison of the retention times with those of authentic samples, comparing their linear retention indices relative to the series of n-hydrocarbons, and by computer matching against commercial (NIST 98 and ADAMS) and homemade library mass spectra built up from pure substances and components of known oils and MS literature data [16].

2.4 Antioxidant activity

The capacity of essential oil extracted from *Thymus numidicus* Poiret. leaves to reduce the radical 2,2-diphenyl-1-picrylhydrazyl (DPPH) was assessed using the method of Masuda *et al.* [17] modified in the laboratory. 15 μl of the essential oil at different concentrations was added to 1500 μl of a DPPH ethanolic solution. The mixture was shaken vigorously and left standing at room temperature for 05 min in the dark. The absorbance of the resulting solution was then measured at 517 nm. The normal purple color of DPPH will turn into yellow when its singlet electron is paired with a hydrogen atom coming from a potential antioxidant. The scavenging activity of essential oil was evaluated according to the formula:

$$\text{DPPH scavenging effect (\%)} = [(A_0 - A_1)/A_0] \times 100$$

Where: A_0 is the absorbance of the control at 05 min, and A_1 is the absorbance of the sample at different times. All samples were analyzed in three replications.

3. Results and Discussion

The composition and percentage of the compounds are summarized in Table 1. They are listed by order of their retention times. The oil yield was 0.8 % (w/w) based on the dried weight which means that the organs are a potential oil source. Sixty compounds were identified in the essential oil, representing 94.0% of the total oil. The essential oils were dominated by a large amount of oxygenated monoterpenes (12.4%), monoterpene hydrocarbons (2.6%) and sesquiterpenes hydrocarbons (2.3%), while the oxygenated sesquiterpenes (0.9%) contents were very low.

The main constituents of the essential oil were found to be, thymol (41.2%), β-cymene (12.9%), chlorocresol (11.2%), β-linalool (10.7%) and methyl thymol ether (3.3%) and carvacrol (2.8%) and some other compounds were only present in minor amounts. In total, essential oil composition of *Thymus numidicus* Poiret. was

considered as a rich source of oxygenated Monoterpenes

The predominance of phenolic compounds is in agreement with previous results reported from *Thymus numidicus* Poiret. essential oil from Constantine (North-Eastern of Algeria) [18] which was mainly represented with thymol (68.2%), carvacrol (16.9%) and linalool (11.5%). Whereas, *T.numidicus* (poiret) essential oil from Tizi Ouzou (North of Algeria) [19] was mainly represented with thymol (51.0%) followed by carvacrol (9.4%), linalool (3.3%), thymol-methyl-ether (3.2%) and *iso-*

caryophyllene (2.7%); in the same of *Thymus numidicus* Poiret. essential oil from Berrahal (area located 500 km East of Algiers) during the flowering stage, which was characterized by thymol (66.31%) as the major component, followed by linalool (8.61%), *p*-cymene (6.20%), γ -terpinene (6.12%) and carvacrol (4.31%) and *Thymus numidicus* Poiret. from Souk aharas (East of Algeria) that the major components were thymol (57.20%), linalool (9.26%), γ -terpinene (9.19%) and *p*-cymene (7.55%) [20].

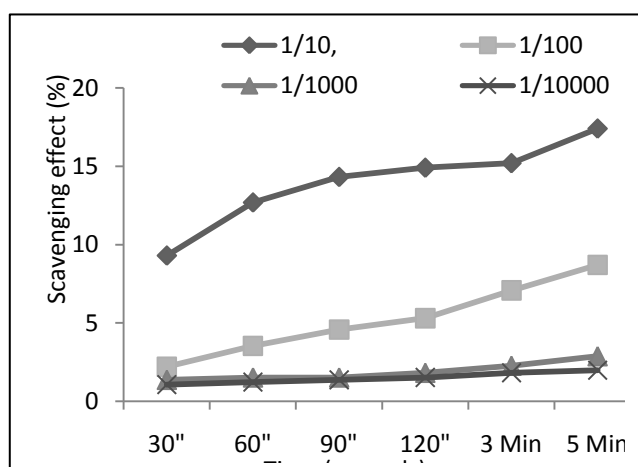
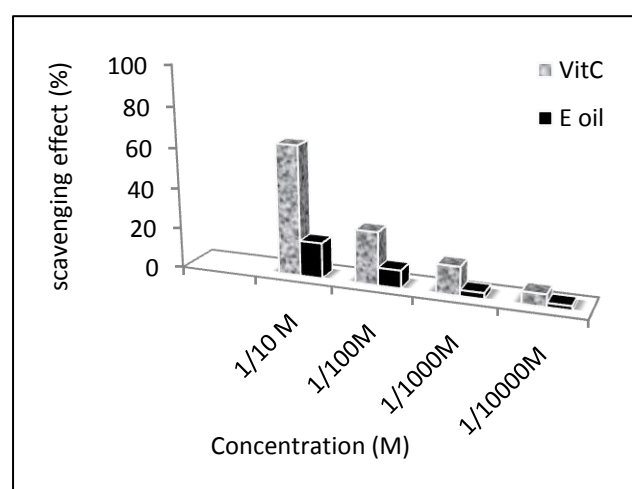
Table 1. Composition of the leaves essential oil of *Thymus numidicus* Poiret. growing in Mila

Pic	Chemical constituents	T _r	%
1	α -Thujene	4.535	0.2
2	Cyclofenchene	4.683	0.4
3	α -Phellandrene	4.935	0.1
4	α Pinene	5.078	0.1
5	Pentyl vinyl ketone	5.928	0.5
6	β -Myrcene	6.452	0.6
7	β -Pinene	6.760	0.4
8	1,3-Cyclohexadiene, 1-methyl-4-(1-methylethyl)-	7.219	0.3
9	β-Cymene	7.334	12.9
10	D-Limonene	7.917	0.2
11	c-Terpinen	8.781	0.2
12	Bicyclo[3.1.0]hexan-2-ol, 2-methyl-5-(1-methylethyl)-, (1.alpha.,2.alpha.,5.alpha.)-	8.958	0.7
13	Octanol	9.433	0.1
14	Octyl formate	9.604	0.1
15	1-Nonen-3-ol	9.715	0.1
16	5-Isopropyl-2-methylbicyclo[3.1.0]hexan-2-ol	10.187	0.1
17	β-Linalool	10.440	10.7
18	α -Campholenal	10.953	0.1
19	cis-Verbenol	12.063	0.1
20	Borneol	12.827	0.1
21	α -Terpieol	13.407	0.6
22	Thymol methyl ether	16.069	3.3
23	(1R,2R,3S,5R)-(-)-2,3-Pinandediol	16.636	0.2
24	(+)-3-Carene, 2-(acetylmethyl)-	17.662	0.1
25	2-Chlorooctane	18.276	0.1
26	Thymol	18.968	41.2
27	Carvacrol	19.201	2.8
28	Chlorocresol	20.278	11.2
29	cis-Verbenol	21.834	0.1
30	Copaene	22.589	0.1
31	β -Bourbonene	22.850	0.1
32	β -Caryophyllene	24.201	0.9
33	Germaecene D	24.661	0.1
34	β -cis-Ocimene	25.558	0.1
35	β -Famesene	26.216	0.1
36	α -Amorphene	26.635	0.2

37	4aH-cycloprop[e]azulen-4a-ol, decahydro-1,1,4,7-tetramethyl-	27.035	0.1
38	Ylangene	27.289	0.1
39	Ethanol, 2-(2-chloroethoxy)-1-phenyl-	27.397	0.1
40	α -Methylcyclohexene	28.191	0.6
41	α -Cubebene	28.523	0.3
42	α -Zingiberene	28.657	0.1
43	α -Caryophyllene=Humulene	29.512	0.2
44	Spathulenol	30.160	0.1
45	Caryophyllene oxide	30.277	0.3
46	Ethyl iso-allocholate	30.515	0.1
47	3,4-Dimethyl-2,5-diprop-2-enyl-2,5-dihydrothiophene 1,1-dioxide	31.558	0.1
48	δ -Cadinol, (-)-	32.739	0.1
49	Cubenol	32.893	0.1
50	alpha-Cadinol	33.187	0.1
51	Patchoulane	34.194	0.1
52	3-Ethoxy-1,1,1,7,7,7-hexamethyl-3,5,5-tris(trimethylsiloxy)tetrasiloxane	36.433	0.3
53	Ledol	36.626	0.1
54	1-Cyclohexene-1-butanol, 2,6,6-trimethyl-	38.894	0.1
55	1,2-Benzenedicarboxylic acid, bis(2-methylpropyl) ester	40.430	0.1
56	Hexahydrofarnesyl acetone	40.779	0.1
57	Cyclopropane, 2-methylene-1-pentyl-1-trimethylsilyl-	42.199	0.1
58	Stearic acid	44.857	0.3
59	Cycloisolongifolene, 8,9-dehydro-9-formyl-	45.548	0.3
60	Diazoprogesterone	46.709	0.1
94.0			

Table 2. Classification of the constituents of the *Thymus numidicus* Poiret.

Component	Peak area, %
Oxygenated monoterpenes	12.4
Monoterpene hydrocarbons	2.6
Oxygenated sesquiterpenes	0.9
Hydrocarbons Sesquiterpene	2.3
Aromatics	70.4

**Figure 1.** DPPH radical scavenging activity of essential oil at different times.**Figure 2.** DPPH radical scavenging activity of essential oil and Vitamin C.

The antioxidant activity of *Thymus numidicus* Poiret. essential oil was measured by using DPPH assay. The scavenging activity of the essential oil was tested at concentrations of 10^{-1} M, 10^{-2} M, 10^{-3} M and 10^{-4} M; Vitamin C was used as a standard. It has been showed that the radical scavenging capacity of the tested essential oil increased in a concentration and time dependent manner (figure 1). The highest DPPH radical scavenging activity (%) was shown by essential oil at 10^{-1} M (17.4 %), which was lower than the antioxidant activity of the standard vitamin C (Figure 2). Similar results were reported in a study of antioxidant effect of essential oils of *Thymus linearis* and *Thymus serpyllum* by different *in-vitro* tests [21].

There are a few reports about the antioxidant activity of *Thymus* essential oils [21,22,23] showed that essential oils containing high amounts of thymol and carvacrol were reported to possess the highest antioxidant activity [24,25,26] and the principal active compounds of these oils are principally carvacrol, thymol, citral, eugenol, 1-8 cineole, limonene, pinene, linalool and their precursors [27].

4. Conclusion

Our results demonstrate the high chemical variability of constituents found in genus *Thymus* in general and especially in *Thymus numidicus* Poiret. species and stresses the importance of investigations dealing with the chemistry of separate plant organs. our results showed that thymol was the main phenolic compound of the leaves of *Thymus numidicus* Poiret. essential oil collected from Grarem - Mila (Eastern Algerian) in flowering stage and possess a moderate antioxidant activity.

References

- [1] Z. Maksimovic, D. Stojanovic, I. Sostaric, Z. Dajic and M. Ristic, Composition and radical-scavenging activity of *Thymus glabrescens* Willd. (Lamiaceae) essential oil, Journal of the Science of Food and Agriculture, 88 (2008) 2036-2041.
- [2] P. Quezel, S. Santa, Nouvelle Flore de L'Algérie et des Régions Désertiques Méridionales. Tome II. Editions du Centre National de la Recherche Scientifique (C.N.R.S), 15 Quai Anatole France, Paris 1963.
- [3] S. Karaman, M. Digrak, V. Ravid and A. Iclim, Antibacterial and antifungal activity of the essential oils of *Thymus revolutus* Celak from Turkey, Journal of Ethnopharmacology, 76(2) (2001) 183-186.
- [4] C. Rota, J.J. Carraminana, J. Burillo and A. Herrera, In-vitro antimicrobial activity of essential oils from aromatic plants against selected foodborne pathogens, Journal of Food Protection, 67 (2004) 1252-1256.
- [5] B. Nickavar, F. Mojab, R. Dolat-Abadi, Analysis of the essential oils of two *Thymus* species from Iran, Food Chemistry, 90 (2005) 609-611.
- [6] M. Oussalah, S. Caillet, L. Saucier et M. Lacroix, Inhibitory effects of selected plant essential oils on the growth of four pathogenic bacteria: *E. coli* O157:H7, *S Typhimurium*, *S aureus* and *L monocytogenes*, Foods Control. 18 (2007) 414- 420.
- [7] M. Hazzit, A. Baaliouamer, A.R. Veríssimo, M.L. Faleiro et M.G. Miguel, Chemical composition and biological activities of Algerian *Thymus* oils, Food Chemistry, 116 (2009) 714-721.
- [8] H. Ghorab, A. Kabouche, Z. Semra, A. Ghannadi, E.B. Sajjadi, R. Touzani et Z. Kabouche, Biological activities and compositions of the essential oil of *Thymus ciliatus* from Algeria, Scholars Research Library, 5 (2013) 28-32.
- [9] L.A. El Ouali, F. El-akhal, W. Ouedrhiri, C.F. Ouazzani, R. Guemmouh et H. Greche. Thymus essential oils (*Thymus vulagris* and *Thymus satureioidis*) from center of Morocco: chemical composition and antimicrobial activity, les technologies de laboratoire, Vol 8 (2013) N°31.

- [10] M.A. Blázquez, M.C. Zafra-Polo et A. Villar, Effects of *Thymus* species extracts on rat duodenum isolated smooth muscle contraction. *Phytotherapy Research*. 3(1989) 41-42.
- [11] J.H. Safaei-Ghomi, A. Ebrahimabadi, Z. Djafari-Bidgoli & H. Batooli, GC/MS analysis and in vitro antioxidant activity of essential oil and methanol extracts of *Thymus caramanicus* Jalas and its main constituent carvacrol, *Food Chemistry*, 115 (2009) 1524-1528.
- [12] N. Zouari, N. Fakhfakh, S. Zouari, A. Bougatef, A. Karray, M. Neffati et M.A. Ayadi, Chemical composition, angiotensin I-converting enzyme inhibitory, antioxidant and antimicrobial activities of essential oil of Tunisian *Thymus algeriensis* Boiss. et Reut. (Lamiaceae), *Food and Bioprocess Technology*, 89 (2011) 257- 265.
- [13] M.H.H. Roby, M.A. Sarhan, K.A. Selim et K.I. Khalel, Evaluation of antioxidant activity, total phenols and phenolic compounds in thyme (*Thymus vulgaris* L.), sage (*Salvia officinalis* L.), and marjoram (*Origanum majorana* L.) extracts, *Industrial Crops and Products*, 43 (2013) 827- 831.
- [14] M. Razzaghi-Abyaneh, M. Shams-Ghahfarokhi, M.B. Rezaee, K. Jaimand, S. Alinezhad, R. Saberi & T. Yoshinari Chemical composition and antiaflatoxic activity of *Carum carvi* L., *Thymus vulgaris* and *Citrus aurantifolia* essential oils, *Food Control*, 20 (2009) 1018-1024.
- [15] I. Jabri-Karoui, I. Bettaieb, K. Msaada, M. Hammami, B. Marzouk Research on the phenolic compounds and antioxidant activities of Tunisian *Thymus capitatus*, *Journal of functional foods*, 4 (2012) 661 - 669.
- [16] P. Adams. Identification of Essential oils Components by Gas Chromatography/Mass Spectrometry, 4th Ed. Allured Publishing Corporation. Carol Stream, Illinois, 2007.
- [17] T. Masuda, S. Yonemori, Y. Oyama, Y. Takeda et T. Tanaka, Evaluation of the antioxidant activity of environmental plants: Activity of the leaf extracts from seashore plants, *J. Agric. Food Chem.*, 47(4) (1999) 1749-1754.
- [18] A. Kabouche, Z. Kabouche and C. Bruneau, Analysis of the essential oil of *Thymus numidicus* (Poiret) from Algeria, *Flavour. Frag. J.*, 20 (2005) 235-236.
- [19] F. Saidj, S.A. Rezzoug, F. Bentahar, C. Boutekedjiret Chemical Composition and Insecticidal Properties of *Thymus numidicus* (Poiret) Essential Oil from Algeria, *Journal of essential oil-bearing plants*, 11 (4) (2008) 397-405.
- [20] R. Giordani, Y. Hadeif et J. Kaloustian, Compositions and antifungal activities of essential oils of some Algerian aromatic plants, *Fitoterapia*, 79 (2008) 199-203.
- [21] A.I. Hussain, F. Anwar, S.A.S. Chatha, S. Latif, S.T.H. Sherazi, A. Ahmad, J. Worthington et S.D. Sarker, Chemical composition and bioactivity studies of the essential oils from two *Thymus* species from the Pakistani flora, *LWT - Food Science and Technology*, 50 (2013) 185-192.
- [22] M. Jukic et M. Milo, Catalytic Oxidation and Antioxydant Properties of Thyme Essential Oils (*Thymus vulgaris* L.), *Croatica Chemica Acta*, 78 (1) (2005) 105-110.
- [23] S. Bouhdid, M. Idaomar, A. Zhiri, D. Bouhdid, N.S. Skali, J. Abrini, *Thymus* essential oils: chemical composition and in vitro antioxidant and antibacterial activities. *Biochimie, Substances Naturelles et environnement, Congrès International de biochimie, Agadi*, (2006) 324-327.
- [24] A. Dapkevicius, T.A. Van Beek, G.P. Lelyveld, A. Van Veldhuizen, A.E. De Groot, J.P.H. Linssen & R. Venskutonis. Isolation and structure elucidation of radical scavengers from *Thymus vulgaris* leaves, *Journal of Natural Products*, 65(2002) 892-896.
- [25] B. Schwämmle, E. Winkelhausen, S. Kuzmanova et W. Steiner, Isolation of Carvacrol Assimilating Microorganisms, *Food Technol. Biotechnol.*, 39 (4) (2001) 341-345.
- [26] B. Sultana, F. Anwar & R. Przybylski, Antioxidant activity of phenolic components present in barks of *Azadirachta indica*, *Terminalia arjuna*, *Acacia nilotica*, and *Eugenia jambolana* Lam. *Trees, Food Chemistry*, 104 (3) (2007) 1106-1114.
- [27] M. Oussalah, S. Caillet, L. Saucier and M. Lacroix, Antimicrobial effects of selected plant essential oils on the growth of a *Pseudomonas putida* strain isolated from meat, *Meat Science*, 73 (2006) 236-244.